FEEDBACK ON TOOL-TISSUE INTERACTIONS WITH OPTICAL COHERENCE TOMOGRAPHY AND DEEP LEARNING

Dissertation (cumulative) approved by the
Doctoral Degree Committee of
Hamburg University of Technology

in pursuit of the academic degree of

Doktor-Ingenieur (Dr.-Ing.)

written by
Till Robin Mieling

from
Hamburg, Germany

2026

Chair of Examination Board:
Prof. Dr.-Ing. Hoc Khiem Trieu

Referees:
Prof. Dr.-Ing. Alexander Schlaefer
Prof. Dr. rer. nat. Gereon Hüttmann

Date of oral examination:
10.02.2026

https://doi.org/10.15480/882.16712.
ORCID: https://orcid.org/0000-0003-0262-2519

Contents

List of Figures

List of Abbreviations

1D One-dimensional

2D Two-dimensional

3D Three-dimensional

4D Four-dimensional

A-Scan Axial scan

ANN Artificial neural network

AUPRC Area under the precision-recall curve

AUROC Area under the receiver operating characteristic curve

B-M-Scan B-scans over time

B-Scan Cross-sectional OCT scan

BN Batch normalization

C-M-Scan C-scans over time

C-Scan Volumetric OCT scan

CNN Convolutional neural network

convGRU Convolutional gated recurrent unit

convRNN Convolutional recurrent neural network

CT Computed tomography

DOF Degrees of freedom

DR Detection rate

FBG Fiber bragg grating

FE Fourier estimator

FOV Field of view

FPI Fabry pérot interferometer

GRIN Graded-index

GRU Gated recurrent unit

IVOCT Intravascular optical coherence tomography

LSTM Long short-term memory

M-Scan A-scans over time

MAE Mean absolute error

MAPE Mean absolute percentage error

MEMS Micro-eletrco-mechanical systems

MIS Minimally invasive surgery

MLP Multilayer perceptron

MRI Magnetic rsonance imaging

MSE Mean squared error

MUX Multiplexer

NMAE Normalized mean absolute error

OCE Optical coherence elastography

OCT Optical coherence tomography

PCC Pearson correlation coefficient

RAMIS Robot-assisted minimally invasive surgery

RANI Robot-assisted needle insertion

RAS Robot-assisted surgery

RE Relative error

ReLU Rectified linear unit

RGB Red, green, and blue

RGB-D Red, green, blue, and depth

RMSE Root mean square error

RNN Recurrent neural network

RoPE Rotary position encodings

ROS Robot operating system

SMF Single mode optical fiber

US Ultrasound

VIT Vision transformer

List of Symbols

A	Area
f	Activation function
α	Gain
a	Amplitude
C	Cost function
c_{ph}	Phase velocity
c_S	Shear wave velocity
d	Distance, depth
d_k	Dimension of keys
E	Young's modulus
e	Error
η	Learning rate
F	Force
G	Shear modulus
I	Interference signal
k	Wavenumber
K	Key
λ	Wavelength
n	Refractive index
ν	Poisson's ratio
ω	Angular frequency
ϕ	Phase angle
S	Power spectral dependence
Q	Query
r	Reflectivity
R	Reflectance
ρ	Density
s	Electic field amplitude
σ	Cauchy stress
t	Time
τ	Torque
u	Axial displacement
V	Value
ε	Strain
ϱ	Responsivity
w	Width
$\boldsymbol{w}$	Weight vector
x_d	Desired robot position
$\boldsymbol{x}$	Input vector
$\boldsymbol{y}$	Output vector

Abstract

Robot-assisted surgery can greatly improve minimally invasive procedures by offering enhanced precision, dexterity, and ergonomics. However, a critical limitation of robot-assisted systems is the absence of real-time haptic feedback. Current systems generally lack appropriate sensors to assess interaction forces and tissue properties during tool manipulation. The resulting lack of feedback limits effectiveness of robotic manipulation, especially for novice operators, and is detrimental to increased autonomy for robotic systems.

Consequently, there is a need for novel sensor technology that can provide the desired intraoperative sensing. However, tool-tissue interactions are highly complex and difficult to measure. They are affected by the relationship between the applied interaction forces, the observable deformation, and the biomechanical properties of the sample. Quantitative measurements of these values are difficult to obtain during minimally invasive procedures, e.g. due to the required sensor miniaturization or friction. To address these challenges, this work explores the application of optical coherence tomography (OCT) for intraoperative sensing. We consider fiber-optic probes and high-speed, phase-sensitive OCT for quantitative estimates of tool-tissue interactions.

In the context of robotic-assisted needle insertions, we develop OCT needle probes for enhanced feedback on needle-tissue-interactions. Our contributions include OCT-based needle tip force sensing, depth-sensing of tissue interfaces, and estimating elastic properties in deep tissue. We also couple our approaches with collaborative robotics to provide novel guidance during needle insertions with haptic feedback. Furthermore, we contribute to the development of intelligent OCT-based sensing systems by integrating end-to-end deep learning approaches. We show how the fusion of deformation and elastography data in a single model can benefit optical force estimation. We further explore transformer models tailored to the unique spatio-temporal nature of OCT and demonstrate improved accuracy and robustness for elasticity estimation.

Our findings demonstrate that OCT, especially when combined with machine learning, offers a powerful tool for a better understanding of tool-tissue interactions during robot-assisted interventions. Our miniaturized OCT sensors improve needle placement and demonstrate superior feedback to external measurements. The conducted studies show how optical sensing can enable the measurement of both the interaction forces and biomechanical tissue properties. Adopting end-to-end learning-based approaches further demonstrates an effective alternative to conventional processing that can be error-prone and difficult to optimize manually. Our studies thus highlight the potential of OCT for versatile intraoperative feedback. Further investigation will be needed to develop and validate our approaches for clinical applications and future advancements in intelligent robotic surgery.

1 Introduction

Robot-assisted surgery (RAS) can improve patient outcomes due to improved dexterity and safety, and its clinical availability is steadily increasing [1, 2]. Most importantly, robotic assistance can provide greater efficiency and enhanced precision, resulting in less trauma and shorter recovery times for patients [3, 4] and improved ergonomics for surgeons [5]. However, the broad clinical application of robot-assisted interventions is still limited. Besides costs, one of the major limitations of current RAS systems is their lack of sensory feedback on the interactions between tool and tissue [2, 6].

While current systems generally lack sensors for assessing tool-tissue interactions, such feedback is associated with numerous benefits, e.g. shorter operating times, higher success rates, greater accuracy, or reduced mental workload [7, 8]. Haptic feedback can be particularly helpful during challenging procedures, reduce interaction forces and is beneficial for shortening training times of young surgeons [9–12]. In addition to generally reducing the strength of applied forces, force feedback can provide safety features to prevent soft tissue damage [13]. Furthermore, the feedback of the applied forces in combination with the observation of the resulting tissue deformation can enable the assessment of biomechanical tissue properties. The estimated elasticity of soft tissue can be an important indicator for differentiating between healthy and cancerous tissue [14–18]. Since surgeons rely on their sense of touch to manipulate tissues and localize anatomical structures and pathologies, enabling such remote palpation through sensors has been a goal for decades [19]. A sensor-based quantitative assessment of tissue properties could additionally alleviate the problem of subjective perception in traditional palpation.

Furthermore, feedback on interaction forces and a better understanding of tissue properties will be essential for greater autonomy in RAS [6, 20, 21]. Ultimately, the potential of robotic applications lies in intelligent systems that enable significant automation. Feedback on tool-tissue interactions is therefore not only relevant to current collaborative approaches but will also become increasingly essential as robotic systems slowly transition to autonomous systems, beginning with routine tasks such as suturing.

Still, the lack of real-time force feedback remains and currently limits clinical systems in practice [2, 6, 22–25]. In particular, there is limited sensory feedback on the magnitude of applied forces and the assessment of elastic tissue properties during manipulation. The development of quantitative sensors is challenging due to the required miniaturization for minimally invasive surgery (MIS). The interplay between applied forces, tool mechanics, tissue deformation and biomechanical properties is complex and difficult to assess externally. Existing approaches for sensing forces or elastic properties are generally not compatible for the intraoperative environment. Therefore, novel sensors are needed to recreate the haptic sensations commonly exploited in open surgery, e.g. palpation. Additionally, such sensors could create new possibilities for navigation in minimally invasive procedures such as robot-assisted needle insertion (RANI). This work therefore investigates new approaches for sensors that enable quantitative assessment of tool-tissue interactions during robot-assisted interventions.

In particular, this work explores the application of optical coherence tomography (OCT)

for the intraoperative sensing of applied forces and tissue elasticity. OCT is a laser-based technology that provides high temporal and spatial resolution imaging. OCT is ideally suited for the visualization of microstructures with a typical resolution around 10 µm with high-resolution OCT systems reaching around 1 µm [26, 27]. However, the main disadvantage of OCT compared to other imaging modalities such as ultrasound (US) or magnetic resonance imaging (MRI) is the high attenuation of near-infrared light by the abundant water and melatin molecules present in soft tissue [28]. The maximum imaging depth of OCT is therefore limited to approximately 2 mm in most tissues [29, 30]. OCT thus fills an important niche between confocal microscopy and ultrasound imaging in terms of image resolution and image depth and is best suited for imaging superficial structures. OCT was therefore originally proposed for retinal imaging [31] and has become the gold standard for diagnosis in ophthalmology [32–34]. Since, OCT has been considered for numerous other applications, e.g. intravascular optical coherence tomography (IVOCT) for the detection of arterial plaques or the assessment of stents in cardiology [35–38], in dermatology for the assessment of skin tissue [39–41], or in oncology as an alternative to histopathology for e.g. breast cancer detection [42–44].
By extending OCT to phase-sensitive imaging, submicrometer displacements can be detected with high spatial and temporal resolution, which subsequently can be used for optical coherence elastography (OCE) that enables the biomechanical characterization of tissue [45–52]. This makes OCT especially interesting when it comes to assessing the interaction forces between the tool and tissue as well as the tissue properties. However, OCT is usually coupled with lateral scanning to obtain cross-sectional or volumetric images. In contrast, the surgical regions of interest during RAS often lie deep within soft tissue, e.g. cancerous tissue during percutaneous biopsy or robot-assisted minimally invasive surgery (RAMIS), where surface scanning with table-top systems is not possible. To this end, miniaturized fiber optic probes offer the opportunity to develop new approaches for intraoperative sensor technology, e.g. handheld scanners [53–66], endoscopic imaging probes [67–81] or fiber optic sensors and needle probes [82–141]. However, most approaches focus on morphological imaging and prior investigations considering sensors for tool-tissue interactions have been limited.
This work therefore addresses the potential application of OCT for sensing tool-tissue interactions in two surgical scenarios: robot-guided insertion of needles and manipulation of tissue with robotic instruments in MIS. In the first case of RANI, the primary challenge is quantitatively measuring relevant properties at the needle tip, where the most relevant tool-tissue interactions occur. We are therefore exploring the adaptation of OCT for needle-based probes to improve placement accuracy and enable novel guidance during needle insertion. In the second case of RAMIS, access to the region of interest remains constrained but access is less restricted than in needle-based procedures. Laparoscopic imaging and existing incisions facilitate better sensor integration. Compared to needle insertions, the larger instrument size and target region also provide greater flexibility with respect to sensor miniaturization. In this context, our focus shifts to advanced data processing techniques for extracting interaction forces and tissue elasticity from OCT data. Achieving robust data processing with conventional approaches can be challenging due to the high-resolution spatio-temporal data from optical sensors and the modeling of complex biomechanical interactions. Tool-tissue interactions depend on numerous uncertain factors, including contact conditions, surrounding structures, and material properties. Learning-based approaches present a promising tool to address these challenges. Deep learning has been established as a powerful method in processing

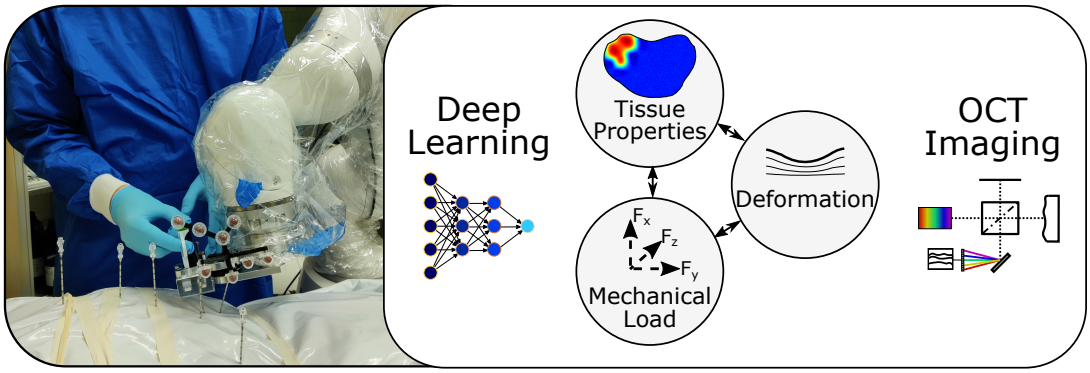

Fig. 1.1: Graphical abstract visualizing the main topics covered in this work. We investigate how we can utilize OCT for detection of sample deformations coupled with deep learning to derive feedback on interaction forces or tissue properties in robotic-assisted interventions, e.g. for needle guidance in RANI.

high-dimensional data and modeling non-linear dependencies. This has resulted in the widespread success of deep learning in many fields, including medical image analysis. Therefore, this work explores learning-based approaches integrated with OCT to achieve effective and versatile sensor calibration for tool-tissue interactions (Fig. 1.1).
From these considerations, we derive two principal research topics covered in this work.

1. How can we utilize OCT for sensing tool-tissue interactions at the tip of medical needles for new and improved methods of navigation during robot-assisted insertions?

2. How can we improve end-to-end deep learning to more accurately estimate interaction forces and tissue elasticity from spatio-temporal OCT data?

1.1 Contributions

Building on previous work, this thesis covers our contributions [142–147] to ongoing efforts to realize OCT-based sensing of tool-tissue interactions related to these two topics.

OCT-guided Robotic Needle Insertions: Forward-facing OCT needle probes have been considered for the guidance of needle insertions through critical structures and the visualization of important events such as tissue ruptures [136, 137]. Building on these findings, we develop a forward-facing OCT needle depth sensor coupled with a collaborative robotic setup. Our work demonstrates that we can provide feedback on the proximity of the needle to critical tissue interfaces during puncture, and we show that this could improve the accuracy of needle placement during RANI [142].
In addition to depth sensing at the needle tip, OCT has previously been considered as an alternative for needle tip force estimation [133–135]. We improve upon these investigations by adapting the OCT sensor and combining it with our robotic system for automated biopsy sampling [148] for collaborative robotic needle guidance with tip force feedback [143]. Our work illustrates how needle tip forces can be measured using OCT and how important the local measurements are for identifying and navigating through

tissue interfaces, as otherwise the frictional forces are superimposed on the measurement of forces at the base of the needle.
Based on these contributions, we show that forward-facing OCT can be combined with force sensing to simultaneously measure tissue deformation and the applied load locally at the tip of a beveled needle to enable elasticity estimation [144]. Thus, we propose a dual-fiber probe that enables biomechanical characterization of deep tissues using OCE. We also show how these local measurements at the needle tip provide superior feedback compared to external sensors.

Deep Learning for OCT-based Sensors in Robotic Tissue Manipulation: Previously, volumetric OCT has been used in conjunction with deep learning for various tasks, such as pose estimation and motion tracking [149, 150]. It has also been considered in tool-tissue interactions for elasticity reconstruction [151–154] and vision-based force estimation [155–157]. Extending these investigations, we consider deep learning for optical force estimation, but in combination with the simultaneous reconstruction of sample elasticity [145]. Thereby, we emphasise that sample elasticity must be considered in image-based force estimation, as it reflects the relationship between the unknown applied load and the observed deformation. Our work demonstrates how deep learning models can effectively integrate elasticity estimates to improve end-to-end force estimation across different tissue types and properties.
Finally, we consider a new learning-based approach tailored to processing of spatio-temporal data from OCT and OCE. Previous deep learning applications in OCT have predominantly focused on convolutional neural networks (CNN) to study tool-tissue interactions [138–141, 149–159], but OCT data is inherently a sequence of one-dimensional (1D) axial scans (A-Scan) acquired in rapid succession over time. While previous work has addressed recurrent convolutional architectures tailored to this spatio-temporal data [133, 134, 156] we show how transformers can effectively process sequences of A-scans to improve elasticity reconstruction during tool-tissue interaction [147]. Using excitation of waves in the sample with a modified robotic manipulator [146] we show how transformers outperform conventional and CNN-based approaches for this task.

1.2 Outline

The following thesis covers these contributions in detail and is structured as follows. Chapter 2 provides relevant background, including the interactions between tool and tissue in RAMIS and RANI as well as the basics of OCT. Chapter 2 describes the current state of the art in sensors for tool-tissue interactions, intraoperative applications of OCT and OCE, and includes an introduction to deep learning approaches relevant to this work. Chapter 3 presents the OCT sensors and experimental setups and describes the acquired data sets and the deep learning methodology for processing spatio-temporal OCT data. Chapter 4 gives an overview of the results of the experiments performed and summarizes the most important findings of the individual contributions. Chapter 5 provides a discussion of the approaches in comparison to the state of the art, evaluates the limitations and considers the contributions with respect to our two main research topics. Chapter 6 provides a summary and presents suggestions for promising direction of future research. Finally, the published manuscripts related to this thesis are collected in chapter 7.

2 Background and State of the Art

This chapter provides an introduction to the main topics relevant to this work. These include tool-tissue interactions during robot-assisted manipulation, OCT, state-of-the-art sensors, and lastly relevant deep learning approaches.

2.1 Tool-Tissue-Interactions

In this work, we consider tool-tissue interactions during the manipulation of tissue with robotic instruments in RAMIS and RANI. We specifically want to sense tool-tissue interactions optically, therefore deriving applied forces from the observed tissue deformation or deriving elastic properties from observing the response to a known mechanical stimulus. Conventionally, this requires modeling the elastic behavior of the manipulated tissue. While our contributions mostly focus on the application of deep learning to model the tool-tissue interactions, we include the elementary modeling of elastic tissue deformation assuming a linear, homogeneous and isotropic medium. We then introduce the considered tool-tissue interactions in RANI and RAMIS together with a short overview of the state of the art for sensors in these fields, excluding OCT-based approaches that are presented separately in section 2.2.5.

2.1.1 Linear Elastic Model

The following is based on [51] and [52]. The relation between the Cauchy stress σ and strain ε in three-dimensional (3D) space is given by

$$\begin{Bmatrix} \varepsilon_{11} \\ \varepsilon_{22} \\ \varepsilon_{33} \\ 2\varepsilon_{12} \\ 2\varepsilon_{13} \\ 2\varepsilon_{23} \end{Bmatrix} = \begin{bmatrix} \frac{1}{E} & -\frac{\nu}{E} & -\frac{\nu}{E} & 0 & 0 & 0 \\ -\frac{\nu}{E} & \frac{1}{E} & -\frac{\nu}{E} & 0 & 0 & 0 \\ -\frac{\nu}{E} & -\frac{\nu}{E} & \frac{1}{E} & 0 & 0 & 0 \\ 0 & 0 & 0 & \frac{1}{G} & 0 & 0 \\ 0 & 0 & 0 & 0 & \frac{1}{G} & 0 \\ 0 & 0 & 0 & 0 & 0 & \frac{1}{G} \end{bmatrix} \begin{Bmatrix} \sigma_{11} \\ \sigma_{22} \\ \sigma_{33} \\ \sigma_{12} \\ \sigma_{13} \\ \sigma_{23} \end{Bmatrix} \tag{2.1}$$

where ν denotes the Poission's ratio, E the Young's modulus relating uniaxial strain and stress in normal directions ($i = j$) and G the shear modulus for shear strain and stress in any ij-direction ($i \neq j$). We can the describe the relation between the Young's modulus E and the shear modulus G with

$$E = 2(1 + \nu)G \tag{2.2}$$

that further simplifies to $E = 3G$ as tissue is generally considered incompressible ($\nu \approx 0.5$). For uniaxial compression along the first spatial dimension, we obtain

$$\sigma_{11} = 3G\varepsilon_{11} = E\varepsilon_{11}. \tag{2.3}$$

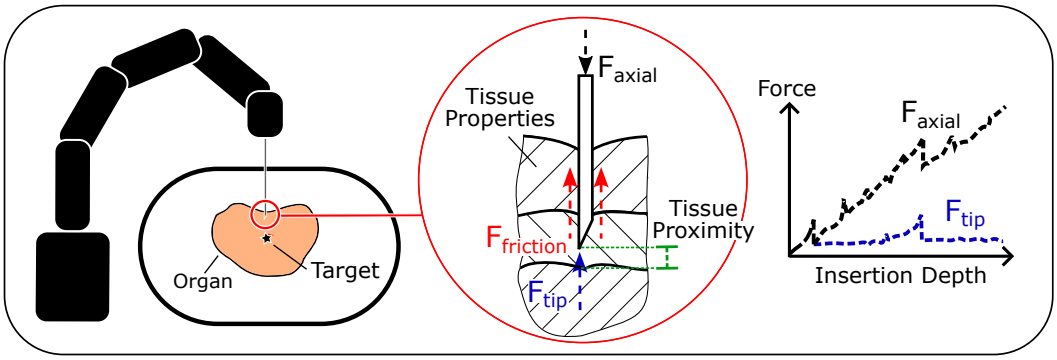

Fig. 2.1: Illustration of needle-tissue interactions during RANI. Surgical needles are driven through multiple tissue layers to reach the desired target placement. Image-guided robotic assistance can facilitate accurate placement along a planned trajectory, but there exists limited sensory feedback on important needle-tissue interactions. Friction forces superimpose with needle tip forces and tissue deformation is difficult to observe. Therefore, detection of important interactions such as ruptures, the proximity of critical structures or the estimation of biomechanical properties at the needle tip is commonly unavailable.

The strain component ε_{11} can be measured as the derivative of the axial displacement. We regard the z direction as the first spatial direction and denote axial displacement, stress and strain as u, σ and ε, respectively.

$$\varepsilon = \frac{\delta u}{\delta z}. \tag{2.4}$$

During compression tests, the applied stress is often assumed to be uniform resulting in

$$\sigma = \frac{F}{A}, \tag{2.5}$$

where F denotes the applied force and A the contact area. In addition to compression, the relation between the shear modulus, the density ρ and the velocity of shear waves c_S is governed by

$$G = \rho c_S^2. \tag{2.6}$$

Therefore, equivalent elastic properties of tissue may be obtained through the application of uniaxial stress and measuring the single normal strain component ε_{11} or by exciting and detecting the velocity of the propagating wave. The image-based measurement of elasticity is called elastography. Note that for quantitative elasticity reconstruction, both the applied load and the strain must be measured locally during compression. For wave-based elastography, only wave propagation is measured and the approach is therefore heavily reliant on correctly modeling wave propagation in tissue, e.g. type of wave or boundary conditions. As exciting and observing shear waves with OCT can be challenging, Rayleigh-Lamb surface waves are often considered for elasticity reconstruction [52, 160–162] and their observed phase velocity c_{ph} can be related to the shear modulus via

$$c_S = \frac{c_{ph}}{(0.862 + 1.14\nu)/(1+\nu)}. \tag{2.7}$$

2.1.2 Robot-assisted Needle Insertions

The placement of needles is an important task in numerous diagnostic and therapeutic procedures, e.g. biopsy, brachytherapy, injection or ablation. Precise positioning directly determines the effectiveness of these approaches, e.g. false-negative sampling in biopsy or incorrect dosage in brachytherapy. In clinical practice, needles are still generally placed manually under image guidance with accuracy depending heavily on the operator [163–166]. But it has been shown that robot assistance can improve standardization and accuracy, e.g. for stereotactic cranial needle and electrode placement or prostate biopsy [167–169]. While RANI systems have not reached a similar level of commercialization and widespread clinical application as the da Vinci platform (Intuitive Surgical, Inc., USA), they have been considered for over three decades [170] and are commonly coupled with image guidance to navigate the insertions, e.g. US [171–176], computed tomography (CT) [177–182] or MRI [183–187]. Proposed RANI platforms vary greatly in design, ranging from small patient-mounted actuators to large serial robots.

The research effort has also led to the introduction of commercial RANI systems, e.g. Cirq (Brainlab, Germany) or ROSA (Zimmer, Inc., USA). Consequently, there is an opportunity to utilize these robotic platforms not just for accurate needle placement but also as a way to render additional feedback obtained through sensing needle-tissue interactions. In comparison to the manipulation with surgical tools which can be non-destructive, e.g. pushing or grasping with forceps, needle insertions inherently involve tissue rupture (see Fig. 2.1). Needle-tissue interactions are therefore commonly considered in multiple phases, e.g. pre- and post-rupture, and containing multiple components, e.g. needle tip and friction force [188, 189].

The focus commonly lies on needle tip force estimation to provide feedback on the interactions occurring locally at the needle-tissue interface. Needle forces displayed to the physician in teleoperated or collaborative systems enhance the navigation during percutaneous insertions [190–194]. There has been a large effort to model needle insertion forces [195–201] to provide indirect feedback on needle tip forces. Alternatively, direct force feedback uses miniaturized sensors integrated in surgical needles, e.g. strain gauges [202], fiber Bragg gratings (FBG) [191, 192] or Fabry Pérot interferometer (FPI) [203–207]. A detailed overview of embedded sensors for guiding needle-based interventions is also discussed in [196, 201]. Other feedback on needle-tissue interactions besides force range from estimating the proximity to the target [208] to shape sensing [183] or detecting puncture events [194]. In addition, assessing the elasticity of tissue during needle insertion could provide valuable insights during navigation and allow in-vivo tissue characterization. This has been considered by coupling needle tip force sensing with tracking of robot indentation depth for stiffness reconstruction [209]. But relating external displacement to local loads can make it difficult to distinguish between tissue deformation and bulk tissue displacement. Displacement might occur when applying a force to a solid organ in soft surroundings, e.g. prostate displacement during biopsy [186, 187]. Alternatively, a dual FPI sensor in a flat tip needle for measuring both the applied load and indentation depth has been proposed for deriving Young's modulus [210]. Still, these approaches do not directly visualize the tissue during the needle insertion and OCT provides a unique opportunity for novel sensors of needle-tissue interactions, e.g. to combine local load sensing with strain estimation for elasticity reconstruction.

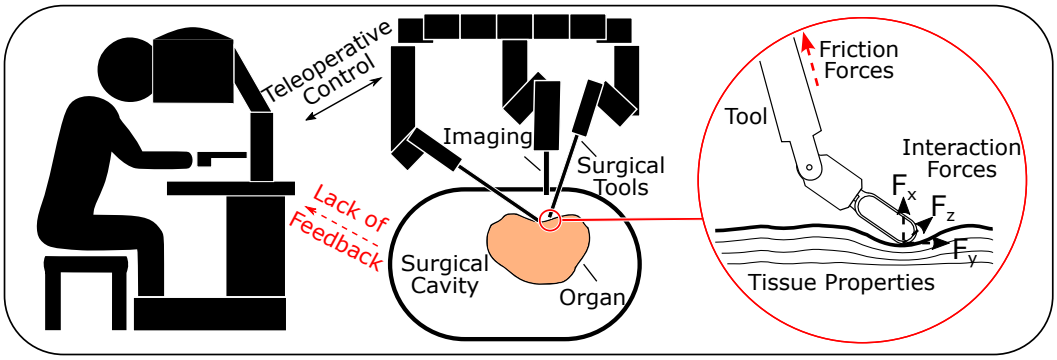

Fig. 2.2: Illustration of RAMIS systems that are typically controlled teleoperatively and commonly provide no feedback on tool-tissue interactions. It would be desirable to reinstate the surgeons ability to palpate tissue for assessing tissue properties or to provide feedback on applied forces during tissue manipulation, e.g. during grasping or pushing tissue. Observing tissue deformations during manipulation with surgical tools could enable the indirect estimation of interaction forces and tissue properties.

2.1.3 Robot-assisted Minimally Invasive Surgery

For RAMIS, versatile systems offering robotic assistance in different surgical scenarios from urology to general surgery are growing continuously, with multiple commercial systems, e.g. Senhance (Asensus Surgical, Inc., USA) or Hugo (Medtronic plc, Ireland), joining the well-established da Vinci (Intuitive Surgical, Inc., USA) system [211, 212]. These systems generally feature a master-slave robot configuration and allow the surgeons to precisely control the robotic manipulators teleoperatively (see Fig. 2.2). The types of tool-tissue interactions in RAMIS vary greatly in complexity between surgical steps and the used tool, e.g. pushing and grasping tissue, cutting and cauterization or suturing. Due to the minimally invasive and teleoperative configuration, surgeons can not rely on their sense of touch for feedback on tool-tissue interactions. Modeling and sensing these interactions will be essential for improving RAMIS but providing meaningful feedback to the physicians can be difficult, especially for complex manipulation. Research is predominantly focused on feedback on the magnitude of applied forces during non-destructive basic tasks, e.g. elastic deformation during pushing or grasping. Coupling load sensing with tracking tissue deformation additionally enables assessment of elastic tissue properties next to intraoperative force estimation. Fig. 2.2 schematically visualizes these tool-tissue interactions during palpation. We consequently want to investigate the interplay between applied forces of the tools that can displace or deform tissue and the elastic properties of tissue that affect how these interactions take place, e.g. a stiffer tissue will require a larger load to deform.

For sensing interaction forces or torque in RAMIS or laparoscopic surgery, multiple direct and indirect approaches have been considered analogous to RANI. Direct approaches involve the integration of sensors into the surgical tools or the design of dedicated tools for intraoperative force sensing, e.g. strain gauge-based sensors, optical approaches like FBG or capacitive sensors. Alternatively, indirect approaches do not involve dedicated sensors at the tool tip and instead derive interaction forces from external data, e.g. by

modeling tool mechanics and evaluating actuator inputs [213]. We refer to [214–218] for recent surveys covering the topic in detail. However, we want to highlight the indirect image-based approach for which OCT is a promising imaging modality due to it's high temporal and spatial resolution. In the image-based approach tool-tissue interaction forces are derived from the observed tissue deformation [219–238]. While early methods used to involve modeling tissue elasticity, e.g. via finite element methods or deformable template matching [219–225], recent approaches have focused on the application of deep learning to implicitly learn the relation between tissue properties, observed deformation and interaction load [226–238]. In contrast to interaction forces, there are few proposed solutions for the quantitative assessment of tissue properties during tool-tissue interactions. Approaches investigating robotic palpation often involve the discussed force or pressure sensors without additionally imaging the resulting tissue deformation, e.g. comparing interaction forces or tactile sensations for qualitative elasticity contrast [239–241] or relating the measured forces to the driven indentation distance of the robot [242–244]. Recently, a membrane-based sensor for robotic palpation has been considered that allows quantification of tissue elasticity without external sensors for measuring actuation [245]. But without visualizing tissue deformation direct differentiation of tissue deformation and bulk tissue movement is still limited. There exist other approaches enabling quantitative elasticity reconstruction but which are not designed for the limited space of MIS, e.g. handheld tactile sensors [246–248]. Therefore, there remains a need for quantitative sensory feedback on tool-tissue interactions during RAS.

2.2 Optical Coherence Tomography

In the following, an introduction to the underlying principle of OCT and subsequent image reconstruction is given. Additionally, scientific works relevant to the intraoperative use of OCT and OCE for tool forces and tissue properties are presented.

2.2.1 Fundamentals

OCT is based on a Michelson interferometer paired with low-coherence near-infrared light (Fig. 2.3). The light is directed at a beam splitter that splits into one path reflected by a reference mirror and a second path targeting the measured sample. The light backscattered from the sample is recombined with the reference. The resulting interference pattern can be measured at the detector. Due to the low-coherence light source, only light that has travelled the same path length will result in a measurable interference. This allows the measured interference signal to be matched to a specific axial location that depends on the path length of the reference mirror [29–31]. Miniaturized fiber optic OCT probes may use common-path imaging, in which the interferometer design is simplified and the partial reflection at the probe interface is used as the reference signal. In early TD-OCT systems, axial line scans were obtained by changing the axial positions of the reference mirror which severely limited the maximum line scan rate [31, 249]. But with the introduction of Fourier-domain OCT, the interference signal can be resolved for different wave lengths which encode the reflectance as a funciton of depth (Fig. 2.3). The spectral information can be acquired simultaneously for axial depth without moving the reference arm, so Fourier-domain OCT can provide significantly higher sampling frequencies and sensitivity [29, 32, 250].

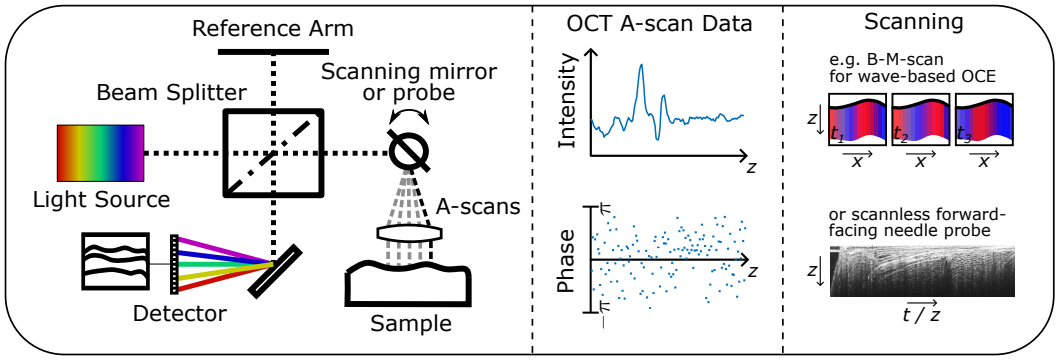

Fig. 2.3: Schematic of interferometry used in OCT. Fourier-domain OCT enables fast successive acquisition of axial scans. An OCT measurement is inherently a sequence of A-scans acquired at different temporal or spatial locations. Each A-scan contains intensity data visualizing the reflectivity of the sample over the axial depth z. In contrast, the OCT phase over depth is generally random but observing phase differences between A-scans at the same location enables the detection of micrometer displacements, e.g. for wave-based OCE. Multidimensional images can be acquired through scanning systems or through the movement of miniaturized handheld OCT probes. For scanless forward-facing needle probes, temporal and depth dimension are superimposed during needle insertion.

2.2.2 Scanning

The combined measurement of interference signals over the depth $I(z)$ denotes a single axial scan, commonly referred to as A-scan or line scan. Multidimensional OCT scans are the sequential accumulation of 1D A-scans at different spatial or temporal locations. A sequence of 1D A-Scans over time t is referred to as an M-Scan (1D+t). Optical scanning is employed to acquire cross-sectional or even volumetric images via galvanometer or micro-eletrco-mechanical systems (MEMS) scanners [251, 252]. B-Scan refers to cross-sectional two-dimensional (2D) images with the beam deflected along a single lateral axis and C-Scan denotes 3D measurements with scanning along both lateral axes. Successively acquired B-scans over time commonly used for dynamic OCT imaging such as elastography are consequently denoted as a B-M-Scan. Other approaches consider scanless OCT probes that are moved directly for imaging different regions of interest, e.g., by rotation and simultaneous pullback for catheter-based probes or manual movement of handheld fiber optic probes. OCT data is therefore always a temporal sequence of A-scans that can be reconstructed to multidimensional images befitting the scanning scheme (Fig. 2.3).

2.2.3 Signal Reconstruction

In the following, the reconstruction of the depth-resolved interference signal is described briefly. Additional information and an in-depth description of OCT signal reconstruction can be found in [29, 253]. The following overview is summarized on the basis of these works and was presented in a similar way in [254]. The OCT light source emits electromagnetic waves with wavenumber k and angular frequency ω. The electrical field

at the distance z at time t with the field amplitude $s(k,\omega)$ can be described with

$$E(z,t) = s(k,\omega)e^{i(kz-\omega t)}. \tag{2.8}$$

Assuming an ideal beam splitter and mirror, the electrical field of the reference path is

$$E_R = \frac{E}{\sqrt{2}} r_R e^{2ikz_R}. \tag{2.9}$$

The depth-dependent reflectivity r along the axial axis in the sample path can be described by a convolution

$$E_S = \frac{E}{\sqrt{2}}[r_S(z_S) * e^{2ikz_S}] \tag{2.10}$$

where index r_R and r_S denote the reflectivity of the reference and sample, respectively. Considered the sample as a series of N real-valued discrete reflector layers with a reflectivity r_{S_i} at layer i resulting in

$$r_S(z_S) = \sum_{i=1}^{N} r_{S_i}\delta(z_s - z_{S_i}). \tag{2.11}$$

Considering the responsivity of the detector ϱ the detector generates a photocurrent proportional to the square of the sum of the fields and the detector signal I can be written as

$$I(k,\omega) = \frac{\varrho}{2}\Big\langle \Big| \frac{s(k,\omega)}{\sqrt{2}} r_R e^{i(2kz_R-\omega t)} + \frac{s(k,\omega)}{\sqrt{2}} \sum_{i=1}^{N} r_{S_i} e^{i(2kz_S-\omega t)} \Big|^2 \Big\rangle. \tag{2.12}$$

The dependency on ω can be neglected because the frequency is too high for the detector to resolve and equation 2.12 can be written as time invariant. Introducing the reflectance $R = |r|^2$ and the light source's power spectral dependence $S(k)$, the signal can be fractured into three parts using Euler's rule.

$$\begin{aligned} I(k) = {} & \frac{\varrho}{4}\Big[S(k)\Big(R_R + \sum_{i=1}^{N} R_{S_i}\Big)\Big] \\ & + \frac{\varrho}{2}\Big[S(k)\sum_{i=1}^{N}\sqrt{R_R R_{S_i}}(cos[2k(z_R - z_{S_i})])\Big] \\ & + \frac{\varrho}{4}\Big[S(k)\sum_{i\neq m=1}^{N}\sqrt{R_{S_i} R_{S_m}}(cos[2k(z_{S_i} - z_{S_m})])\Big]. \end{aligned} \tag{2.13}$$

The first constant "DC" component is independent of pathlength and is dominated by the source spectrum and the reference reflectivity. The remaining signal contains the desired interference spectrum of the sample and auto-correlation noise caused by the interference between different discrete reflectors. The depth-dependent reflectivity $I(z)$ can be acquired from the spectral measurement via the Fourier transform. To improve image quality, the measured signal typically undergoes "DC" subtraction, k-space re-interpolation, dispersion compensation and spectral windowing prior to Fourier transformation [32]. Note that in reality, the sample reflectivity r_S is continuous and may

also encode complex phase information. Therefore, the obtained complex interferogram in phase-sensitive OCT can be expressed with an amplitude a and a phase angle ϕ component. The intensity of the OCT signal $\propto a(z)^2$ enables structural imaging and is therefore most commonly used in OCT. It enables detailed visualization of tissue morphology, e.g., established clinical applications in ophthalmology or cardiology [255, 256].
Far less explored is the additionally available phase information $\phi(z)$. The phase $\phi(z)$ for a discrete reflector is random but changes to the axial position of the reflector correspond to changes of it's phase signal (Fig. 2.3). The phase shift between two A-scans can be used to calculate the depth dependent displacement $\delta u(z)$ via

$$\delta\phi(z) = \frac{4\,\pi\,n\,\delta u(z)}{\lambda_0} \tag{2.14}$$

where n denotes the refractive index and λ_0 the central wavelength. Phase-sensitive OCT can therefore visualize displacement over time (between successive A-scans) with a resolution far above the axial resolution [257, 258]. Phase-resolved OCT consequently offers great potential for the intraoperative use of OCT when sensing dynamic tissue mechanics or interaction forces. However, the phase information of the complex OCT signal is bounded by $[-\pi, \pi]$ and large displacements consequently cause phase wrapping. Processing phase-sensitive OCT therefore often requires sophisticated algorithms for accurately estimating larger displacements or strain [259, 260].

2.2.4 Optical Coherence Elastography

Phase-sensitive measurements of displacements is particularly valuable for the assessment of tissue elasticity in OCE under a mechanical stimulus, e.g. strain estimation during compression. In the following, we give a brief overview of OCE techniques. A detailed picture of different OCE approaches and their applications has been covered comprehensively in [45–52].
OCE techniques can be grouped by their respective method of mechanical stimulation ranging from active methods, e.g. acoustic radiation force or bulk compression, to passive methods, e.g. intraocular pressure or pulse [46, 48]. The most important and promising stimuli are bulk compression and wave excitation. Compression based OCE is a quasi-static approach has been considered since shortly after the introduction of OCT for qualitative elastograms [261–267]. Quantitative Young's modulus reconstruction was then achieved by the additional estimation of local stress via a compliant reference layer [268]. Compression OCE offers high spatial resolution but requires direct contact and must consider friction and misalignment for accurate estimation of local stress [269–271]. Compression OCE can provide complete loading and unloading curves and therefore can be extended to monitor non-linear behavior, e.g. for breast tissue characterization [272, 273]. Compression OCE has been considered for the intraoperative use in multiple applications, e.g., in ophthalmology [274–276] or oncology [268, 272, 277–283].
In comparison to compression OCE, in wave-based OCE elastic properties of the sample are reconstructed by the excitation of waves in the sample with subsequent observation of their propagation. Wave excitation allows for more flexible mechanical stimulation, e.g. contactless air-puff excitation [284–287], and can also readily reveal dynamic biomechanical properties of tissue, e.g. viscoelasticity [288, 289]. But because only wave propagation and no local stresses are measured, wave-based OCE is heavily reliant on

correctly modeling wave propagation in tissue, e.g. type of wave or boundary conditions. Applications for wave-based OCE also vary greatly from dermatology [40, 41] and ophthalmology [161, 162, 287–290] to oncology [286, 291].

2.2.5 Miniaturized Probes for Intraoperative Application

Intraoperative or perioperative use of OCT has considered early for retinal surgery [292] and examining microstructures similar to histopathology [293]. Since, it has seen great success in microscope integrated systems for ophthalmic surgery with numerous comprehensive reviews covering relevant research and clinical application [252, 256, 294–299]. But due to the bulk of tabletop systems, OCT is often only applicable for examining ex-vivo or superficial tissue, e.g. skin or eyes. Therefore, miniaturization is key for the intraoperative use of OCT. The following state of the art will focus on applications besides microscope integrated OCT and only feature selected approaches from ophthalmology particularly relevant in the context of this work.

Multiple handheld OCT scanners have been proposed [53–60] and handheld scanners have also been used for assessing tissue properties via OCE [61–66]. But while some of the proposed scanners are small enough for specific applications of in-vivo tissue assessment, e.g. for breast tumor detection in the surgical cavity [63–65], only further miniaturization to fiber-based endoscopic and needle probes enables applications of OCT in a truly minimally invasive setting [300, 301]. These approaches therefore lay the foundation for the feedback on interaction forces and tissue properties during RAMIS and RANI considered in this work.
Fiber-based OCT probes have been previously considered for multiple applications besides IVOCT, e.g. high-resolution endoscopic imaging for robotic or laparoscopic surgery [67–70] or endoscopic visualization of the upper airway [71–79]
Miniaturized OCT probes can also enable the detection of breast tumor tissue [82–85], intraocular image guidance during eye surgery [86–96], feedback on critical structures during epidural anesthesia [97–100] or Veress needle insertion [101], avoidance of blood vessels during stereotactic brain surgery [102–105], or differentiating tissues during biopsy, e.g. for pulmonary lymph nodes [106–110] or prostate biopsy [111–114]. Minaturized OCT approaches may enable forward viewing [80] or radial imaging [115] and range from scanless fiber probes [116] to 3D endoscopic scanning [81].
Besides miniaturized approaches that focus on morphological imaging, OCT has been considered for assessing tissue properties during mechanical interaction via in-vivo OCE. Qualitative OCE has been considered for strain imaging with flat tipped needle probes with grated-index (GRIN) lenses [117, 118], single mode fibers [119] and GRIN rod lenses [120]. The extension of spatially multiplexed stress sensing enabled quantitative, compression-based elasticity reconstruction in a needle format [121–123]. Miniaturized wave excitation has also been considered for intravascular and intrabronchial OCE applications. Rotating catheter-based OCT systems were coupled with miniature transducers for intravascular acoustic radiation force elastography [124, 125]. Similarly, intravascular OCE has been considered with needle probes and external US-based shear wave excitation [126, 127] as well as a distally motorized OCT probe modulating the intraluminar fluid pressure to apply a load in-vivo [128]. Intraoperative OCE has been considered for assessing airway compliance and airway wall injuries employing a pressure catheter [129–131]. Recently, a highly compact endoscopic OCE probe has been proposed

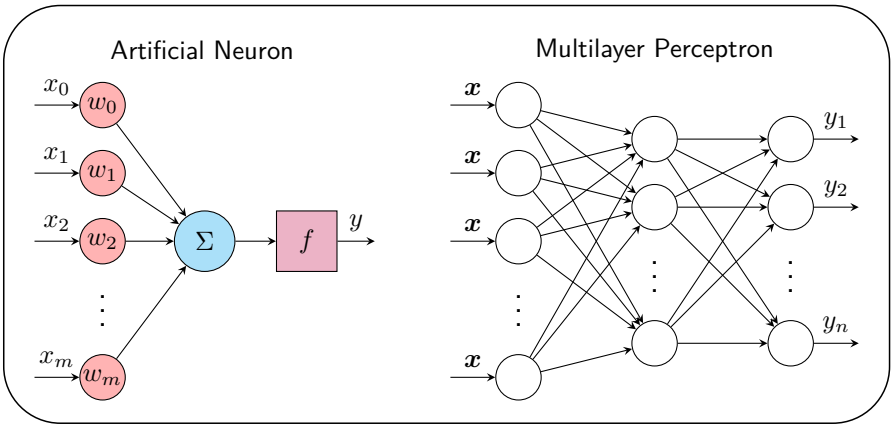

Fig. 2.4: An artificial neuron that computes a weighted sum of the input. An MLP is a fully connected network assembled from numerous neurons stacked in multiple layers.

for intraluminal OCE with an integrated US transducer for wave excitation [132].

In addition to tissue elasticity, needle-based OCT has been considered as an optical alternative to FBG or FPI for sensing tool interactions. OCT fibers can be integrated into needles with a deformable layer for the estimation of needle tip forces [133–135]. It has also been shown that forward viewing OCT can be employed to detect rupture events during needle insertions [136], estimate needle insertion depth [137] and that OCT can be used to measure the distance between tools and tissue during minimally invasive interventions [90, 101], particularly for guiding subretinal injections [91–96].

2.3 Deep Learning

This work considers the potential application of OCT for intraoperative feedback on tool-tissue interactions. Deep learning could help overcome the challenges of calibrating complex optical setups and extract meaningful feedback from the complicated mechanical behavior of tissue, e.g. elasticity or interaction force. Particularly, we focus on supervised learning and consider regression tasks, where feedback on tool-tissue interactions is learned directly from spatio-temporal OCT data in an end-to-end fashion.

In the following, we provide a brief introduction to artificial neurons. For detailed information on deep learning fundamentals refer to [302, 303] and for a broader perspective on deep learning for medical image analysis to e.g. [304]. Afterwards, different model architectures most relevant to processing spatio-temporal OCT data will be presented. These include CNN, recurrent neural networks (RNN) and self-attention-based transformer models (Fig. 2.5). For each architecture, the state of the art with respect to our research objectives will be presented. Additionally, selected research considering deep learning combined with other imaging modalities for estimating intraoperative interaction forces will be included, e.g. RGB or RGB with depth (RGB-D) images [218].

2.3.1 Artificial Neural Networks

Artificial neural networks (ANN) are computational models designed to learn mappings between inputs and outputs, and they are recognized as universal approximators capable of representing a wide variety of functions. The fundamental component of a ANN is the artificial neuron (Fig. 2.4), which computes a sum of the inputs $\boldsymbol{x} \in \mathbb{R}^m$ weighted by learnable parameters $\boldsymbol{w}$, and applies an activation function f

$$y = f\Big(\sum_{j=0}^{m} w_j x_j\Big). \tag{2.15}$$

j indexes the inputs, and $x_0 = 1$ for the addition of bias. Neurons can be organized into layers to form ANNs that can have multiple outputs $\boldsymbol{y} \in \mathbb{R}^n$, e.g. a multilayer perceptron (MLP) that contains fully connected artificial neurons (Fig. 2.4). The layers between input and output layers are commonly referred to as hidden layers. By considering nonlinear activation functions such as the rectified linear unit (ReLU) [305] defined as $f(x) = max(0, x)$, the network can learn non-linear relations and approximate complex functions. Training ANNs involves optimizing a cost function, which measures the discrepancy between the predicted and target outputs. The gradient of the cost function $C(\boldsymbol{w})$ with respect to the network weights is calculated using backpropagation, and weights are updated using gradient-based methods such as gradient descent

$$\boldsymbol{w} := \boldsymbol{w} - \eta \nabla C(\boldsymbol{w}) \tag{2.16}$$

where $\eta > 0$ is the learning rate. However, modern approaches commonly employ stochastic gradient-based optimization descent with adaptive learning rates to improve training efficiency and convergence, e.g. Adam [306]. Deep neural networks extend the concept of ANNs and contain multiple stacked layers.

2.3.2 Convolutional Neural Networks

CNNs are a well-known class of deep learning architectures developed specifically for image processing. In contrast to the dense vector-matrix multiplications in MLPs, CNNs introduce convolutions to process the image data and learn filters to extract increasingly abstract features. The operation is equivalent to sliding the kernel over each pixel in the input image and computing an output value that depends on the kernel size and weights. An illustration of a 2D convolution can be found in Fig. 2.5, but the same approach can be extended to any multidimensional grid data, e.g. four-dimensional (4D) volumetric video. A CNN typically consists of convolutional layers, each containing multiple adaptive kernels to extract spatial feature maps; pooling layers that reduce the spatial dimensions of the features while preserving important information through operations such as max or average pooling; activation functions to model nonlinearity; and normalization layers, e.g. batch normalization (BN) [308], to improve stability during training (Fig. 2.5). An MLP is commonly used as a the final stage and allows the network to predict the desired output based on the extracted features. Examples of notable CNN architectures include ResNet [309], DenseNet [310], SENets [311], MobileNets [312] and U-Net [313].

CNNs have long been at the forefront of deep learning for medical image analysis in general and have also been successfully used for OCT. Being the largest application for

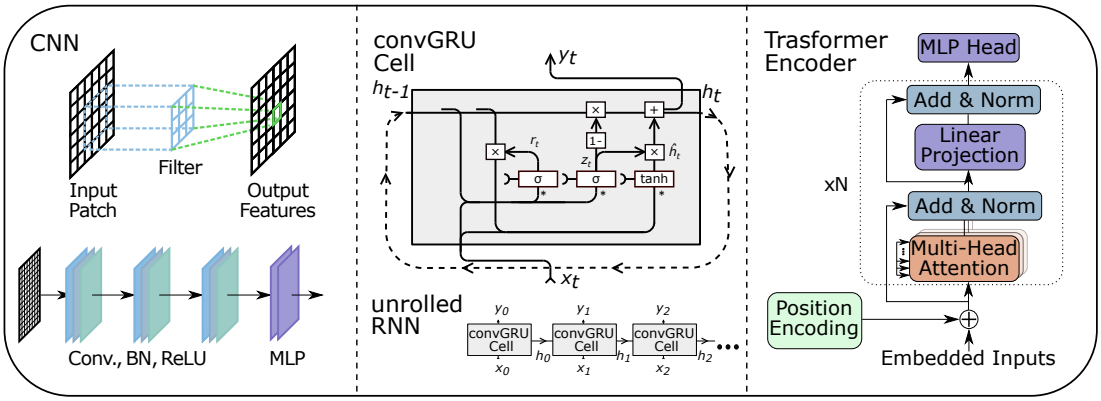

Fig. 2.5: Overview of architectures considered in this work. Left: CNN with an illustration of a 2D convolution that enables the extraction of abstract feature maps. Middle: A convGRU cell that contains convolutions instead of dot products in traditional RNNs to better model spatial dependencies. Sequential data is processed recurrently and the hidden state h is updated each iteration. Right: Transformer encoder [307] with N layers containing multi-headed attention blocks for effective processing of long input sequence in parallel that maintain global context. The approach can be adopted for vision tasks, by considering image patches as sequential inputs.

OCT, most approaches for CNNs with OCT are related to ophthalmology. CNNs for retinal OCT have shown better performance than conventional approaches in various tasks such as disease classification or retinal layer segmentation, and these considerations have been extensively covered in several reviews [314–318]. CNNs have also been considered for IVOCT, e.g., for automatic plague detection or segmentation [319–321]. Particularly relevant to this work is that CNNs can be used for intraoperative and miniaturized OCT to better understand tool-tissue interactions and avoid error-prone system calibrations. CNNs can enable automatic tissue classification or segmentation during OCT needle insertion [138–141]. CNNs can provide robust feedback on rupture events [136] and were considered for needle tip force estimation [133–135]. 3D CNNs have demonstrated tissue pose estimation [149] and markerless motion tracking [150] with volumetric OCT. It has also been shown that CNNs can provide robust phase unwrapping for Doppler imaging [158] or strain estimation during tissue deformation [159]. Furthermore, they can enable end-to-end reconstruction of sample elasticity from spatio-temporal OCT data [151–154]. CNNs in conjunction with high-speed OCT can also enable vision-based force estimation during tool manipulation [155–157].
Considering imaging modalities beyond OCT, CNNs have been considered for image-based force estimation, e.g. in fluoroscopy via a dual-path architecture [230] or combined with graph neural networks for processing RGB and robot state data [230]. CNNs have also been explored for image-based estimation of tissue elasticity, e.g. with US [322] or MRI [323].

2.3.3 Recurrent Neural Networks

RNNs are model architectures that have been specially developed for processing sequential and time-serial data, e.g. speech, text or video [302, 324]. In contrast to feedforward

models such as CNNs, the sequential inputs are processed iteratively, while recurrent connections allow the model to retain the information across the different time steps. To illustrate this behavior, RNNs can be represented in an unrolled state, where a very deep network with numerous cells sharing the same weights sequentially process the output of the previous cell (Fig. 2.5). However, early RNN approaches were unable to store information over long sequences of input time steps. To overcome these challenges, the long short-term memory (LSTM) [325] and its variant, the gated recurrent unit (GRU) [326], were introduced. These models feature redesigned hidden layers and trainable gates to better preserve the history of past time steps and more effectively determine what information is retained, edited, and removed at each iteration. As described in Sec. 2.2.2, OCT data is usually displayed as volumetric (C-scans) or cross-sectional (B-scans) but originally it is a time series of consecutive A-scans. Therefore, recurrent models are well suited for processing OCT data when viewed in their raw spatio-temporal form of successive A-scans. Of particular interest are convolutional recurrent neural networks (convRNN), that combine convolutional operations with recurrent structures to process both spatial and temporal information. This hybrid architecture is particularly effective for tasks with sequential image data, where the convolutional layers extract spatial features, while the recurrent layers model temporal dependencies. A convolutional gated recurrent unit (convGRU) is a particularly interesting hybrid architecture where the dot product is replaced by convolutions to combine spatial and recurrent processing in a single cell [327, 328].

Several approaches have considered RNN architectures for processing OCT data. To account for spatial dependencies in OCT, these approaches have often combined RNN and CNN layers or used fused architectures such as convRNNs. For example, CNN-based processing of single B-scans were coupled with an LSTM module to process the temporal dependency between the slices of each OCT volume for retinal image classification [329] or ovarian cancer detection [330]. Similarly, CNN and RNN modules were used to process spatial features from longitudinal OCT images [331]. A convolutional LSTM and a temporal attention unit have been recently considered for scene dynamics prediction to improve OCT scanning speed compared to rasterized scanning [332].

For OCT-based detection of tool-tissue interactions, convGRU architectures and models combining RNN and CNN layers have been considered for sequences of A-scans in OCT-based needle tip force estimation [133, 134]. Similar architectures were also considered for processing volumetric OCT sequences to estimate tool-tissue interaction forces [156]. Recently, needle-tissue interaction forces were also observed through an OCT integrated microscope and processed using CNN and RNN modules [333].

Besides OCT, RNNs have been widely used for image-based estimation of tool-tissue interaction forces. RNNs can enable processing of sequential robot motion states and deformation maps derived from RGB-D [226–229]. Similar to OCT, the combination of CNN and RNN modules architectures is particularly prominent [234–238].

2.3.4 Transformer

In recent years, transformer architectures [307] have overtaken recurrent neural networks in the effective processing of long input sequences. The key building block of the transformer is the scaled-dot product attention, which allows the model to learn dependencies

between input tokens. It can be described as

$$\text{Attn}(Q, K, V) = \text{Softmax}(\frac{QK^{\text{T}}}{\sqrt{d_k}})V \tag{2.17}$$

with Q, K, V as query, key and value and d_k as the dimension of the keys. The sequences Q, K, V are obtained from the input sequence $\boldsymbol{x}$ via learnable weight matrices. This approach allows the model to calculate the attention values between the query, key and value and then perform a weighted summation. Transformers typically include linear embedding; multi-headed attention with multiple parallel attention blocks to independently learn different attention patterns, e.g., self-attention or cross-attention; fully connected MLPs with nonlinear activation functions; and layer normalization and residual connections to mitigate vanishing gradients and stabilize training (Fig. 2.5). Depending on the task, e.g. sequence-to-sequence learning, transformers optionally use an encoder-decoder framework. The encoder processes the input sequences, while the decoder generates output sequences, taking into account the encoder's representations with the help of cross-attention layers. In contrast to RNNs, transformers process all sequential input tokens in parallel and therefore offer drastically improved scalability. However, transformers have no inherent notion of order and require additional position encoding to preserve this information during processing. Position encodings are added to the input embeddings to provide information about the order, e.g. sinusoidal encodings [307].

The Vision transformer (VIT) [334] has transferred the transformer approach to the image domain by treating the input images as a sequence of patches. VITs and hybrid models combined CNNs with self-attention mechanisms have shown great success in the natural image domain and have also recently gained attention when processing OCT images. Most works have focused on ophthalmology, with notable approaches targeting retinal disease classification [335–337] including foundation models [338, 339], as well as improving image quality [340–342], or retinal segmentation tasks [343–345]. Transformer-based models have recently been considered for image-based force estimation with spatio-temporal US [232] and RGB images [231].

3 Methods and Material

In the following, we first introduce needle-integrated OCT sensors and present our robotic setups for needle insertions. We also provide an overview of the conducted experiments to quantitatively and qualitatively evaluate OCT-based guidance of needle placement. We then look at deep learning for the end-to-end calibration of our OCT systems and present our experimental setups that enable the acquisition of OCT data during robotic tool-tissue interactions. We give an overview of the applied deep learning approaches, the collected data sets, and the performed experiments.

3.1 Experiments for OCT-based Feedback on Needle-Tissue-Interactions

During needle insertions, access to the interface where the interactions between the needle and the tissue take place is extremely limited. Therefore, we integrate fiber-based OCT into surgical needles and needle prototypes to enable measurement directly at the needle tip.

3.1.1 OCT Probes for Robotic Needle Insertions

We are particularly interested in **1.** estimating the proximity and contact of tissue interfaces in front of the needle tip, **2.** sensing the needle tip forces applied to the tissue during the insertion, and **3.** estimating tissue deformations and the applied load to enable elasticity reconstruction via a compression-based OCE needle. An overview of the three OCT needle probes proposed for these applications is shown in Fig. 3.1.

OCT Imaging System

For all our OCT needle probes, we use a spectral domain OCT imaging system (Telesto I, Thorlabs GmbH, Germany) with a central wavelength λ_0 of 1310 nm. The system has an axial resolution of 6.5 µm and a maximum imaging depth of 2.6 mm in air. Ignoring optical attenuation, the imaging depth in tissue is limited to about 1.7 mm, assuming a constant refractive index of 1.45. The detector has 1024 elements, resulting in A-scans resolved over 512 pixels. The OCT system enables the acquisition of A-scans at a sampling rate of up to 91.3 kHz. However, when providing feedback to the operator during collaborative robot-assisted insertions, the robot controller runs at a much lower frequency of 1 kHz. Therefore, the acquisition rate is limited to 5.5 kHz to improve the signal-to-noise ratio for OCT-based force acquisition at the tip [143] and proximity measurement [142]. For all needle probes, we consider single-mode optical fibers (SMF) (SMF-28, Thorlabs GmbH, Germany) cleaved at a 90° angle to achieve common-path OCT imaging.

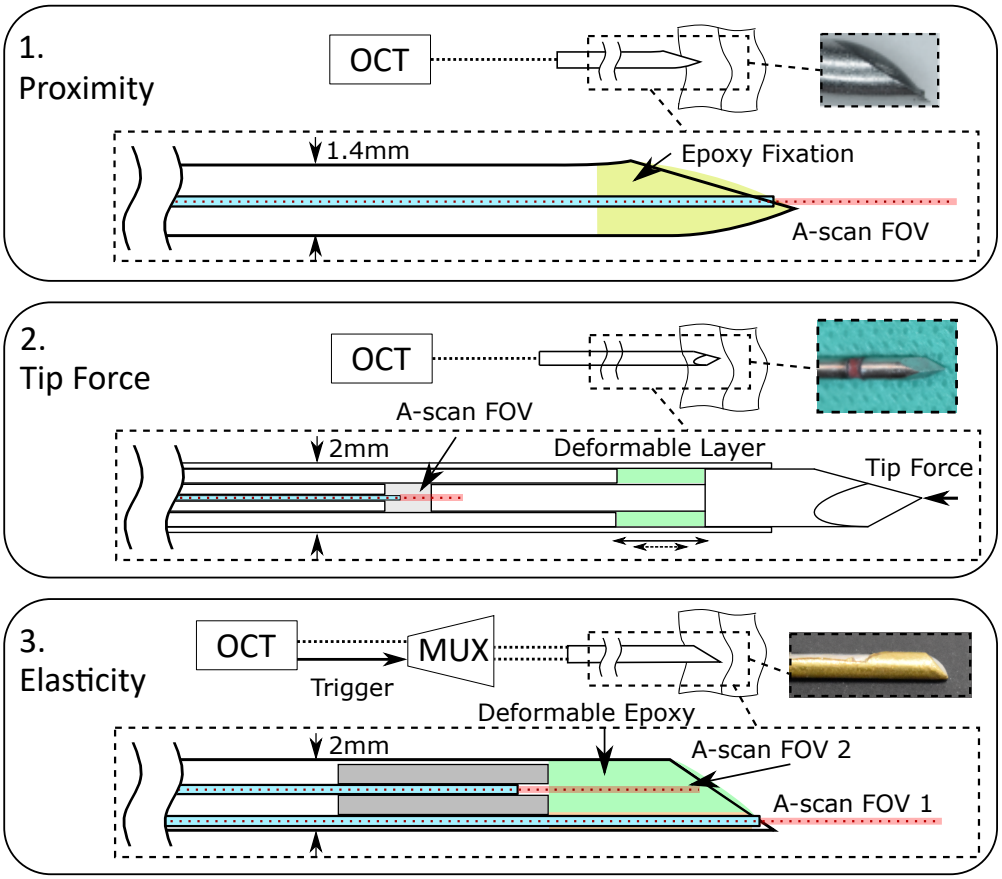

Fig. 3.1: OCT needle probes for sensory feedback during RANI. Cleaved optical fibers (blue) enable miniaturized common-path OCT imaging (red) at the visualized needle tips. **Probe 1:** Forward-facing OCT needle for visualizing tissue and detecting the proximity to distinct tissue layers to safely guide punctures near vulnerable structures [142]. **Probe 2:** OCT needle probe for estimating needle tip forces during insertion. The biopsy introducer needle is modified to include a deformable layer (green) that contracts under load. The resulting movement is detected by the integrated OCT fiber and enables the measurement of tip forces after calibration (Figure adapted from [143], © 2023 IEEE). **Probe 3:** OCE needle with beveled tip and a temporally multiplexed dual-fiber setup for simultaneous measurement of tissue deformation and load sensing. The setup enables quantitative reconstruction of elasticity for biomechanical characterization of deep tissue (Figure adapted from [144] with permission from Springer Nature).

Probe 1

For an OCT needle probe that enables proximity sensing [142], we adapt the needle design proposed in [136] for collaborative robotic needle insertion. We secure an SMF in a standard Tuohy needle used for epidural anesthesia with UV-cured epoxy (NOA 63, Norland Products Inc., USA) (Fig. 3.1, 1.). The needle has an outer diameter of 1.4 mm. The optical fiber and the epoxy resin are placed in such a way that the cutting edges of the needle were not affected. This enables a forward-facing field of view (FOV)

to detect the distance to tissue interfaces with high intensity reflections. This distance d denoted as the proximity can then be used to avoid contact with critical structures, e.g. the spinal cord during epidural anesthesia. We measure the proximity d_{prox} to tissue interfaces by detecting the closest intensity peak of each A-scan relative to the maximum imaging depth d_{max}. We employ temporal and spatial averaging of the A-scan prior to peak detection to increase robustness and stability during collaborative control. However, we desire a force output for our kinesthetic feedback and consequently map our proximity output to a resistive force F_{prox} via:

$$F_{\text{prox}} = \tanh(2(1 - \frac{d_{\text{prox}}}{d_{\text{max}}})), \tag{3.1}$$

where $d_{\text{max}} = 1.77\,\text{mm}$. The hyperbolic mapping enables the operator to maintain transparent control at larger distances while a large resistive force occurs in close proximity to sample interfaces, effectively preventing accidental puncture or needle overshoot.

Probe 2

For force sensing at the needle tip [143], we build on previous works [133–135] and redesign our probe to increase the robustness required for repeated collaborative robotic insertions into deep tissue, e.g. for pancreatic biopsy. The OCT sensor technology is therefore integrated into the introducer needle of a clinical biopsy system. A trocar tip facilitates insertion into deep tissue and the symmetrical design helps to minimize lateral bending during insertion. The OCT needle probe consists of a symmetrical needle tip, a needle sheath with an outer diameter of 2.05 mm, and an inner tube in which a SMF is centered (Fig. 3.1, 2.). The fiber is positioned within 0.5 mm of the proximal end of the needle tip to create an air cavity. A compression layer between the needle tip and the sheath deforms under the applied forces, resulting in a change in the length of the air cavity. This deformation can be detected in the OCT signal and thus enables tip force estimation. To process the OCT, we employ a hybrid convGRU-CNN model similar to previous approaches in [133, 134] that enables accurate real-time force estimation in our collaborative system [143].

Probe 3

For the reconstruction of elasticity during palpation of deep tissue [144], we consider a needle with two SMF for simultaneous load sensing and strain imaging (Fig. 3.1, 3.). The needle has an outer diameter of 2.0 mm and is equipped with a beveled tip that enables percutaneous insertion. The first fiber (FOV 1) enables a forward-facing view in OCT. Here, we consider phase-sensitive measurements of strain in the samples under load instead of the intensity-based proximity sensing considered in [142]. The second fiber (FOV 2) visualizes the displacement of a soft epoxy resin (NOA 1625, Norland Products Inc., USA), which serves as a reference layer for estimating the applied tip force. We use temporal multiplexing to alternate between the two fibers. Compared to spatial multiplexing [121–123], this enables utilization of the full FOV and signal strength, but at the cost of halving the acquisition frequency. To alternate switching at the OCT scan rate of 91.3 kHz, we employ a multiplexer (MUX) consisting of a microcontroller (Arduino™ Mega 2560, Arduino, USA), a solidstate optical switch

(NSSW 1x2 NanoSpeed™, Agiltron, USA), and a switch driver (SWDR DC-100KHz NS Driver, Agiltron, USA) running at 100 kHz. For quantitative OCE measurements, we reconstruct the phase signal for both fiber signals separately. We then perform phase unwrapping and determine the depth dependent displacement (Eq. 2.14) for each A-scan. For needle tip force estimation (FOV 2), we calculate the mean displacement over the entire depth of the epoxy. We assume a linear relation between the observed displacement of the epoxy $\bar{u}_2$ and the applied tip force F_{tip}. Through calibration with tear resistant silicone samples, we obtain

$$F_{\text{tip}} = 174.4\,\text{mN}\,\mu\text{m}^{-1}\bar{u}_2. \tag{3.2}$$

For the forward-facing fiber (FOV 1), we calculate finite differences in displacement u_1 over an axial depth of 1 mm to estimate the axial strain (Eq. 2.4). For biomechanical characterization, we consider pseudo-elasticity values $\text{mN}\,\%^{-1}$ for each sample as we can not assume a uniform distribution to calculate stress (Eq. 2.5) and true Young's modulus.

3.1.2 Robotic Setups for OCT-guided Needle Insertions

We consider two robotic setups to evaluate the proposed OCT needle sensors. For proximity measurement (**Probe 1**) and tip force measurement (**Probe 2**), we investigate how we can effectively use and display OCT-based sensory feedback during RANI. To this end, we consider a collaborative RANI system and integrate our OCT probes to guide needle placement. For tissue elasticity (**Probe 3**), we investigate the feasibility of deep tissue elasticity reconstruction with a bevelled tip needle in our experiments. Our second robotic setup therefore does not yet include collaborative feedback, but serves as a test bed to quantitatively evaluate our OCE needle in comparison to external sensors attached to the needle base.

Collaborative Robotic System for OCT-guided Needle Insertions

As the basis of our collaborative approach, we design a flexible robotic system that enables automated needle insertion under CT guidance [148]. CT images are acquired with the Philips Incisive system and the biopsy target is annotated by medical experts. A customised planning system provides suggested entry points before insertion, taking into account the insertion depth, insertion angle and collision avoidance for bone structures. The registration between CT and the lightweight medical robot (LBR Med 14, KUKA AG, Germany) with 7 degrees of freedom (DOF) is done with an optical tracking camera (fusionTrack 500, Atracsys LLC, Puidoux, Switzerland). This enables the robot to align the needle along a trajectory annotated by the physician in the CT scan. During automated post-mortem biopsy sampling, the robot can insert the needle directly without any additional operator input. We refer to [148] for more details on our robotic biopsy sampling system. For OCT-guided insertions, however, we extend the robotic system with kinesthetic feedback. The LBR robot is designed for human-robot interaction and we extend our setup from [148] for collaborative insertions by adding a 6-DOF force-torque sensor (M3703, Sunrise Instruments) to measure the forces and torques applied by the operator (see Fig. 3.2, left and center). The robot is controlled at a frequency of 1 kHz, while handle forces for haptic control update at a frequency of

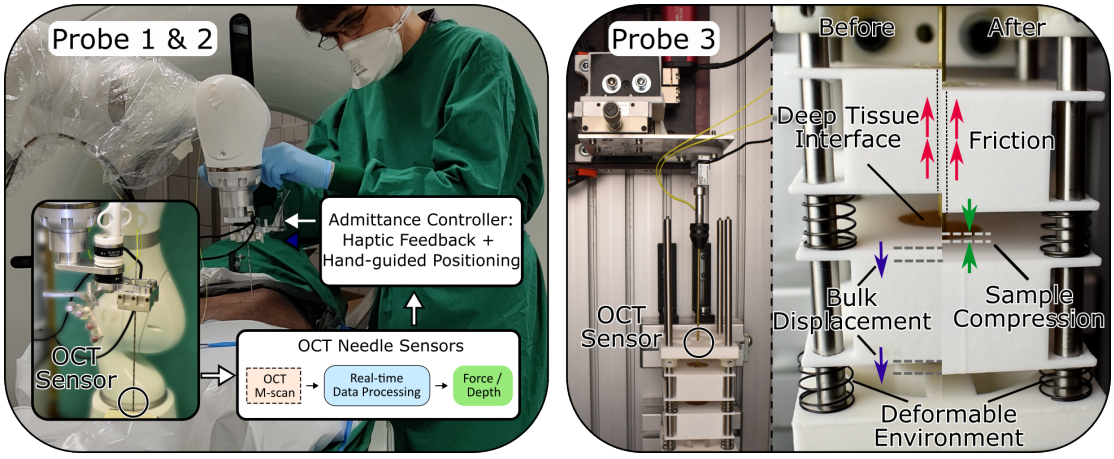

Fig. 3.2: Robotic setups combined with OCT-based feedback on needle-tissue interactions. Left: We consider a collaborative system that displays the force at the needle tip (**Probe 1**) and the proximity (**Probe 2**) of tissue layers. The system comprises a 7-DOF medical robot with two force sensors for measuring the operator and needle shaft forces as well as a custom handle for adapting the OCT biopsy introducer needle and the OCT Tuohy needle. Right: For elasticity (**Probe 3**), we consider an experimental setup to simulate deep tissue indentations with a linear actuator, an axial force sensor, the OCE needle probe and an adapted sample holder. The configuration can be modified to investigate the influence of friction and bulk displacement on the elasticity reconstruction. Figures adapted from [143], © 2023 IEEE and [144] with permission from Springer Nature.

200 Hz. The system is implemented with the Robot Operating System (ROS).

For collaborative insertions, the system uses an admittance controller to convert the operator's forces into the desired robot movement (Fig. 3.3). The inner control loop is governed by the position controller of the LBR robot via the fast research interface [346]. The outer control loop marks an implicit force trajectory-tracking controller analogous to [193, 347]. Similar control loops were also tested in [194] where admittance control showed better performance in needle insertion experiments than impedance control. During insertions, the task space of the needle is restricted to the needle axis. The physician can control the axial placement by the forces exerted on a 3D printed handle while feedback on needle-tissue interactions is implemented by an opposing resistive force. The needle trajectory can be manually controlled by the operator via admittance control, e.g. as for OCT-based depth sensing [142], or can be automatically aligned with a registered CT with a trajectory chosen by the physician in our planning module, e.g. as for needle tip force sensing [143]. The control error e_f of the outer loop is defined as the difference between the force applied at the handle F_{handle} and the resistive force derived from needle-tissue feedback F_{feedback}. The desired robot position x_d is obtained based on

$$x_d(t) = \alpha_i \int_0^t e_f(t)\,dt + \alpha_p e_f(t) \tag{3.3}$$

with controller gains α_i and α_p. No derivative term is used to reduce the impact of noisy force measurements. The resistive feedback force F_{feedback} can be selected based

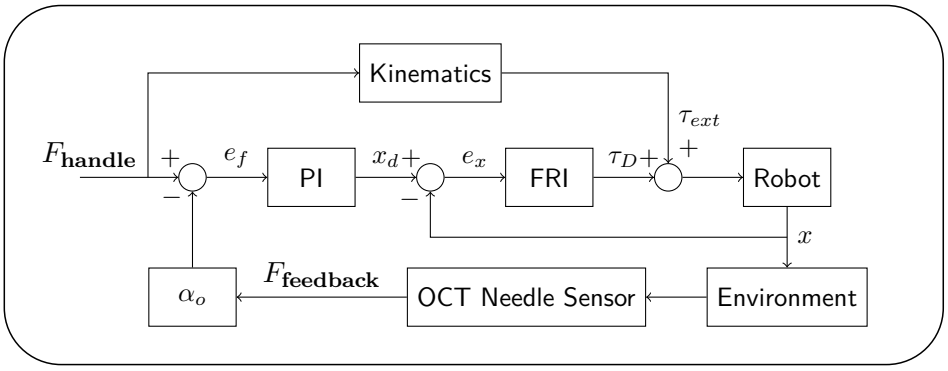

Fig. 3.3: We employ admittance controll to display OCT-based feedback on needle-tissue-interactions during collaborative insertions [142, 143]. The control scheme contains the outer implicit force trajectory loop to set the desired robot position x_d based on the force error e_f operator's handle force F_{handle} and the resistive feedback force F_{feedback}. The resistive feedback of the OCT-based sensors can be amplified by the operator using the gain α_o. The FRI position controller tries to reach the desired position based on the position error e_x. Besides the desired torque τ_d of the controller, the robot is also affected by the externally applied torque τ_{ext}.

on the conducted experiments and the desired operating mode. These include feedback on the OCT derived resistive force depending on the proximity to sample interfaces F_{prox} (**Probe 1**, Eq. 3.1), the estimated needle tip force F_{tip} (**Probe 2**), the total axial forces F_{axial} measured at the needle base, or set to $F_{\text{feedback}} = 0$, e.g. for purely visual feedback [142]. Feedback on needle-tissue interactions can be optionally amplified by scaling the resistive force via the gain α_o chosen by the operator

$$e_f = F_{\text{handle}} - \alpha_o F_{\text{feedback}}. \tag{3.4}$$

However, control output is restricted to prevent uncontrolled movement and oscillations in the opposite direction of F_{handle} due to large feedback forces. The physician can thus perceive needle-tissue interactions when controlling axial placement of the needle while the robot maintains the insertion trajectory.

To evaluate our collaborative approaches, we consider experiments with phantom setups. For depth sensing of critical structures, we emulate a 3 mm epidural space in tissue mimicking gelatin gels [142]. We let ten novice participants place needles within the simulated cavity under three different modes of feedback. These include haptic feedback on F_{prox} and F_{axial} via admittance control (Fig. 3.3) and purely visual feedback on the proximity to sample interfaces d_{prox}. For feedback on needle tip forces, we simulate deep percutaneous insertions through multiple tissue layers by embedding ex-vivo chicken tissue in gelatin gels [143]. We systematically observe tip and friction forces during automatic robotic insertions. We then perform user experiments investigating the reliability with which the five participants are able to perceive interfaces between tissue layers during insertion.

Test Bed for Deep Tissue Indentation Experiments

For evaluating the feasibility of our third needle probe for deep tissue OCE estimates [144], we consider a different experimental setup. We want to systematically conduct surface and deep tissue indentations with our needle probe while simulating friction forces and bulk displacements that would also be present during in-vivo needle insertions (Fig. 3.2, right). To add friction during measurements, we puncture additional phantom layers prior to tissue indentation. To simulate bulk displacement of the sample, we place samples on flexible springs that compress under load and therefore combines actual sample deformation with sample displacement. For actuation, we use a linear motion stage (ZFS25B, Thorlabs GmbH, Germany) for needle insertion. We then acquire OCE data and log motor positions as well as axial needle forces at the base of the needle via a high-resolution force sensor (KD24s 20N, ME-Meßsysteme GmbH, Germany). We thus obtain external measurements to which we compare our OCE-based approach.

In our experiments, we consider two gelatin gels with different elastic properties mimicking healthy and cancerous tissue. For the two materials (A and B), we obtain reference values for Young's moduli of 53.4 kPa and 112.3 kPa through uniaxial compression tests. We perform 10 measurements for samples from each material. Of those, three surface indentations exclude perturbations and seven measurements include simulated friction and bulk displacements of varying degree. Elasticity measurements are targeted for the pre-rupture phase [188, 189] and we therefore consider a measurement window between needle tissue contact (≥ 50 mN) and a sample strain below 20 % based on the OCT tip force and strain imaging. To quantify elasticity based on the OCE tip-force-strain and external axial-force-position curves, we perform linear regression.

3.2 Deep Learning for OCT-based Sensing of Tool-Tissue Interactions

In contrast to RANI, the surgical cavity in RAMIS provides better access to the site of tissue manipulation, which can be used for endoscopic imaging systems to provide optical feedback. In our case, we consider OCT to be a particularly interesting imaging modality due to its depth-resolved imaging with high spatial and temporal resolution. We consider deep learning approaches to calibrate our OCT-based sensors for end-to-end estimation of applied interaction forces and tissue elasticity during optical palpation.

3.2.1 Deep Learning Architectures

We therefore consider two deep learning architectures (Fig. 3.4) for **1.** CNN-based feedback of interaction forces via volumetric high-speed OCT coupled with wave-based elasticity estimates [145] and **2.** wave-based elasticity reconstruction with a modified surgical tool [146] and a transformer-based approach tailored to the sequential A-scan sequences obtained with OCT [147]. In the following, we briefly present the respective approaches. For further implementation and training details, please refer to the corresponding publications.

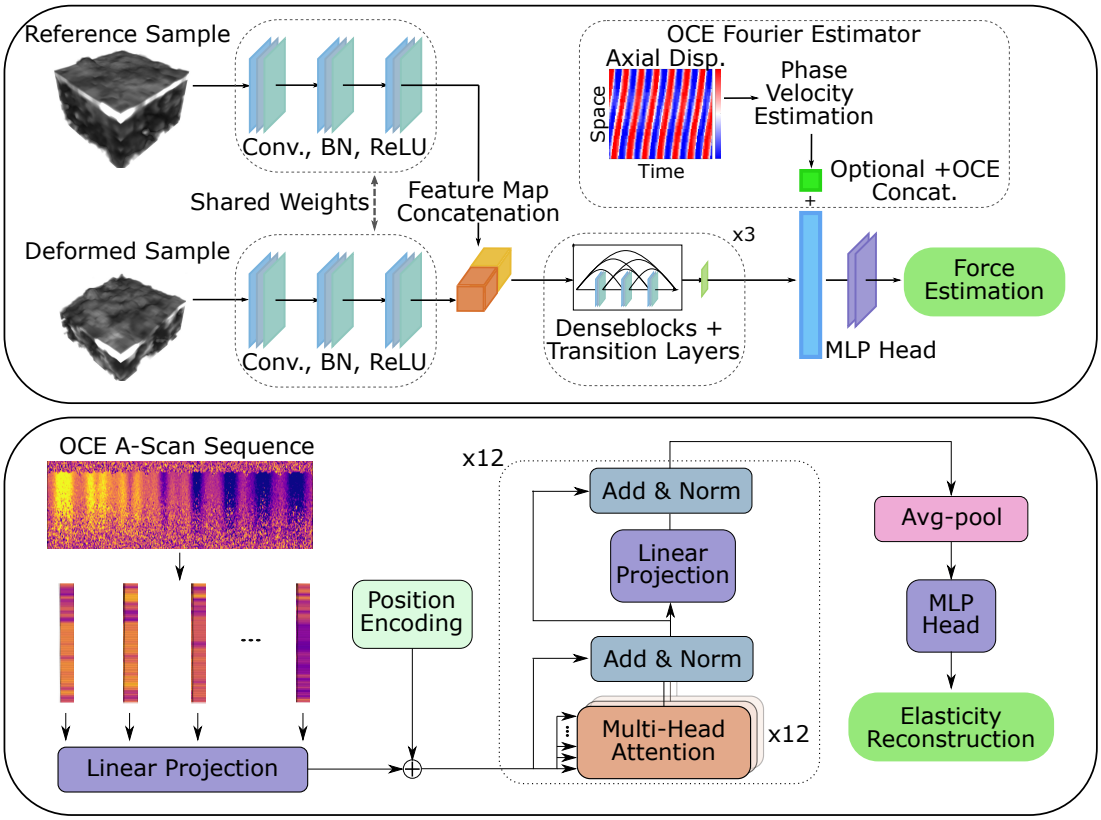

Fig. 3.4: Deep learning architectures for processing spatio-temporal OCT data. Top: A Siamese CNN structure infers the interaction force from OCT volumes of a deformed and reference sample. The model can optionally incorporate conventional OCE wave velocity estimates for improved force estimation. Bottom: A transformer-based approach that leverages the spatio-temporal nature of OCT for end-to-end elasticity reconstruction from sequences of A-scans. A-scans are directly processed as sequential inputs and their position is encoded before passing through the encoder. It consists of 12 layers and each self-attention block has 12 heads. (Figures adapted from [145], licensed under CC BY 4.0 and from [147] with permission from © Optica Publishing Group)

Force Estimation

For optical force estimation, we design a CNN that builds on previous research on OCT-based force estimation [155, 157]. We keep the densely connected convolutional network (DenseNet) approach [310], but consider a Siamese architecture. Thus, in addition to the deformed sample for which we want to estimate the applied interaction force, the model also receives a reference input (see Fig. 3.4). The reference data is acquired before the tool-tissue interaction takes place. The Siamese structure enables efficient processing of both inputs through shared parameters. Optionally, the wave-based OCE phase velocity obtained via the conventional Fourier estimator (FE) can be fused with the generated features before the final, fully connected layers (Fig. 3.4). Further details on conventional Fourier estimation can be found in our work [145, 147]. We also derive 2D surface deformation maps from the volumetric OCT. This allows us to investigate the

potential utility of elasticity fusion for deformation maps that can also be obtained by stereoscopic imaging, e.g., as in [226, 227]. Therefore, we design our end-to-end learning approach to be compatible with 2D and 3D operations. We chose model width and depth to maintain similar capacity for 2D and 3D inputs. In our results, we refer to models with OCE fusion with the suffix +OCE.

Elasticity Estimation

For optical elasticity estimation, we consider a transformer-based architecture that enables direct processing of spatio-temporal OCT data, i.e., sequential accumulation of one-dimensional A-scans at different spatial or temporal positions. In wave-based OCE, the excited wave propagates through the tissue while the scanning mirror continuously steers the sample beam back and forth (Fig. 2.3). Raw OCE data is therefore a sequence of A-scans, e.g. $\mathbb{R}^{(wt)\times d}$ for B-M-scans in OCE, where w and d correspond to the width and depth, respectively. Our approach directly considers each A-scan as input tokens that are linearly projected to an embedding dimension of 768, similar to VIT [334]. The model maintains the position information during self-attention by considering different approaches for position encodings that are added to each embedded token. In particular, we consider rotary position encodings (RoPE) [348] as an efficient implementation of the relative distance between tokens in the long sequence of A-scans. We also consider the learnable position encoding [334] and the sinusoidal encoding used in [307]. After adding the position encoding, each embedded token is processed to key, query and value embeddings in multi-headed self-attention, followed by normalization and linear projection. Our approach uses Flash-Attention [349] and root mean square layer normalization. The model consists of 12 layers and a width of 12 heads per multi-headed attention block to achieve good performance with a reasonable parameter size. To directly reconstruct the sample elasticity in our regression task, we average the embeddings over the encoder output sequence. A final fully connected layer serves as the regression head.

3.2.2 Experimental Setups and Acquired Data Sets

The supervised learning strategies require the acquisition of training data with known ground truth values for sample elasticity and interaction forces. We therefore consider two experimental setups (Fig. 3.5) that allow us to systematically investigate the effectiveness of our approaches.

OCT Imaging System

For optical feedback of interaction forces [145] and tissue elasticity [147], we use a high-speed swept-source system (SS-OCT, OMES, Optores, Germany) operating at a temporal sampling rate of 1.5 MHz. The central wavelength of the system is 1315 nm and provides an axial resolution of 15 µm in air. An optical lens system with a focal length of 300 mm is located between the scan head and the sample.

Force Estimation Data

For optical force estimation in conjunction with elasticity estimation, we acquire both volumetric OCT and B-M-mode OCE data (Fig. 3.5, left). The former is needed to

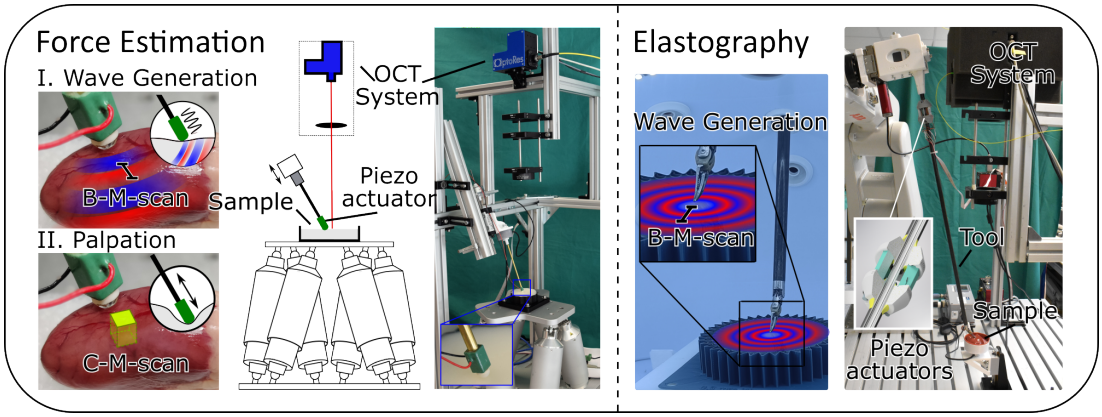

Fig. 3.5: Robotic setups to acquire large data sets for supervised learning of tool-tissue interactions based on OCT. Left: We design an experimental setup for the acquisition of wave-based OCE data and volumetric OCT data during tool palpation with simultaneous ground truth measurement of interaction forces (Figure adapted from [145], licensed under CC BY 4.0). Right: We also consider a modified surgical tool to facilitate wave excitation during RAMIS and acquire B-M-mode wave-based OCE data for phantoms with known elastic properties for end-to-end elastic modulus reconstruction (Figure adapted [147] with permission from © Optica Publishing Group).

visualize the deformations of the sample and derive the interaction forces. The latter can be used to condition the model on the expected relationship between the elasticity of the sample, the deformation and the interaction force. First, we excite surface waves for wave-based OCE measurements using a piezoelectric element and a sinusoidal excitation with a frequency of 1000 Hz. At the same time, we acquire B-M-scans with a spatial resolution of 476×32 pixels for depth d and width w, respectively. The B-scans correspond to a lateral FOV of 3.5 mm and are acquired with a temporal resolution of 14.2 kHz. Second, we create volumetric scans to track the deformation of the sample during the interaction between the tool and the tissue. We simulate a pushing task commonly performed in minimally invasive surgery [224]. To do this, we scan each sample while driving random and sinusoidal position profiles at different speeds with a maximum palpation depth of 2.5 mm. We use the same scan head and acquire data with a spatial resolution of 476×32×32 pixels for depth d and lateral dimensions, respectively. We acquire C-M-Scans with a temporal frequency of 833 Hz. Simultaneously, we perform force measurements with a high-resolution force sensor (Nano 43, ATI, USA) at a frequency of 500 Hz. We then interpolate and synchronize our force measurements to the volumetric OCT data.

The data set consists of samples from seven different gelatin gels with different weight ratios ranging from 5 % to 20 %. We also perform OCT and OCE measurements on 10 ex-vivo chicken hearts to test the generalizability of our models to soft-tissue. We use a hexapod robot (H-820.D1, Physik Instrumente, Germany) to streamline data acquisition and measure samples repeatedly at different locations. The scanned FOV remains fixed relative to the probing tool and only the sample is moved. Before running the OCT data through our learning-based approach, the OCT volumes are preprocessed to a size of $32 \times 32 \times 32$. This includes surface detection, cropping, and downsampling to obtain

more uniform data. The surface map obtained by projecting the maximum intensity along the depth axis also allow us to obtain 2D deformation data. In our experiments, we then compare the effectiveness of our approach for 2D and 3D data representations with 5-fold sample stratified cross-validation.

Elasticity Estimation Data

In [147] we exclusively consider the accurate estimation of sample elasticity for wave-based OCE. Therefore, we only obtain B-M-mode OCE data during surface wave excitation. In contrast to our previously discussed work [145], we use a modified surgical tool for wave excitation (Fig. 3.5, right). We provide a more detailed description of this approach in [146]. We also use a different scan head that enables a higher axial sampling rate by resolving the FOV of 3.5 mm over 118 instead of 32 pixels. Since we target the end-to-end processing directly from the obtained sequence of A-scans, we keep preprocessing to a minimum and omit surface detection. We crop all A-scans to a depth of 256 pixels. We excite the piezoelectric actuators in our tool with 1000 Hz and for each OCE measurement we acquire 30×10^3 A-scans. If we ignore the A-scans during the pivot points of the resonant scanners, this corresponds to 208 cross-sectional images in the conventional reconstruction of B-scans. Each measurement of our spatio-temporal OCE data representing propagating surface waves therefore has a size of $(208 \times 118) \times 256$ pixels.
To test our transformer-based approach, we acquire a data set with samples of four gelatin gels with different elastic properties. To apply our supervised learning strategy, we obtain ground-truth measurements for the samples by uniaxial compression tests. The elastic moduli of the considered phantoms ranged from 17 kPa to 139 kPa. To simplify data acquisition, we mount the modified surgical manipulator on a six-axis serial robot (IRB120, ABB, Switzerland). Our training data set consists of 20 samples for which we take measurements at 25 different locations. We select one independent sample from each elasticity as a test data set and then perform sample stratified cross-validation with the remaining data. In addition to our homogeneous training data, we manufacture phantoms simulating hard lesions in a soft environment. We scan the phantoms and acquire measurements at different locations in a grid to visualize elastography maps. Thus, we simulate a tumor detection task and consider the second data set for generalization to heterogeneous phantoms. Finally, we perform OCE measurements with post-mortem heart, kidney and liver tissue. We do not obtain ground-truth measurements, but perform qualitative comparisons between elasticity estimates and the maximum force observed during sample palpation with our robotic tool, analogous to the pushing task in [145]. In our experiments, we compare our transformer-based approach with state-of-the-art CNN-based approaches and conventional processing using FE and the Rayleigh-Lamb wave model (Eq. 2.2, Eq. 2.6, and Eq. 2.7).

3.3 Evaluation Metrics

In our works, we consider a number of different error metrics. For the evaluation of the regression tasks of force and elasticity estimation, these are mainly the mean absolute error (MAE) and the root mean square error (RMSE). The mean square error (MSE) is used to train our learning-based approaches. For optical force estimation [145], we additionally consider the Pearson correlation coefficient (PCC) and a normalized MAE

(NMAE), which scales the MAE based on the range of observed forces that vary for samples with different elasticities. For learning-based elasticity reconstruction [147], we also consider the mean absolute percentage error (MAPE), the R2 value, and a statistical permutation test to identify significant differences between models. When considering elasticity estimates for the classification of samples [144, 147], we examine the area under the receiver operating characteristic (AUROC) and the area under the precision recall curve (AUPRC). In our user studies [142, 143], we also evaluate the detection rate with which the participants are able to perceive the target interfaces.

4 Experiments

In the following, we present the main findings of our contributions [142–147]. For a more detailed description of the experiments and results, please refer to the corresponding publications.

4.1 OCT-based Feedback on Needle-Tissue Interactions during Robotic Insertions

Our experiments in [142–144] show that fiber-based OCT can be integrated into surgical needles to provide sensory feedback during RANI. We show that a fiber-based OCT sensor can be attached directly to the needle tip and that this has major advantages for guiding the needle and understanding needle-tissue interactions compared to sensors attached to the needle base. The three approaches include online estimation and haptic display of proximity to boundary layers, estimation of needle tip forces, and quantitative estimation of tissue elasticity during deep tissue compression-based OCE.

4.1.1 Proximity-based Haptic Feedback for Collaborative Robotic Needle Insertion

Our experiments in [142] show that needle-integrated OCT can provide feedback on the proximity to tissue interfaces based on the change in refractive index (**Probe 1**). Our setup makes it possible to estimate the depth of these interfaces and indicate them to the operator visually and through kinesthetic feedback. This facilitates precise and safe placement in cavities by preventing overshooting into critical structures. In a user study with phantoms simulating the epidural space, we perform 150 insertions and show that our approach enables the most accurate placement of the needle in the target cavity (Fig. 4.1). While the visual indication of depth-sensing to the operator improves placement accuracy, only the combined visual and haptic feedback effectively prevents overshooting that would correspond to dural puncture during epidural anesthesia. Our approach achieves the lowest MAE and a 94 % success rate in stopping the needle before the dura. Only 6 % of insertions result in needle overshoot. In comparison, with force-based haptic feedback, only 38 % of insertions result in successfully placed needles in the 3 mm cavity. Displaying forces acting on the needle shaft is often insufficient to differentiate between the recreated ligamentum flavum, which must be punctured to reach the epidural space, and the recreated dura, which is associated with nerve damage when punctured. The results therefore show that OCT can be used to determine the distance to critical structures and displayed through kinesthetic feedback in collaborative RANI to improve needle placement in our experiments.

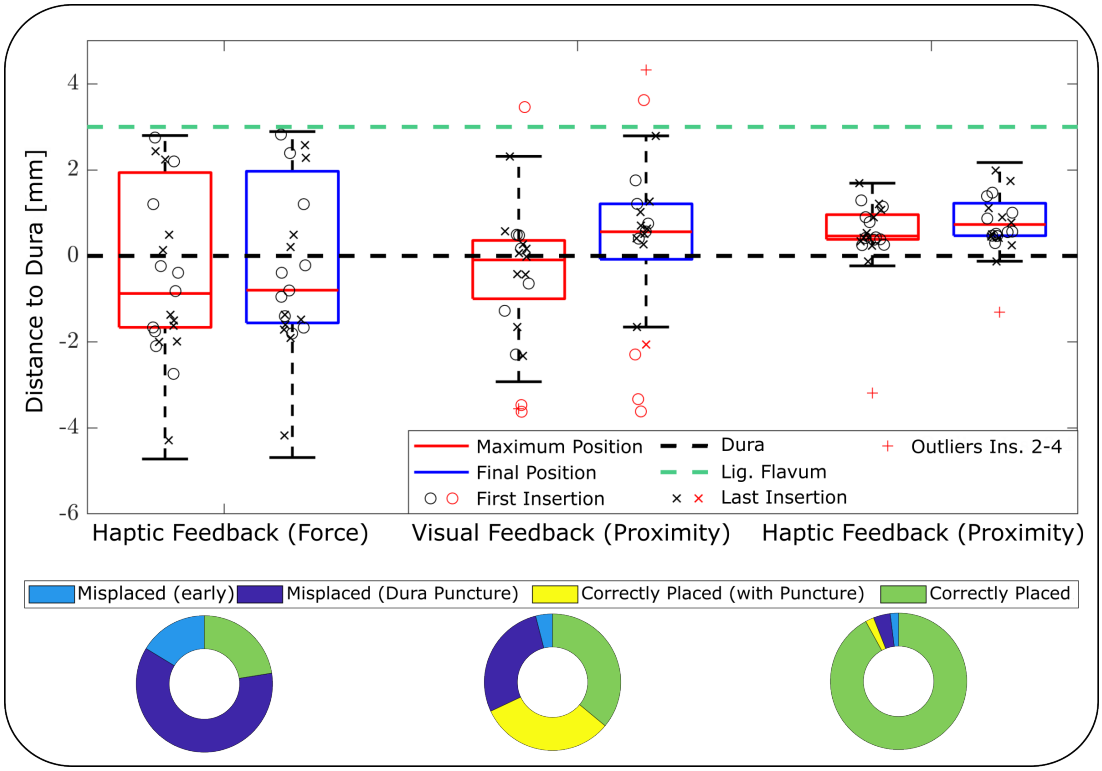

Fig. 4.1: Results of our user study with an OCT-based proximity sensor. Maximum extension and final placement in the simulated epidural cavity are shown for force-based feedback, visual proximity feedback and our combined haptic and visual proximity feedback. The success rate for final placement and overshooting into the critical structure (dura), which must be prevented, is visualized below (Figure adapted from [142], licensed under CC BY 4.0).

4.1.2 Collaborative Robotic Biopsy with Trajectory Guidance and Needle Tip Force Feedback

Our results in [143] show that it is furthermore possible to reliably measure the forces at the needle tip of a clinical biopsy introducer needle (**Probe 2**) using OCT. Based on our convGRU-CNN data processing, we achieve online tip force estimation at 200 Hz and with an MAE of 0.11 N. We then perform automated and collaborative insertions in phantoms and ex-situ pancreatic tissue to illustrate the value of tip force estimation compared to measurements at the needle base. Automated insertions reveal that needle tip forces consistently indicated entry and exit points at tissue junctions of ex-vivo tissue embedded in gelatin phantoms (Fig. 4.2, left). However, there remains a small spatial offset for the detection of the tissue interfaces 2.08±1.08 mm and 5.13±1.88 mm after entering and exiting the ex vivo tissue, respectively. Our experiments also show that friction forces vary significantly. As expected, forces vary between different tissue and phantom materials but we also observe inconsistent forces for different layers of the same homogeneous gelatin. The user study further demonstrates the ability to detect tissue transitions during collaborative insertion. Operators receiving haptic feedback on needle tip forces perceive transitions with an overall detection rate of 91%. Detection errors are lower for transitions from soft, homogeneous gelatin to stiffer ex-vivo tissue

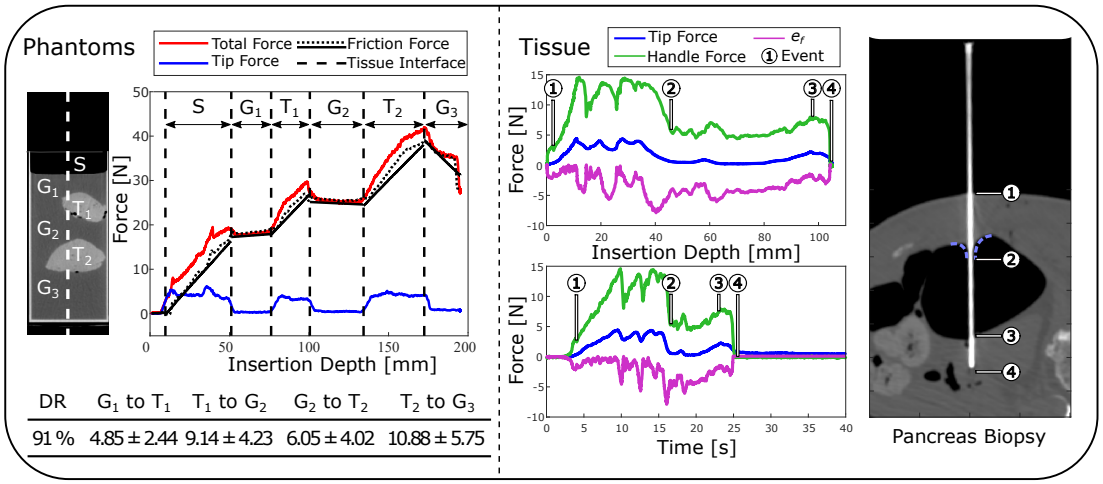

Fig. 4.2: Deep tissue insertions with OCT-based needle tip force estimation with a biopsy introducer needle. Left: Examples of automated insertion into phantoms with ex-vivo tissue show that needle tip forces can effectively indicate tissue interfaces. The detection rate (DR) and distances [mm] between the pre-insertion position and the positions recognised by the user study participants are also shown below. Insertions are segmented into skin (S), gelatin (G) and tissue (T) layers. Right: Demonstration of a collaborative pancreatic biopsy with percutaneous needle insertion through the stomach. Histopathology confirms successful tissue sampling. (Figures adapted from [143], © 2023 IEEE).

than for tissue-to-gelatin transitions, where forces decrease after exiting the tissue. The feasibility of the proposed haptic assistance in robotic insertions is further underlined by a collaborative pancreatic biopsy procedure (Fig. 4.2, right). The successful removal of pancreatic tissue is confirmed by histopathologic examination. Our experiments in [143] thus successfully demonstrate how OCT-based tip force measurements can be displayed to the physician via kinesthetic feedback and coupled with image-based trajectory guidance to enable precise needle placement.

4.1.3 Optical Coherence Elastography Needle for Biomechanical Characterization of Deep Tissue

Our probe design in [144] demonstrates how forward-facing OCT combined with force sensing provides a novel approach for quantitative elasticity estimation during deep tissue needle insertion (**Probe 3**). We successfully combine force measurement at the tip and imaging of sample strain in a beveled-tip needle using temporally multiplexed dual-fiber OCT. Using our laboratory setup to simulate frictional forces and bulk displacement during needle insertion (Sec. 3.1.2), we compare our needle OCE approach with external measurements of motor encoder position and force measurements at the needle base. We perform surface and deep tissue indentations with each of the two materials and the indentation curves for both approaches are shown in Fig. 4.3. For external sensors, friction forces increase the total axial force measured at the base of the needle. Bulk displacement partially reduces the resistance and leads to lower resistance during indentation. Furthermore, depending on the environment of the sample, the bulk displacement can be non-linear, e.g. simulated by stick-slip, as seen in two cases

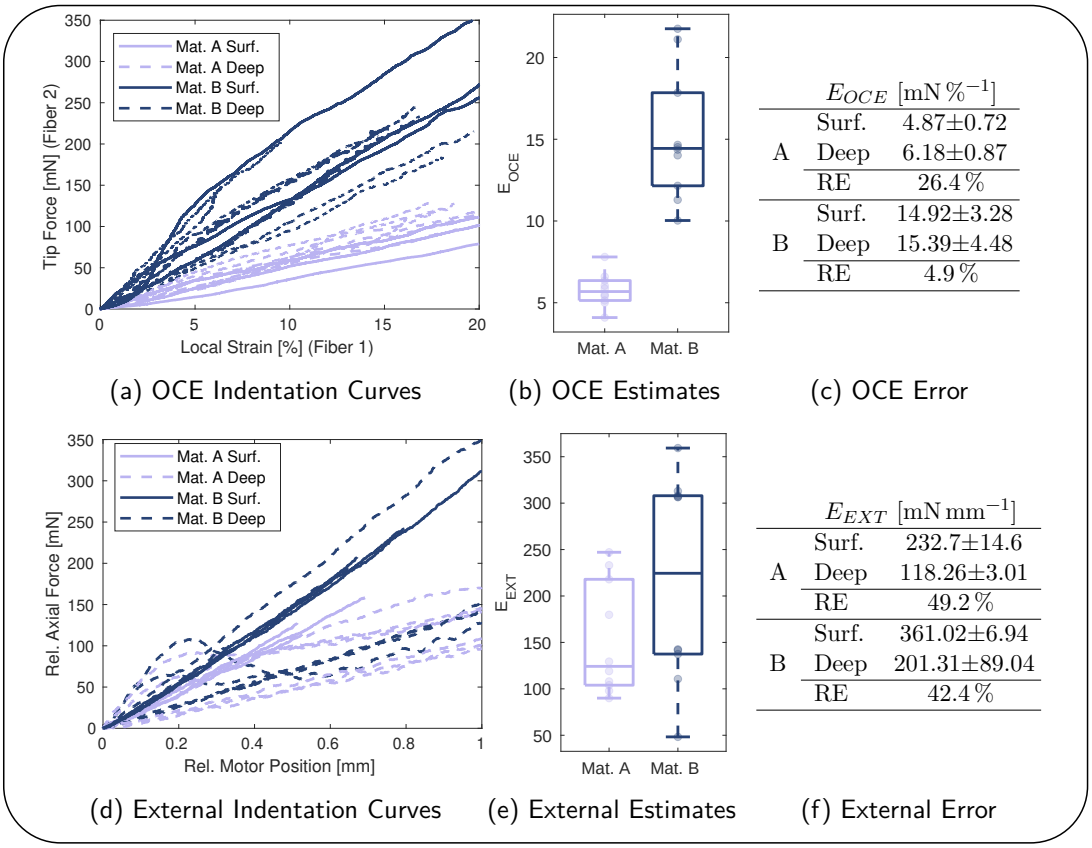

		E_{OCE} [mN %$^{-1}$]
A	Surf.	4.87±0.72
	Deep	6.18±0.87
	RE	26.4 %
B	Surf.	14.92±3.28
	Deep	15.39±4.48
	RE	4.9 %

		E_{EXT} [mN mm^{-1}]
A	Surf.	232.7±14.6
	Deep	118.26±3.01
	RE	49.2 %
B	Surf.	361.02±6.94
	Deep	201.31±89.04
	RE	42.4 %

Fig. 4.3: Results for needle OCE in surface and deep tissue indentations. Curves for (a) OCT-based tip force estimation plotted against the local strain of the OCE and (d) axial force-position measurements from external force sensor and motor encoder. The materials A and B refer to soft and stiff phantoms, respectively. Pseudo-elasticities obtained by linear fitting of indentation curves are shown for (b) our OCE needle approach and (e) external measurements. Measured elasticity and the relative error (RE) between the mean values of surface and deep tissue indentations for (c) OCE needle E_{OCE} and (f) external sensors E_{EXT}. Figures adapted from [144] with permission from Springer Nature.

of material B. In contrast to external sensors, our OCE needle approach shows good separation of the two materials. More importantly, the elasticity estimates for the surface and deep tissue measurements are much more consistent. We also perform a linear regression to quantify elasticity for each approach with E_{OCE}[mN %$^{-1}$] and E_{EXT}[mN mm^{-1}] from the tip force-strain and axial force-position curves respectively. When comparing surface measurements with deep indentations, our approach achieves a reduction in relative errors from 49.2% and 42.4% to 26.4% and 4.9% for gelatin samples mimicking healthy (A) and cancerous (B) tissue (Fig. 4.3). Consequently, needle-based compression OCE enables quantitative elasticity reconstruction that is less affected by systematic perturbations such as frictional forces and bulk displacement. This also becomes clear when the measured elasticity is used for the biomechanical characterization of the two materials. The measured pseudo-elasticity of our OCE approach allows a complete separation between the materials, with AUROC and AUPRC values of 1.00.

In contrast, external measurements are strongly influenced by frictional forces and bulk displacement. The external measurement therefore do not provide a robust quantitative elasticity estimate. Discrimination of materials with external measurements results in AUROC and AUPRC values of 0.85 and 0.861, respectively. Our results in [144] therefore show that local measurements of strain and load at the needle tip are essential for biomechanical characterization of deep tissue and that compression-based OCE has the potential to provide such combined sensory feedback even in needle format.

4.2 Deep-learning for End-to-end Estimation of Interaction Forces and Tissue Elasticity

Our second research topic revolves around the use of deep learning to calibrate optical setups for improved feedback on tool-tissue interactions based on spatio-temporal OCT data. Our results in [145, 146] show that OCT with end-to-end CNN-based deep learning has the potential to facilitate accurate reconstruction of interaction forces and elasticity during intraoperative tissue manipulation. In particular, transformer models tailored to directly process A-scans in spatio-temporal OCT data could provide better feedback than conventional or CNN-based approaches [147].

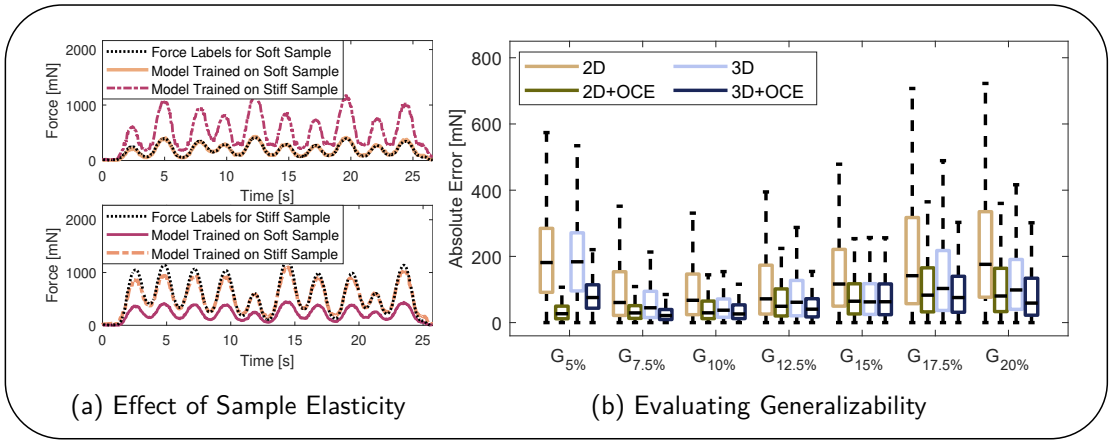

(a) Effect of Sample Elasticity (b) Evaluating Generalizability

Fig. 4.4: **(a)** Examples showing the effects on force estimates when elasticity is not considered. A model trained on "stiff" samples applied to a "soft" material overestimates the interaction forces due to the large deformations. Conversely, the forces are underestimated when a model is applied to stiffer materials. **(b)** Absolute error of force estimation models generalizing to each sample elasticity with gelatin weight ratios from 5 % to 20 %. Model performance is compared between 2D and 3D inputs and with and without integration of wave-based OCE velocity estimates. Figures adapted from [145], licensed under CC BY 4.0.

4.2.1 Optical Force Estimation for Interactions between Tool and Soft Tissues

In our work in [145], we investigate the effect of tissue elasticity on optical force estimation using OCT and deep learning. Our results show that tissue properties need to be taken

into account to enable accurate and versatile image-based force estimation for different tissue types and properties. We conduct three experiments: We investigate the effects of elasticity on force estimation when different elastic properties are not considered during training, we evaluate the generalization of deep learning models with OCE integration, and we consider the transition from gelatin phantoms to ex-vivo soft tissue. In these experiments, we compare volumetric OCT with 2D surface representations similar to the surface deformation maps obtained with stereoscopic imaging.

To demonstrate the influence of elasticity, the CNN models without wave-based OCE velocity estimates (Fig. 3.4) are trained on data from single gelatin phantoms. The models must therefore implicitly learn the relationship between the observed deformation and the applied load via the tool. When testing the models with the same material from the training set, the RMSE ranges from 0.19 mN to 235 mN for the most and least elastic phantoms, respectively. However, applying the models to materials with elastic properties different from those of the training data results in large errors due to the change in relative deformation per force. Consequently, the forces are underestimated when generalizing to more elastic samples and overestimated for less elastic samples (Fig. 4.4, (a)) with an RMSE of up to 679 mN.

In our second evaluation, we consider larger and more versatile training data to evaluate the generalization of 2D and 3D models with and without OCE. Models trained on 3D OCT performed better than 2D models and achieve a lower RMSE (143.7 mN versus 216.7 mN). The integration of OCE data into our model significantly improves the estimation accuracy and reduces the RMSE to 91.0 mN and 97.2 mN for 3D+OCE and 2D+OCE, respectively (see Fig. 4.4 and Fig. 4.5). OCE mitigates the extrapolation errors especially for the softest samples by reducing the errors by 81 % and 56 % for 2D+OCE and 3D+OCE, respectively.

			Gelatin	Tissue
Without OCE	2D	RMSE	216.7±60.3	129.5±82.6
		NMAE	0.26±0.26	0.26±0.17
		PCC	0.78±0.07	0.93±0.03
	3D	RMSE	143.7±62.3	283.5±212.9
		NMAE	0.20±0.28	0.60±0.48
		PCC	0.89±0.03	0.94±0.04
With OCE	2D	RMSE	97.2±47.3	**51.2±24.8**
		NMAE	0.09±0.03	0.10±0.04
		PCC	0.90±0.01	0.91±0.06
	3D	RMSE	**91.0±34.7**	76.6±35.6
		NMAE	0.11±0.11	0.16±0.09
		PCC	0.93±0.02	0.94±0.03

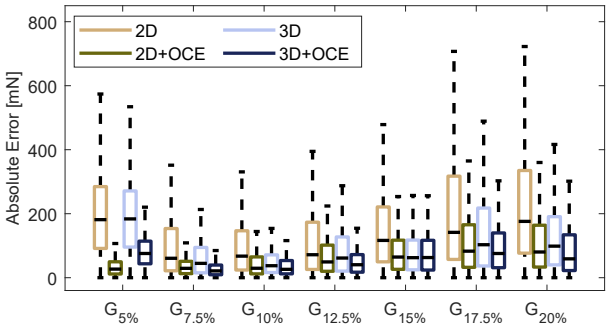

Fig. 4.5: Left: Performance of models trained with homogeneous phantoms during generalization to unseen gelatin materials and ex-vivo tissue. Right: Example showing how wave-based OCE can be integrated into the end-to-end learning-based approach to improve force estimation on unseen samples. Figure adapted from [145], licensed under CC BY 4.0.

Finally, we validate our approach on ex-vivo chicken heart tissue (Fig. 4.5). OCE fusion models outperform 2D and 3D models without phase velocity information, achieving the lowest RMSE of 51.2 mN for fused elasticity estimates and surface deformation maps. In contrast, models without OCE yield significantly higher errors, with an RMSE of

283.15 mN and a normalized MAE of up to 0.6. Examples show that force estimates from 2D+OCE and 3D+OCE models provided more accurate predictions and benefited from phase velocity calibration (Fig. 4.5).
Our results in [145] consequently show that deep learning can be used to combine volumetric OCT with wave-based OCE in an end-to-end approach. In our experiments, such consideration of elastic properties is essential for a robust and versatile image-based estimation of interaction forces.

4.2.2 A-scan Sequence Transformers for Palpation with Optical Coherence Elastography

Tab. 4.1: Error metrics for conventional Fourier-based OCE elasticity reconstruction, CNN baselines and our transformer-based approach. Best results are marked in bold. * Conventional FE processing resulting in unrealistically high values in 15.4 % of measurements which are excluded here.

Model	RMSE [kPa]	MAE [kPa]	MAPE	R2	Weights
FE*	9.25	7.80	0.12	0.949	
Dense-S [146, 151]	13.85±1.68	10.48±1.26	0.22±0.04	0.906±0.002	109K
VP-NET [153]	15.76±6.15	5.55±2.69	0.12±0.05	0.862±0.008	8.7M
VP-NET-L [153]	14.33±5.16	6.03±2.74	0.14±0.07	0.888±0.006	17.7M
Ours [147]	**2.49±1.37**	**1.64±0.89**	**0.03±0.02**	**0.996±0.001**	85.8M

In [146], we propose a modified robotic instrument for mechanical wave excitation in a minimally invasive setting. Since the surgical tool is already in contact with the tissue during tool-tissue manipulation, we excite the shaft of the manipulator proximally to transfer the vibrations to the distal tool tip. In this way, we achieve wave-based OCE without the need for a separate device for wave excitation, such as the previous wave-based OCE in [145]. We demonstrate that our method of wave excitation can be coupled with CNN-based processing to enable end-to-end reconstruction of the elastic modulus in OCE. Building on this, we show that a transformer model can further improve the reconstruction of the elastic modulus by using a model architecture that can directly process sequences of A-scans [147].
In [147], we compare the elasticity reconstruction of our transformer-based approach (Fig. 3.4) with state-of-the-art CNNs and conventional processing. Our approach based on self-attention is tailored to directly process A-scans that are inherently obtained during OCE scanning, and spatial dependencies are fully learned during training. In our experiments, we consider homogeneous phantoms, heterogeneous inclusion phantoms and ex-vivo human tissue samples. First, we optimize our approach in terms of architecture structure, position encoding, and data processing using the homogeneous phantoms. Our approach, which directly processes the A-scan sequences, achieves significantly better performance than previous methods for all error metrics considered (Tab. 4.1).
We then consider the generalization of our approach and all baselines to heterogeneous phantoms that simulate cancerous inclusions (Fig. 4.6). The experiments with simulated lesions emphasize the improved elasticity reconstruction of our transformer-based approach with an MAE of 7.44±14.43 kPa compared to 13.27±20.16 kPa, 24.76±11.59 kPa and 28.97±20.46 kPa for FE, Dense-S and VP-NET, respectively. Earlier CNN-based approaches [146, 151, 153] consequently perform worse when generalizing to the inclu-

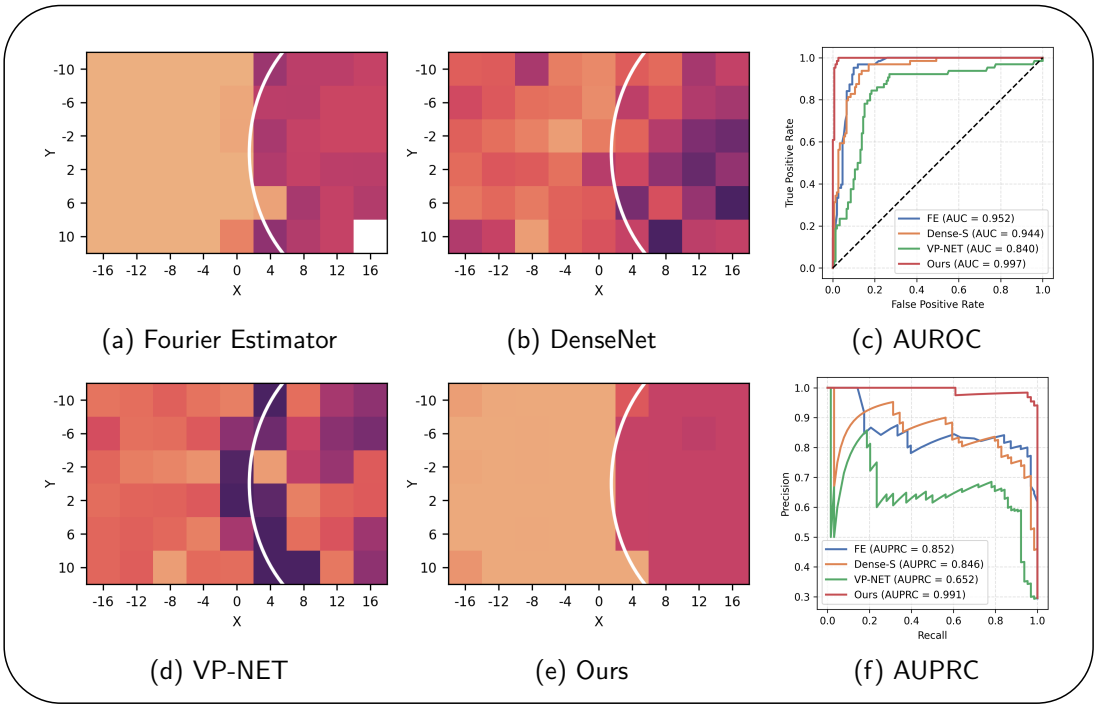

Fig. 4.6: Model predictions for (a) FE, (b) Dense-S, (d) VP-NET and (e) our approach for a heterogeneous phantom. The phantom contains a cylindrical inclusion (white circle, Young's modulus of 56 kPa) embedded in softer surroundings (Young's modulus of 17 kPa). Failed processing for FE is marked in white. (c) AUROC and (f) AUPRC curves for the discrimination between simulated lesions and soft surroundings for each approach. Figures adapted with permission from [147] © Optica Publishing Group.

sion phantoms and show poor contrast between soft and stiff regions. These methods also partially overestimate the elasticity, especially at the edges of the inclusion. The improved generalization of our approach is also evident when we consider the detection of the inclusion via the AUROC and AUPRC (Fig. 4.6). Our method outperforms the previous methods and yields the highest values of 0.997 and 0.991 for AUROC and AUPRC, respectively. Finally, we qualitatively evaluate our approach on human ex vivo tissue samples of heart, kidney and liver. With our approach, we obtain elasticity estimates that are within the expected range reported in the literature, and we observe the highest correlation with a surrogate reference obtained by monitoring the contact force during tissue indentation [147].
In summary, our results in [147] show that transformer architectures are well suited to process spatio-temporal sequences of A-scans naturally acquired during OCE scanning, as demonstrated by the improved end-to-end elasticity reconstruction.

5 Discussion

Current robotic surgery systems are commonly hindered by the absence of feedback on tool-tissue interactions [2, 6]. This restricts surgeons ability to feel tool-tissue interactions, affecting their capacity to manipulate tissue effectively and safely. Novel technologies are required to provide such feedback that can shorten operating times, quicken training, enhance procedural success rates, and reduce the mental workload of surgeons [7, 8, 11, 12]. Additionally, sensory feedback on biomechanical tissue properties could enable tissue characterization [15, 18], potentially providing new means for the intraoperative differentiation between healthy and pathological tissues.
Due to it's high spatial and temporal resolution and the potential miniaturization with fiber-based probes, OCT is a promising technology in light of these challenges. However prior investigations into the application of OCT for intraoperative feedback on tool-tissue interactions have been limited. Therefore, this work explores novel adaptations of OCT-based sensor technologies. We particularly investigate how we can use OCT to sense tool-tissue interactions at the tip of medical needles and, when integrated with robotic systems, provide enhanced navigation and guidance during RANI. Secondly, we consider how end-to-end deep learning models can improve accuracy and reliability for reconstruction of interaction forces and tissue elasticity from spatio-temporal OCT data. In the following, we consequently discuss the findings presented in chapter 4 and evaluate our contributions with respect to these two research topics. We first assess our contributions to the first research topic considering needle-based OCT to guide robotic insertions. We discuss our approaches on collaborative RANI with force [143] and proximity [142] feedback. We then evaluate our findings regarding quantitative elasticity reconstruction for deep tissue [144]. Afterwards, we discuss our contributions for our second research topic considering advancements in end-to-end deep learning for feedback on tool-tissue interactions. These include our findings on optical force estimation with OCT and OCE [145] and the improved elasticity reconstruction during optical palpation with transformer models [147]. We discuss limitations and strengths for each contribution and position our work with respect to existing research. Additionally, we provide an outlook on future work and the clinical need for sensory feedback on interaction forces and tissue properties during robotic manipulation.

5.1 Fiber-based OCT Sensors for Feedback on Needle-Tissue-Interactions

Our works in [142–144] investigate approaches for needle-based sensors and demonstrate that OCT can be used to measure a multitude of valuable details benefiting RANI. Our contributions show that OCT enables the measurement of interaction forces, the distance to critical structures and elastic properties of samples at the tip of medical needles with a diameter of $\leq 2\,\text{mm}$. In comparison to previous works that considered needle-based OCT for retrospective analysis, e.g. for needle tip force estimation [133–135],

the visualization of critical structures and insertion events in epidural anesthesia [97–100, 136], or brain surgery [102–105], we show the feasibility of real-time force and depth sensing in collaborative RANI with kinesthetic feedback [142, 143]. Real-time feedback on proximity sensing has been proposed for subretinal injections [91–96, 141] but these approaches do not consider haptic feedback and mostly focus on handheld insertions without robotic assistance. In comparison to previous works, we consequently do not just demonstrate the feasibility of our own OCT-based needle sensors. Instead we also show how such sensor technology could be used in conjunction with collaborative robotics to provide novel means of navigational feedback during needle insertions (Fig. 3.2). We directly compare our collaborative approaches to external force sensors mounted at the needle base, highlighting the potential of OCT for the force-based detection of tissue interfaces (see Fig. 4.2) and accurate placement in critical structures (see Fig. 4.1). Using robotic trajectory guidance for manual insertions can improve needle placement [182, 350] and our approaches additionally provide real-time haptic feedback on tissue interfaces to the physician. Such feedback during collaborative insertions, e.g. force or depth sensing, in principle also enables the physician to adapt to changes that might occur between pre-operative imaging and the insertions, e.g. due to bulk tissue motion commonly observed for prostate sampling [186, 187]. The operator can consequently proceed insertion until the expected rupture event occurs or the desired distance to the target has been reached without exclusively relying on pre-operative image guidance. However, while our approaches enable such behavior in theory, our experiments in [142, 143] did not specifically include bulk tissue displacement.

We first consider depth sensing that is particularly interesting when accurate needle placement is required in between tissue layers or cavities in close proximity to vulnerable and sensitive structures. Such insertions can greatly benefit from additional feedback to prevent complications, e.g. drug injection in the epidural space next to the spinal cord or between the retinal pigment epithelium and the internal limiting membrane. In our study on collaborative insertions with feedback on the proximity to sample interfaces [142], we consider phantoms to demonstrate that forward-facing OCT could provide improved placement accuracy and significantly reduce accidental overshoot. The experiments (see Sec. 4.1.1) show that axial forces measured at the needle base provided limited value. This could be expected as we do not decouple the needle tip from shaft forces but which has been shown to improve needle placement, e.g. in [193]. Consequently, the superposition of friction and tip forces makes distinguishing between interface rupture events based on shaft forces extremely challenging. More interestingly, our results show that purely visual feedback on the distance to sample interfaces improves placement accuracy but is unable to effectively prevent needle overshoot. We therefore conclude that it is difficult to process the OCT-based sensory information for the participants in real-time. In contrast, taking advantage of the robotic insertion and transforming the measured proximity to kinesthetic feedback enables the participants to process the novel sensory information and effectively prevents accidental overshoot of the simulated cavity.

For OCT-based tip force sensing [143], we improve upon prior sensor designs [133–135] by adding compatibility to a clinical spring-loaded biopsy system. Additionally, prior needle designs were prone to breaking due to shear forces at the tip and were limited by a conical tip shape without cutting edges. Our modifications improve needle robustness to enable repeated deep tissue insertions, as demonstrated in in-situ pancreatic biopsy

sampling with insertion depths of more than 100 mm (see Fig. 4.2). Simultaneously, the experiments in [142–144] showcase how external force sensors are strongly affected by needle friction forces hindering effective feedback on needle-tissue interactions. Automatic robotic insertions in [143] allow us to investigate tip and friction forces during insertions in a controlled environment. These experiments highlight that friction forces are not only affected by insertion velocity and needle tip geometry but are also greatly influenced by previously punctured tissue layers. Due to previously punctured layers, we observe inconsistent and non-linear behavior for friction forces even in our phantom setups (see Fig. 4.2). In comparison to our direct approach, some indirect methods involve modeling and subtracting friction forces to assess interactions at the tip, e.g. [190]. However, the observed perturbations in our experiments, potentially caused by relaxations mechanisms in the punctured tissue [188, 200], make modeling friction extremely challenging in deep tissue insertions as the complete geometry and biomechanical property of all tissue layers along the insertion trajectory are generally unknown. The findings therefore emphasize the advantages of direct needle tip force estimation as also proposed in [191–193] for feedback during difficult insertion tasks.

Being able to model needle insertion forces [188, 195–201, 351–355] is an important step towards understanding needle-tissue interactions, but direct measurements currently provide feedback that indirect methods are unlikely to match. On the other hand, the required sensor miniaturization and associated cost also prevents widespread clinical adaptation, especially if sensor technology drastically increases the complexity of an otherwise quick and simple percutaneous procedure. In comparison to other sensor technologies for tip force sensing, e.g. strain gauges [202], FBG [191, 192] or FPI [203–207], OCT requires highly complex optical systems and therefore even greater investments. However, the proposed needle probes themselves (Fig. 3.1) only require inexpensive SMF glass fibers that are attached to the expensive imaging system that is kept externally. The additional hardware requirements could consequently be significantly reduced in operating rooms where OCT systems might already be present due to other clinical applications, e.g. retinal OCT or IVOCT. More importantly, alternative optical approaches like FBG or FPI only provide feedback on interaction forces while OCT offers the unique potential to provide structural and functional imaging of tissue at the needle tip. OCT therefore enables far more versatile feedback on needle-tissue interactions, e.g. via morphological tissue characterization or previously discussed depth sensing, with OCT-based force sensing as a additional benefit.

Our experiments in [142] and [143] highlight the importance of real-time processing and an appropriate mechanism to display the OCT-based sensing to the operator. Performing retrospective analysis of needle-based OCT sensors is a vital first step to to demonstrate the feasibility of the respective sensor, e.g. previous retrospective studies considering lumbar [97–100] or brain [102–105] insertions. But our work indicates that if we want to harness the full potential of OCT, it is similarly essential to display the OCT data in a way such that the feedback is easy to interpret and use. The robotic system we consider provides one way to render the sensor information to the operator and we observe similar benefits to other RANI systems with added haptic feedback on needle-tissue interactions [190–194].

Our robotic system provides a versatile approach for needle insertions across the entire body [148] and our user studies demonstrate that novice operators are able to intuitively control the system, resulting in high detection rates for proximity and force feedback (Fig 4.1 and 4.2). However, it is also a complex setup that could be simplified with a

smaller robot with fewer degrees of freedom, e.g. for epidural anesthesia or Veress needle insertion. Alternatively needle integrated motion control could also provide feedback during insertion, e.g. considered for handheld retinal injection [94]. Also, our approach currently considers CT for trajectory guidance but the extension to other imaging modalities would further improve versatility. Especially US-imaging offers great potential enabling real-time trajectory guidance for many target regions, e.g. as in [171–176]. For the application of our OCT in MRI-guided insertions, an alternative robotic system and modified needle-probes would be required that offer MRI compatibility [183–187, 192, 205].

In contrast to the collaborative robotic system for real-time force and proximity sensing, we investigate the feasibility of needle-based OCE [144] in a different experimental setup for simulating deep tissue insertions. Combining forward-facing OCT [142] with tip force sensing [143] enables the quantitative assessment of elastic properties during deep tissue needle insertion [144]. Our findings suggest that needle-based OCE could provide valuable information to distinguish different tissue types through combined tip force sensing and sample strain imaging. In comparison to previous approaches for needle-based compression OCE with flat tip distal ends [118, 121–123], we demonstrate our bevelled needle for the insertion into deep tissue structures. We therefore could not follow the previously applied approach to spatially multiplexed stress and strain imaging [121–123] via GRIN lenses. We instead achieve separate tip force and strain imaging by adapting to a dual-fiber probe for the beveled needle (see Fig. 3.1). However, this affects elasticity reconstruction as measured elasticity is strongly dependent on indenter geometry [356]. For previous flat tip geometries [121–123], the distribution of the applied strain was assumed to be uniform across the circular GRIN surface and these approaches consequently reported equivalent Young's moduli instead of the pseudo-elasticity we report (Sec. 4.1.3). Still, it is unclear if such an assumption is valid even for flat tips and values for reconstructed Young's modulus greatly vary between different samples and sensor technologies in general [18, 357–361]. Our overall goal is to provide a sensor technology that provides a reproducible and reliable measurement to distinguish samples with different elastic properties. We therefore do not focus on modeling bevel tipped needle-tissue interactions with respect to the Young's modulus. We instead report the tip force per strain as a pseudo-elasticity reconstruction that still enables quantitative measurements, similar to the approach in [275] that considered pseudo-elasticity for corneal stiffness measurements. We demonstrate that this can achieve the desired biomechanical characterization independent of systematic perturbations that affect external measurements. Our study shows robust discrimination of the samples with quantitative OCE despite friction forces and bulk tissue displacement (see Fig. 4.3). OCE shows better agreement between surface and deep tissue measurements, once again highlighting the benefit of measurements obtained at the needle tip. In comparison to approaches relating applied load to indentation depth [209, 210], needle-based OCE offers a powerful tool to measure elasticity through quantitative strain imaging. Besides the compression-based OCE we consider, wave-based endoscopic OCE provides an alternative that has shown promising results for quantitative elasticity reconstruction. Needle-based wave excitation is not as straightforward as the needle-based indentations we consider, but novel miniaturized approaches proposed in recent years could be adapted for percutaneous insertions [127, 128, 131, 132].
Being able to reliably differentiate between cancerous and healthy tissue could greatly

improve needle guidance during biopsy of suspected lesions. Currently, there is generally no intraoperative feedback that enables the physician to assess whether the correct tissue was sampled during biopsy. But incorrect placement can cause false-negative results during histopathological examination. Clinical approaches currently aim to prevent incorrect sampling through different aids such as intraoperative imaging and systematic or repeated sampling to improve likelihood of placing the needle in the desired region. However, intraoperative image guidance can be challenging, e.g. endobronchial US guidance in pulmonary lymph node biopsy. Increasing the biopsy core count through systematic sampling increases risk of surgical complications, e.g. pain and erectile dysfunction for prostate biopsy [362, 363]. Added feedback obtained directly from the needle tip could provide valuable intraoperative information on the sampled tissue without the delay of histopathological examination, potentially reducing the need for repeated core sampling or preventing faulty sampling in cases where image guidance is challenging. As elastic properties can serve as a biomarker to differentiate the often stiff lesions from there soft surroundings, the demonstrated measurements on quantitative elastic properties could fill this role. Our OCE measurements are however only a first step towards this goal and are still limited to gelatin phantoms. While the two phantoms have similar elasticity to healthy and cancerous tissue [15, 209], extensive evaluation on biological soft tissue will be required to validate the feasibility for clinical application. Our previously discussed experiments also highlight the importance of appropriate feedback with novel sensor technologies. Consequently, mapping measured elasticity to intuitive forms of feedback need to be investigated, and the kinesthetic display we consider in [142, 143] will be ill-suited for this task.

5.2 Deep Learning for OCT-based Estimation of Tool-Tissue Interactions

In addition to our works investigating needle-tissue interactions, we consider deep-learning coupled with high-speed OCT for sensing tool-tissue interactions in RAMIS. Our findings highlight that tailoring learning-based approaches to the spatio-temporal nature of OCT can greatly improve accurate force estimation [145] and elasticity reconstruction [147]. The advancements we propose include a Siamese architecture conditioned with OCE elasticity estimates for feedback on interaction forces and the direct processing of A-scan sequences in a transformer architecture to more effectively learn Young's modulus reconstruction in wave-based OCE. While mathematical models offer theoretical frameworks to represent tissue mechanics and system behavior, they often fall short in capturing real-world complexities due to the need for extensive parameter tuning and idealized assumptions. In contrast, learning-based approaches enable capturing of system- and tissue-specific patterns that are otherwise difficult or impossible to model explicitly. The considered end-to-end calibration of complex optical sensors via deep learning can thus provide more accurate and robust sensing. Our results show that appropriate selection of architecture and data processing greatly affects model performance and we provide new methods that particularly focus on the spatio-temporal nature of OCT data. Providing physicians with such estimates of interaction forces and tissue properties could significantly improve intraoperative guidance and safety. Similarly to the discussion for OCT-needle sensors, rendering sensory outputs such as the measured elasticity to the physician will additionally require appropriate feedback mechanisms.

Considering the feedback on interaction forces during robotic or laparoscopic manipulation, we expand on previous works [155–157] that have investigated the feasibility of optical force estimation based on 3D and 4D OCT as an alternative to RGB or RGB-D. Our experiments focus on the importance of sample elasticity that must be considered during indirect image-based force measurements [145]. Similar to our findings in [144] where both the applied load and tissue deformation are required to derive elasticity, our experiments demonstrate that it is essential to measure both deformation and tissue properties to accurately derive the applied force. We therefore specifically consider this when designing our model architecture. The elasticity conditioned Siamese architecture (Fig. 2.5) enables the models to learn the relation between deformation and applied load due to the added information on tissue properties, as seen in improved model performance for phantom and tissue samples (see Fig. 4.4 and Fig. 4.5). This enables more versatile force estimation in comparison to models for single organs, e.g. brain [219], or multiple manually selectable organs, e.g. as proposed in [228]. Furthermore, potential changes to elasticity due to pathological tissue drastically change the observed magnitude of deformation per applied force. Neglecting such changes would cause large errors during indirect force estimation, as illustrated in our examples with phantoms simulating stiff lesions and soft healthy tissue (Fig 4.4). Our experiments show that models trained on more diverse data sets are able to partially generalize to varying elastic properties. But directly fusing wave velocity into the model greatly reduces force estimation errors for previously unseen elasticities. This holds true for both surface deformation maps and volumetric deformation data fused with OCE estimates. Our improved generalization capabilities does also not come at the cost of good performance for individual samples, e.g. in comparison to heart model phantoms investigated in [227, 228]. Considering the generalization to unseen samples, our RMSE of below 100 mN for fusion models were highly competitive with previous works investigated RGB-based force estimation, e.g. 1865 mN [237] and 1100 mN [236] for stereoscopic images. However, these approaches additionally considered pulling forces making the task more challenging than the exclusive pushing task we investigate.

Following our work, mixing of multiple data sets, generalizing input representations, and combining vision transformers for encoding RGB images and a recurrent model to integrate robot states was shown to reduce the relative errors during generalization [231]. Our elasticity conditioned model offers the opportunity to reduce generalization errors during domain shifts without additional data sets, but increasing training set size and variability could also reduce the problem of models limited to specific elastic properties. OCT-based optical force estimation has recently been considered with a hybrid CNN and RNN model for retinal surgery [333] but comparisons to our approach are difficult as the authors only provided qualitative results. However, the publicly available data set could provide an interesting comparison for feature work.

In contrast to our research, most approaches considering optical force estimation have focused on RGB images and additionally considered actuator torque or kinematic data in hybrid CNN and RNN models [226–229, 231, 233–238]. These robot state vectors can provide an alternative to elasticity estimates when deriving forces from the observed deformation. The effort required during manipulation should in theory reflect changes in biomechanical properties indirectly. However, the proposed approaches have generally considered laboratory setups and therefore the state data would be less affected than in the surgical cavity, e.g. nonlinear cable mechanics, bending, friction, or tissue dis-

placement could compromise robot state accuracy. It has also been considered to derive tissue elasticity from indirect force estimates [233] but our findings show that robust optical force estimation requires modeling of local elasticity and vice-versa. It is also unclear how RGB-based methods of elasticity estimation such as [364, 365] could be adapted for intraoperative use and OCT holds significant advantages in this regard. Our approach enables direct assessment of elasticity but requires additionally hardware to excite the surface waves for OCE. The observed benefits of OCE fusion slightly vary dependent on the accuracy of phase velocity estimates, as we observe greater relative improvements for more robust OCE measurements of softer samples. Consequently, our force estimation approach could further benefit from improved learning-based elasticity reconstruction, e.g. previously considered CNN and convRNN approaches [155–157] or our transformer-based approach [147]. Our modified tool for wave excitation [146] reduces the need for a separate excitation tool used in our setup (Fig. 3.5) but this only marks an intermediate solution as our goal is to entirely prevent modifications to the robotic manipulator for image-based force estimation.

Finally, our work [147] considers the reconstruction of tissue properties via transformers to improve learning-based feedback on tool-tissue interactions. Our experiments show that the self-attention mechanism coupled with appropriate position encoding enables improved Young's modulus reconstruction directly from the purely sequential data representation obtained in OCT (Sec. 4.2.2). We thereby aim to address two challenges of wave-based OCE. Firstly, the robust detection of wave propagation from the OCT phase data and secondly, the accurate modeling of wave mechanics to derive accurate Young's modulus values. Our results underline these challenges as the detection of wave propagation with a conventional Fourier estimator fails in multiple measurements for both phantom and tissue samples (Tab. 4.1 and Fig. 4.6). Additionally, we alleviate the need for explicit selection of wave propagation models that significantly affect accuracy [358, 359]. This also includes assumptions on material properties that may vary besides sample elastic, e.g. density or Poisson's ratio. Instead, the model implicitly learns to relate the wave propagation to elastic properties obtained in gold-standard compression test in an end-to-end fashion. Our approach outperforms conventional processing and state of the art CNNs [146, 151–154] in our experiments (Sec. 4.2.2). We achieve better generalization to phantoms simulated stiff lesions (Fig. 4.6) with respect to elasticity errors and the ability to detect the inclusions, as indicated by higher AUROC and AUPRC scores. For soft tissue samples, ground truth values for elasticity were not available and our results are limited to demonstrating better agreement between our approach and a surrogate elasticity defined as the maximum palpation force during robotic palpation with the surgical tool. Increasing errors when transitioning from homogeneous training data to more complex heterogeneous samples also highlights that further validation with a multitude of soft tissue samples and intraoperatively acquired data will be required going forward.

In comparison to our approach, previous learning-based approaches have generally considered OCT data as multidimensional images and mostly focused on CNNs to derive tool-tissue interactions from OCT [138–141, 149–159]. But we observe improved performance when considering the purely sequential nature of OCT A-scans via self-attention and entirely learn spatial dependencies without inducing this bias in the model. However, the experiments show that appropriate position encoding is essential for this approach and we obtain the best performance for RoPE that feeds positional information

in each attention layer. We also observe better scalability with respect to computational load and model capacity in comparison to previous learning-based approaches [151–154]. Our work does not represent the first time transformer architectures are considered for processing OCT data. These include VIT approaches or hybrid CNN and transformer models (Sec. 2.3.4). However, similar to previous CNN-based models, these approaches again considered the reconstructed B-scans as multidimensional images instead of the raw sequence of A-scans.
One exception is [345], where each pixel was considered an input token for retinal layer segmentation. In contrast, we regard each A-scan as one input token to derive sample elasticity from the phase differences between A-scans. Our experiments suggests that it is advantageous to follow this sequential nature of OCT data for accurate and robust elasticity reconstruction. The model is therefore able to implicitly learn system sampling and wave propagation dependencies with reduced bias. However, further validation with additional tissue samples is required as our experiments are mostly limited to phantom setups. Adaptation of our learning objective to a classification task or the intermediate prediction of wave velocity [153] could simplify the acquisition of additional labeled data.

5.3 Limitations and Outlook

Our contributions highlight the potential of intraoperative OCT. The successful demonstrations merit further exploration but must also address significant challenges that still remain. Regarding our proposed needle-integrated OCT sensors [142–144], an important next step will be the direct comparison to alternative methods of needle guidance, e.g. manual insertion under US imaging and alternative methods for feedback on needle-tissue interactions such as loss-of-resistance [366], mechanical mechanisms [367] or alternative sensor technologies discussed in Sec. 2.1.2. Additionally, we consider tip force, depth sensing and tissue elasticity estimates in separate experiments to highlight their respective value. But an approach such as our needle in [144] could also provide comprehensive feedback on these properties in a single sensor. Furthermore, future research could combine such versatile sensing with the morphological imaging OCT provides. Promising extensions therefore include classification of tissue through structural imaging but also additional contrast such as polarization-sensitive OCT [99] or attenuation imaging [64]. However, the temporal sequence of A-scans obtained with our sensors superimposes spatial and temporal data and is particularly difficult for physicians to interpret, e.g. as also indicated above (see Sec. 4.1.1). Adequate sensory output will therefore require appropriate data processing and feedback to display the relevant information to the physicians. Our experiments demonstrate the great potential of learning-based approaches for processing spatio-temporal OCT data [143, 145–147] and could address the challenging interpretation of OCT data. Consequently, learning-based tissue classification from morphological imaging has already been demonstrated during needle insertion [98, 136, 138–140]. Given accurate estimates of needle-tissue interactions, further investigations into appropriate forms of rendering sensor outputs should also consider combined methods, e.g. kinesthetic [142, 143], visual [142], and vibrotactile [190] feedback.
Considering the tool-issue interactions during robotic manipulation in RAMIS, our works [145–147] explore OCT as it offers visualization of depth-resolved tissue deformations for versatile sensing. However, OCT is not readily available during RAMIS and

would require appropriate scanning for use in the surgical cavity, e.g. through endoscopic OCT probes [154]. In contrast, stereoscopic RGB is commonly available and offers a greater FOV in comparison to OCT. Future work should consequently explore how our findings might also benefit RGB-based estimation of tool-tissue interactions, e.g. through the fusion of elasticity estimates with depth maps for improved optical force estimation. In addition, while our works demonstrate the feasibility of indirect force estimation and optical palpation, further design improvements are needed to completely remove the need for hardware modifications currently employed for wave excitation [146, 147], e.g. through contactless wave excitation [284–287]. More complex tool-tissue interactions must be also considered, including destructive tissue manipulation, bulk displacement, or partially occluded regions of interest.

Lastly, our experiments mostly focus on tissue-mimicking phantoms and laboratory environments to evaluate the feasibility of our approaches [142–145, 147]. While these experiments are important first steps in evaluating the potential of our methods in a controlled setting, they do not accurately reflect the complex intraoperative applications. Particularly tissue mechanics are highly non-linear in reality, generally violating assumptions such as heterogeneity and isotropy. The linear elasticity considered in [144] does not address these mechanics adequately and appropriate extensions will be required for tissue-specific applications. Still, our compression-based OCE needle enables measurement of load-strain-curves and could be extended to non-linear models that also provide additional contrast [121, 272, 273]. Similarly, our fused OCE velocity for optical force estimation [145] represent a limited simplification of the nonlinear mechanics observed for heterogeneous, anisotropic soft tissue samples. Nevertheless, we show that our approach is able to leverage the additional information when generalizing to unseen samples. Further adaptation of our model architecture could include end-to-end elasticity processing similar to [147].

Our proposed learning-based approaches offer a valuable tool to address the challenge of modeling tissue-mechanics. These methods can facilitate the complex calibration of system- and sample-specific parameters. For example, in wave-based elastography, accurate reconstruction is otherwise only possible through extensive structural, histological, and rheological studies, as well as numerical simulations [52]. Still, further validation of our approaches and the inclusion of additional tissue samples representing the large variety of intraoperative conditions will be necessary. Only then can we fully utilize the benefits of end-to-end estimation of tool-tissue interactions. We have also observed how the considered model architecture and data representations greatly affect accuracy and robustness. Further investigations should build on these findings, considering additional inputs such as robot state data in hybrid models for force estimation [226–229, 231, 233–238], evaluating the approaches on additional data sets [231, 333] and exploring new applications where intraoperative OCT can provide unique opportunities.

Addressing the outlined objectives and improving accuracy, robustness and versatility for OCT-based sensors will be essential. There remains the need for appropriate sensor technologies offering estimates of interaction forces and tissue properties in surgical procedures. This will be especially important to increase autonomy for robotic systems [6, 20, 21]. OCT is a promising candidate that can address many requirements with respect to miniaturization and versatility, particularly for RANI. Further investigations will show if OCT might become a crucial part not just in ophthalmology, but in building intelligent surgical robots.

6 Conclusion

In this work, we considered OCT as an optical sensor technology for tool-tissue interactions during robot-assisted interventions. Particularly, robotic systems are often limited by the absence of appropriate sensors to assess interaction forces and tissue properties during tool manipulation. In this context, we investigated how we can use fiber-based OCT to capture tool-tissue interactions at the needle tip and how end-to-end deep learning can facilitate the effective processing of spatio-temporal OCT when observing tissue manipulations. First, we developed and experimentally validated fiber-based OCT sensors directly integrated into the needle tip. Our results show that such integration enables localized measurements of key properties during needle-tissue interaction. Needle-integrated OCT enables estimation of needle tip forces, depth sensing and tissue elasticity during percutaneous insertion. We have also shown how such sensors can be combined with robotic platforms to provide real-time feedback to the operator and improve needle placement. The combination of morphological and functional imaging of fiber-based OCT probes represents a unique advantage over other sensing technologies as it improves needle placement but can also enable tissue characterization. However, the experiments indicate that intuitive forms of feedback are essential to realize the full potential of OCT in surgical guidance. Second, we have developed learning-based approaches for processing OCT data in robotic tissue manipulation tasks. We have shown that deep learning architectures tailored to the spatio-temporal nature of OCT signals enable accurate estimation of tool-tissue interaction forces and tissue elasticity. Our findings confirm that the choice of model architecture and the handling of temporal features are crucial for maximizing the information encoded in OCT data. The combination of deep learning with OCT provides a valuable tool for sensing tool-tissue interactions, as the models capture non-linear, context-dependent patterns in the data that are otherwise difficult to represent with analytical or physically-derived models.
In conclusion, our investigations have explored OCT-based sensor technology that could enable versatile measurement of tool-tissue interactions during robotic manipulation. Enabling such feedback in minimally invasive procedures would be of great benefit to both physicians and patients. Physicians could once again use their sense of touch for intraoperative guidance, especially to localize important anatomical structures and pathological tissue. A display of applied forces would also increase safety and enable more effective tissue manipulation, especially for physicians who are less experienced with robotic surgical systems. In addition, understanding and recognizing tool-tissue interactions is essential for greater autonomy in RAS. While physicians may be able to manually associate the observed tissue deformation with a particular load or tissue property, robotic systems require appropriate sensing to achieve similar feedback loops. However, our contributions are mostly limited to phantom experiments and only represent first steps towards clinical application. Further research will show whether OCT can prevail over other sensor technologies. This work has discussed possible next steps so that OCT-based feedback on tool-tissue interactions can hopefully contribute to the widespread availability of intelligent robotic systems in the near future.

7 Research papers

7.1 Proximity-based Haptic Feedback for Collaborative Robotic Needle Insertion

Conference: International Conference on Human Haptic Sensing and Touch Enabled Computer Applications - EuroHaptics 2022

Published: 20.05.2022

R. Mieling, C. Stapper, S. Gerlach, M. Neidhardt, S. Latus, M. Gromniak, P. Breitfeld, and A. Schlaefer, "Proximity-based haptic feedback for collaborative robotic needle insertion," in *International Conference on Human Haptic Sensing and Touch Enabled Computer Applications EuroHaptics 2022*, ser. Lecture Notes in Computer Science, Springer, 2022, pp. 301–309

Proximity-Based Haptic Feedback for Collaborative Robotic Needle Insertion

Robin Mieling[1(✉)], Carolin Stapper[1(✉)], Stefan Gerlach[1], Maximilian Neidhardt[1], Sarah Latus[1], Martin Gromniak[1], Philipp Breitfeld[2], and Alexander Schlaefer[1]

[1] Institute of Medical Technology and Intelligent Systems, Hamburg University of Technology, Hamburg, Germany
{robin.mieling,carolin.stapper}@tuhh.com
[2] Department of Anesthesiology, University Medical Center Hamburg-Eppendorf, Hamburg, Germany
https://mtec.et8.tuhh.de/

Abstract. Collaborative robotic needle insertions have the potential to improve placement accuracy and safety, e.g., during epidural anesthesia. Epidural anesthesia provides effective regional pain management but can lead to serious complications, such as nerve injury or cerebrospinal fluid leakage. Robotic assistance might prevent inadvertent puncture by providing haptic feedback to the physician. Haptic feedback can be realized on the basis of force measurements at the needle. However, contact should be avoided for delicate structures. We propose a proximity-based method to provide feedback prior to contact. We measure the distance to boundary layers, visualize the proximity for the operator and further feedback it as a haptic resistance. We compare our approach to haptic feedback based on needle forces and visual feedback without haptics. Participants are asked to realize needle insertions with each of the three feedback modes. We use phantoms that mimic the structures punctured during epidural anesthesia. We show that visual feedback improves needle placement, but only proximity-based haptic feedback reduces accidental puncture. The puncture rate is 62% for force-based haptic feedback, 60% for visual feedback and 6% for proximity-based haptic feedback. Final needle placement inside the epidural space is achieved in 38%, 70% and 96% for force-based haptic, visual and proximity-based haptic feedback, respectively. Our results suggest that proximity-based haptic feedback could improve needle placement safety in the context of epidural anesthesia.

Keywords: Force feedback · Collaboration · Human-robot interaction · Epidural anesthesia · Optical coherence tomography

R. Mieling and C. Stapper—Contributed equally.

H. Seifi et al. (Eds.): EuroHaptics 2022, LNCS 13235, pp. 301–309, 2022.
https://doi.org/10.1007/978-3-031-06249-0_34

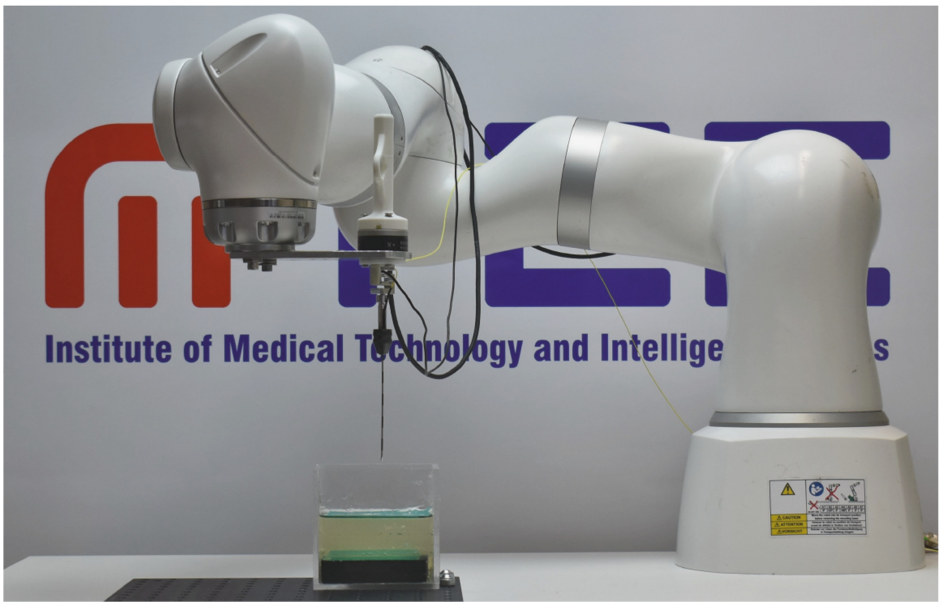

Fig. 1. Robotic system with proximity-based haptic feedback for collaborative needle insertions into tissue mimicking phantoms.

1 Introduction

Epidural anesthesia plays an important role for perioperative pain management, e.g. during orthopedic, urologic and general surgery. The procedure requires placing a needle that guides a catheter into the epidural space (ES). The ES is located directly behind the ligamentum flavum (LF) and surrounds the dura that protects the spinal cord and the cerebrospinal fluid. Major complications during epidural anesthesia are not common but potentially serious, including hematoma, post-operative neurologic deficits, infections and even death [1]. Nerve injury and long-term headache result from accidental dural perforation [2,3]. Placement within the ES without dura injury can be challenging given the small size of only 2 mm to 6 mm [4].

The most common technique for identifying the correct needle placement is loss-of-resistance (LOR). It is based on the different tissue densities in LF and ES. The entry into ES is visually or haptically perceived by the performing surgeon [5]. However, LOR requires frequent training, false-positives are possible and dura punctures still occur [5,6].

We consider robot-assisted needle insertions in the context of epidural anesthesia. CT-guided robotic needle insertions have shown promising results for soft tissue biopsy sampling [7]. In epidural anesthesia, external image guidance is challenging and tissue deformation as well as patient movement make a fully automated needle placement difficult. We consider a collaborative approach where the trajectory is guided by a robot but additional feedback is required to enable the correct axial placement by the operator. Besides LOR, experienced physicians rely on the haptic impression at the needle shaft to navigate. Consequently, haptic feedback based on force measurements has been intuitively

considered for robotic needle insertions. Multiple force sensors [8] or force modeling [9] can provide enhanced feedback on needle tip forces that are otherwise superimposed with friction forces. However, force measurements always require physical contact first, potentially damaging delicate structures.

Instead, we propose a method that can detect structures before physical contact occurs. We have recently shown that an optical coherence tomography (OCT) fiber embedded into an epidural needle can enable the detection of rupture events during needle insertions [10]. We now employ high resolution OCT needles to measure the distance to structures. During collaborative needle insertions, the distance is converted to a resistive force and employed as haptic feedback. We perform experiments on tissue mimicking phantoms simulating the epidural cavity. We compare haptic feedback based on force measurements as well as the visual representation of the proximity with and without additional haptic feedback. We evaluate our methods in a user study with ten participants that each conduct needle insertions with the three different feedback modes.

2 Methods

Our system setup contains an optical needle probe, a 7-degree-of-freedom (DOF) medical robot with a custom handle for collaborative robot manipulation and a tissue mimicking phantom (see Fig. 1).

2.1 Sensor and Phantom Setup

The proximity sensor is based on OCT imaging. An optical fiber is fitted into a standard Tuohy needle with a diameter of 1.4 mm for forward-facing, common-path OCT imaging. Axial depth scans (A-scans) are acquired with a spectral domain OCT system (Telesto I, Thorlabs) with a axial resolution of 6.5 µm in air. The maximum imaging depth in tissue is approximately 1.77 mm, assuming a constant refractive index of 1.45 for tissue. Our proximity sensor output is the distance d to structures, which are positioned along the insertion trajectory in front of the needle tip. It is obtained from detecting the closest intensity peak within the processed A-scan (see Fig. 2, top right).

To evaluate our system, we employ phantoms from tissue mimicking gelatin gels. We replicate the ES within the gelatin gels with two successive layers of cellulose (see Fig. 2, bottom right). The layers are spaced 3 mm apart and represent the LF and the dura respectively. The synthetic dura is supported by polyethylene foam that represents the area of the subdural space.

2.2 Robotic System

The robotic system consists of a 7-DOF light-weight robot (LBRMed 14, KUKA) and a specially manufactured handle for the collaborative control by the surgeon. The handle (see Fig. 2, left) includes a 6-DOF force-torque sensor (M3703, Sunrise Instruments) that measures the forces and torques applied to the handle

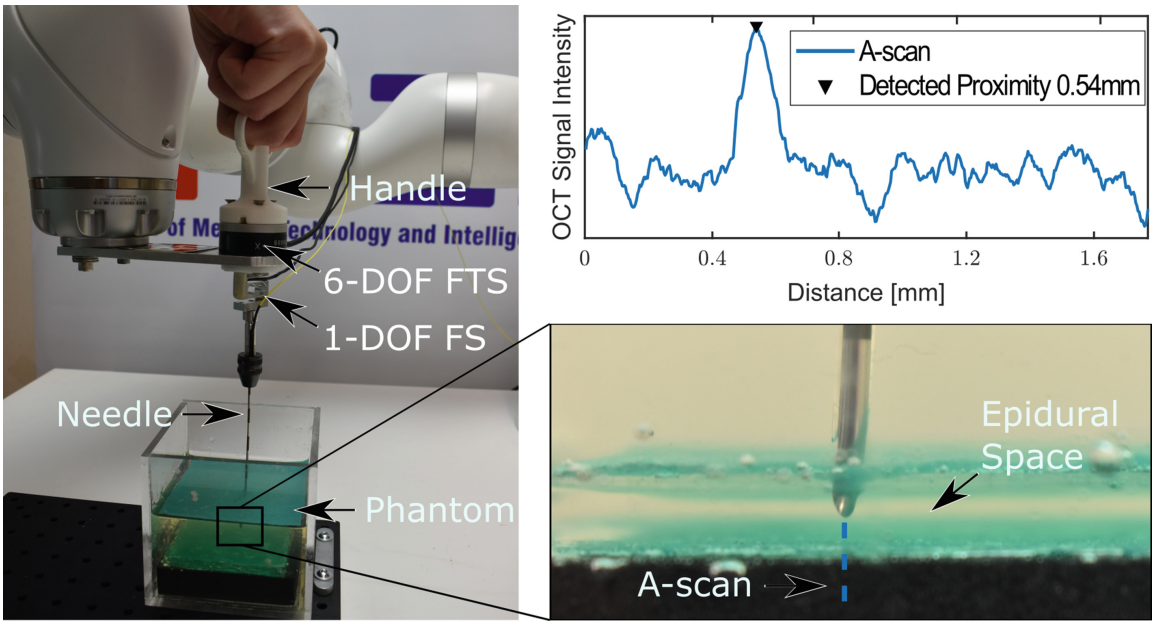

Fig. 2. The custom handle for collaborative needle insertions is shown on the left. A 6-DOF force-torque sensor (FTS) detects the users input and the 1-DOF force sensor (FS) registers forces acting on the needle. A close-up of the needle tip within the ES mimicking phantom and the visualization of approaching structures via the A-scan are shown on the right.

by the surgeon. Additionally, a 1-DOF force sensor (KD24s, ME-measurement systems GmbH) measures the forces acting on the needle shaft.

The outer control loop is designed with an admittance controller. Prior to insertion, the 6-DOF force-torque sensor allows the operator to freely position the needle axis along a desired trajectory. During collaborative insertion, the task space is restricted to the needle axis. The operator controls the 1-D movements by the forces exerted on the handle. Haptic feedback is implemented by an opposing resistive force. We employ a feedback control loop as illustrated in Fig. 3. The input value of the control loop is the control error e. It is defined as the difference between the feedback force F_{Fb} and the handle force applied in the insertion axis F_{Handle}. Negative values of e are not considered in order to prevent stability problems caused by oscillations. The control error is converted to the desired movement $\dot{x}_{i,d}$ by the PID controller. Execution by the robot results in the new insertion depth x of the needle tip. For $F_{\mathrm{Handle}} < 0$ the handle force is directly mapped to the corresponding motion without any feedback to allow retraction.

The handle enables three different feedback modes. Switching between the three modes changes the source of the applied feedback force F_{Fb}. In mode 1, haptic feedback consists of the measured needle force. In mode 2, the user is provided no haptic feedback, but a visual representation of the OCT signal (see Fig. 2, top right). In mode 3, this visual feedback is supplemented by the haptic feedback of the computed distance. During mode 1, we measure the force acting on the needle, which is then used as direct feedback $F_{\mathrm{Fb}} = F_{\mathrm{Needle}}$. As mode 2 contains only visual feedback, the feedback loop is not closed with $F_{\mathrm{Fb}} = 0$ at

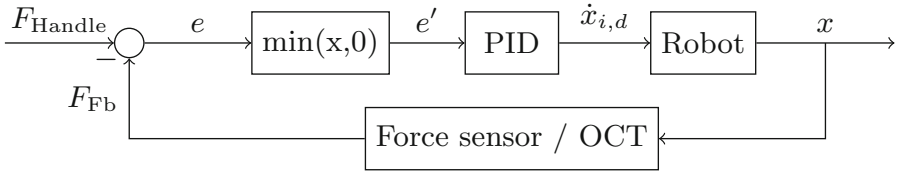

Fig. 3. Control Scheme during Insertion. Three modes are considered for the feedback loop. In mode 1, the needle shaft force is used as feedback. In mode 2, no feedback is used and in mode 3, a force is generated based on the proximity according to Eq. 1.

all times. For the proximity-based haptic feedback (mode 3), the sensor output d computed from the OCT signal is mapped to a corresponding resistive force $F_{\text{Fb}} = F_{\text{Prox}}$, for which

$$F_{\text{Prox}}(d) = \tanh(2 * (1 - \frac{d}{d_{\text{Max}}})), d_{\text{Max}} = 1.77 \text{ mm} \quad (1)$$

is used. Robot communication and control is realized with the Robot Operating System (ROS). The controller runs with a frequency of 1 kHz, both force sensors update with 200 Hz and the computed distance is updated with a frequency of 100 Hz. The latency of the system is 30 ms.

2.3 Experiments

Ten participants with limited experience in needle insertions are asked to position the needle tip within the ES. We conduct five insertions per participant per feedback mode. Pullback is permitted and the insertion is stopped once the participant releases the handle. The participants are granted one test run in each mode to familiarize with the system behaviour. The order in which the three modes are employed is randomized for each participant.

For evaluation, we determine the position of our mimicked dura relative to our robot coordinate system. Based on the end-effector robot poses, we consider the distance to the target height in mm. We report mean and standard deviation at maximum extension d_{Max} and for the final position d_{End}. Insertions with correct needle placement refer to all insertions where 0 mm $< d_{\text{End}} <$ 3 mm. Insertions with $d_{\text{Max}} < 0$ mm correspond to dura puncture. The insertion is aborted if the operator inserts the needle more than 15 mm beyond the dura.

3 Results

In total, we conduct 150 insertions. A single insertion is aborted as the participant fails to identify the ES in mode 2. Figure 4 shows the dura puncture rate and the successful needle placement separated by the three feedback modes. For force-based haptic feedback (mode 1), placement within the ES is successful in 38% of cases. 62% of insertions result in dura puncture and no insertions are stopped before the LF. For purely visual feedback (mode 2), one insertion is

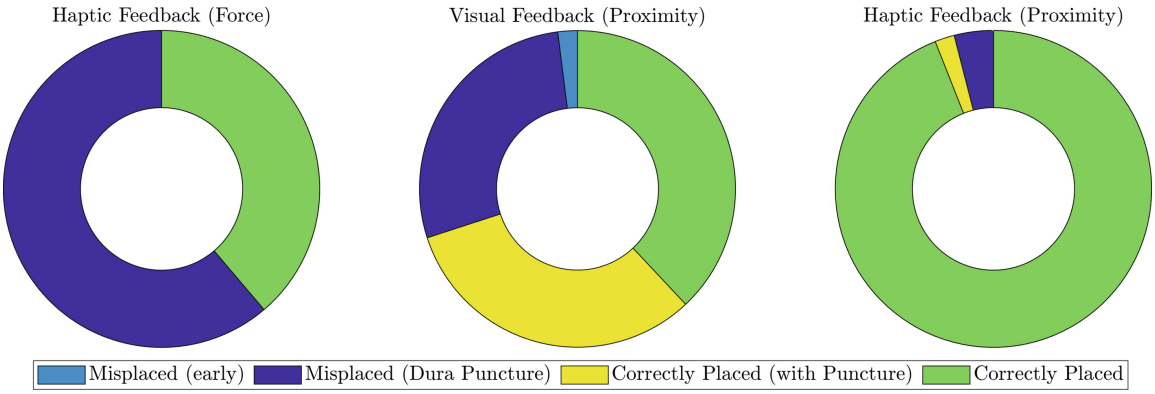

Fig. 4. Combined results for the dura puncture rate (including overshoot) and the placement success rate based on the maximum and final insertion position respectively.

Table 1. Needle placement accuracy for each feedback mode in comparison of the first and last insertion.

Feedback mode		1	2	3
d_{Max} [mm]	First	-0.35 ± 1.86	-1.96 ± 4.37	0.62 ± 0.38
	Last	-0.75 ± 2.07	-0.15 ± 1.25	0.67 ± 0.53
d_{End} [mm]	First	-0.08 ± 1.66	-1.37 ± 4.63	0.76 ± 04.08
	Last	-0.67 ± 2.06	0.39 ± 1.38	0.80 ± 0.66

stopped prematurely and 38% of insertions are correctly stopped in front of the dura. Dura puncture occurs in 60% of cases, but is detected and corrected by a subsequent pullback in 32% of all insertions. The proximity-based haptic feedback (mode 3) increases the correctly placed insertions without dura puncture to 94%. The dura is punctured during three insertions (6%), one position is successfully corrected.

We further report the distance to the dura for the three feedback modes (see Fig. 5). Considering d_{Max} (red boxes), needle insertions with both mode 1 and 2 are extended below the dura, with a mean of (-0.33 ± 2.01) mm and (-0.65 ± 2.37) mm, respectively. On average, insertions with proximity-based haptic feedback (mode 3) are sto pped (0.58 ± 0.68)mm before the dura. Mean distances to the dura at the final needle position d_{End} are (-0.19 ± 1.98) mm, (-0.19 ± 1.98) mm and (0.21 ± 0.62) mm for mode 1 to 3, respectively.

In order to evaluate the learning effect of the participants, the positions from the first and the last attempt of each mode are displayed in Fig. 5. The mean accuracy and standard deviation (SD) is also given in Table 1.

4 Discussion and Outlook

The results from our phantom study show that the needle shaft forces (mode 1) provide insufficient haptic feedback for the operator to accurately place an epidural needle within the ES. The large variation in final needle placements

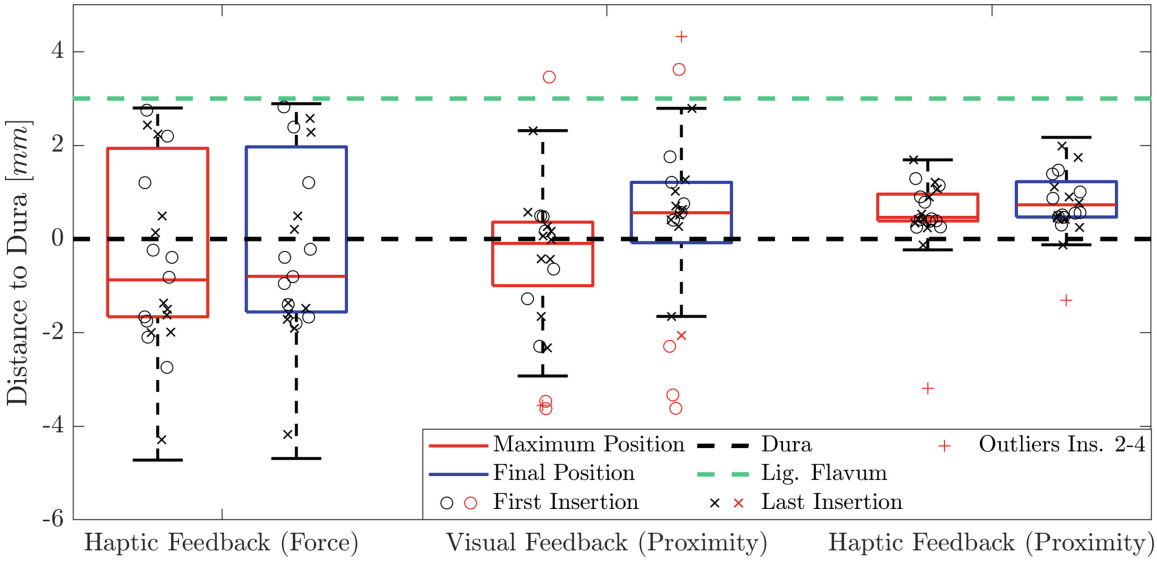

Fig. 5. Distance to the dura for the maximum and final extension for each of the three feedback modes. Additionally, the first and the last attempt from each participant is displayed. Outliers are marked in red, the aborted insertion is not shown.

implies that the participants have difficulty distinguishing the two boundary layers. Multiple insertions are stopped after only partially rupturing the mimicked LF signified by points directly under the 3 mm line in Fig. 5. With visual feedback (mode 2), the puncture rate is nearly identical to mode 1. The higher transparency compared to mode 1 and 3 also results in the only aborted attempt posing a significant safety issue. However, the participants are able to detect and correct the overshoot in half of the cases. This implies that they are able to detect the dura but fail to react in time. Higher damping for finer movements and a more intuitive visual representation could help mitigate the overshoot. In mode 3, the number of needle placements where no puncture occurs and the needle is stopped inside the ES increases to 94% from 38% in mode 1 and 2. This indicates that users have less difficulty distinguishing the two boundary layers and can more intuitively insert the needle within the ES.

Regarding the learning effect, the comparison between the first and last attempt for each mode results in relatively small differences compared to their standard deviations. This makes definitive conclusions difficult, considering the small sample size. Nevertheless, it indicates that the lack of adequate feedback in mode 1 and 2 is not intuitively compensated within five attempts.

Previously, proximity-based haptic feedback has been proposed for ultrasound imaging [11] and endovascular catheterization [12]. However, these approaches provide an insufficient resolution, are not designed to work in-vivo or rely on external imaging that is not typically available in epidural anesthesia. Our proximity sensor with μm resolution can resolve small scale structures like the ES and can be easily integrated into medical needles. Our system does not decouple the needle tip from shaft forces which has been shown to improve needle placement in [8]. However, this requires a more complex needle tip sensor.

In conclusion, we show that our collaborative approach has the potential to improve placement accuracy and highlight the importance of haptic feedback. The haptic response is decoupled from the puncture resistance of the dura and no physical contact is required. Proximity-based haptic feedback is therefore suited to avoid delicate structures and drastically reduces accidental puncture in our phantom study. Further evaluation will address the operation by medical experts and the applicability within real tissue samples.

References

1. Kang, X.H., et al.: Major complications of epidural anesthesia: a prospective study of 5083 cases at a single hospital. Acta Anaesthesiol. Scand. **58**(7), 858–866 (2014). https://doi.org/10.1111/aas.12360. https://onlinelibrary.wiley.com/doi/full/10.1111/aas.12360
2. Bezov, D., Lipton, R.B., Ashina, S.: Post-dural puncture headache: Part I diagnosis, epidemiology, etiology, and pathophysiology. Headache J. Head Face Pain 50(7), 1144–1152 (2010). https://doi.org/10.1111/j.1526-4610.2010.01699.x. https://headachejournal.onlinelibrary.wiley.com/doi/full/10.1111/j.1526-4610.2010.01699.x
3. Webb, C.A.J., et al.: Unintentional dural puncture with a tuohy needle increases risk of chronic headache. Anesth. Analg. **115**(1), 15–25 (2012). https://doi.org/10.1213/ANE.0b013e3182501c06. https://journals.lww.com/anesthesia-analgesia/Fulltext/2012/07000/Unintentional_Dural_Puncture_with_a_Tuohy_Needle.22.aspx
4. Manchikanti, L., Atluri, S.: Chapter 152 - lumbar epidural nerve block. In: Waldman, S.D., Bloch, J.I. (eds.) Pain Management, pp. 1281–1293. W.B. Saunders, Philadelphia (2007). https://doi.org/10.1016/B978-0-7216-0334-6.50156-4. https://www.sciencedirect.com/science/article/pii/B9780721603346501564
5. Dhansura, T., Shaikh, T., Maadoo, M., Chittalwala, F.: Identification of the epidural space-loss of resistance to saline: an inexpensive modification. Indian J. Anaesth. **59**(10), 677–679 (2015). https://doi.org/10.4103/0019-5049.167483
6. Yang, J., et al.: The development of a novel device based on loss of guidewire resistance to identify epidural space in a porcine model. J. Healthc. Eng. **2020**, 8899628 (2020). https://doi.org/10.1155/2020/8899628
7. Neidhardt, M., et al.: Robotic tissue sampling for safe post-mortem biopsy in infectious corpses. IEEE Trans. Med. Robot. Bionics **4**, 94–105 (2022)
8. de Lorenzo, D., Koseki, Y., de Momi, E., Chinzei, K., Okamura, A.M.: Coaxial needle insertion assistant with enhanced force feedback. IEEE Trans. Biomed. Eng. **60**(2), 379–389 (2013). https://doi.org/10.1109/TBME.2012.2227316
9. Okamura, A.M., Simone, C., O'Leary, M.D.: Force modeling for needle insertion into soft tissue. IEEE Trans. Bio-med. Eng. **51**(10), 1707–1716 (2004). https://doi.org/10.1109/TBME.2004.831542
10. Latus, S., et al.: Rupture detection during needle insertion using complex OCT data and CNNS. IEEE Trans. Biomed. Eng. (2021). https://doi.org/10.1109/TBME.2021.3063069

11. Antonello, R., Oboe, R.: Force controller tuning for a master-slave system with proximity based haptic feedback. In: IECON 2014–40th Annual Conference of the IEEE Industrial Electronics Society, pp. 2774–2779 (2014). https://doi.org/10.1109/IECON.2014.7048900
12. Dagnino, G., Liu, J., Abdelaziz, M.E.M.K., Chi, W., Riga, C., Yang, G.Z.: Haptic feedback and dynamic active constraints for robot-assisted endovascular catheterization. In: 2018 IEEE/RSJ International Conference on Intelligent Robots and Systems (IROS), pp. 1770–1775 (2018). https://doi.org/10.1109/IROS.2018.8593628

7.2 Collaborative Robotic Biopsy with Trajectory Guidance and Needle Tip Force Feedback

Conference: 2023 IEEE International Conference on Robotics and Automation (ICRA)

Published: 04.07.2023

R. Mieling, M. Neidhardt, S. Latus, C. Stapper, S. Gerlach, I. Kniep, A. Heinemann, B. Ondruschka, and A. Schlaefer, "Collaborative robotic biopsy with trajectory guidance and needle tip force feedback," in *2023 IEEE International Conference on Robotics and Automation (ICRA)*, IEEE, 2023, pp. 6893–6900

2023 IEEE International Conference on Robotics and Automation (ICRA 2023)
May 29 - June 2, 2023. London, UK

Collaborative Robotic Biopsy with Trajectory Guidance and Needle Tip Force Feedback

Robin Mieling[1]*, Maximilian Neidhardt[1]*, Sarah Latus[1], Carolin Stapper[1], Stefan Gerlach[1], Inga Kniep[2], Axel Heinemann[2], Benjamin Ondruschka[2] and Alexander Schlaefer[1]

***Abstract*— The diagnostic value of biopsies is highly dependent on the placement of needles. Robotic trajectory guidance has been shown to improve needle positioning, but feedback for real-time navigation is limited. Haptic display of needle tip forces can provide rich feedback for needle navigation by enabling localization of tissue structures along the insertion path. We present a collaborative robotic biopsy system that combines trajectory guidance with kinesthetic feedback to assist the physician in needle placement. The robot aligns the needle while the insertion is performed in collaboration with a medical expert who controls the needle position on site. We present a needle design that senses forces at the needle tip based on optical coherence tomography and machine learning for real-time data processing. Our robotic setup allows operators to sense deep tissue interfaces independent of frictional forces to improve needle placement relative to a desired target structure. We first evaluate needle tip force sensing in ex-vivo tissue in a phantom study. We characterize the tip forces during insertions with constant velocity and demonstrate the ability to detect tissue interfaces in a collaborative user study. Participants are able to detect 91 percent of ex-vivo tissue interfaces based on needle tip force feedback alone. Finally, we demonstrate that even smaller, deep target structures can be accurately sampled by performing post-mortem in situ biopsies of the pancreas.**

Fig. 1. **Collaborative Robotic Biopsy**: The robot guides the needle trajectory while the physician inserts the needle. Needle tip forces are sensed by the physician through haptic feedback allowing him to feel tissue interfaces during the needle insertion.

I. INTRODUCTION

Needles are a valuable tool for reaching soft tissue lesions to extract tissue biopsies for diagnosis or to perform therapy, e.g. radiofrequency ablation or brachytherapy. In clinical practice, needles are placed manually under image guidance, with accuracy depending heavily on the operator [1], [2], [3], [4]. Still, tissue sampling relies on precise positioning of the biopsy needle inside the target tissue [5]. Robotic systems have proven to be beneficial for this task with respect to accuracy, standardization and the number of insertions required [6]. Robots for needle insertions have been proposed with CT-guidance [7], [8], [9] or MRI-guidance [10], [11], [12].

Fully automated insertions have been considered for post-mortem biopsy [8], [9] but are still not practical in a clinical environment due to safety concerns. Alternatively, robots align the needle trajectory in the clinic, while needle insertion is performed manually by the physician [13], [14], [15], [16]. Thereby, the physician relies on anatomical knowledge and his or her sense of touch when forwarding the needle into tissue. Similarly, teleoperative systems [17], [18], [19], [20], [21], [22], [23] provide haptic feedback to the surgeon when inserting a needle. Forces at the needle tip can be estimated and displayed to the physician [18], [20], [24], [25] to further enhance the navigation during percutaneous insertions. Tip forces can be provided by subtracting modeled friction forces from externally measured forces [18], [25]. Similarly, miniaturized force sensors can be embedded in needles composed of fiber Bragg gratings [20], [24], Fabry Pérot imaging sensors [26], [27], [28], or imaging optics [29], [30]. Needle tip forces have been shown to be superior to forces measured at the shaft for membrane detection [20], [25] but research is limited to phantom studies with synthetic materials and non-commercial robots with small operational spaces and limited degrees of freedom.

In this study, we propose a collaborative robotic system with haptic feedback from the needle tip for minimally invasive tissue biopsies. The physician plans the needle insertion using CT imaging while a lightweight robot aligns the needle according to the planned trajectory. We estimate the ideal trajectory based on the CT-Hounsfield units [31], [32].

Subsequently, needle insertion is performed collaboratively under haptic feedback with both robot and physician

[1]Institute of Medical Technology and Intelligent Systems, Hamburg University of Technology, 21073 Hamburg, Germany robin.mieling@tuhh.de
[2]Institute of Legal Medicine, University Medical Center Hamburg-Eppendorf, 22529 Hamburg, Germany
This research was partially funded by the NATON project (grant agreement no 01KX2121), by the Calls for Transfer initiative (BWFGB Hamburg, C4T535) and the TUHH i^3 initiative
Ethical approval: The Ethics Committee of the Hamburg Chamber of Physicians approved the study (No.: 2020-10353-BO-ff)
* Both authors contributed equally.

2023 IEEE International Conference on Robotics and Automation (ICRA) | 979-8-3503-2365-8/23/$31.00 ©2023 IEEE | DOI: 10.1109/ICRA48891.2023.10161377

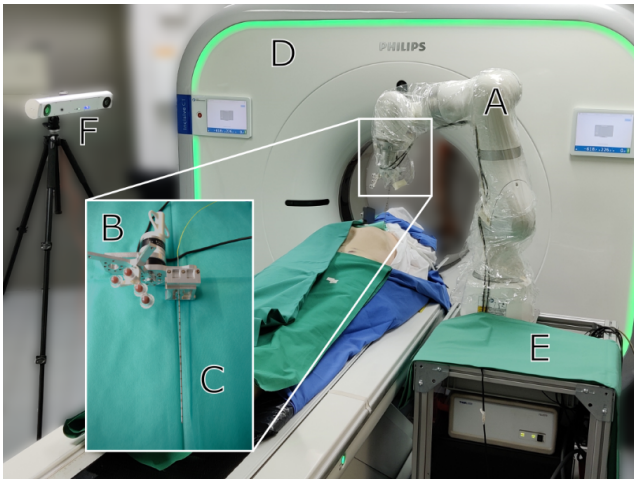

Fig. 2. **Collaborative Robotic System**: The experimental setup consists of the robot (A), the needle mount (B) with integrated force sensors and tracking markers, the *smart* needle (C), the CT system (D), the robot cart (E) with the built-in OCT system and the optical tracking system (F).

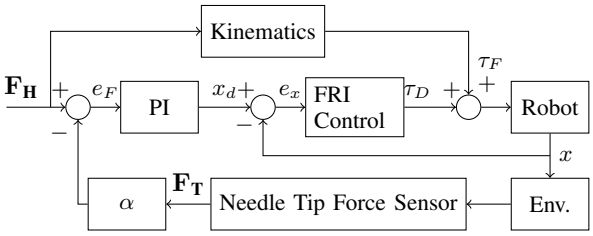

Fig. 3. **Control Loop:** Admittance control loop employed to display the forces between needle tip and tissue to the operator. In the outer control loop, the desired robot pose x_d is controlled with a PI controller based on the operator's handle force $\mathbf{F_H}$ and the amplified tip force $\mathbf{F_T}$. The inner control loop is governed by the position controller of the fast research interface [41]. e_F denotes the outer loop force error, x the actual robot pose, e_x the inner loop pose error, τ_D the controller torque and τ_F the externally applied torque.

on site as shown in Fig. 1. Needle path planning and robot motion are executed in a custom software framework [9]. We present a *smart* needle with an embedded optical fiber for sensing forces acting on the needle tip. We estimate forces based on optical coherence tomography (OCT) imaging and perform real-time data processing with deep learning [29], [33], [34].

The advantages of our system are: (1) safety; the physician can feel critical events and is in control of the robot motion at all times, (2) compensation for displacements and deformations of soft tissue structures during needle insertion [9], [35], [36], [37], [38] and (3) flexible puncture of different soft tissue targets with a 7 degree of freedom (DOF) robot.

We evaluate the robotic system in three stages. Firstly, we perform fully robotic insertions with a constant velocity to demonstrate how unpredictable friction forces are in heterogeneous phantoms, and we show that the forces at the needle tip can help identify the location of tissue interfaces. Secondly, we show that operators can determine the topology of the tissue phantoms while purely relying on needle tip force feedback. Lastly, we extract in situ pancreas tissue from corpses which is a challenging target to reach in the clinic requiring CT [39] or endoscopic ultrasound [40] due to the long insertion path and anatomical localization.

II. Methods

A. Collaborative Robotic System

The robotic system is depicted in Fig. 2 and combines trajectory guidance with haptic needle tip force feedback. The collaborative procedure is performed with a 7-DOF light-weight medical robot (LBR Med 14, KUKA AG, Augsburg, Germany) designed for human-robot interaction. CT images are acquired with the Philips Incisive system and the biopsy target is annotated by medical experts. A custom planning system is used to estimate an entry point prior to the insertion, considering insertion depth, insertion angle and collision avoidance for bone structures. Registration between CT and robot is performed with an optical tracking camera (fusionTrack 500, Atracsys LLC, Puidoux, Switzerland) as described in [9] and the robot aligns the needle along the chosen trajectory. Forces acting on the tip of our *smart* needle are estimated and fed back to the physician as a resistive force. A 3D printed handle allows the surgeon to easily move the *smart* needle along its axis while the robot guides the motion. Two force-torque sensors (M3703, Sunrise Instruments) enable the measurement of needle shaft forces and operator inputs, respectively. Note, that shaft forces are only measured for comparison. During the insertion, the movement is restricted to the axial needle direction. To include haptic feedback into the position control we employ the control loop depicted in Fig. 3. The inner control loop is governed by the position controller of the fast research interface [41]. In the outer control loop an implicit force trajectory-tracking controller similar to [42] is implemented. The robot position

$$x_d(t) = k_i \int_0^t e_f(t)\,dt + k_p e_f(t) \tag{1}$$

is choosen such that the error $e_F = F_\mathrm{H} - \alpha F_\mathrm{T}$ between the handle force F_H and the amplified measured tip force F_T is minimized. The magnitude e_F is limited between 0 and F_H to prevent involuntary movement. The gain α can be chosen by the operator. The control loop and robot communication is implemented with the Robot Operating System (ROS). Force measurements and haptic control run at a frequency of 200 Hz.

B. Smart Needle

We build custom needle probes with an integrated optical force sensor which we refer to as *smart* needle. Our *smart* needle is integrated into an introducer needle of a clinical biopsy system and allows sensing of forces at the needle tip. The *smart* needle components are depicted in Fig. 4, left. A symmetrical needle tip is guided by the needle sheath with an outer diameter of 2.05 mm. An inner tube centers the optical fibre within the needle sheath. The fiber is cleaved for common-path imaging and placed within 0.5 mm of the

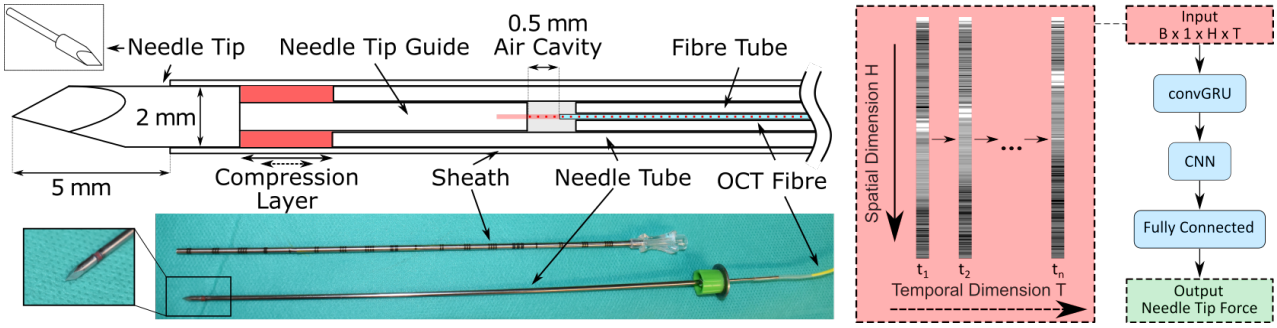

Fig. 4. ***Smart* Needle:** Optical needle probe (left) for the estimation of needle tip forces during the insertion. Forces applied at the needle tip cause the compression layer to deform. The resulting change in air cavity length is resolved in the OCT signal. A symmetric needle tip reduces lateral bending of the needle during insertion. We consider a cGRU-CNN model (right) for real-time processing of the OCT data stream ($H \times T = 512 \times 50$) and compare the performance to a 2D ResNet baseline. The output of the cGRU layer is processed in the regression head containing a ResNet based 1D CNN and fully connected layers.

proximal end of the needle tip's guide. The compression layer between needle tip and sheath causes the OCT signal to change under load. OCT data is recorded with a spectral domain OCT system (Telesto Telesto I, Thorlabs GmbH, GER). The system records one-dimensional depth scans (A-scans) with a maximum imaging depth of approximately 2.6 mm in air resolved over 512 pixels.

For real-time data processing, we consider convolutional gated recurrent units (cGRU) with a subsequent 1D CNN designed for spatio-temporal input data (Fig. 4, right).Similar to Gessert et al. [29], we replace the dot products in the GRU cells with 1D convolutions such that

$$
\begin{aligned}
z_t &= \sigma(W_{hz} * h_{t-1} + W_{xz} * x_t + b_z), \\
r_t &= \sigma(W_{hr} * h_{t-1} + W_{xr} * x_t + b_r), \\
\hat{h}_t &= tanh(W_h * (r_t \odot h_{t-1}) + W_x * x_t + b) \text{ and} \\
h_t &= (1 - z_t) \odot h_{t-1} + z_t \odot \hat{h}_t
\end{aligned}
$$

defines the update gate z_t, the reset gate r_t, the candidate activation vector $\hat{h}_t$ and the hidden state h_t, respectively. By updating the trainable filers W, spatial information is processed for each A-scan and temporal information is extracted in the recurrent unit. The tip force is estimated based on the resulting feature vector h_n in the regression head (Fig. 4). We compare our cGRU-CNN model with a basic 2D residual neural network (ResNet) [43].

To calibrate our *smart* sensor prior to insertion, we manually apply cyclic axial loads on a rigid surface. We record $6{\times}10^4$ synchronized OCT A-scans and force labels for tuning our model, with forces between 0 N-5 N. We train our models on input sequences of 50 A-scans over 50 epochs with a learning rate of $5{\times}10^{-4}$ and a batch size (B) of 128, using the mean squared error (MSE) as our loss function. We use Adam optimization with default parameters [44]. We test the model employment over $1{\times}10^4$ A-scans implementing a cyclic buffer to maintain the input dimensions for the ResNet model. We compare the two architectures with regard to accuracy and check for real time applicability. We report mean absolute errors (MAE) and Pearson correlation coefficient (pCC). To evaluate real time application, we report timings for forward and backward pass and the inference time for individual samples processed on the GPU (RTX 3070, NVIDIA Corporation, USA). The model with the lowest MAE during calibration is used for phantom and in-situ insertions.

C. Phantom Experiments

We perform a phantom study to evaluate if the needle tip forces are beneficial in the detection of tissue interfaces. For this purpose, we embed ex-vivo chicken muscle tissue into gelatin gels that fixate the tissue and prevent bulk displacement (Fig. 5). A skin layer at the top of the phantom consists of polyethylene foam and silicone rubber to simulate the superposition of friction forces in percutaneous insertions. We manufacture in total four phantoms and acquire CT scan to determine the location of interfaces based on the measured Hounsfield units. Firstly, we perform 25 fully robotic insertions with a constant velocity of $5\,\mathrm{mm\,s^{-1}}$ to evaluate needle forces independent of operator inputs. We compare absolute forces at the needle tip with the location of tissue interfaces marked in the pre-insertion CT scan. To underline the importance of local tip force measurements, we additionally analyze friction forces by subtracting the tip force from the total axial force. We report changes in friction force per material — skin layer, gelatin and ex-vivo tissue — by calculating the slope of a linear regression through the friction forces of each segment separated by tissue interfaces.

Secondly, we conduct a user study in which five participants are tasked to sense interfaces during collaborative needle insertions. We provide kinesthetic feedback on tip forces and the participants are tasked to enable a trigger if a tissue interface is perceived. We report the distance between the estimated needle tip position triggered by the user and the position of the tissue interface in the CT reference frame. We evaluate the number of correctly detected and missed tissue interfaces. We distinguish between entry and exit events for each of the two tissue layers, resulting in up to four marked locations per insertion. Participants perform three test insertions to choose the gain α with which the tip forces are scaled.

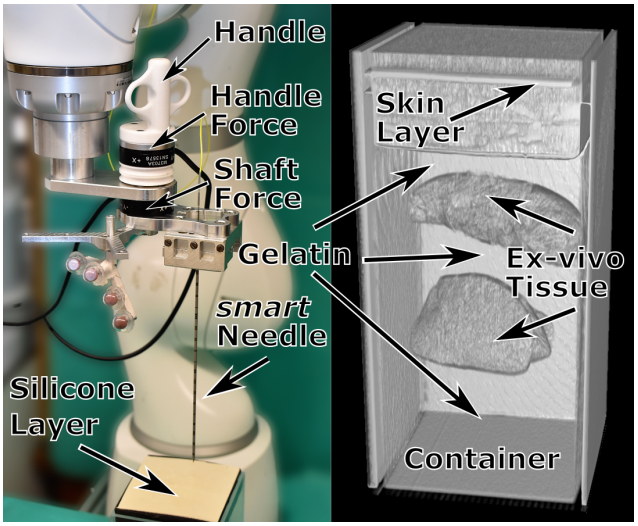

Fig. 5. **Phantom Experiments:** The *smart* needle and the haptic system with regard to tissue interface detection are evaluated in a phantom study. The system (left) allows for both fully robotic and collaborative insertions. (Right) CT scan of a phantom containing ex-vivo tissue embedded in gelatin to prevent bulk displacement. A skin layer with silicone and polyethylene foam emulates friction forces from the skin.

D. In Situ Pancreas Biopsy

We demonstrate the collaborative system in a forensic setup by performing post-mortem pancreatic biopsy in two different cases. The target area is marked by an expert in the pre-insertion CT and a path through the center of the pancreatic tail is planned for robotic trajectory guidance (Fig. 6). The needle is pre-aligned by the robot and the insertion is switched to collaborative control. An incision is made into the skin in order to reduce forces upon dermal entry and the pathologist controls the placement of the needle. The pathologist performs collaborative needle insertion and stops the motion once he felt the tissue transition of the target structure. With the needle sheath held in place, the *smart* needle is retracted and a sample is taken with the biopsy gun at the chosen position. A post-insertion CT is acquired to visualize final needle placement.

III. Results

In the following, we report the accuracy of our needle tip force calibration. We then present our ex-vivo tissue study and finally demonstrate the application of our system for post-mortem pancreas biopsy.

A. Smart Needle Calibration

Needle tip force estimations for both models are reported in Tab. I. While the total time per sample for the forward and backward pass is longer for the recurrent model, samples can be processed independently during use and both models can be integrated into the control loop running at 200 Hz. The spatio temporal cGRU-CNN model outperforms the ResNet architecture with a MAE of 0.11 N and the more accurate model is consequently chosen during phantom and post-mortem insertions. An example of the calibrated tip force

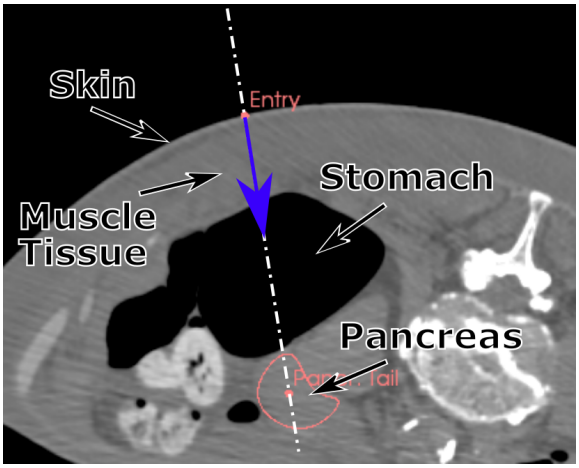

Fig. 6. **Pancreas Biopsy:** Biopsy of the tail of the pancreas is performed in a collaborative approach. Image guidance is used to globally align the needle along the planned trajectory (white dashed line) based on the selection of the surgeon. Local needle placement is performed by the surgeon controlling axial motion along the trajectory (blue arrow).

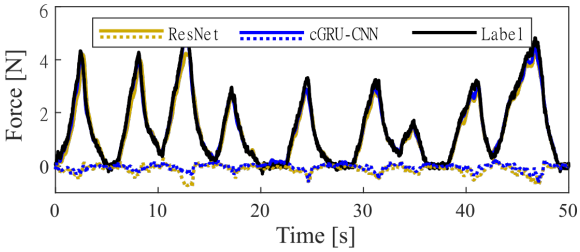

Fig. 7. ***Smart* Needle Calibration:** Example plot of the needle tip force calibration with estimations for both model architectures and the ground truth measurements (black). The absolute errors for both models are displayed as dotted lines.

estimation during loads exclusively applied at the tip can be seen in Fig. 7.

B. Phantom Experiments

Two examples of the robotic insertions into ex-vivo tissue with constant velocity can be seen in Fig. 8. During 25 automatic insertions, an increase in tip force $F_T > 1\,N$ can be noted 2.08±1.08 mm below the entry into ex-vivo tissue marked in the pre-insertion CT scan. Similarly, the return to tip forces $F_T < 1\,N$ corresponding to the re-entry into homogeneous gelatin occurs 5.13±1.88 mm below the locations marked prior to the insertion. We further report the friction force per unit length in Tab. II separated by skin layer (S), gelatin (G) and ex-vivo tissue (T). Large variations over different segments of the same material can be seen. Especially for segments where the needle tip is cutting through homogeneous gelatin, friction forces vary between 0.05 N/mm and −0.56 N/mm. Examples of this can be seen in Fig. 8, indicated by decreasing (e.g. G_1, top) and increasing slopes (e.g. G_1, bottom) in gelatin for different insertions.

The results of the user study can be seen in Tab. III where participants are tasked to feel for the topology of

TABLE I

ERROR METRICS AND TIMINGS FOR THE NETWORK ARCHITECTURES. THE INFERENCE TIME (IT) AND THE TOTAL TIME (TT) FOR FORWARD AND BACKWARD PASS ARE GIVEN FOR INDIVIDUAL EXAMPLES.

Model	MAE [N]	pCC	IT [ms]	TT [ms]
ResNet	0.15	0.99	0.30	15.13
cGRU-CNN	0.11	0.99	1.03	52.96

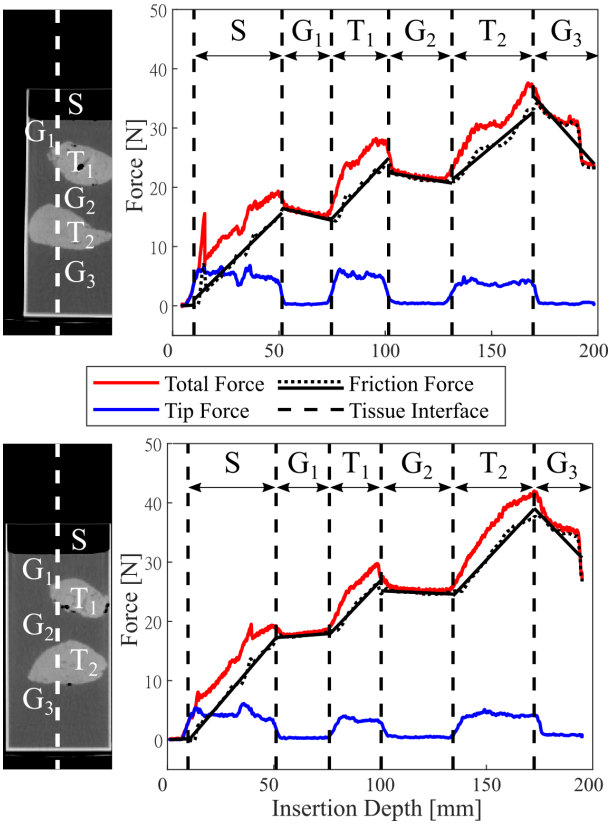

Fig. 8. **Phantom Needle Insertions:** Two examples (top and bottom) for insertions with constant velocity through ex-vivo tissue with pre-insertion imaging and trajectory (dleft) and corresponding force plots (right). Location of tissue interfaces (dashed), tip forces (blue), total forces measured at the shaft (red), friction forces (dotted) and linear regression of friction forces (black) are plotted over the insertion depth. Insertions are segmented into the topmost skin segment (S), gelatin segments (G) and tissue segments (T).

the phantoms. The mean distance between tissue interfaces estimated from CT and user inputs ranges from 5.77 mm to 11.74 mm for all participants. For the interfaces from gelatin to tissue layers the mean distance for all performed experiments is smaller (5.45±3.31 mm) compared to interfaces between tissue and gelatin (9.85±4.89 mm). The distance to interfaces from gelatin to tissue are 4.85±2.44 mm and 6.05±4.02 mm for the two tissue layers, respectively. For the interfaces from tissue to gelatin we report increased distances of 9.14±4.23 mm and 10.88±5.75 mm for the two tissue layers, respectively. In total, users do not recognize 9 tissue interfaces resulting in a total detection rate of 91 %. Of the missed cases, 80 % correspond to the interface between tissue and gelatin.

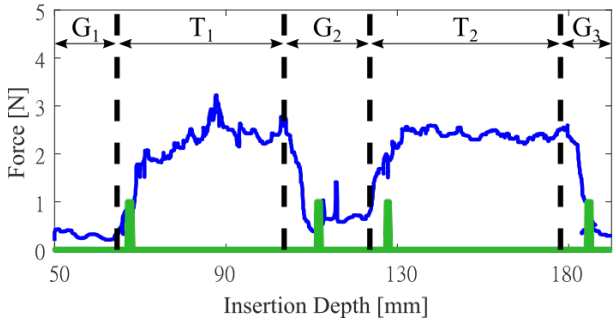

Fig. 9. **Example Needle Insertion with Haptic Feedback:** Depicted are the needle tip forces (blue) and trigger (green) enabled manually by the user when a tissue transition is sensed. The position of the gelatin layers (G) and tissue layers (T) are indicated on top.

TABLE II

MEAN, STANDARD DEVIATION AND RANGE FOR FRICTION PER UNIT LENGTH [N/mm] FOR EACH MATERIAL.

Material	Skin Layer	Tissue	Gelatin
Mean	0.38±0.04	0.36±0.08	−0.15±0.19
Min	0.25	0.13	−0.56
Max	0.45	0.54	0.05

C. *In Situ Pancreas Biopsy*

A visualization of a collaboratively performed pancreatic biopsies can be seen in Fig. 10. With the needle aligned along the planned trajectory, the pathologist advances the needle through the initial resistance of skin and muscle tissue and passes into the stomach (2). As the needle exits the partially gas-filled stomach the pathologist detects the force peak and subsequent rupture (3) and is able to place the needle in the tail of the pancreas. The samples taken are subjected to a histopathological examination, which confirms the successful insertion (Fig. 11).

IV. DISCUSSION AND CONCLUSION

In this work, we present a concept for a collaborative robotic biopsy system that combines trajectory guidance with real-time feedback of needle tip forces. Haptic feedback is provided by the robot on site, enabling the physician to locate tissue interfaces during insertion.

We perform ex-vivo tissue experiments for validation and systematic analysis of estimated forces acting on the needle

TABLE III

DETECTION RATE (DR) AND DISTANCES [mm] BETWEEN PRE-INSERTION POSITION AND POSITIONS DETECTED BY THE USER FOR THE FIVE PARTICIPANTS.

DR	G_1 to T_1	T_1 to G_2	G_2 to T_2	T_2 to G_3	Mean
95 %	2.86±1.50	10.23±4.49	5.95±2.10	10.94±3.90	7.31±4.45
80 %	7.21±1.47	14.30±2.57	11.86±7.14	14.90±5.80	11.74±4.97
95 %	4.20±3.36	6.46±4.09	3.35±1.74	12.80±8.66	6.38±5.70
90 %	4.85±1.67	7.89±2.88	4.14±2.87	6.47±3.83	5.77±2.95
95 %	5.12±2.20	6.81±1.78	7.27±2.63	8.63±3.47	6.77±2.53
Mean	4.85±2.44	9.14±4.23	6.05±4.02	10.88±5.75	

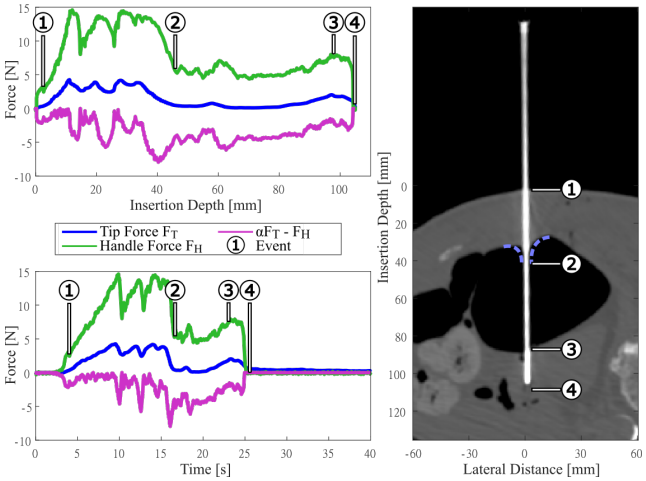

Fig. 10. **Haptic Guided Pancreas Biopsy:** Needle tip forces (blue), axial handle force (green) and the difference $\alpha F_{\mathrm{T}} - F_{\mathrm{H}}$ (magenta) displayed over the insertion depth (top, left) and insertion time (bottom, left). Corresponding CT scan after the insertion (right) with marked events denoting percutaneous entry (1), entry (2) and exit (3) of the stomach and final needle position (4). Inward deformation of the stomach wall (dashed blue line) causes the rupture (2) to occur at a greater depth than can be seen on the pre- or post-insertion CT scan.

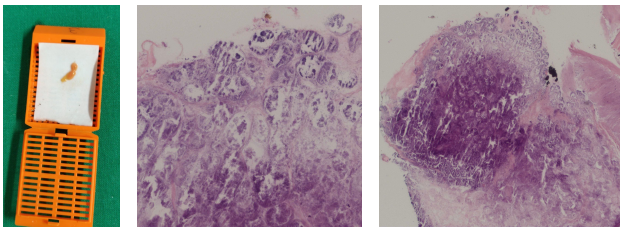

(a) (b) (c)

Fig. 11. **Pancreatic Tissue Biopsy:** Extracted sample (a) corresponding to the insertion shown in Fig. 10) and histopathological imaging (b) confirming the success of the pancreatic biopsies in both cases (although tissue is already affected by putrefaction).

tip and the corresponding kinesthetic feedback. Insertions with a constant velocity show that friction forces per unit length vary within the same material even in a phantom setup with ex-vivo tissue embedded in gelatin. In Fig. 8 the friction forces show either falling (top) or rising slopes (bottom) within the homogeneous gelatin and the inconsistent behavior is most likely due to the mechanics of relaxation in tissue [45], [46]. Consequently, the friction forces are not only strongly dependent on the insertion velocity, tissue properties and needle geometry, but also on the combination of already punctured tissue. Our findings underline the benefit of directly obtaining absolute tip force values as demonstrated in [20], [25], [47] and highlight the limitations of friction model based approaches [18]. We have observed that the sharp tip of our *smart* needle results in nearly constant tip forces between tissue interfaces cutting through each layer and limiting tissue compression.

The user study shows that the provided kinesthetic feedback was interpreted more reliably by the participants for increasing forces, corresponding to needle punctures into tissue (T). Tissue to gelatin interfaces were detected with less accuracy. This can be partially explained by the design of the needle as approximately 5 mm of the needle tip protrudes beyond the needle sheath (Fig. 4) and a fraction of the load remains until the tip is fully extended beyond the tissue interface. In addition, gelatin prevents bulk displacement, but limited tissue deformation can still occur especially during the transition from one layer to the next. Adjustments to the needle design e.g. a shorter tip could further enhance detection as resistance decreases. The current system is limited to kinesthetic feedback that the users must first learn to interpret. Additional sensations, e.g. vibrotactile feedback could help improve detection rates and reduce user dependence [18]. Variability between naive users shows that the haptic feedback is not equally intuitive to every participant with detection rates ranging from 80 % to 95 %. In comparison, the detection of membrane puncture events in a phantom setup were reported with a 75 % success rate in [20] and 98.9 % in [47]. In [25], success rates ranged from 50.0 % to 83.3 %. However, comparisons to previous works are challenging as they are highly dependent on tissue and experimental setup, e.g. the perception of membrane puncture with uni-axial motion stages [47].

Lastly, we demonstrate collaborative robotic biopsy in a real-word scenario. The pancreas represents a challenging target for biopsies within the retroperitoneal space as ultrasound image guidance is hampered for imaging deep tissues [48]. Manual insertions with robotic trajectory guidance can assist in needle placement [13], [15]. Here we provide haptic feedback on tissue interfaces to the physician, potentially increasing needle placement accuracy. The pathologist was able to perceive the interface between stomach and pancreas, as indicated in Fig.10, and successfully position the needle relative to this target structure. The biopsy of the pancreas demonstrates the feasibility of the approach for anatomically difficult located tissue. But this approach would also be suitable for other soft tissue biopsy targets, e.g. lung or prostate. The in-situ application demonstrates the needle tip sensor under realistic load but sensitivity under strong lateral forces needs to be further evaluated. Our initial results with a small sample size and a single operator are promising, but further evaluations regarding applicability and clinical workflow integration need to be explored in the future.

In conclusion, our results suggest that haptic feedback is a valuable alternative to fully automated robotic needle placement. Our results demonstrate that it is possible to sense tissue interfaces with a collaborative robot for versatile needle insertions in a large operating space. With our system the physician is at all times in control of the needle insertion which is crucial in a clinical environment. Further studies will show how collaborative robotic biopsy compares to exclusive trajectory guidance and manual placement, and how much training is required for the adaptation processes.

ACKNOWLEDGMENT

The authors state no conflict of interest.

REFERENCES

[1] Ather Adnan and Rahul A. Sheth, "Image-guided percutaneous biopsy of the liver," *Techniques in Vascular and Interventional Radiology*, vol. 24, no. 4, p. 100773, 2021.

[2] G. A. McLeod, "Novel approaches to needle tracking and visualisation," *Anaesthesia*, vol. 76 Suppl 1, pp. 160–170, 2021.

[3] J. I. Son, S. Y. Rhee, J.-T. Woo, W. S. Park, J. K. Byun, Y.-J. Kim, J. M. Byun, S. O. Chin, S. Chon, S. Oh, S. W. Kim, and Y. S. Kim, "Insufficient experience in thyroid fine-needle aspiration leads to misdiagnosis of thyroid cancer," *Endocrinology and metabolism (Seoul, Korea)*, vol. 29, no. 3, pp. 293–299, 2014.

[4] U. Fehrenbach, R. Thiel, P.-D. Bady, T. A. Auer, A. Kahl, D. Geisel, E. Lopez Hänninen, R. Öllinger, J. Pratschke, B. Gebauer, and T. Denecke, "Ct fluoroscopy-guided pancreas transplant biopsies: a retrospective evaluation of predictors of complications and success rates," *Transplant international : official journal of the European Society for Organ Transplantation*, vol. 34, no. 5, pp. 855–864, 2021.

[5] K. P. H. Pritzker and H. J. Nieminen, "Needle biopsy adequacy in the era of precision medicine and value-based health care," *Archives of pathology & laboratory medicine*, vol. 143, no. 11, pp. 1399–1415, 2019.

[6] F. J. Siepel, B. Maris, M. K. Welleweerd, V. Groenhuis, P. Fiorini, and S. Stramigioli, "Needle and biopsy robots: a review," *Curr Robot Rep*, vol. 2, no. 1, pp. 73–84, 2021.

[7] Y. Wang and H. Li, "Penetration detection with intention recognition for cooperatively controlled robotic needle insertion," *Transactions of the Institute of Measurement and Control*, vol. 44, no. 10, pp. 1979–1992, 2022.

[8] S. Franckenberg, T. Sieberth, T. Frauenfelder, M. J. Thali, and L. C. Ebert, "Semiautomated robotic, ct-guided needle placement for post-mortem csf sampling – a novel application of the virtobot," *All Life*, vol. 14, no. 1, pp. 75–79, 2021.

[9] M. Neidhardt, S. Gerlach, R. Mieling, M.-H. Laves, T. Weiß, M. Gromniak, A. Fitzek, D. Möbius, I. Kniep, A. Ron *et al.*, "Robotic tissue sampling for safe post-mortem biopsy in infectious corpses," *IEEE transactions on medical robotics and bionics*, vol. 4, no. 1, pp. 94–105, 2022.

[10] D. Yakar, M. G. Schouten, D. G. Bosboom, J. O. Barentsz, T. W. Scheenen, and J. J. Fütterer, "Feasibility of a pneumatically actuated mr-compatible robot for transrectal prostate biopsy guidance," *Radiology*, vol. 260, no. 1, pp. 241–247, 2011.

[11] J. C. Vilanova, A. Pérez de Tudela, J. Puig, M. Hoogenboom, J. Barceló, M. Planas, S. Sala, and S. Thió-Henestrosa, "Robotic-assisted transrectal mri-guided biopsy. technical feasibility and role in the current diagnosis of prostate cancer: an initial single-center experience," *Abdominal radiology (New York)*, vol. 45, no. 12, pp. 4150–4159, 2020.

[12] J. J. Fütterer and J. O. Barentsz, "Mri-guided and robotic-assisted prostate biopsy," *Current opinion in urology*, vol. 22, no. 4, pp. 316–319, 2012.

[13] B. Guiu, T. de Baère, G. Noel, and M. Ronot, "Feasibility, safety and accuracy of a ct-guided robotic assistance for percutaneous needle placement in a swine liver model," *Sci Rep*, vol. 11, no. 1, p. 5218, 2021.

[14] J. Kettenbach, L. Kara, G. Toporek, M. Fuerst, and G. Kronreif, "A robotic needle-positioning and guidance system for ct-guided puncture: Ex vivo results," *Minimally invasive therapy & allied technologies : MITAT : official journal of the Society for Minimally Invasive Therapy*, vol. 23, no. 5, pp. 271–278, 2014.

[15] S. Levy, S. N. Goldberg, I. Roth, M. Shochat, J. Sosna, I. Leichter, and S. Flacke, "Clinical evaluation of a robotic system for precise ct-guided percutaneous procedures," *Abdominal radiology (New York)*, 2021.

[16] R. M. Martinez, W. Ptacek, W. Schweitzer, G. Kronreif, M. Fürst, M. J. Thali, and L. C. Ebert, "Ct-guided, minimally invasive, postmortem needle biopsy using the b-rob ii needle-positioning robot," *Journal of forensic sciences*, vol. 59, no. 2, pp. 517–521, 2014.

[17] E. Abdi, D. Kulic, and E. Croft, "Haptics in teleoperated medical interventions: Force measurement, haptic interfaces and their influence on user's performance," *IEEE transactions on bio-medical engineering*, vol. 67, no. 12, pp. 3438–3451, 2020.

[18] M. Aggravi, D. A. Estima, A. Krupa, S. Misra, and C. Pacchierotti, "Haptic teleoperation of flexible needles combining 3d ultrasound guidance and needle tip force feedback," *IEEE Robotics and Automation Letters*, vol. 6, no. 3, pp. 4859–4866, 2021.

[19] Y. Tai, K. Qian, X. Huang, J. Zhang, M. A. Jan, and Z. Yu, "Intelligent intraoperative haptic-ar navigation for covid-19 lung biopsy using deep hybrid model," *IEEE Transactions on Industrial Informatics*, vol. 17, no. 9, pp. 6519–6527, 2021.

[20] S. Elayaperumal, J. H. Bae, B. L. Daniel, and M. R. Cutkosky, "Detection of membrane puncture with haptic feedback using a tip-force sensing needle," in *IEEE/RSJ International Conference on Intelligent Robots and Systems*. IEEE, 2014, pp. 3975–3981.

[21] E. Mendoza and J. P. Whitney, "A testbed for haptic and magnetic resonance imaging-guided percutaneous needle biopsy," *IEEE Robotics and Automation Letters*, vol. 4, no. 4, pp. 3177–3183, 2019.

[22] M. Wartenberg, J. Schornak, K. Gandomi, P. Carvalho, C. Nycz, N. Patel, I. Iordachita, C. Tempany, N. Hata, J. Tokuda, and G. S. Fischer, "Closed-loop active compensation for needle deflection and target shift during cooperatively controlled robotic needle insertion," *Annals of Biomedical Engineering*, vol. 46, no. 10, pp. 1582–1594, 2018.

[23] P. Baksic, H. Courtecuisse, and B. Bayle, "Shared control strategy for needle insertion into deformable tissue using inverse finite element simulation," in *2021 IEEE International Conference on Robotics and Automation (ICRA)*. IEEE, 2021, pp. 12 442–12 448.

[24] A. K. Han, J. H. Bae, K. C. Gregoriou, C. J. Ploch, R. E. Goldman, G. H. Glover, B. L. Daniel, and M. R. Cutkosky, "Mr-compatible haptic display of membrane puncture in robot-assisted needle procedures," *IEEE Transactions on Haptics*, vol. 11, no. 3, pp. 443–454, 2018.

[25] D. De Lorenzo, Y. Koseki, E. De Momi, K. Chinzei, and A. M. Okamura, "Coaxial needle insertion assistant with enhanced force feedback," *IEEE Transactions on Biomedical Engineering*, vol. 60, no. 2, pp. 379–389, 2012.

[26] D. Uzun, O. Ulgen, and O. Kocaturk, "Optical force sensor with enhanced resolution for mri guided biopsy," *IEEE Sensors Journal*, vol. 20, no. 16, pp. 9202–9208, 2020.

[27] S. Beekmans, T. Lembrechts, J. van den Dobbelsteen, and D. van Gerwen, "Fiber-optic fabry-pérot interferometers for axial force sensing on the tip of a needle," *Sensors (Basel, Switzerland)*, vol. 17, no. 1, 2016.

[28] H. Su, M. Zervas, G. A. Cole, C. Furlong, and G. S. Fischer, "Real-time mri-guided needle placement robot with integrated fiber optic force sensing," in *2011 IEEE International Conference on Robotics and Automation*. IEEE, 2011, pp. 1583–1588.

[29] N. Gessert, T. Priegnitz, T. Saathoff, S.-T. Antoni, D. Meyer, M. F. Hamann, K.-P. Jünemann, C. Otte, and A. Schlaefer, "Spatio-temporal deep learning models for tip force estimation during needle insertion," *International journal of computer assisted radiology and surgery*, vol. 14, no. 9, pp. 1485–1493, 2019.

[30] M. Ourak, J. Smits, L. Esteveny, G. Borghesan, A. Gijbels, L. Schoevaerdts, Y. Douven, J. Scholtes, E. Lankenau, T. Eixmann, H. Schulz-Hildebrandt, G. Hüttmann, M. Kozlovszky, G. Kronreif, K. Willekens, P. Stalmans, K. Faridpooya, M. Cereda, A. Giani, G. Staurenghi, D. Reynaerts, and E. B. Vander Poorten, "Combined oct distance and fbg force sensing cannulation needle for retinal vein cannulation: in vivo animal validation," *International journal of computer assisted radiology and surgery*, vol. 14, no. 2, pp. 301–309, 2019.

[31] S. Gerlach, M. Neidhardt, T. Weiß, M.-H. Laves, C. Stapper, M. Gromniak, I. Kniep, D. Möbius, A. Heinemann, B. Ondruschka *et al.*, "Needle insertion planning for obstacle avoidance in robotic biopsy," *Current Directions in Biomedical Engineering*, vol. 7, no. 2, pp. 779–782, 2021.

[32] M. Neidhardt, S. Gerlach, M.-H. Laves, S. Latus, C. Stapper, M. Gromniak, and A. Schlaefer, "Collaborative robot assisted smart needle placement," *Current Directions in Biomedical Engineering*, vol. 7, no. 2, pp. 472–475, 2021.

[33] S. Latus, J. Sprenger, M. Neidhardt, J. Schädler, A. Ron, A. Fitzek, M. Schlüter, P. Breitfeld, A. Heinemann, K. Püschel *et al.*, "Rupture detection during needle insertion using complex oct data and cnns," *IEEE Transactions on Biomedical Engineering*, vol. 68, no. 10, pp. 3059–3067, 2021.

[34] R. Mieling, C. Stapper, S. Gerlach, M. Neidhardt, S. Latus, M. Gromniak, P. Breitfeld, and A. Schlaefer, "Proximity-based haptic feedback for collaborative robotic needle insertion," in *International Conference on Human Haptic Sensing and Touch Enabled Computer Applications*. Springer, 2022, pp. 301–309.

[35] D. Halstuch, J. Baniel, D. Lifshitz, S. Sela, Y. Ber, and D. Margel, "Assessment of needle tip deflection during transrectal guided prostate

biopsy: Implications for targeted biopsies," *Journal of endourology*, vol. 32, no. 3, pp. 252–256, 2018.
[36] C. Yang, Y. Xie, S. Liu, and D. Sun, "Force modeling, identification, and feedback control of robot-assisted needle insertion: A survey of the literature," *Sensors (Basel, Switzerland)*, vol. 18, no. 2, 2018.
[37] S. Jiang, P. Li, Y. Yu, J. Liu, and Z. Yang, *Experimental study of needle-tissue interaction forces: effect of needle geometries, insertion methods and tissue characteristics*. Elsevier, 2014, vol. 47.
[38] A. Muthigi, A. K. George, A. Sidana, M. Kongnyuy, R. Simon, V. Moreno, M. J. Merino, P. L. Choyke, B. Turkbey, B. J. Wood, and P. A. Pinto, "Missing the mark: Prostate cancer upgrading by systematic biopsy over magnetic resonance imaging/transrectal ultrasound fusion biopsy," *The Journal of urology*, vol. 197, no. 2, pp. 327–334, 2017.
[39] U. Fehrenbach, R. Thiel, P.-D. Bady, T. A. Auer, A. Kahl, D. Geisel, E. Lopez Hänninen, R. Öllinger, J. Pratschke, B. Gebauer *et al.*, "Ct fluoroscopy-guided pancreas transplant biopsies: a retrospective evaluation of predictors of complications and success rates," *Transplant International*, vol. 34, no. 5, pp. 855–864, 2021.
[40] A. Syed, O. Babich, B. Rao, S. Singh, N. Carleton, A. Gulati, A. Kulkarni, M. Garg, K. Farah, G. Kochhar, S. Morrissey, M. Mitre, A. Kulkarni, M. Dhawan, J. F. Silverman, M. Pharaon, and S. Thakkar, "Endoscopic ultrasound guided fine-needle aspiration vs core needle biopsy for solid pancreatic lesions: Comparison of diagnostic accuracy and procedural efficiency," *Diagnostic Cytopathology*, vol. 47, no. 11, pp. 1138–1144, 2019.
[41] G. Schreiber, A. Stemmer, and R. Bischoff, "The fast research interface for the kuka lightweight robot," in *IEEE workshop on innovative robot control architectures for demanding (Research) applications how to modify and enhance commercial controllers (ICRA 2010)*. Citeseer, 2010, pp. 15–21.
[42] J. Roy and L. Whitcomb, "Adaptive force control of position/velocity controlled robots: theory and experiment," *IEEE Transactions on Robotics and Automation*, vol. 18, no. 2, pp. 121–137, 2002.
[43] K. He, X. Zhang, S. Ren, and J. Sun, "Deep residual learning for image recognition," in *Proceedings of the IEEE conference on computer vision and pattern recognition*, 2016, pp. 770–778.
[44] D. P. Kingma and J. Ba, "Adam: A method for stochastic optimization," *arXiv preprint arXiv:1412.6980*, 2014.
[45] M. Mahvash and P. E. Dupont, "Mechanics of dynamic needle insertion into a biological material," *IEEE Transactions on Biomedical Engineering*, vol. 57, no. 4, pp. 934–943, 2009.
[46] A. M. Okamura, C. Simone, and M. D. O'leary, "Force modeling for needle insertion into soft tissue," *IEEE transactions on biomedical engineering*, vol. 51, no. 10, pp. 1707–1716, 2004.
[47] A. K. Han, J. H. Bae, K. C. Gregoriou, C. J. Ploch, R. E. Goldman, G. H. Glover, B. L. Daniel, and M. R. Cutkosky, "Mr-compatible haptic display of membrane puncture in robot-assisted needle procedures," *IEEE transactions on haptics*, vol. 11, no. 3, pp. 443–454, 2018.
[48] S. Malek, S. Potdar, J. Martin, M. Tublin, R. Shapiro, and J. Fung, "Percutaneous ultrasound-guided pancreas allograft biopsy: a single-center experience," in *Transplantation proceedings*, vol. 37, no. 10. Elsevier, 2005, pp. 4436–4437.

7.3 Optical Coherence Elastography Needle for Biomechanical Characterization of Deep Tissue

Conference: Medical Image Computing and Computer Assisted Intervention – MICCAI 2023

Published: 01.10.2023

R. Mieling, S. Latus, M. Fischer, F. Behrendt, and A. Schlaefer, "Optical coherence elastography needle for biomechanical characterization of deep tissue," in *Medical Image Computing and Computer Assisted Intervention – MICCAI 2023*, ser. Lecture Notes in Computer Science, Cham: Springer, 2023, pp. 607–617

Optical Coherence Elastography Needle for Biomechanical Characterization of Deep Tissue

Robin Mieling(✉), Sarah Latus, Martin Fischer, Finn Behrendt and Alexander Schlaefer

Institute of Medical Technology and Intelligent Systems, Hamburg University of Technology, Hamburg, Germany
robin.mieling@tuhh.com

Abstract. Compression-based optical coherence elastography (OCE) enables characterization of soft tissue by estimating elastic properties. However, previous probe designs have been limited to surface applications. We propose a bevel tip OCE needle probe for percutaneous insertions, where biomechanical characterization of deep tissue could enable precise needle placement, e.g., in prostate biopsy. We consider a dual-fiber OCE needle probe that provides estimates of local strain and load at the tip. Using a novel setup, we simulate deep tissue indentations where frictional forces and bulk sample displacement can affect biomechanical characterization. Performing surface and deep tissue indentation experiments, we compare our approach with external force and needle position measurements at the needle shaft. We consider two tissue mimicking materials simulating healthy and cancerous tissue and demonstrate that our probe can be inserted into deep tissue layers. Compared to surface indentations, external force-position measurements are strongly affected by frictional forces and bulk displacement and show a relative error of 49.2% and 42.4% for soft and stiff phantoms, respectively. In contrast, quantitative OCE measurements show a reduced relative error of 26.4% and 4.9% for deep indentations of soft and stiff phantoms, respectively. Finally, we demonstrate that the OCE measurements can be used to effectively discriminate the tissue mimicking phantoms.

Keywords: Optical Coherence Tomography · Tissue Elasticity · Prostate Biopsy

1 Introduction

Healthy and cancerous soft tissue display different elastic properties, e.g. for breast [19], colorectal [7] and prostate cancer [4]. Different imaging modalities

Supplementary Information The online version contains supplementary material available at https://doi.org/10.1007/978-3-031-43996-4_58.

H. Greenspan et al. (Eds.): MICCAI 2023, LNCS 14228, pp. 607–617, 2023.
https://doi.org/10.1007/978-3-031-43996-4_58

can be used to detect the biomechanical response to an external load for the characterization of cancerous tissue, e.g., ultrasound, magnetic resonance and optical coherence elastography (OCE). The latter is based on optical coherence tomography (OCT), which provides excellent visualization of microstructures and superior spatial and temporal resolution in comparison to ultrasound or magnetic resonance elastography [8]. One common approach for quantitative OCE is to determine the elastic properties from the deformation of the sample and the magnitude of a quasi-static, compressive load [10]. However, due to the attenuation and scattering of the near-infrared light, imaging depth is generally limited to approximately 1 mm in soft tissue. Therefore, OCE is well suited for sampling surface tissue and commonly involves bench-top imaging systems [26], e.g. in ophthalmology [21,22] or as an alternative to histopathological slice examination [1,16]. Handheld OCE systems for intraoperative assessment [2,23] have also been proposed. While conventional OCE probes have been demonstrated at the surface, regions of interest often lie deep within the soft tissue, e.g., cancerous tissue in percutaneous biopsy.

Taking prostate cancer as an example, biomechanical characterization could guide needle placement for improved cancer detection rates while reducing complications associated with increased core counts, e.g. pain and erectile dysfunction [14,18]. However, the measurement of both the applied load and the local sample compression is challenging. Friction forces superimpose with tip forces as the needle passes through tissue, e.g., the perineum. Furthermore, the prostate is known to display large bulk displacement caused by patient movement and needle insertions [20,24] in addition to actual sample compression (Fig. 1, left). Tip force sensing for estimating elastic properties has been proposed [5] but bulk tissue displacement of deep tissue was not considered. In principle, compression and tip force could be estimated by OCT. Yet, conventional OCE probes typically feature flat tip geometry [13,17].

To perform OCE in deep tissue structures, we propose a novel bevel tip OCE needle design for the biomechanical characterization during needle insertions. We consider a dual-fiber setup with temporal multiplexing for the combined load and compression sensing at the needle tip. We design an experimental setup that can simulate friction forces and bulk displacement occurring during needle biopsy (Fig. 1). We consider tissue-mimicking phantoms for surface and deep tissue indentation experiments and compare our results with force-position curves externally measured at the needle shaft. Finally, we consider how the obtained elasticity estimates can be used for the classification of both materials.

2 Methods

In the following, we first present our OCE needle probe and outline data processing for elasticity estimates. We then present an experimental setup for simulating friction and bulk displacement and describe the conducted surface and deep tissue indentation experiments.

2.1 OCE Needle for Deep Tissue Indentation

Our OCE needle approach is illustrated in Fig. 2. It consists of an OCT imaging system, a time-division multiplexer and our OCE needle probe. The needle features two single-mode glass fibers (SMF-28, Thorlabs GmbH, GER) embedded into a bevel tip needle. The forward viewing fiber (Fiber 1) images sample compression while the load sensing fiber (Fiber 2) visualizes the displacement of a reference epoxy layer that is deformed under load. We cleave the distal ends of both fibers to enable common path interference imaging. The outer diameter of the OCE needle prototype is 2.0 mm. We use a spectral domain OCT imaging system (Telesto I, Thorlabs GmbH, GER) with a center wavelength λ_0 of 1325 nm to acquire axial scans (A-scans) at a sampling rate of 91.3 kHz. A solid state optical switch (NSSW 1x2 NanoSpeed^{TM}, Agiltron, USA), a 100 kHz switch driver (SWDR DC-100KHz NS Driver, Agiltron, USA) and a microcontroller (Arduino^{TM} Mega 2560, Arduino, USA) alternate between the two fibers every second A-scan. Compared to spatial multiplexing [17], our temporal multiplexing maximizes the field-of-view and signal strength while effectively halving the acquisition frequency.

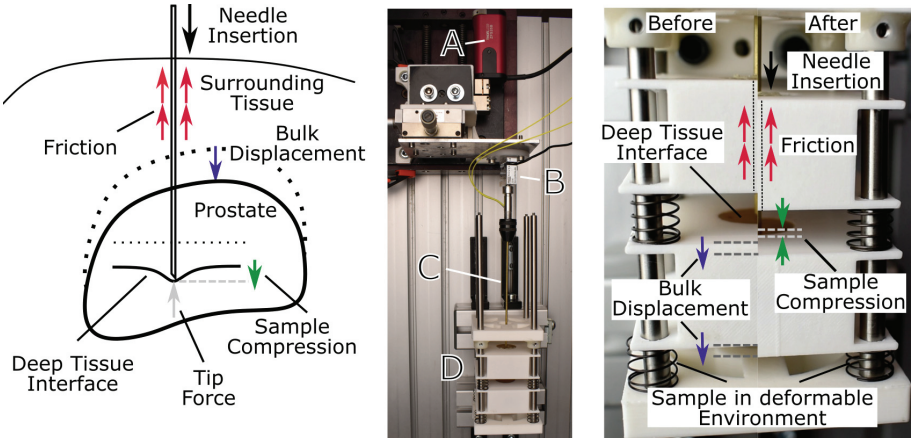

Fig. 1. Left: Schematic of deep tissue indentation during needle insertion. Friction forces (red) and tip forces (grey) are superimposed and the forward motion of the needle (black) only partially results in sample compression (green) due to bulk displacement (blue). Middle: Experimental setup used for indentation experiments, with a linear actuator (A), an axial force sensor (B), the OCE needle probe (C) and the sample layers (D). Right: Simulated deep tissue indentation before and after needle motion. Friction can be added by puncturing multiple layers and bulk displacement is simulated by placing the sample on springs. (Color figure online)

2.2 OCE Measurement

In unconfined compression, the elasticity of the sample can be determined by the relation between stress σ and bulk strain ϵ denoted by the Young's modulus

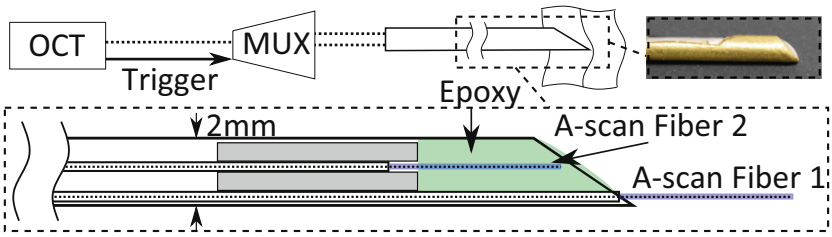

Fig. 2. Illustration of our OCE needle probe for deep tissue indentation. Axial scans (blue) are alternately recorded from fiber 1 and 2 with the OCT and multiplexer (MUX) setup. We use optical fiber 1 to measure sample compression and fiber 2 for the displacement of a reference epoxy layer (green) that is deformed under tip forces. (Color figure online)

$$E = \frac{\sigma}{\epsilon} = \frac{F/A}{\Delta L/L_0}, \tag{1}$$

with the force F, the area A, initial sample length L_0 and assuming incompressibility, quasi-static loading and neglecting viscoelasticity. However, the indentation with our bevel tipped needle will not result in uniform stress and we hypothesize instead that the elasticity is only relative to the applied tip force F_T and the resulting local strain ϵ_l. To obtain a single parameter for comparing two measurements, we assume a linear relation

$$E_{OCE}(F_T, \epsilon_l) \approx \frac{F_T}{\epsilon_l} \tag{2}$$

in the context of this work. To detect strain (Fiber 1) and applied force (Fiber 2), we consider the phase ϕ of the complex OCT signals for fiber i at time t and depth z. The phase shift between two A-scans is proportional to the depth dependent displacement $\delta u_i(z,t)$

$$\delta\phi_i(z,t) = \frac{4\,\pi\,n\,\delta u_i(z,t)}{\lambda_0}, \tag{3}$$

assuming a refractive index n of 1.45 and 1.5 for tissue (Fiber 1) and epoxy (Fiber 2), respectively. We obtain the deformation $u_i(z,t)$ from the unwrapped phase and perform spatial averaging to reduce noise. For fiber 1, we employ a moving average with a window size of 0.1 mm. We estimate local strain based on the finite difference along the spatial dimension over an axial depth Δz of 1 mm.

$$\epsilon_l(t) = \frac{u_1(z_0 + \Delta z, t) - u_1(z_0, t)}{\Delta z} \tag{4}$$

For fiber 2, we calculate the mean $\bar{u}_2(t)$ over the entire depth of the epoxy. We assume a linear coefficient a_F to model the relation between the applied tip force F_T and the mean deformation $\bar{u}_2$ of the reference epoxy layer.

$$F_T(t) = a_F * \bar{u}_2(t). \tag{5}$$

2.3 Experimental Setup

We build an experimental setup for surface and deep tissue indentations with simulated force and bulk displacement (Fig. 1). For deep tissue indentations, different tissue phantoms are stacked on a sample holder with springs in between. For surface measurements, we position the tissue phantoms separately without additional springs or tissue around the needle shaft. We use a motorized linear stage (ZFS25B, Thorlabs GmbH, GER) to drive the needle while simultaneously logging motor positions. An external force sensor (KD24s 20N, ME-Meßsysteme GmbH, GER) measures combined axial forces. We consider two gelatin gels as tissue mimicking materials for healthy and cancerous tissue. The two materials (Mat. A and Mat. B) display a Young's modulus of 53.4 kPa and 112.3 kPa, respectively. Reference elasticity is determined by unconfined compression experiments of three cylindrical samples for each material according to Eq. 1, using force and position sensor data (See supplementary material). The Young's modulus is obtained by linear regression for the combined measurements of each material. We calibrate tip force estimation (Fiber 2) by indentation of silicone samples with higher tear resistance to ensure that no partial rupture has taken place. We

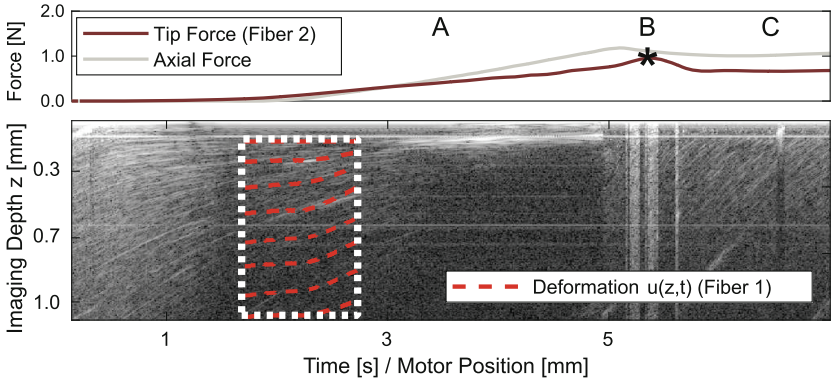

Fig. 3. Demonstration of the dual-fiber needle in insertion with puncture event (B) and post-rupture cutting phase (C). The needle is inserted with a velocity of 1 mm s^{-1}. Visualization of the magnitude of the complex OCT signal from fiber 1 (bottom) displayed over needle motion/time. Estimated tip forces from fiber 2 and axial forces are displayed at the top. Acquisition window during pre-deformation phase (A) considered for OCE measurements is indicated by dashed white line. Local strain is calculated based on the tracked deformation from the OCT phase difference as visualized in red.

then determine a linear fit according to Eq. 5 and obtain $a_F = 174.4\,\mathrm{mN\,mm^{-1}}$ from external force sensor and motor position measurements (See supplementary material).

2.4 Indentation Experiments

In total, we conduct ten OCE indentation measurements for each material. Three surface measurements with fixed samples and seven deep tissue indentations with simulated friction and bulk displacement. For each indentation, we place the needle in front of the surface or deep tissue interface and acquire OCT data while driving the needle for 3 mm (Fig. 1). As the beginning of the needle movement might not directly correspond to the beginning of sample indentation, we evaluate OCE measurements only if the estimated tip force is larger than 50 mN. To further ensure that measurements occur within the pre-rupture deformation phase [6,15], only samples below 20 % local strain are considered. A visualization of the OCE acquisition window from an example insertion with surface rupture and post-rupture cutting phase [6,15] is shown in Fig. 3. We evaluate external needle shaft measurements of relative axial force and relative motor position with the same endpoint obtained from local strain estimates. We perform linear regression to determine the slopes $E_{OCE}[\mathrm{mN\,\%^{-1}}]$ and $E_{EXT}[\mathrm{mN\,mm\%^{-1}}]$ from tip-force-strain and axial-force-position curves, respectively. As we can consider surface measurements as equivalents to the known elasticity, we regard the relative error (RE) of the mean value obtained for deep indentations, with respect to the average estimate during surface indentations. We report the RE

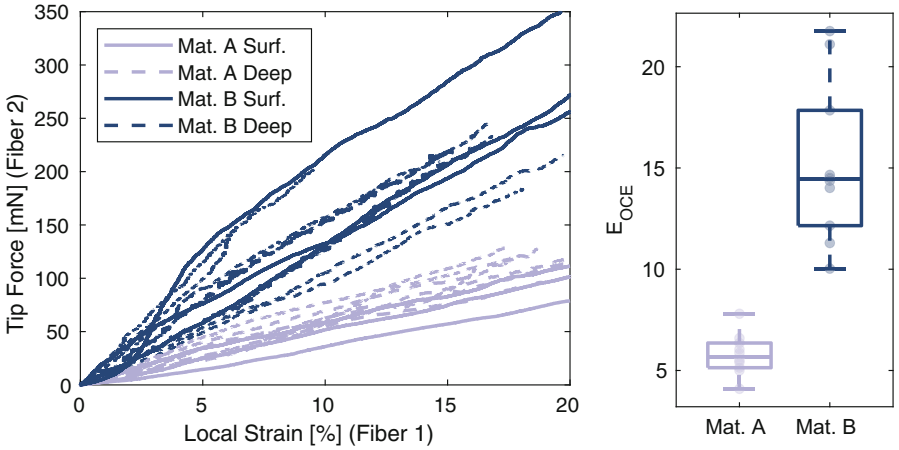

(a) Indentation Curves (b) Elasticity Estimates

Fig. 4. (a) OCE needle measurements for surface and deep tissue indentations based on the estimated tip force (fiber 2) and the detected local strain (fiber 1). (b) Resulting OCE elasticity estimates show good separation between the two materials, enabling quantitative biomechanical characterization during deep tissue indentations.

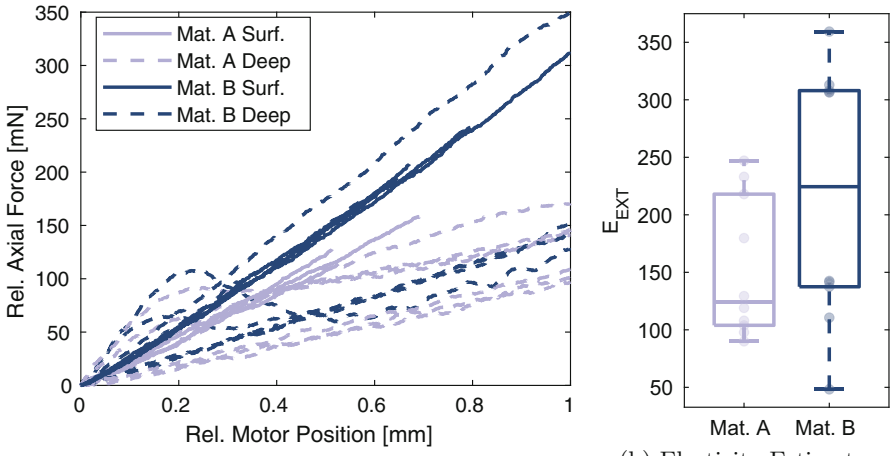

(a) Indentation Curves (b) Elasticity Estimates

Fig. 5. (a) Axial force-position-curves for surface and deep tissue indentations from external force sensor and motor encoder. Friction increases the measured axial force, while bulk displacement decreases the observed slope. Bulk displacement can occur suddenly due to stick-slip, as seen in two cases of material B. (b) Resulting elasticity estimates show overlap between the two materials, hampering quantitative biomechanical characterization.

for both OCE and external measurements and material A and B, respectively. Finally, we consider the measured elasticities for the biomechanical classification of the material. We report the area under the receiver operating characteristic (AUROC) and area under the precision recall curve (AUPRC) for both external and OCE sensing.

3 Results

The OCE measurements for surface and deep tissue indentations are displayed in Fig. 4a. In comparison, external force-position curves are shown in Fig. 5a. The resulting estimates E_{OCE} and E_{EXT} are shown in Fig. 4b and Fig. 5b, respectively. It can be seen that OCE measurements result in separation of both materials while an overlap is visible for external sensors. The sample elasticities and relative error are also accumulated in Table 1. Biomechanical characterization based on the OCE estimates allows complete separation between materials, with AUROC and AUPRC scores of 1.00 (See supplementary material). External measurements do not enable robust discrimination of materials and yielded AUROC and AUPRC scores of only 0.85 and 0.861, respectively.

4 Discussion and Conclusion

We demonstrate our approach on two tissue mimicking materials that have similar elastic properties as healthy and cancerous prostate tissue [5,11]. The con-

Table 1. Measured elasticity E_{OCE} and external sensors E_{EXT} for both materials with sample size n. We also report the relative error (RE) between the mean values obtained from surface and deep tissue indentations.

		E_{OCE} [mN %$^{-1}$]			E_{EXT} [mN mm^{-1}]			n
		Mean	Min	Max	Mean	Min	Max	
Mat. A	Surf	4.87 ± 0.72	4.04	5.42	232.7 ± 14.6	217.97	247.08	3
	Deep	6.18 ± 0.87	5.05	7.80	118.26 ± 3.01	89.99	179.75	7
	RE	26.4 %			49.2 %			
Mat. B	Surf	14.92 ± 3.28	12.10	18.53	361.02 ± 6.94	353.37	366.92	3
	Deep	15.39 ± 4.48	10.02	21.75	201.31 ± 89.04	136.56	354.60	7
	RE	4.9 %			42.4 %			

ducted indentation experiments demonstrate the feasibility of OCE elasticity estimates for deep tissue needle insertions. OCE estimates show better agreement between surface and deep tissue indentations compared to external measurements, as displayed by reduced relative errors of 26.4% and 4.9% for both phantoms, respectively. Bulk displacement causes considerate underestimation of elasticity estimates when only needle position and axial forces are considered, shown by relative errors of 49.2% and 42.4% for material A and B, respectively. Additionally, quantitative OCE estimates allow the robust discrimination between the two materials as shown by Fig. 4b and the AUROC and AUPRC scores of 1. Note that the high errors for external measurements at the needle shaft are systematic, as friction and bulk displacement are unknown. In contrast, our probe does not suffer from these systematic errors. Moreover, considering the standard deviation for OCE estimates, improved calibration of our dual-fiber needle probe is expected to further improve performance. Deep learning-based approaches for tip force estimation could provide increased accuracy and sensitivity compared to the assumed linear model [3]. Weighted strain estimation based on OCT signal intensity [26] could address the underestimation of local strain during segments of low signal-to-noise-ratio (See supplementary material). We are also currently only considering the loading cycle and linear elastic models for our approach. However, soft-tissue displays strong non-linearity in contrast to the mostly linear behavior of gelatin gels. Compression OCE theoretically enables the analysis of non-linear elastic behavior [26] and future experiments will consider non-linear models and unloading cycles better befitting needle-tissue-interaction [15,25].

Interestingly, our needle works with a beveled tip geometry that allows insertion into deep tissue structures. During insertion, tip force estimation can be used to detect interfaces and select the pre-rupture deformation phase for OCE estimates (Fig. 3). This was previously not possible with flat tip needle probes [9,13,17]. While the cylindrical tip is advantageous for calculating the

Young's modulus, it has been shown that the calculation of an equivalent Young's modulus is rarely comparable across different techniques and samples [4,12]. Instead, it is important to provide high contrast and high reproducibility to reliably distinguish samples with different elastic properties. We show that our dual-fiber OCE needle probe enables biomechanical characterization by deriving quantitative biomechanical parameters as demonstrated on tissue mimicking phantoms. Further experiments need to include biological soft tissue to validate the approach for clinical application, as our evaluation is currently limited to homogeneous gelatin. This needle probe could also be very useful when considering robotic needle insertions, e.g., to implement feedback control based on elasticity estimates.

Acknowledgements. This work was partially funded by Deutsche Forschungsgemeinschaft under Grant SCHL 1844/6-1, the i^3 initiative of Hamburg University of Technology, and the Interdisciplinary Competence Center for Interface Research (ICCIR) on behalf of the University Medical Center Hamburg-Eppendorf and the Hamburg University of Technology.

References

1. Allen, W.M., et al.: Wide-field quantitative micro-elastography of human breast tissue. Biomed. Opt. Express **9**(3), 1082–1096 (2018). https://doi.org/10.1364/BOE.9.001082
2. Fang, Q., et al.: Handheld probe for quantitative micro-elastography. Biomed. Opt. Express **10**(8), 4034–4049 (2019). https://doi.org/10.1364/BOE.10.004034
3. Gessert, N., et al.: Needle tip force estimation using an OCT fiber and a fused convGRU-CNN architecture. In: Frangi, A.F., Schnabel, J.A., Davatzikos, C., Alberola-López, C., Fichtinger, G. (eds.) MICCAI 2018. LNCS, vol. 11073, pp. 222–229. Springer, Cham (2018). https://doi.org/10.1007/978-3-030-00937-3_26
4. Good, D.W., et al.: Elasticity as a biomarker for prostate cancer: a systematic review. BJU Int. **113**(4), 523–534 (2014). https://doi.org/10.1111/bju.12236
5. Iele, A., et al.: Miniaturized optical fiber probe for prostate cancer screening. Biomed. Opt. Express **12**(9), 5691–5703 (2021). https://doi.org/10.1364/BOE.430408
6. Jiang, S., Li, P., Yu, Y., Liu, J., Yang, Z.: Experimental study of needle-tissue interaction forces: effect of needle geometries, insertion methods and tissue characteristics. J. Biomech. **47**(13), 3344–3353 (2014). https://doi.org/10.1016/j.jbiomech.2014.08.007
7. Kawano, S., et al.: Assessment of elasticity of colorectal cancer tissue, clinical utility, pathological and phenotypical relevance. Cancer Sci. **106**(9), 1232–1239 (2015). https://doi.org/10.1111/cas.12720
8. Kennedy, B.F., Kennedy, K.M., Sampson, D.D.: A review of optical coherence elastography: fundamentals, techniques and prospects (2014). https://doi.org/10.1109/JSTQE.2013.2291445
9. Kennedy, K.M., et al.: Needle optical coherence elastography for the measurement of microscale mechanical contrast deep within human breast tissues. J. Biomed. Opt. **18**(12), 121510 (2013). https://doi.org/10.1117/1.JBO.18.12.121510

10. Kennedy, K.M., et al.: Quantitative micro-elastography: imaging of tissue elasticity using compression optical coherence elastography. Sci. Rep. **5**(Apr), 1–12 (2015). https://doi.org/10.1038/srep15538
11. Krouskop, T.A., Wheeler, T.M., Kallel, F., Garra, B.S., Hall, T.: Elastic moduli of breast and prostate tissues under compression. Ultrason. Imaging **20**(4), 260–274 (1998). https://doi.org/10.1177/016173469802000403
12. McKee, C.T., Last, J.A., Russell, P., Murphy, C.J.: Indentation versus tensile measurements of young's modulus for soft biological tissues. Tissue Eng. Part B Rev. **17**(3), 155–164 (2011). https://doi.org/10.1089/ten.TEB.2010.0520
13. Mieling, R., Sprenger, J., Latus, S., Bargsten, L., Schlaefer, A.: A novel optical needle probe for deep learning-based tissue elasticity characterization. Curr. Dir. Biomed. Eng. **7**(1), 21–25 (2021). https://doi.org/10.1515/cdbme-2021-1005
14. Oderda, M., et al.: Accuracy of elastic fusion biopsy in daily practice: results of a multicenter study of 2115 patients. Int. J. Urol. **25**(12), 990–997 (2018). https://doi.org/10.1111/IJU.13796
15. Okamura, A.M., Simone, C., O'Leary, M.D.: Force modeling for needle insertion into soft tissue. IEEE Trans. Biomed. Eng. **51**(10), 1707–1716 (2004). https://doi.org/10.1109/TBME.2004.831542
16. Plekhanov, A.A., et al.: Histological validation of in vivo assessment of cancer tissue inhomogeneity and automated morphological segmentation enabled by optical coherence elastography. Sci. Rep. **10**(1), 11781 (2020). https://doi.org/10.1038/s41598-020-68631-w
17. Qiu, Y., et al.: Quantitative optical coherence elastography based on fiber-optic probe for in situ measurement of tissue mechanical properties. Biomed. Opt. Express **7**(2), 688 (2016). https://doi.org/10.1364/boe.7.000688
18. Rosenkrantz, A.B., et al.: Prostate magnetic resonance imaging and magnetic resonance imaging targeted biopsy in patients with a prior negative biopsy: a consensus statement by AUA and SAR. J. Urol. **196**(6), 1613–1618 (2016). https://doi.org/10.1016/j.juro.2016.06.079
19. Samani, A., Zubovits, J., Plewes, D.: Elastic moduli of normal and pathological human breast tissues: an inversion-technique-based investigation of 169 samples. Phys. Med. Biol. **52**(6), 1565 (2007)
20. Schouten, M.G., et al.: Evaluation of a robotic technique for transrectal MRI-guided prostate biopsies. Eur. Radiol. **22**(2), 476–483 (2012). https://doi.org/10.1007/s00330-011-2259-3
21. Singh, M., Nair, A., Aglyamov, S.R., Larin, K.V.: Compressional optical coherence elastography of the cornea. Photonics **8**(4), 111 (2021). https://doi.org/10.3390/photonics8040111
22. de Stefano, V.S., Ford, M.R., Seven, I., Dupps, W.J.: Live human assessment of depth-dependent corneal displacements with swept-source optical coherence elastography. PLoS ONE **13**(12), e0209480 (2018). https://doi.org/10.1371/journal.pone.0209480
23. Wang, X., Wu, Q., Chen, J., Mo, J.: Development of a handheld compression optical coherence elastography probe with a disposable stress sensor. Opt. Lett. **46**(15), 3669 (2021). https://doi.org/10.1364/ol.429955
24. Xu, H., et al.: MRI-guided robotic prostate biopsy: a clinical accuracy validation. In: Jiang, T., Navab, N., Pluim, J.P.W., Viergever, M.A. (eds.) MICCAI 2010. LNCS, vol. 6363, pp. 383–391. Springer, Heidelberg (2010). https://doi.org/10.1007/978-3-642-15711-0_48

25. Yang, C., Xie, Y., Liu, S., Sun, D.: Force modeling, identification, and feedback control of robot-assisted needle insertion: a survey of the literature. Sensors **18**(2) (2018). https://doi.org/10.3390/S18020561
26. Zaitsev, V.Y., et al.: Strain and elasticity imaging in compression optical coherence elastography: the two-decade perspective and recent advances (2021). https://doi.org/10.1002/jbio.202000257

7.4 Optical force estimation for interactions between tool and soft tissues

Journal: Scientific Reports

Published: 10.01.2023

M. Neidhardt, R. Mieling, M. Bengs, and A. Schlaefer, “Optical force estimation for interactions between tool and soft tissues,” *Scientific Reports*, vol. 13, no. 1, p. 506, 2023

scientific reports

Check for updates

OPEN

Optical force estimation for interactions between tool and soft tissues

Maximilian Neidhardt[1,2], Robin Mieling[1,2]✉, Marcel Bengs[1] & Alexander Schlaefer[1]

Robotic assistance in minimally invasive surgery offers numerous advantages for both patient and surgeon. However, the lack of force feedback in robotic surgery is a major limitation, and accurately estimating tool-tissue interaction forces remains a challenge. Image-based force estimation offers a promising solution without the need to integrate sensors into surgical tools. In this indirect approach, interaction forces are derived from the observed deformation, with learning-based methods improving accuracy and real-time capability. However, the relationship between deformation and force is determined by the stiffness of the tissue. Consequently, both deformation and local tissue properties must be observed for an approach applicable to heterogeneous tissue. In this work, we use optical coherence tomography, which can combine the detection of tissue deformation with shear wave elastography in a single modality. We present a multi-input deep learning network for processing of local elasticity estimates and volumetric image data. Our results demonstrate that accounting for elastic properties is critical for accurate image-based force estimation across different tissue types and properties. Joint processing of local elasticity information yields the best performance throughout our phantom study. Furthermore, we test our approach on soft tissue samples that were not present during training and show that generalization to other tissue properties is possible.

Robotic-assisted surgery (RAS) systems such as DaVinci or Senhance are becoming more available in surgical practice[1] and even less complex medical procedures are performed by RAS, e.g., cholecystectomy and hernia repair[2]. RAS offers a better outcome for the patient by reducing trauma through a minimally invasive approach and results in shorter recovery time[3]. For the surgeon ergonomics are improved during an intervention[4]. However, these benefits come at the expense of the natural haptic perception that surgeons rely on when palpating tissue in open surgery. In RAS, force feedback is associated with shorter operating times, fewer errors during surgery and a reduced mental workload[5]. Force feedback is particularly important for complex procedures and can increase the learning curve for trainees when it is available[6,7]. Force estimates can also be used to implement safety features that limit forces and prevent soft tissue damage[8]. The lack of real-time force feedback remains a challenge and limits clinical systems in practice[9–12]. Feedback on tool-tissue interaction forces will also be essential for greater autonomy and intraoperative tissue assessment in robotic surgery[13].

Intuitively, the integration of force sensors into surgical tools, e.g., Bragg sensors, strain gauges and piezoelectric sensors, has been considered and is commonly referred to as the direct approach[14,15]. Direct approaches offer high accuracy but also have major drawbacks—most notably cost and sensor sterilizability. These limitations have kept direct approaches from widespread clinical application, although research has been ongoing for over 20 years[16]. Alternatively, indirect approaches aim to separate force sensing from the surgical tool, e.g., by considering force models and actuator inputs[17,18]. Recently, indirect methods for image-based force estimation have attracted more attention[15], especially machine learning-based approaches. Image-based force estimation aims to derive the tool-tissue interaction forces based on the observed deformation of the soft tissue. However, the relationship between load and deformation is tissue dependent and exclusively observing tissue deformation is generally not sufficient (see Fig. 1a). Previous approaches assumed a predefined material model for each organ but soft tissue properties are highly dependent on the patient and mechanical properties change locally due to pathological conditions[19,20], limiting these approaches in practice. Therefore, the question arises of how to adequately account for tissue elasticity in image-based force estimation.

Initial approaches for image-based force estimation used an explicitly defined biomechanical model. Miller et al. proposed a hyper-viscoelastic constitutive model to estimate soft tissue properties for brain tissue[21]. The

[1]Institute of Medical Technology and Intelligent Systems, Hamburg University of Technology, Am Schwarzenberg-Campus 3, Hamburg 21073, Germany. [2]These authors contributed equally: Maximilian Neidhardt and Robin Mieling. ✉email: Robin.Mieling@tuhh.de

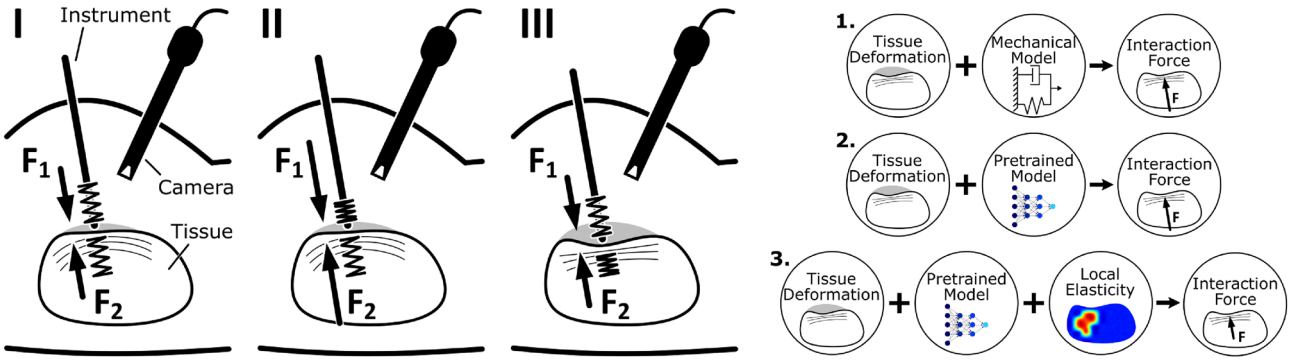

(a) Tissue Dependent Interaction Forces **(b)** Image-based Force Estimation

Figure 1. Image-based Force Estimation: **(a)** Abstract illustration of the fundamental problem underlying force estimation without integrated sensors. The springs indicate elastic properties and the camera observes tissue deformations. (I) During tool-tissue interaction, the applied force F_1 will deform the tissue and the opposing reaction force F_2 will be equal in magnitude. However, the same deformation can be related to greater forces for stiffer tissue (II) or the same force may result in larger deformations for softer tissue (III). Therefore, observing only the deformation will generally not allow estimating the interaction forces if the tissue elasticity is unknown. **(b)** Previous approaches have not considered changes in elastic properties and relied on predefined biomechanical models (1.) or pretrained neural networks (2.) to derive interaction forces from the observed deformation. We instead propose an image-based force estimation model that additionally considers local tissue properties via elastography (3.) and that does not require the material to be known in advance.

model was tuned by performing in-vivo indentation experiments. Subsequently, forces on similar brain tissue could be estimated by tracking the position of a tool relative to the tissue. This approach was further adapted by using optical cameras to track the surface of the tissue and then mapping depth values to force estimations. Typically, deformable template matching methods were used to match the measured surface profile to an assumed biomechanical model[22,23] Instead of a biomechanical model, the relationship between load and deformation is implicitly learned for deep learning approaches and the trained model is highly dependent on the provided training data. Deep learning approaches with RGB-D images as input have been demonstrated for individual materials with recurrent neural networks[24,25] and convolutional neural networks (CNN)[26]. However, the generalization of deep learning models to other material properties has not been investigated extensively. Without the ability to generalize to new samples, training data for all relevant tissue types and pathological stages need to be acquired. Moreover, even with accurate models for different tissues, local changes in material properties demand a more versatile solution that doesn't depend on the manual selection of models[27].

We therefore propose to employ optical coherence tomography (OCT) and shear wave optical coherence elastography (OCE) to directly consider tissue properties for image-based force estimation (see Fig. 1b). OCT offers volumetric imaging with high spatial and temporal resolution, enabling elastography and visualization of tissue deformations in a single modality. OCT has been considered for accurate image-based force estimation with single volumes[28] and 4D temporal sequences as input[29]. Promising results with OCT based force estimation were also demonstrated on xenograft mouse models with vascularized prostate tumors[30]. Additionally, OCE is ideal for local elasticity estimates due to the small field of view (FOV) and its high spatial and temporal resolution. Multiple methods for quantitative OCE with different loading mechanisms have been proposed. Miniaturized compression based OCE can provide estimates at a high spatial resolution but requires complex and sensitive sensors at the tool tip[31,32]. Instead, we implement shear wave elastography imaging (SWEI), where a shear wave is excited on the tissue surface, e.g., by a piezoelectric element[33] or an air-pulse[34], and the high frequency imaging can be used to track the propagating wave. The elasticity of the tissue is directly related to the velocity of the shear wave which can be estimated by detecting the dominant local wavenumber in the frequency domain[35–37]. We combine OCT and OCE, jointly perform data processing with a multi-input deep learning network and estimate tool-tissue interaction forces. We additionally derive surface deformation data from our OCT volumes to demonstrate the advantage of our approach in a case where only surface deformation data is available. Note that our system does not rely on knowing the biomechanical properties of the soft tissue in advance, as suggested in the literature[21–23].

The main contributions of this work are: (1) Demonstrating the impact of tissue elasticity on image-based force estimation by evaluating deep learning models on elasticities that are not considered during training. (2) Showing that neural networks are able to generalize to unknown materials and demonstrating the advantage of our system that incorporates local elasticity estimates. (3) Combining the findings into a single setup that provides force estimation even when the application is shifted from phantoms to ex-vivo soft tissue samples.

Methods

In the following, we present our experimental setup with a robot for data acquisition on phantoms with varying elasticity as well as ex-vivo soft tissue and define our deep learning approach.

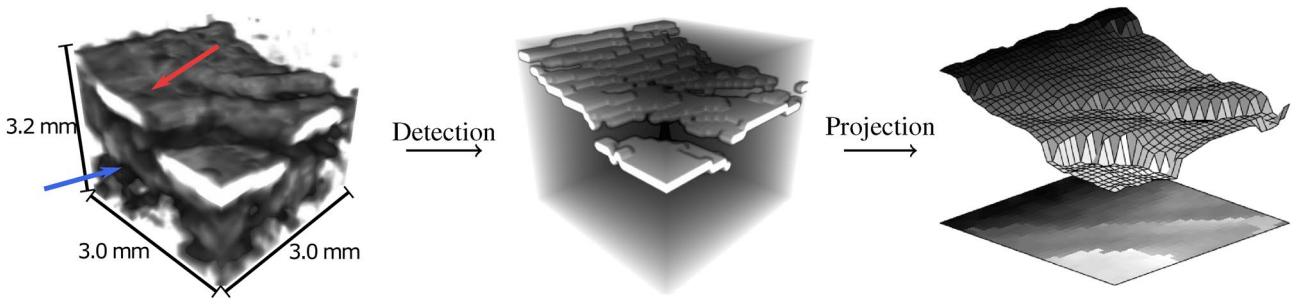

(a) OCT Volume V_t **(b)** Surface Data **(c)** Deformation Map D_t

Figure 2. Data Representation: Visualization of the two data representations considered during our learning tasks. **(a)** The volumetric OCT scan V_t contains the surface data (red arrow) and the depth information (blue arrow). **(b)** We detect the sample surface data in the OCT volume. **(c)** We project the surface data onto our 2D deformation map D_t. During training, the influence of depth information is analyzed by comparing volumetric data (left) and surface projection data (right).

Problem definition and data representations. We consider image-based force estimation for tool-tissue interactions with regard to tissue elasticity. We estimate the axial force $F_t \in \mathbb{R}$ at a time step t based on spatio-temporal OCT volume data $V_t \in \mathbb{R}^{hxwxd}$. V_t visualizes the deformations caused by tool-tissue interaction in comparison to a reference volume V_{ref}. For the observed location L on a given sample S, the relation between the applied force and the resulting deformation depends on the sample elasticity $E_{S,L} \in \mathbb{R}^{hxwxd}$. Prior to the force application, we acquire a sequence of OCT cross-section images $I_\tau \in \mathbb{R}^{hxw}$ at time step τ with simultaneous shear wave excitation. We approximate the elasticity at location L via the shear wave phase velocity $v_{S,L} \in \mathbb{R}$. We further consider an alternative input representation by a projection $P : \mathbb{R}^{hxwxd} \rightarrow \mathbb{R}^{wxd}$ which maps the sample's surface in V_t to a deformation map D_t. A visualization of the data representations are given in Fig. 2. Our multi-input learning problems are $V_t, V_{ref}, v_{S,L} \rightarrow F_t$ and $D_t, D_{ref}, v_{S,L} \rightarrow F_t$, respectively. We initially regard tissue mimicking gelatin phantoms with seven different elasticities G_i. Afterwards, we evaluate our methods on chicken heart soft tissue unseen during training.

Experimental setup. For data acquisition we present an experimental setup depicted in Fig. 3a. We employ a high-speed swept-source OCT system (OMES, Optores, Germany) with an axial scan rate of 1.5 MHz, a central wavelength of 1315 nm and an axial resolution of 15 μm in air. A scan head deflects the OCT beam to acquire $2D + T$ SWEI data ($h \times w \times t$) with a spatial resolution of 476×32 pixels (3.5×3 mm) along the depth h and lateral axis w and a temporal resolution of 14.2 kHz. The same scan head is also used for high-speed volumetric data acquisition ($h \times w \times d$) with a spatial resolution of 476×32×32 pixels (3.5×3×3 mm) and a temporal resolution of 833 Hz. An optical lens system with a focal length of 300 mm is positioned between scan head and tissue. A hexapod robot (H-820.D1, Physik Instrumente, Germany) positions the sample for data acquisition at multiple locations. The robot allows us to move the tissue relative to the FOV of the OCT volumes. Please note, that the FOV relative to the palpation position is fixed. Before data acquisition we drive the robot along the lateral axes w and d of the volume to the desired location L. Next, we drive along the axis h of the volume until the surface of the tissue is positioned inside the OCT volume at a depth of approximately 0.5 mm. Surface detection is performed by maximum intensity detection along the depth axis. In our experimental setup design the direction of the robot's axes correspond to the volume axes. We acquire ground truth for our force data using a high resolution force sensor (Nano 43, ATI, USA) with a temporal resolution of 500 Hz.

Experimental data acquisition. We prepare seven different gelatin gels G_i with a weight ratio of gelatin to water of 5 %, 7.5 %, 10 %, 12.5 %, 15 %, 17.5 % and 20.0 %. For in-house gelatin preparation we carefully follow a recipe. Titanium dioxide is added to the heated mixture to increase OCT contrast. The phantoms as seen in Fig. 3a have a diameter of 100 mm and a cylindrical height of 10 mm. We manufacture six phantoms for each gelatin gel G_i and acquire data at 9 locations on each phantom. In addition, we record data from 10 ex-vivo chicken hearts at 2 locations. At each location we first estimate the local tissue elasticity (SWEI Data) and subsequently palpate the tissue for the acquisition of force estimation data.

SWEI data. Shear waves are excited at the surface of the tissue during high-frequency 2D OCT imaging. A piezoelectric element is driven continuously by a sinusoidal signal with a frequency of 1000 Hz for 0.8 s and a peak-to-peak voltage of 210 V. The tip of the piezo is fitted with an epoxy dome to facilitate shear wave excitation inside the tissue, as seen in Fig. 3b, top.

Force estimation data. We acquire OCT volumes for image-based force estimation with the piezo element as the palpating tool tip (see Fig. 3b, bottom). First, the tool tip is positioned on the surface of the phantom by carefully driving towards the sample until a force threshold of 0.01 N is exceeded. Second, training data is acquired while driving a sinusoidal profile. The stepper motor is actuated over three cycles with an insertion distance of

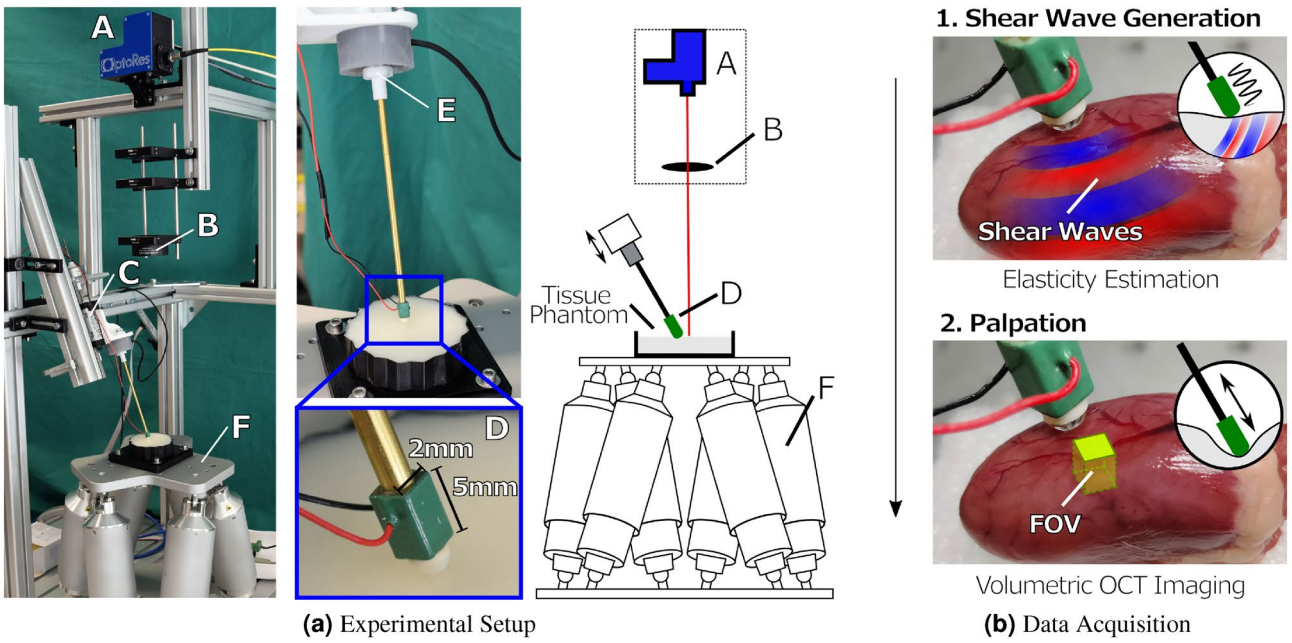

Figure 3. Experimental setup and data acquisition: **(a)** The experimental setup includes a high frequency scan head (A), a lense system (B), a stepper motor (C) which drives the palpation tool fitted with a piezoelectric element (D) along its central axis, a high resolution force sensor (E) for ground truth data annotation and a hexapod robot (F) for positioning the sample. Depicted is the setup with a gelatin phantom. **(b)** For data acquisition, we excite shear waves through vibration of the piezoelectric element (as indicated in red and blue) and OCE data is recorded. During tool-tissue interaction, we acquire volumetric image data as seen on the chicken heart.

2.5 mm and velocities ranging between 0.5mm s^{-1}–3mm s^{-1}. Additionally, we record OCT data while driving to 20 positions randomly chosen within an insertion distance of 0.5 mm–2.5 mm and a palpation velocity of 2mm s^{-1}–7mm s^{-1}. The motion represents a pushing task that is commonly performed in minimally invasive surgery[38]. The random palpation data set is used for evaluating the robustness of our methods and is excluded from training.

Pre-processing. We crop OCT volumes along the depth axis h to a length of 200 px and downsample the volumetric data $V_t \in \mathbb{R}^{hxwxd}$ to a size of 32 × 32 × 32 pixels for efficient data processing. We assign a force value to each volume by matching timestamps and interpolating the force sensor data. For the 2D deformation map representation D_t, we employ a maximum intensity projection along axis h for $\forall(w, d) \in \mathbb{R}^+$. To ensure surface detection only maximum intensity values above 50% of the mean intensity of the whole volume are utilized, holes in the deformation map are closed by 2D interpolation.

Shear wave phase velocity estimation. We crop each 2D image to a length of 32 px beneath the surface along axis h resulting in an images size $I_\tau \in \mathbb{R}^{hxw}$ of 32 × 32 pixels. We ensure shear wave propagation along the lateral image axis w. To estimate the shear wave velocity we unwrap the phase of the complex OCT data at each spatial position along the temporal axis. Next, we take the mean along the depth axis resulting in a 2D space-time representation as shown in Fig. 4, top right. Shear wave phase velocity estimation is performed in the frequency domain similar to[36,37]. First, we define 30 randomly sampled subsets with a length of 800 time steps. For each subset we evaluate the phase velocity and report the mean of all estimates. We transform the 2D space-time phase data into the k-space by using the 2D discrete FFT. We apply a high-pass filter and an angular sector filter to remove amplitude signals around 0 Hz. To further reduce background noise we apply a threshold filter which removes signals with < 10% of the overall maximum amplitude in the k-space. We determine the index i, j of the maximum amplitude in k-space and estimate the shear wave phase velocity $v_{S,L} = f_i/k_j$ with the temporal frequency f and the wavenumber k.

Deep learning architectures. We follow the approach of densely connected convolutional networks (DenseNet)[39]. 3D and 2D operations are used for volumetric inputs and surface inputs, respectively. We consider a Siamese architecture where the model is provided with a reference input in addition to each input at time step t as depicted in Fig. 4. The reference is acquired prior to sample-instrument interactions for each location and sample with $F = 0$ N. Both input and reference volume are processed within the initial Siamese stage consisting of three convolutional layers. Model parameters are shared for both inputs and the obtained feature maps are concatenated. DenseNet blocks with transition layers follow after concatenation. For 3D kernels, we employ three DenseNet-blocks of 3 layers each and a growth rate of 6. For 2D inputs, we adjust model width and depth

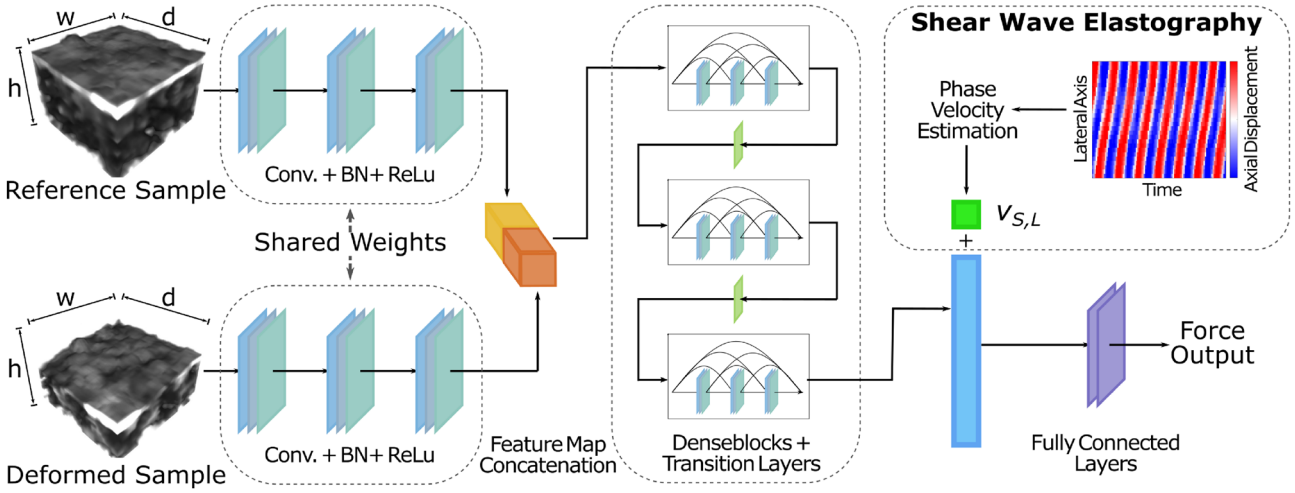

Figure 4. Data Processing: Siamese DenseNet architecture with fusion of SWEI phase velocity. The input and a reference sample are initially processed separately and the obtained feature maps are aggregated. SWEI fusion can optionally be conducted by appending the phase velocity $v_{S,L}$ after the GAP. Convolutional layers employ 3D convolutions for V_t (depicted above) and 2D convolutions for D_t. Input sizes $h \times w \times t$ are $32 \times 32 \times 32$ and $1 \times 32 \times 32$ for V_t and D_t, respectively.

to achieve a similar size regarding model parameters. We therefore add an additional DenseNet-Block with a growth rate of 8. Global average pooling layer (GAP) is followed by two successive fully connected layers with one scalar output. We employ the rectified linear activation function[40]. Batch normalization is implemented to provide regularization and to speed up training[41]. The additional SWEI information can optionally be fused into the architecture by appending the phase velocity $v_{S,L}$ to the feature vector after GAP. In the following, our multi-input models combining OCT data with the phase velocity will be denoted 2D+SWEI and 3D+SWEI for surface and volumetric inputs, respectively. Models without the fusion of SWEI information will simply be denoted 2D and 3D with respect to the selected data representation. GPU (RTX 3090, NVIDIA Corporation, USA) inference times are 3.34 ± 30 ms and 3.30 ± 37 ms for architectures with surface and volumetric inputs, respectively.

Training. Our phantom data set consists of $3.7{\times}10^5$ labeled volumes recorded during sinusoidal palpation and $4.5{\times}10^5$ samples acquired during random palpation, equally distributed across all elasticities. For soft tissue, we collect $4.1{\times}10^4$ and $4.3{\times}10^4$ samples for sinusoidal and random palpation, respectively. In general, we train our models with sinusoidal force trajectories and evaluate with random movement exclusively. We train all models using the mean squared error (MSE) as our loss function for 150 epochs with a batch size of 128. Following the one cycle learning rate policy[42], learning rates between $1{\times}10^{-4}$ and $1{\times}10^{-3}$ are used. We use the Adam algorithm with default parameters[43]. Model weights of all convolutional layers are initialized using He initialization[44].

Experiments. We perform three experiments: (1) We train our network for force estimation exclusively on a single gelatin gel G_i and illustrate the impact of elasticity by applying the model to other gelatin gels G_j with $i, j \in 1, 2, ...7$. (2) We investigate if the models can generalize to elastic properties not included in the training data ($G_i \, \forall G \in \mathbb{A} \backslash \{G_j\}$) when training data includes multiple tissue elasticities and evaluate the impact on performance when including local elasticity estimates. (3) Finally, we evaluate our models performance on unknown soft tissue palpation data when trained on gelatin phantom data with multiple elasticities. Our data splits are chosen accordingly. First, we consider the impact of elasticity by training separate models for each gelatin gel. Therefore, we split our data into 6 subsets separated by the different phantoms for each gel. We then consider generalization to new material properties by dividing our data into 7 subsets based on the different gelatin gels. In both cases, we follow a cross-validation scheme where one subset is split into a validation and a test set and the remaining subsets are used for training. Finally, we evaluate our previously trained models on the adaptation from phantom to tissue data. To increase the robustness of the final models, we consider a cross-validation ensemble using the mean as our voting method. Model performance is reported based on the test sets with mean and standard deviation. We evaluate the root mean square error (rMSE) and Pearson correlation coefficient (pCC). As the range of applied forces increases with elasticity, we additionally report the normalized mean absolute error (nMAE), defined as the mean absolute error (MAE) divided by the observed range of forces F_{G_i} for each gelatin gel i.

Force estimation for individual materials. For visualizing the impact of elasticity, models are initially trained separately for each material Fig. 5a. The shown models do not consider elastic properties via SWEI fusion and are only trained on data from a single gelatin gel. By way of example, results are only displayed for models trained with volumetric inputs. The rMSE ranges from 0.19 to 235 mN for the application on samples from the same material (diagonal of Fig. 5a). Considering the surface deformation, the maximum range of movement and

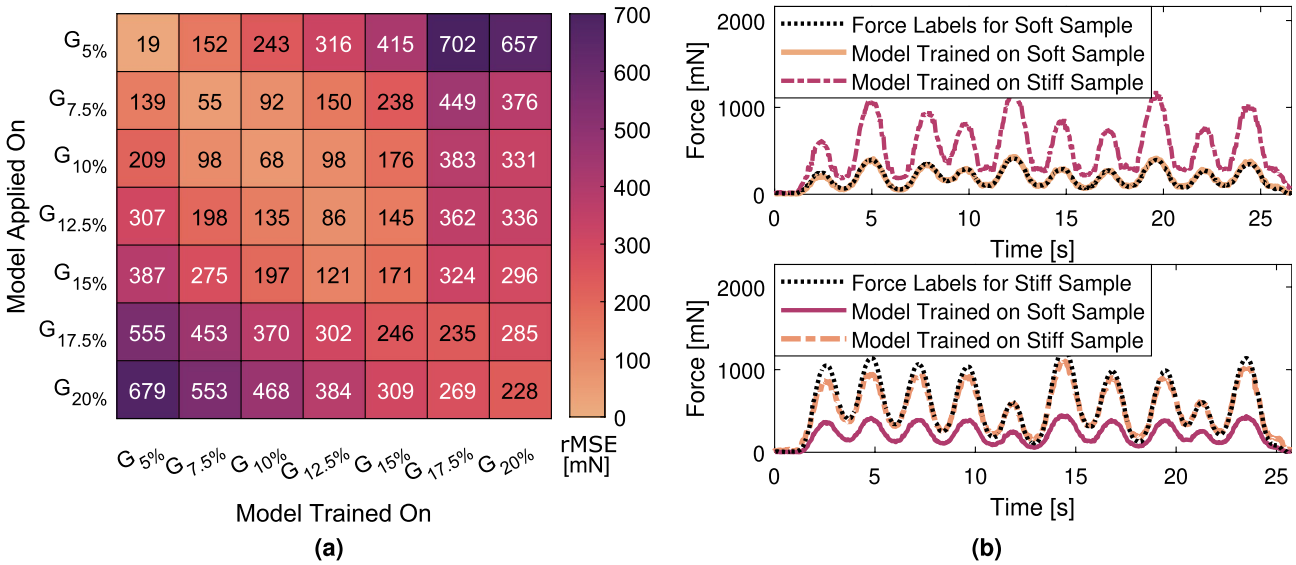

Figure 5. Force estimation: **(a)** Heatmap of the rMSE [mN] of all force estimates for individually trained models with 3D inputs V_t. The x-axis denotes the gelatin gel on which the model is trained and the y-axis the gelatin gel used for evaluation. Better performance is given if the applied gelatin gel is similar to the training data. **(b)** Examples that display the impact of elasticity on force estimates when elasticity is not considered. A model trained on "stiff" samples ($G_{17.5\%}$) applied on a "soft" material ($G_{7.5\%}$) overestimates the applied forces due to the large deformations (top). Vice versa, forces are underestimated when transferring a model to stiffer materials (bottom). Line color is based on the rMSE and the colormap in **(a).**

G_i [%]	5	7.5	10	12.5	15	17.5	20
Deformation Range [px]	5.31 ± 0.64	5.34 ± 1.00	4.94 ± 0.72	5.08 ± 1.02	5.67 ± 1.70	4.66 ± 1.38	6.01 ± 1.74
Relative Deformation [px N^{-1}]	25.80 ± 4.51	12.06 ± 2.28	8.31 ± 1.66	6.33 ± 1.43	5.78 ± 1.75	3.56 ± 1.40	3.84 ± 1.24

Table 1. Experimental Data: Range of minimal and maximum mean surface deformation in px during palpation experiments and deformation relative to the ground truth force given for all experiments performed for each gelatin concentration.

the displacements relative to the applied forces are given in Table 1 for each material. The range of the surface movements is similar for all experiments performed on gelatin phantoms with a mean of 5.28(0.45) px. The surface deformation relative to the applied force decrease for stiffer phantoms correlating with the increase in force estimation errors (pCC= −0.76). Transferring the application to other materials with different elastic properties visualizes the impact of elasticity, resulting in increased errors for the force estimation. Under- and overestimation of the forces is visible for more and less elastic samples, respectively (see e.g. in Fig. 5b). The largest differences in elasticity also correspond to the largest average errors.

Generalization of force estimation models. We report the results for models tasked to generalize to elastic properties not present in the training data. We compare the models with only 2D and 3D deformation inputs to our fusion models which additionally consider elasticity via the phase velocity information (2D+SWEI and 3D+SWEI). The velocity estimates from all locations across all samples are displayed in Fig. 6a. Overall, the method displays good differentiation between the different sample types. Within-group variation increases with increasing sample stiffness and phase velocity, especially for 15 % and 17.5 % gels. Regarding model performance, all evaluation metrics for each fold representing a new elasticity, as well as the mean across all folds in Table 2. The absolute errors for the force estimation models are also displayed in Fig. 6b. Considering models without SWEI fusion, 3D inputs clearly outperform the 2D surface data with an average rMSE of 143.7 mN and 216.7 mN, respectively. Normalized errors are also lower with 0.26 for the former and 0.20 for the latter. Introducing our SWEI fusion models results in performance increases for both 3D and 2D, reducing the cross-validation rMSE to 91.0 mN and 97.2 mN, respectively. When generalizing to unknown elastic properties we can further differentiate between inter- and extrapolation problems. Evaluating the pCC shown in Table 2, models trained with volumetric data but without SWEI information offer improved ability to interpolate between different elasticities compared to their 2D counterpart. Out-of-distribution generalization leads to considered increases in MAE, specifically for surface data inputs. Moreover, the extrapolation to $G_{5\%}$ is especially challenging, leading to the highest absolute and normalized errors for 2D and 3D models (see Table 2 and Fig. 6b). Phase

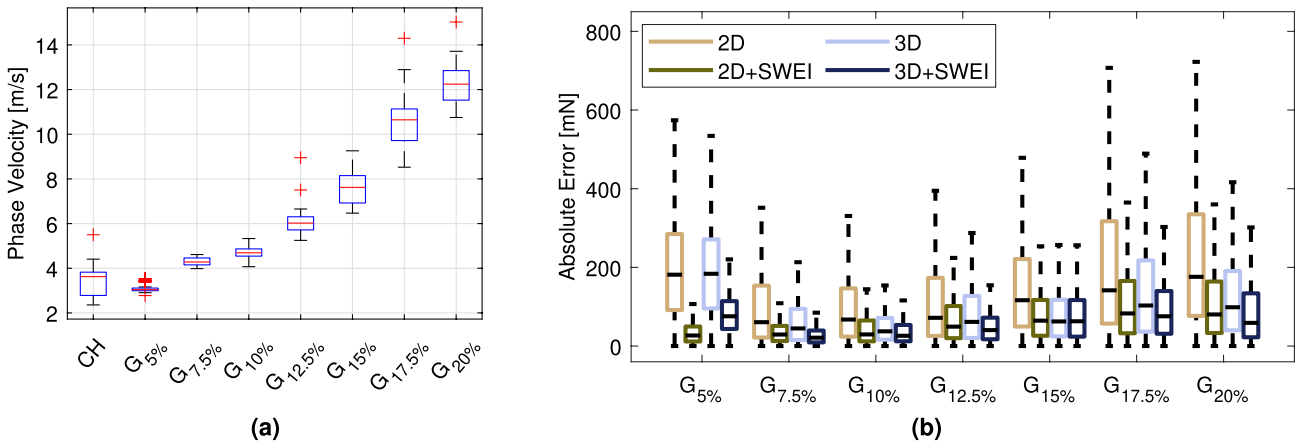

Figure 6. **(a)** Estimated phase velocities in gelatin phantoms and chicken heart (CH) soft tissue. **(b)** Absolute error of the force estimation models generalizing to each sample elasticity. Model performance is compared between 2D and 3D inputs as well as with and without SWEI fusion. Outliers are omitted and colors follow scientifically derived recommendations.[45]

		G_i [%]	5	7.5	10	12.5	15	17.5	20	Mean
Without SWEI	2D	rMSE	233.5 ± 35.3	157.1 ± 68.1	138.0 ± 23.9	186.9 ± 8.1	193.8 ± 81.4	263.5 ± 79.6	295.8 ± 119.2	216.7 ± 60.3
		nMAE	0.85 ± 0.14	0.22 ± 0.09	0.15 ± 0.02	0.15 ± 0.01	0.15 ± 0.07	0.14 ± 0.06	0.14 ± 0.06	0.26 ± 0.26
		pCC	0.87 ± 0.04	0.81 ± 0.06	0.70 ± 0.07	0.85 ± 0.08	0.84±0.12	0.80 ± 0.06	0.85 ± 0.06	0.78 ± 0.07
	3D	rMSE	227.1 ± 48.4	82.1 ± 11.7	69.1 ± 31.2	114.7 ± 17.5	110.5 ± 36.5	181.9 ± 109.0	180.5 ± 54.0	143.7 ± 62.3
		nMAE	0.84 ± 0.18	0.13 ± 0.03	0.08 ± 0.04	0.10 ± 0.01	0.08 ± 0.02	0.10 ± 0.07	0.08 ± 0.02	0.20 ± 0.28
		pCC	0.92 ± 0.01	0.83 ± 0.08	0.94 ± 0.01	0.93 ± 0.02	0.94 ± 0.03	0.94 ± 0.03	0.90 ± 0.03	0.89 ± 0.03
With SWEI	2D	rMSE	**45.5 ± 7.4**	52.6 ± 20.9	61.2 ± 9.3	92.0 ± 16.1	104.3 ± 23.5	152.9 ± 39.0	160.5 ± 31.0	97.2 ± 47.3
		nMAE	0.15 ± 0.02	0.08 ± 0.02	0.07 ± 0.01	0.08 ± 0.02	0.08 ± 0.02	0.08 ± 0.02	0.07 ± 0.01	0.09 ± 0.03
		pCC	0.90 ± 0.01	0.92 ± 0.08	0.94 ± 0.02	0.95 ± 0.01	0.94 ± 0.01	0.92 ± 0.04	0.94 ± 0.03	0.90 ± 0.01
	3D	rMSE	100.7 ± 15.7	**44.7 ± 25.6**	**50.8 ± 17.7**	**67.7 ± 17.1**	**101.7 ± 8.7**	**133.2 ± 26.2**	**127.3 ± 11.0**	**91.0 ± 34.7**
		nMAE	0.36 ± 0.06	0.07 ± 0.03	0.06 ± 0.02	0.06 ± 0.01	0.08 ± 0.01	0.07 ± 0.01	0.05 ± 0.01	0.11 ± 0.11
		pCC	0.96 ± 0.01	0.90 ± 0.11	0.97 ± 0.01	0.97 ± 0.02	0.95 ± 0.01	0.93 ± 0.03	0.97 ± 0.01	0.93 ± 0.02

Table 2. Force estimation for models tasked to generalize to unknown elastic properties: Results are compared for 2D and 3D inputs as well as our proposed method with SWEI fusion (2D+SWEI and 3D+SWEI). Mean and standard deviation are given over the 7-fold cross validation where each subset represents the generalization to one unseen elasticity. Results averaged over all folds are also shown and the lowest rMSE [mN] scores are marked in bold.

velocity fusion provides improved generalization to the softer material and results in an error reduction of 81 % and 56 % for 2D+SWEI and 3D+SWEI, respectively.

Force estimation on soft tissue. We ensemble the previously trained models and report the generalization from phantom to ex-vivo tissue data. The evaluation metrics for all test samples are displayed in Table 3. Absolute errors for individual estimations are also shown in the boxplot in Fig. 7a. The mean phase velocity of chicken tissue is 3.59 ± 091 m s^{-1}. Overall, our proposed SWEI fusion models clearly outperform 2D and 3D models without additional phase velocity input. Estimations performed on ex-vivo chicken heart tissue are feasible with an rMSE of 51.2 mN. Without SWEI, rMSE increases up to 283.15 mN with a normalized MAE as high as 0.6. An example of the resulting force estimations for all models can be seen in Fig. 7b. Models without SWEI overestimate the applied force while 2D+SWEI and 3D+SWEI models are more appropriately scaled by the phase velocity measurement.

Discussion

Real-time haptic feedback during minimally invasive RAS is critical to avoid soft tissue damage and to regain the surgeons natural sense of touch[46,47]. We show that the elastic properties of soft tissue have a strong influence in image-based force estimation. To include the biomechanical properties of soft tissue we propose a system which first, identifies the local elasticity of soft tissue with OCE and second, acquires high resolution volumetric images with OCT. We demonstrate a multi-input deep learning network which jointly processes elasticity and

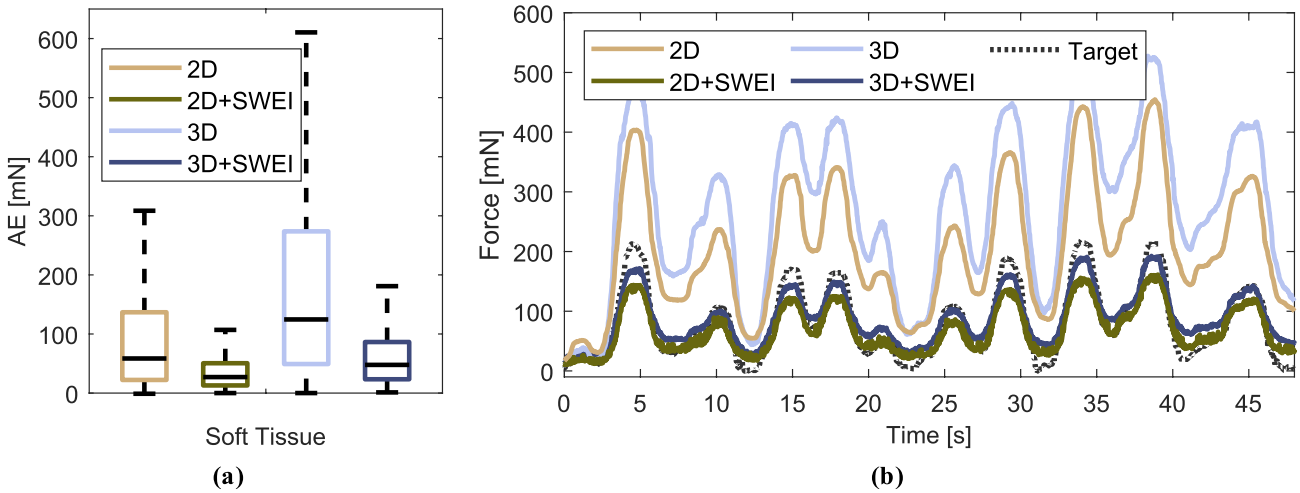

Figure 7. Ex-vivo Soft Tissue: **(a)** Absolute errors across all soft tissue samples plotted for each model. Accounting for sample elasticity results in superior generalization from gelatin to soft tissue. **(b)** Example force estimates for the palpation of a tissue sample for all trained models.

Model	2D	3D	2D+SWEI	3D+SWEI
rMSE [mN]	129.5 ± 82.6	283.5 ± 212.9	**51.2 ± 24.8**	76.6 ± 35.6
nMAE	0.26 ± 0.17	0.60 ± 0.48	**0.10 ± 0.04**	0.16 ± 0.09
pCC	0.93 ± 0.03	0.94 ± 0.04	0.91 ± 0.06	**0.94 ± 0.03**

Table 3. Evaluation metrics for all models trained on phantom data and tested on ex-vivo soft tissue. Results are averaged for all tissue samples and best results are marked bold.

image information. In the following we discuss our results concerning (1) the models performance with respect to the elasticity represented in the training and evaluation data, (2) the models ability to interpolate to elasticities which are not represented in the training data as well as the impact of including elasticity sensing, and (3) the feasibility of force estimation on completely unknown soft tissue images.

Our results for models exclusively trained on a distinct gelatin gel show that force estimation on new samples is only feasibly if the elasticity is in a similar range as the training data. This is an expected results and congruent to reports in the literature that the elasticity needs to be known for accurate force estimation[48]. Although in general training and evaluation on a single bio-mechanical tissue model is feasible[21] it is strongly limited in clinical applications. In practice, soft tissue elasticity ranges for individual tissue types, e.g., the elastic modulus for normal heart muscle is 18 ± 2 kPa and for cardiac fibrosis tissue 55 ± 15 kPa[49]. This case is represented in our data by the gelatin with a weight ratio of 5% (17.42 kPa) and 15% (56.04 kPa)[50]. Consequently, our results show that if the network is trained on healthy heart tissue and evaluated on pathological tissue the MAE could increase 20-fold (see Fig. 5a).

To alleviate this problem, we propose deep learning models that can generalize to changes in material properties. Results in Table 2 show that the fusion of SWEI provides superior performance when generalizing to new elastic properties in our phantom study. Our multi-input fusion models outperform the approaches with only image data as inputs, especially when only surface data is available. Consistent with the results shown in Fig. 6a, the largest reductions in absolute errors are achieved for the softer materials ($G_{5\%}$-$G_{10\%}$) where phase velocity measurements display low variance. For stiffer materials, the variance increases as it is more difficult to accurately detect the faster propagating waves. However, SWEI fusion is beneficial even where phase velocity estimates overlap and errors generally increase for stiffer materials due to the smaller deformations relative to the applied force. Over all elasticities unseen during training, we report a cross-validation average rMSE below 100 mN for our multi-input fusion models. In comparison, the generalization to a second synthetic material by Chua et. al. yielded an rMSE of 1865 mN for vision input data from stereographic cameras and an rMSE of 485 mN while data processing included the robot state and joint torques[18]. However, not only palpation was considered as in our case, but also pulling of the sample, making the learning task more challenging. Similarly in[51], both interactions were regarded simultaneously and the forces along the instrument axis during the palpation task were estimated with an rMSE of 1100 mN and a pCC of 0.55. Our fusion models are also competitive with approaches that have focused on a single material only, especially for soft gelatin samples. A learning-based approach on a single heart model phantom resulted in an rMSE of 60 mN[52]. An extension of the approach was tested on two different samples from the same material and the authors reported a combined rMSE of 20 mN[27] for the training and test set.

Our results show that elasticity information is essential when performing image-based force estimation on unknown soft tissue. It stands out, that we only train our models on gelatin phantoms and evaluate the performance on chicken heart tissue. Even though the SWEI estimates represent a simplified relationship of the

complex nonlinear mechanics present in heterogeneous, anisotropic soft tissue, we show that our models are able to leverage the additional information for an improved force estimation. The networks including elasticity estimates achieve superior performance with lower rMSE and nMAE (see Table 3). Our 2D+SWEI network even outperforms our 3D+SWEI approach on soft tissue. One possible explanation is the complex structure of the soft tissue, which is anisotropic and heterogeneous. Volumetric training data from samples with a similar mechanical structure should improve performance for 3D+SWEI. Additionally, the pre-processing of the surface data also reduces the dependence on speckle properties. Regarding pCC, performance is similar for all networks, suggesting that the networks without SWEI fusion detect deformations but overestimate or underestimate the applied forces, as shown in Fig. 7a. These networks are unable to relate tissue properties and the observed deformation, as demonstrated for gelatin phantom data. Overall performance is lower compared to our cross-validation approach on gelatin phantoms, due to the uneven surface of the soft tissue and the changes in speckle properties. Our 2D+SWEI network even outperforms our 3D+SWEI approach on soft tissue which might be due to the pre-processed surface information, making it independent of speckle variations and surface characteristics. The deviation in chicken heart tissue elasticity estimates is larger than estimates from similar elasticity ranges, e.g., $G_{5\%}$ and $G_{7.5\%}$. This shows that the soft tissue elasticity is not consistent throughout the samples although visually samples look identical. Further investigating our approach on in-vivo data will be essential to study the influence of vascularization, soft tissue heterogeneity and boundary conditions regarding wave reflections. Shear wave elasticity estimates are known to be frequency dependent, as dispersion effects create a nonlinear relationship between the elasticity and frequency[53,54]. To further refine elasticity estimates, stimulating shear waves with multiple frequencies could be implemented.

It is known that the OCE measurements for soft tissue is directly related to tissue pathology[55,56]. Hence, we can adapt our multi-input deep learning approach to real-time classification tasks, e.g., liver fibrosis staging[19], detecting optimal sample points for tissue biopsies or in classifying tumor tissue. One limitation of our system is the piezoelectric element which currently limits the interaction to a pushing task. Therefore, non-contact shear wave excitation via an air-pulse[34] and the pulling task should be considered. Finally, it will be essential to translate the estimated forces into haptic feedback for the physician[57], e.g. as kinesthetic[58] or vibrotactile[59] feedback.

Conclusion

In this work, we propose image-based estimation of tool-tissue interaction forces combined with estimation of local biomechanical properties in a single modality. We present an experimental setup that enables simple and efficient data acquisition of OCE and OCT data needed for robust deep learning approaches. The conducted phantom study highlights that the influence of local elasticity cannot be neglected when estimating interaction forces. Furthermore, we show that our multi-input fusion model can generalize from phantom to soft tissue samples. Thus, a single, versatile model for image-based force estimation is feasible, which could enable real-time haptic feedback and increased autonomy in robotic-assisted interventions.

Data availability

The data analyzed in this study is available from the corresponding authors upon reasonable request.

Received: 25 July 2022; Accepted: 23 December 2022
Published online: 10 January 2023

References

1. Ghezzi, T. L. & Corleta, O. C. 30 years of robotic surgery. *World J. Surg.* **40**, 2550–2557 (2016).
2. Armijo, P. R., Pagkratis, S., Boilesen, E., Tanner, T. & Oleynikov, D. Growth in robotic-assisted procedures is from conversion of laparoscopic procedures and not from open surgeons' conversion: A study of trends and costs. *Surg. Endosc.* **32**, 2106–2113 (2018).
3. Diana, M. & Marescaux, J. Robotic surgery. *J. Br. Surg.* **102**, e15–e28 (2015).
4. Wee, I. J. Y., Kuo, L.-J. & Ngu, J.C.-Y. A systematic review of the true benefit of robotic surgery: Ergonomics. *The Int. J. Med. Robot. Comput. Assist. Surg.* **16**, e2113 (2020).
5. Aviles-Rivero, A. I. *et al.* Sensory substitution for force feedback recovery. *ACM Trans. Appl. Percept.* **15**, 1–19. https://doi.org/10.1145/3176642 (2018).
6. Overtoom, E. M., Horeman, T., Jansen, F.-W., Dankelman, J. & Schreuder, H. W. R. Haptic feedback, force feedback, and force-sensing in simulation training for laparoscopy: A systematic overview. *J. Surg. Educ.* **76**, 242–261. https://doi.org/10.1016/j.jsurg.2018.06.008 (2019).
7. Golahmadi, A. K., Khan, D. Z., Mylonas, G. P. & Marcus, H. J. Tool-tissue forces in surgery: A systematic review. *Ann. Med. Surg.* **65**, 102268. https://doi.org/10.1016/j.amsu.2021.102268 (2021).
8. Lim, S.-C., Lee, H.-K. & Park, J. Role of combined tactile and kinesthetic feedback in minimally invasive surgery. *The Int. J. Med. Robot. Comput. Assist. Surg.* **11**, 360–374 (2015).
9. Marbán, A., Casals, A., Fernández, J. & Amat, J. Haptic feedback in surgical robotics: Still a challenge. In *ROBOT2013: First Iberian Robotics Conference*, 245–253 (Springer, 2014).
10. Simaan, N., Yasin, R. M. & Wang, L. Medical technologies and challenges of robot-assisted minimally invasive intervention and diagnostics. *Annu. Rev. Control Robot. Autonom. Syst.* **1**, 465–490 (2018).
11. Okamura, A. M., Verner, L. N., Reiley, C. E. & Mahvash, M. Haptics for robot-assisted minimally invasive surgery. In *Robotics Research*, (eds Siciliano, B. et al.) vol. 66 of *Springer Tracts in Advanced Robotics*, 361–372, https://doi.org/10.1007/978-3-642-14743-2_30 (Springer Berlin Heidelberg, Berlin, Heidelberg, 2011).
12. Amirabdollahian, F. *et al.* Prevalence of haptic feedback in robot-mediated surgery: A systematic review of literature. *J. Robot. Surg.* **12**, 11–25. https://doi.org/10.1007/s11701-017-0763-4 (2018).
13. Culmer, P., Alazmani, A., Mushtaq, F., Cross, W. & Jayne, D. 15 - haptics in surgical robots. In *Handbook of robotic and image-guided surgery*, (eds Abedin-Nasab, M. H.) 239–263, https://doi.org/10.1016/B978-0-12-814245-5.00015-3 (Elsevier, Amsterdam, Netherlands, 2020).
14. Yang, C., Xie, Y., Liu, S. & Sun, D. Force modeling, identification, and feedback control of robot-assisted needle insertion: A survey of the literature. *Sensors (Basel, Switzerland)*https://doi.org/10.3390/s18020561 *(2018).*

15. Nazari, A. A., Janabi-Sharifi, F. & Zareinia, K. Image-based force estimation in medical applications: A review. *IEEE Sens. J.* **21**, 8805–8830. https://doi.org/10.1109/JSEN.2021.3052755 (2021).
16. Berkelman, P. J., Whitcomb, L. L., Taylor, R. H. & Jensen, P. A miniature instrument tip force sensor for robot/human cooperative microsurgical manipulation with enhanced force feedback. In *International Conference on Medical Image Computing and Computer-Assisted Intervention*, 897–906 (Springer, 2000).
17. Sang, H. *et al.* External force estimation and implementation in robotically assisted minimally invasive surgery. *The Int. J. Med. Robot. Comput. Assist. Surg.* **13**, e1824. https://doi.org/10.1002/rcs.1824 (2017).
18. Chua, Z., Jarc, A. M. & Okamura, A. M. Toward force estimation in robot-assisted surgery using deep learning with vision and robot state. In *2021 IEEE International Conference on Robotics and Automation (ICRA),* 12335-12341. (IEEE, 2021).
19. Sande, J. A. *et al.* Ultrasound shear wave elastography and liver fibrosis: A prospective multicenter study. *World J. Hepatol.* **9**, 38 (2017).
20. Yang, Y.-P. *et al.* Qualitative and quantitative analysis with a novel shear wave speed imaging for differential diagnosis of breast lesions. *Sci. Rep.* **7**, 1–11 (2017).
21. Miller, K., Chinzei, K., Orssengo, G. & Bednarz, P. Mechanical properties of brain tissue in-vivo: Experiment and computer simulation. *J. Biomech.* **33**, 1369–1376 (2000).
22. Haouchine, N., Kuang, W., Cotin, S. & Yip, M. Vision-based force feedback estimation for robot-assisted surgery using instrument-constrained biomechanical three-dimensional maps. *IEEE Robot. Autom. Lett.* **3**, 2160–2165 (2018).
23. Giannarou, S. *et al.* Vision-based deformation recovery for intraoperative force estimation of tool-tissue interaction for neurosurgery. *Int. J. Comput. Assist. Radiol. Surg.* **11**, 929–936. https://doi.org/10.1007/s11548-016-1361-z (2016).
24. Aviles, A. I., Marban, A., Sobrevilla, P., Fernandez, J. & Casals, A. A recurrent neural network approach for 3d vision-based force estimation. In *2014 4th International Conference on Image Processing Theory, Tools and Applications (IPTA)*, 1–6, https://doi.org/10.1109/IPTA.2014.7001941 (IEEE, 2014).
25. Marban, A., Srinivasan, V., Samek, W., Fernández, J. & Casals, A. A recurrent convolutional neural network approach for sensorless force estimation in robotic surgery. *Biomed. Signal Process. Control* **50**, 134–150 (2019).
26. Behrendt, F., Gessert, N. & Schlaefer, A. Generalization of spatio-temporal deep learning for vision-based force estimation. *Curr. Direct. Biomed. Eng.*https://doi.org/10.1515/cdbme-2020-0024 *(2020).*
27. Aviles, A. I., Alsaleh, S. M., Hahn, J. K. & Casals, A. Towards retrieving force feedback in robotic-assisted surgery: A supervised neuro-recurrent-vision approach. *IEEE Trans. Haptics* **10**, 431–443. https://doi.org/10.1109/TOH.2016.2640289 (2017).
28. Gessert, N., Schlüter, M. & Schlaefer, A. A deep learning approach for pose estimation from volumetric oct data. *Med. Image Anal.* **46**, 162–179 (2018).
29. Gessert, N., Bengs, M., Schlüter, M. & Schlaefer, A. Deep learning with 4d spatio-temporal data representations for oct-based force estimation. *Med. Image Anal.* **64**, 101730 (2020).
30. Neidhardt, M. *et al.* Force estimation from 4d oct data in a human tumor xenograft mouse model. *Curr. Directi. Biomed. Eng.* **6**, 20200022. https://doi.org/10.1515/cdbme-2020-0022 (2020).
31. Qiu, Y. *et al.* Quantitative optical coherence elastography based on fiber-optic probe for in situ measurement of tissue mechanical properties. *Biomed. Opt. Express* **7**, 688–700 (2016).
32. Mieling, R., Sprenger, J., Latus, S., Bargsten, L. & Schlaefer, A. A novel optical needle probe for deep learning-based tissue elasticity characterization. *Curr. Direct. Biomed. Eng.* **7**, 21–25 (2021).
33. Neidhardt, M. *et al.* 4d deep learning for real-time volumetric optical coherence elastography. *Int. J. Comput. Assist. Radiol. Surg.* **16**, 23–27 (2021).
34. Wang, S. *et al.* A focused air-pulse system for optical-coherence-tomography-based measurements of tissue elasticity. *Laser Phys. Lett.* **10**, 075605 (2013).
35. Kijanka, P. & Urban, M. W. Local phase velocity based imaging: A new technique used for ultrasound shear wave elastography. *IEEE Trans. Med. Imaging* **38**, 894–908 (2018).
36. Maksuti, E. *et al.* Arterial stiffness estimation by shear wave elastography: Validation in phantoms with mechanical testing. *Ultrasound Med. Biol.* **42**, 308–321 (2016).
37. Beuve, S., Kritly, L., Callé, S. & Remenieras, J.-P. Diffuse shear wave spectroscopy for soft tissue viscoelastic characterization. *Ultrasonics* **110**, 106239 (2021).
38. Kennedy, C. W. & Desai, J. P. A vision-based approach for estimating contact forces: Applications to robot-assisted surgery. *Appl. Bionics Biomech.* **2**, 53–60 (2005).
39. Huang, G., Liu, Z., Van Der Maaten, L. & Weinberger, K. Q. Densely connected convolutional networks. In *Proceedings of the IEEE conference on computer vision and pattern recognition* 4700–4708 (2017).
40. Nair, V. & Hinton, G. E. Rectified linear units improve restricted boltzmann machines. In *Icml* (2010).
41. Ioffe, S. & Szegedy, C. Batch normalization: Accelerating deep network training by reducing internal covariate shift. In *International conference on machine learning*, 448–456 (PMLR, 2015).
42. Smith, L. N. & Topin, N. Super-convergence: Very fast training of neural networks using large learning rates. In *Artificial Intelligence and Machine Learning for Multi-Domain Operations Applications*, vol. **11006**, 1100612 (International Society for Optics and Photonics, 2019).
43. Kingma, D. P. & Ba, J. Adam: A method for stochastic optimization. arXiv preprint arXiv:1412.6980 (2014).
44. He, K., Zhang, X., Ren, S. & Sun, J. Delving deep into rectifiers: Surpassing human-level performance on imagenet classification. In *Proceedings of the IEEE international conference on computer vision*, 1026–1034 (2015).
45. Crameri, F., Shephard, G. E. & Heron, P. J. The misuse of colour in science communication. *Nat. Commun.* **11**, 1–10 (2020).
46. Ouyang, Q. *et al.* Bio-inspired haptic feedback for artificial palpation in robotic surgery. *IEEE Trans. Biomed. Eng.* **68**, 3184–3193 (2021).
47. Wagner, C. R., Howe, R. D. & Stylopoulos, N. The role of force feedback in surgery: Analysis of blunt dissection. In *Haptic Interfaces for Virtual Environment and Teleoperator Systems, International Symposium on*, **73** (Citeseer, 2002).
48. Haouchine, N., Kuang, W., Cotin, S. & Yip, M. Vision-based force feedback estimation for robot-assisted surgery using instrument-constrained biomechanical three-dimensional maps. *IEEE Robot. Autom. Lett.* **3**, 2160–2165. https://doi.org/10.1109/LRA.2018.2810948 (2018).
49. Berry, M. F. *et al.* Mesenchymal stem cell injection after myocardial infarction improves myocardial compliance. *Am. J. Physiol.-Heart Circ. Physiol.* **290**, H2196–H2203 (2006).
50. Neidhardt, M. *et al.* Ultrasound shear wave elasticity imaging with spatio-temporal deep learning. *IEEE Trans. Biomed. Eng.* **69(11)**, 3356-3364 (2022).
51. Marban, A., Srinivasan, V., Samek, W., Fernández, J. & Casals, A. A recurrent convolutional neural network approach for sensorless force estimation in robotic surgery. *Biomedical Signal Processing and Control* **50**, 134-150. (2019).
52. Aviles, A. I., Alsaleh, S., Sobrevilla, P. & Casals, A. Sensorless force estimation using a neuro-vision-based approach for robotic-assisted surgery. In *2015 7th International IEEE/EMBS Conference on Neural Engineering (NER)*, 86–89, https://doi.org/10.1109/NER.2015.7146566 (2015).
53. Yengul, S. S., Barbone, P. E. & Madore, B. Dispersion in tissue-mimicking gels measured with shear wave elastography and torsional vibration rheometry. *Ultrasound Med. Biol.* **45**, 586–604 (2019).

54. Rus, G., Faris, I. H., Torres, J., Callejas, A. & Melchor, J. Why are viscosity and nonlinearity bound to make an impact in clinical elastographic diagnosis?. *Sensors* **20**, 2379 (2020).
55. Yuting, L. *et al.* Microscale characterization of prostate biopsies tissues using optical coherence elastography and second harmonic generation imaging. *Lab. Invest.* **98**, 380–390 (2018).
56. Li, C. *et al.* Detection and characterisation of biopsy tissue using quantitative optical coherence elastography (oce) in men with suspected prostate cancer. *Cancer Lett.* **357**, 121–128 (2015).
57. Patel, R. V., Atashzar, S. F. & Tavakoli, M. Haptic feedback and force-based teleoperation in surgical robotics. *Proc. IEEE* **110**, 1012–1027 (2022).
58. Mieling, R. *et al.* Proximity-based haptic feedback for collaborative robotic needle insertion. In *International Conference on Human Haptic Sensing and Touch Enabled Computer Applications*, 301–309 (Springer, 2022).
59. Aggravi, M., Estima, D. A., Krupa, A., Misra, S. & Pacchierotti, C. Haptic teleoperation of flexible needles combining 3d ultrasound guidance and needle tip force feedback. *IEEE Robot. Autom. Lett.* **6**, 4859–4866 (2021).

Author contributions

M.N. and A.S. conceived the study, M.N. conducted the experiments in the laboratory, R. M. conducted the deep learning experiments, M.N. and R.M. analyzed the results and wrote the article, M.B. assisted in model development, A.S. supervised the project and all authors reviewed the manuscript.

Funding

Open Access funding enabled and organized by Projekt DEAL. This work was partially funded by the TUHH i^3 initiative and the Interdisciplinary Competence Center for Interface Research (ICCIR) supported by Hamburg University of Technology (TUHH) and University Hospital Hamburg-Eppendorf (UKE). Publishing fees funded by the Deutsche Forschungsgemeinschaft (DFG, German Research Foundation) - Projektnummer 491268466 and the Hamburg University of Technology (TUHH) in the funding program *Open Access Publishing*.

Competing interests

The authors declare no competing interests.

Additional information

Correspondence and requests for materials should be addressed to R.M.

Reprints and permissions information is available at www.nature.com/reprints.

Publisher's note Springer Nature remains neutral with regard to jurisdictional claims in published maps and institutional affiliations.

7.5 A-scan Sequence Transformers for Palpation with Optical Coherence Elastography

Journal: Biomedical Optics Express

Published: 16.04.2025

Robin Mieling, Maximilian Neidhardt, Finn Behrendt, Sarah Latus, Axel Heinemann, Benjamin Ondruschka, and Alexander Schlaefer, "A-scan sequence transformers for palpation with optical coherence elastography," *Biomedical Optics Express*, vol. 16, no. 5, pp. 1925–1943, 2025

Research Article Vol. 16, No. 5 / 1 May 2025 / Biomedical Optics Express 1925
Biomedical Optics EXPRESS

A-scan sequence transformers for palpation with optical coherence elastography

ROBIN MIELING,[1,*] MAXIMILIAN NEIDHARDT,[1] FINN BEHRENDT,[1] SARAH LATUS,[1] AXEL HEINEMANN,[2] BENJAMIN ONDRUSCHKA,[2] AND ALEXANDER SCHLAEFER[1]

[1]*Institute of Medical Technology and Intelligent Systems, Hamburg University of Technology, Am Schwarzenberg-Campus 1, 21073 Hamburg, Germany*
[2]*Institute of Legal Medicine, University Medical Center Hamburg-Eppendorf, Butenfeld 34, 22529 Hamburg, Germany*
[*]*robin.mieling@tuhh.de*

Abstract: Recognizing the properties of elastic tissue can facilitate surgical navigation, e.g., when localizing lesions by palpation. However, palpation is very subjective and often unavailable in minimally invasive surgery. High-speed optical coherence elastography (OCE) adapted for intraoperative use could enable elasticity estimation by measuring the propagation of mechanically stimulated waves. However, robust estimation of wave velocity can be challenging, and reconstruction of the elastic modulus is highly dependent on the correct modeling of wave propagation. We therefore consider deep learning for the end-to-end estimation of elasticity from OCE phase data. Since optical coherence tomography inherently produces a temporal sequence of one-dimensional axial scans (A-scans), we consider transformer-based deep learning models to directly process A-scan sequences. For homogeneous tissue phantoms with known elastic properties, we obtain a mean error of 1.64 kPa, which significantly improves elasticity reconstruction compared to conventional processing and the best CNN-based approach with 7.80 kPa and 5.55 kPa, respectively. Furthermore, we demonstrate generalization to heterogeneous phantoms with inclusions and assess the elasticity of soft tissue samples, including heart, kidney, and liver. The results show that transformer architectures are well suited for reconstructing elasticity from A-scan sequences in OCE.

1. Introduction

The elasticity of the soft tissue is an important indicator for differentiating between healthy and pathological conditions [1,2]. During palpation, local differences in elastic properties are used to detect and localize lesions. However, palpation is very subjective and unavailable in laparoscopic and robot-assisted surgery. Therefore, additional sensors are needed to obtain quantitative feedback on elastic properties during minimally invasive surgery. One approach is elastography. In addition to ultrasound and magnetic resonance imaging, optical coherence tomography (OCT) has been considered for such biomechanical tissue characterization [3]. OCT is based on the principle of low-coherence interferometry and uses near-infrared light to acquire one-dimensional, high-resolution depth scans, so-called A-scans. A-scans are recorded sequentially while the beam is moved laterally across the sample. Multi-dimensional images, e.g. B-scans (2D) or C-scans (3D), are generated by restructuring the A-scan sequence along the lateral dimensions. Compared to ultrasound or magnetic resonance imaging, OCT offers superior spatial and temporal resolution [3,4]. With phase-sensitive OCT, sub-micrometer displacements can be detected at high temporal resolution, enabling quantitative assessment of elastic properties in wave-based elastography [4,5]. Fiber-based OCT probes enable small form factors suitable for in-vivo use, e.g. miniaturized imaging probes [6–9], intravascular OCT [10] or sensors integrated

#553849 https://doi.org/10.1364/BOE.553849
Journal © 2025 Received 2 Jan 2025; revised 4 Apr 2025; accepted 4 Apr 2025; published 16 Apr 2025

Biomedical Optics EXPRESS

into medical instruments [11,12] and needles [13,14]. OCT is therefore particularly interesting when it comes to adapting elastography for minimally invasive surgery.

Optical coherence elastography (OCE) has been demonstrated mainly with tabletop systems in numerous applications, e.g. for analysing cornea or breast tissue [4,15]. Obtaining quantitative OCE intraoperatively is considerably more difficult, as the measurement of mechanical stress and tissue deformation must both be performed locally at the tissue surface [14]. Therefore, intraoperative, quantitative elastography is currently unavailable, especially for robot-assisted surgery. As an alternative to wave-based OCE, handheld scanners for quantitative compression-based OCE have been proposed [16–18] and were successfully demonstrated for intraoperative breast cancer detection in the surgical cavity [18]. But for wave-based OCE, we require appropriate in-vivo wave excitation in the intraoperative environment, besides laparoscopic OCT previously considered in [6,19]. Acoustic radiation force excitation has been successfully demonstrated in intravascular and intrabronchial applications by external ultrasound-based shear wave excitation [20] or with integrated piezoelectric elements [21–23]. However, acoustic wave excitation requires an acoustic medium to couple the transducer and tissue, e.g. water or gel. Since surgical instruments are already in contact with tissue during normal tool-tissue interaction, we consider displacement-based piezoelectric excitation for wave-based OCE instead, which provides high bandwidth, load force and precise frequency tuning [4]. Piezoelectric excitation has also recently been coupled with a fiber scanning endoscope for wave-based OCE [24].

We therefore consider a surgical instrument with integrated piezo actuators [25] and excite the instrument itself for OCE imaging (Fig. 1). However, robust detection of wave propagation for accurate elasticity estimates can be challenging due to the optical setup, e.g. imperfect scanning, noise and phase wrapping, and the underlying tissue mechanics, e.g. non-linearity, inhomogeneities and reverberations [4]. Consequently, several approaches for phase velocity estimation similar to ultrasound elastography have been considered, e.g. time-of-flight (TOF) [26,27] or Fourier estimator (FE) [28,29]. Furthermore, the reconstruction of the Young's modulus is highly dependent on the choice of the mechanical model [30], e.g. the shear wave equation or the Rayleigh–Lamb frequency equation. It is often assumed that only surface waves propagating through a thin layer on top of the sample are observed during OCE, and the Rayleigh surface wave equation is therefore chosen for the reconstruction of the elastic modulus [31–33]. However, even in phantom experiments, the reconstructed elasticities based on OCE and the Rayleigh–Lamb frequency equation differ from the values determined by gold standard uniaxial compression testing [30]. So while the assumptions on wave propagation may be justified depending on the experimental setup, a more versatile and accurate model is desirable.

We consequently consider deep learning to calibrate our OCE setup for end-to-end elasticity reconstruction. Applications of deep learning in OCT have long focused on convolutional neural networks (CNNs) [34,35] and similarly CNNs have been considered for wave-based OCE [24,25,36–38]. Spatio-temporal 3D and 4D DenseNets were previously used for processing temporal sequences of B- and C-scans to estimate the elasticity of gelatin phantoms [25,36,37]. Recently, VP-NET has been proposed as an end-to-end approach for estimating wave velocity from a single B-scan [38]. VP-NET combines depth-wise separable convolutions that effectively reduce the model size, e.g. as shown in MobileNets [39], with squeeze-and-excitation blocks presented in [40]. However, these approaches consider the OCE data exclusively as multidimensional images and not as purely temporal sequences. OCT scans are the sequential accumulation of one-dimensional A-scans at different spatial or temporal positions. In the case of OCE, the excited wave propagates through the tissue while the scanning mirror continuously deflects the sample beam back and forth (Fig. 1). In conventional processing and CNNs, the A-scans are rearranged into cross-sectional images (B-scan) over time (B-M-scan). But the obtained measurement is still a sequence of A-scans containing spatio-temporal information about the

Biomedical Optics EXPRESS

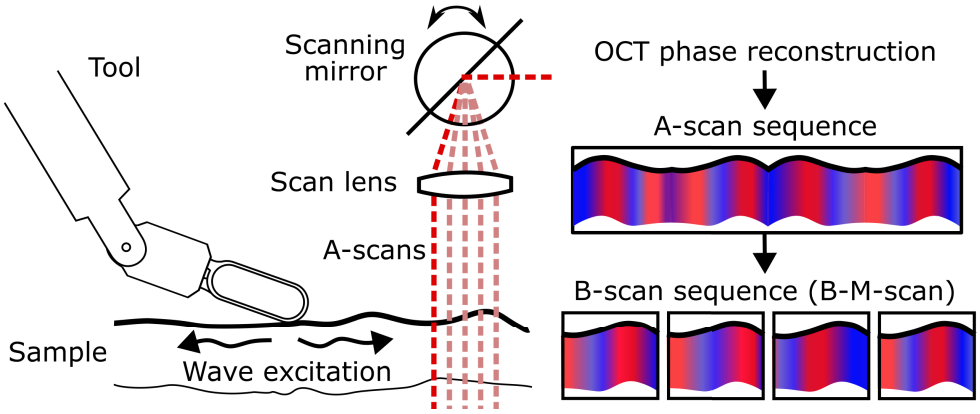

Fig. 1. In wave-based OCE, a wave is excited at the sample surface, e.g. with a modified surgical tool [25], and propagates through the tissue. Simultaneously, A-scans are acquired at a constant rate while the scanning mirrors direct the sample beam back and forth at high speed. The resulting data is therefore a temporal sequence of A-scans that includes both the oscillating scanning motion and the wave propagation. In conventional processing, the A-scans are rearranged according to their spatial position to represent two-dimensional images over time (B-M-scan) and facilitate the analysis of wave propagation.

wave propagation. Therefore, we consider transformers that are characterised by processing sequential data and directly consider the A-scan sequence as our input representation.

Transformers [41] have proven successful in processing long input sequences in natural language processing. Vision transformers (VITs) [42] have transferred the approach to the image domain by treating the input images as a sequence of patches. VITs have recently been considered for OCT processing, either by directly using VIT [43] or by combining CNN and transformers in hybrid models [44] when available data is limited. The applications of transformers in morphological OCT imaging range from disease classification [45] or retinal layer segmentation [46] to noise and artefact reduction [47]. However, earlier approaches of transformers in OCT exclusively followed patch-based sequencing for the self-attention mechanism [43–47], although the data obtained from OCT is already sequential in nature. Thus, the inherently temporal sequence of A-scans is reconstructed into 2D images and then resampled into patches to obtain sequence inputs.

In this work, we directly consider A-scan sequences for elasticity estimation. Compared to B-scan sequences or image patches, this approach decouples temporal and spatial dependencies while retaining the raw input representation typical for OCT. By leveraging transformers, which excel at processing sequential data, we enable the model to learn spatial features of wave propagation and accurately reconstruct sample elasticity. We consider an experimental setup with high-speed OCT imaging and a modified surgical tool (Fig. 2) that enables data acquisition for training transformer encoders without transfer learning. We use tissue-mimicking phantoms with known properties determined by mechanical testing to calibrate our setup for end-to-end Young's modulus reconstruction. We consider transformers for processing the spatio-temporal OCE data and optimize data sequencing and model architecture. We compare our method with conventional wave velocity estimation and subsequent elasticity reconstruction similar to [31,33] and the previously considered learning-based approaches DenseNets [25,36,37] and VP-NET [38]. We train our models on homogeneous phantoms and validate our approach on heterogeneous phantoms with stiff inclusions simulating lesions and ex-vivo tissues.

Biomedical Optics EXPRESS

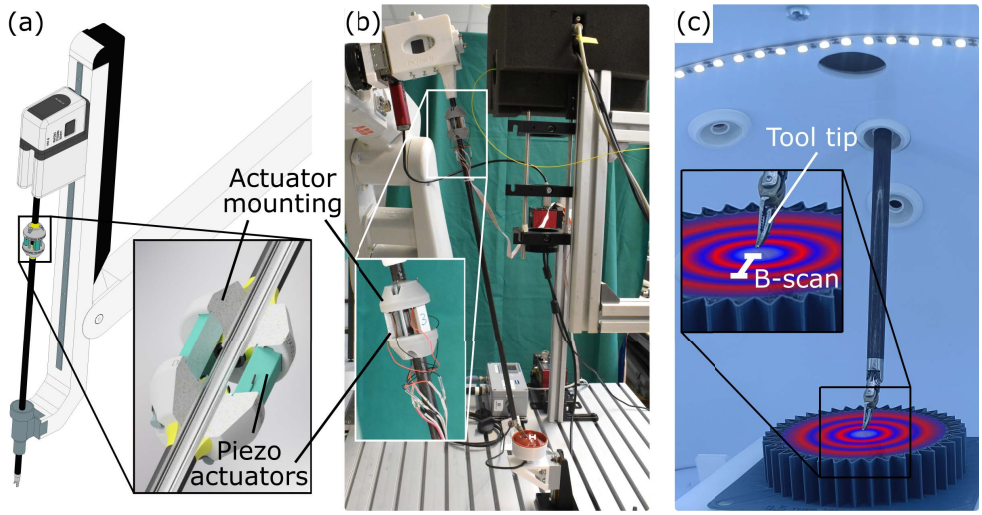

Fig. 2. Experimental setup for OCE with a modified surgical tool and a robotic setup for data acquisition. (a-b) We excite waves in the sample via a modified surgical instrument with integrated piezoelectric elements at the proximal end of the tool. High voltage components are therefore located outside the patient and the waves excited at the proximal end propagate along the instrument into the tissue. (c) Data acquisition in a laparoscopic trainer is demonstrated, illustrating wave excitation via the surgical instrument and simultaneous OCE B-M-mode scanning.

2. Methods

In the following, we introduce our OCE setup and describe the data acquisition. We then present model architectures and illustrate data processing.

2.1. OCE with modified surgical tool

Figure 2 illustrates the configuration used for the experiment. We employ a high-speed swept-source system (SS-OCT, OMES, Optores, Germany) operating at a temporal scan rate of 1.5 MHz. The central wavelength is 1315 nm. The system has an axial resolution of 15 µm in air and the lateral resolution is specified as 50 µm at a focal length of 100 mm. Note, that in our setup the working distance is 300 mm. We use B-M-mode scanning to capture the wave propagation both spatially and temporally. We use oscillating resonant mirrors to record B-scans with a temporal resolution of 11.4 kHz. We disregard A-scans during the pivot points and flip the lateral axis of every other B-scan. The field of view (FOV) is 3.5 mm and each B-scan is resolved over 118 sequential A-scans. For each OCE measurement, we acquire $30{\times}10^3$ A-scans that correspond to 208 cross-sectional images. For elasticity estimation, we then consider the phase between A-scans at identical spatial location over time. B-M-mode scanning results in a spatio-temporal 3D representation of the propagating shear waves (Fig. 3). We crop each A-scan at a depth of 256 pixels to obtain a size of $(208 \times 118) \times 256$ pixels for the temporal and axial dimension, respectively. Simultaneously with OCT data acquisition, we excite shear waves on the sample surface with a modified surgical tool (Fig. 2), as described in [25]. The modified tool is mounted on the end effector of a six-axis serial robot (IRB120, ABB, Switzerland) for automatic data acquisition. We excite the piezoelectric actuators in our tool with 1000 Hz.

Biomedical Optics EXPRESS

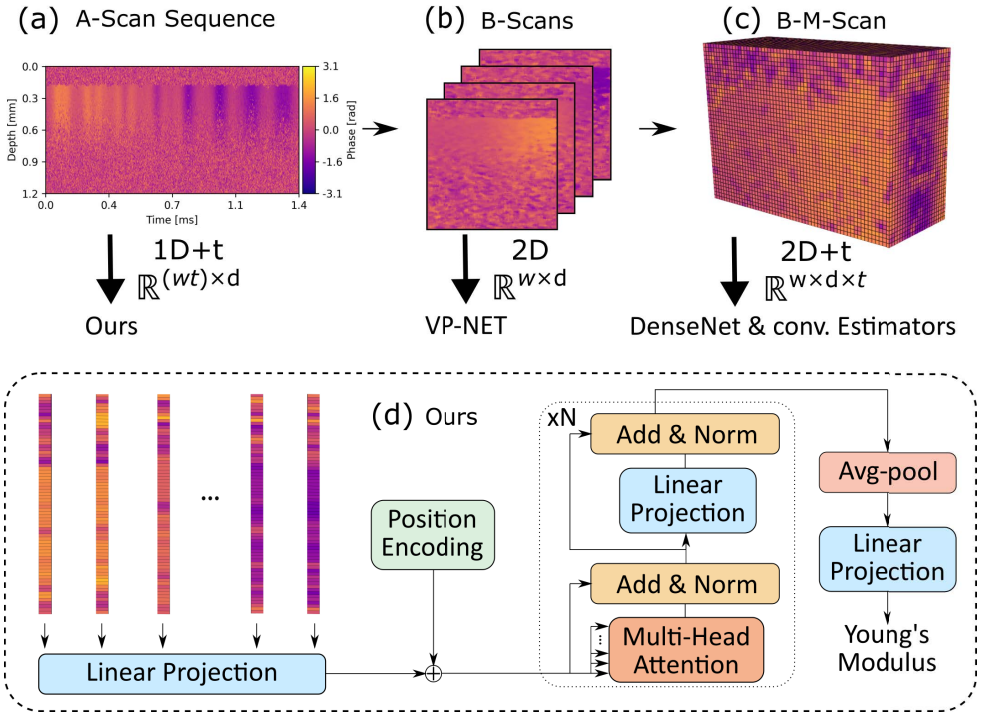

Fig. 3. Overview of the data representations used for processing OCE data. An example recorded with our experimental setup is shown as a raw sequence of A-scans containing phase data (a). A-scans are rearranged according to their spatial position to represent two-dimensional B-scans (b). The B-scans recorded over time (B-M-scan) are partially visualized in 3D (c). VP-NET [38] was proposed for direct processing of individual B-scans, while conventional processing and DenseNets [36] process spatio-temporal 3D OCE data. In contrast, by directly processing the sequence of individual A-scans ($\in \mathbb{R}^{1\times h}$) in our attention-based approach (d), we retain the purely temporal input sequence and learn spatial dependencies during training. The transformer encoder with N layers and a fully connected regression head is trained for end-to-end elasticity reconstruction from A-scan sequences.

2.2. *Transformers for sequential OCE data*

Transformers were originally proposed in [41] and later transferred to the natural image domain with VIT [42]. Compared to recurrent neural networks and CNNs, transformers allow capturing long-term dependencies without an inductive bias that limits attention to local neighbourhoods. This capability enables flexible feature representation and provides a global receptive field, even in shallow layers. Moreover, given sufficient data, transformers can learn advantageous properties similar to those of CNNs, such as local information aggregation in lower layers [48]. The basic concept of transformers is the scaled-dot product attention

$$\mathrm{Attn}(Q,K,V) = \mathrm{Softmax}\left(\frac{QK^{\mathrm{T}}}{\sqrt{d_k}}\right)V \tag{1}$$

with Q, K, V as the query, key and value matrices and d_k as the dimension of the keys. The sequences Q, K, V are obtained from the input sequence x via learnable weight matrices W_Q, W_K, W_V. OCT and thus OCE data is originally a sequence of A-scans $\mathbb{R}^{(wt)\times d}$, with w and d denoting lateral and axial dimension. We therefore consider the direct use of the sequence of

Biomedical Optics EXPRESS

A-scans ($\mathbb{R}^{1\times d}$) as input x (Fig. 3). This corresponds to a purely temporal sequence of inputs and the spatial information must be learned by the model during training. For a comprehensive investigation, we additionally consider transformers for OCE with patch-based sequencing similar to VITs [42]. Here, the sequence x is sampled from flattened patches (size $p \times p \times p$) of the reconstructed image $\in \mathbb{R}^{w\times d\times t}$. In both cases, the sequence passed through the multi-headed self-attention layers undergoes average-pooling over the encoder output sequence before a fully connected layer with a single output as our regression head.

2.2.1. Position encoding

For our transformer-based approach, position encoding (PE) is required to retain the information of the sequence order during self-attention. However, in the case of OCE, we obtain input data that is different from other imaging modalities due to its spatio-temporal nature. Here, we want to reconstruct the elasticity from the observed waves propagating through the tissue and thus through the sequence of A-scans. We therefore specifically consider the relative PE to provide the model with relative distances between the A-scans in the sequence. Overall, we investigate three different approaches for encoding the position of the spatio-temporal OCE data.

Relative PE enables effective training even for long token sequences and is well suited to capture the spatio-temporal nature of the OCE data. We therefore consider rotary position embeddings (RoPE) [49], that have recently been proposed as a powerful and efficient implementation of relative PE. In contrast to the learned absolute embeddings used for VIT [42], relative embeddings produce an increase in PE with increasing distance between tokens. Features of any query or key are paired and considered as 2D coordinates. They are then rotated by an angle θ specific to that pair and depending on the position within the sequence, e.g. for two features x_m^1 and x_m^2 at position m

$$\mathrm{RoPE}(x_m^1, x_m^2, m) = \begin{pmatrix} x_m^1 \cos m\theta - x_m^2 \sin m\theta \\ x_m^2 \cos m\theta + x_m^1 \sin m\theta \end{pmatrix}. \tag{2}$$

Applied to the dot-product for a pair of features at positions m and n,

$$\left\langle \mathrm{RoPE}(x_m^1, x_m^2, m), \mathrm{RoPE}(x_n^1, x_n^2, n) \right\rangle = \left\langle \mathrm{RoPE}(x_m^1, x_m^2, m-n), \mathrm{RoPE}(x_n^1, x_n^2, 0) \right\rangle \tag{3}$$

RoPE therefore offers PE relative to the distance $m-n$. RoPE could provide better performance than the simple relative PE investigated for VIT [42], that did not lead to performance improvements over learned embeddings.

Sinusoidal PE were originally considered for the transformer architecture [41]. The positions thus correspond to sinusoids that are added directly to the embedded features with increasing frequency, according to

$$PE(m, 2i) = sin(m/10000^{2i/d_{emb}}) \tag{4}$$

$$PE(m, 2i+1) = cos(m/10000^{2i/d_{emb}}) \tag{5}$$

where m and i denote the position and the dimension of the token, respectively.

Learnable PE were used for VIT [42]. The embedding is a linear 1D mapping for each input token that is learned during backpropagation. The PE is added to each token after the initial embedding layer and the dimension of the trainable vector is given by the maximum sequence length and the dimension of the embedded tokens.

2.3. Conventional OCE processing

In addition to the CNN baselines, we consider the conventional estimation of the wave velocity and the subsequent reconstruction of the elasticity similar to [31,33]. To do this, we first reconstruct the wave velocity using an FE [4,50]. We reconstruct space-time maps for each OCE

Biomedical Optics EXPRESS

measurement by averaging the B-M-Scan along the depth axis and applying the Fourier transform to obtain a k-space representation. Compared to the learning-based approaches, this additionally requires the evaluation of OCT intensity data for surface smoothing. Surface points are detected based on thresholds and the depth is subsequently clipped to compensate for unevenness. Next, we determine the phase velocity

$$c_{ph} = \frac{\omega}{k_{peak}(\omega)} \tag{6}$$

where ω is the angular frequency and $k_{peak}(\omega)$ is the wave number with the highest amplitude. Assuming that the measured signal corresponds to the Rayleigh surface waves, the bulk shear wave velocity can be calculated according to

$$c_S = \frac{c_{ph}}{(0.862 + 1.14\nu)/(1+\nu)} \approx 1.05\, c_{ph} \tag{7}$$

for a homogeneous, isotropic, linear-elastic and nearly incompressible sample [4,31]. Once we have obtained the bulk wave velocity, we can reconstruct Young's modulus with

$$E = 2\rho(1+\nu)c_S^2. \tag{8}$$

The Poisson's ratio for all gelatin gels and soft tissue samples is assumed to be $\nu = 0.5$. We assume a density of $\rho = 1020$ kg m^{-3} for all gelatin samples, similar to [51]. Estimated velocities for c_S below 1 m s^{-1} and above 10 m s^{-1} are disregarded as they do not correspond to the range of typically observed velocities for soft tissue [52]. We adapt the processing to the data acquisition protocol and reduce the image noise by the known excitation frequency with a bandpass filter. We obtain an improved velocity reconstruction if we disregard the 10$^{\text{th}}$ percentile of pixels with the lowest amplitude.

2.4. Data sets

To generate sufficient training data with known elastic properties, we consider tissue-mimicking phantoms. We prepare gelatin phantoms with a weight ratio of 5 %, 10 %, 15 % and 20 % of gelatin to water. We obtain Young's modulus as a ground truth for training by uniaxial compression tests on cylindrical gelatin samples. We obtain 17 kPa, 56 kPa, 97 kPa and 139 kPa for the four different gelatin concentrations, respectively. We prepare five phantoms per elasticity and perform OCE measurements at 25 different positions on each phantom. We select one independent phantom from each gelatin concentration as a test set and perform cross-validation based on the remaining phantoms during training.

In addition to the main data set used in training, we obtain data for further validation of our models on unseen samples (Fig. 4). First, we consider the generalization from homogeneous to heterogeneous samples with three phantoms that simulate stiff lesions in soft surroundings. The three phantoms are generated by embedding stiff cylindrical inclusions in 5 % gelatin or a Young's modulus of 17 kPa. We consider one inclusion with an elastic modulus of 56 kPa and a diameter of 29 mm and two inclusions with 97 kPa and 18 mm for their Young's modulus and diameter, respectively. We systematically acquire measurements at different locations in a grid and visualize elastography maps of the heterogeneous phantoms. Each location is spaced 4 mm apart in both lateral directions, but we only partially image the larger inclusion. We therefore obtain 54 data points over a range of 20 mm × 32 mm for the 29 mm inclusion phantom and 81 measurements over a range of 32 mm × 32 mm for the two 18 mm inclusions.

Second, we consider fresh post-mortem heart, kidney and liver tissue. One sample of each organ is obtained from two body donors as examples of solid organs and we acquire four measurements per sample (Fig. 4). We are unable to obtain gold standard compression measurements for the organs and instead observe the palpation force during indentation with the tool. We use the robot

Biomedical Optics EXPRESS

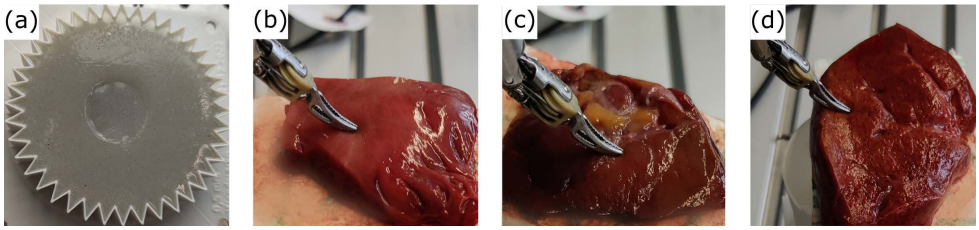

Fig. 4. In addition to the homogeneous training data, we test the generalization of our models to heterogeneous phantoms with stiff inclusions (a). Finally, we evaluate our models on ex-vivo human soft tissue. Samples from one body donor are shown for heart, kidney and liver tissue (b-d). Data acquisition for inclusion phantoms and tissue samples is conducted analogous to homogeneous phantoms (Fig. 2).

to drive the tool 4 mm into the sample and record force data with a high-resolution force sensor (Nano 43, ATI, USA). We then qualitatively compare the maximum observed palpation force with the reconstruction of the elastic modulus by OCE.

For both additional data sets, the OCE data acquisition follows the same methodology as for the training data and the predictions on the additional test sets are based on the ensemble of cross-validation models. Note that we only train on homogeneous gelatin data.

2.4.1. Surface data augmentation

The homogeneous training data show predominantly flat surfaces, which leads to a purely horizontal wave propagation. To account for more complex surface topographies during testing and to generalize better, e.g. for the heterogeneous phantoms and tissue samples, we therefore employ data augmentation during training to simulate different tissue surfaces. We randomly deform the homogeneous sample surface based on a logistic function

$$f(x) = \frac{L}{1 + e^{-kx}} + L_0 \tag{9}$$

with which we shift the depth of the A-scans over the lateral dimension x. L and L_0 are randomly chosen so that the maximum shift is between 0 and 50 pixels and the slope k is randomly sampled between 0 and 4. Examples of the resulting surface augmentation can be found in Fig. 5. Additionally, we employ spatial and temporal flipping and the addition of shot and speckle noise during data augmentation. The same data pre-processing and augmentation steps are used for all learning-based approaches.

2.5. Implementation details

We train all models for 100 epochs using the mean squared error (MSE) loss and the Adam optimizer [53]. We tune hyperparameters based on the validation set. We train the 2D VP-NETs with a batch size of 128. We train the DenseNets variants and our approach with a batch size of 16. We achieve the best performance with a learning rate of $2{\times}10^{-4}$ for DenseNets variants and VP-NET. For both CNN-based approaches, we follow a continuous reduction of the learning rate when the validation error reaches a plateau. For our transformer-based approach, we achieve the best results with a learning rate of $1{\times}10^{-4}$, but with a linear warm-up of the learning rate over 10 % of the training steps, followed by cosine annealing. We also adjust the beta values to 0.9 and 0.95 for Adam and employ gradient clipping. We optimize embedding dimension, depth and width of the encoder and obtain best results with a reasonable parameter size for an embedding dimension of 768, 12 layers and 12 heads. For patch sequencing, we consider cubic patches of size $p = 8 \times 8 \times 8$ and reduce the lateral dimension to the closest dimension divisible

Biomedical Optics EXPRESS

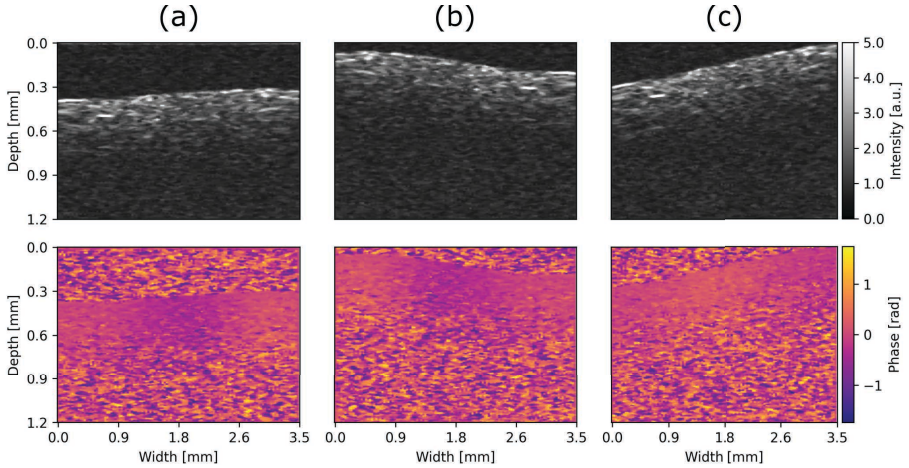

Fig. 5. Example OCE sequence corresponding to a single B-scan from the homogeneous training data (a) and two random augmentations of the same measurement (b-c). The intensity data is also shown on top for better visualization in addition to the phase data (below) used for wave-based OCE. OCE data is standardized during pre-processing.

by p. The architecture of the VP-NET model is implemented according to [38]. But here, VP-NET is also trained to predict the elastic modulus directly, analogous to all other approaches considered here, instead of predicting only the intermediate phase velocity obtained by TOF processing [38]. VP-NET was originally proposed for slightly larger resolution images (320×320 pixels) and we observed better performance for VP-NET without max-pooling layers designed for decreasing image dimensions. 3D CNNs for spatio-temporal processing are implemented according to [36]. Since the number of parameters in CNN and Transformer models is not directly comparable, we additionally consider two larger DenseNet variants to show that the CNN performance is not limited by the model size. We refer to the approach in [36] with 4 DenseNet blocks per layer, 32 initial features and a growth rate of 5 as Dense-S. For Dense-M and Dense-L, the growth rate is increased to 6 and the blocks per layer to [3,6,9,4] and [4,8,12,6] respectively. Dense-L also receives 48 features in the first layer. Similarly, we additionally consider VP-NET-L as proposed in [38] to investigate the model performance with increased model capacity. To keep the input sizes for the 3D data manageable, we do not process each measurement corresponding to 208 consecutive B-scans as a single input. Instead, we divide the inputs into shorter sequences with a sliding window corresponding to t frames. We examine values between $t = 1$ and $t = 32$, which corresponds to a sequence length of up to 3776 A-scans. Based on these experiments, we choose a compromise between computational effort and model performance. For the 3D DenseNet variants, we use the same optimized sliding window size, while for 2D VP-NET $t = 1$. For model tests, we take the median of the predictions obtained over the sliding window for each measurement. To account for the long token sequences in our approach, we use flash attention [54], that reduces the $O(n^2)$ complexity of self-attention (Eq. (1)) by fast and memory-efficient approximation. All models are implemented in Pytorch v2.2 and trained on an NVIDIA RTX 4090 graphics card. Our implementation is based on the x-transformer library (available at https://github.com/lucidrains/x-transformers). To evaluate model performance, we report the root mean square error (RMSE) and the mean absolute error (MAE). In addition, we consider the mean absolute percentage error (MAPE) and the R2 value. For each learning-based approach, we additionally report parameter count, required computational effort and inference time per sample. We employ the MLXtend permutation

Biomedical Optics EXPRESS

test [55] with 10000 permutations and a significance level of $\alpha = 0.05$ to test for statistically significant differences. When testing generalization to heterogeneous phantoms, we additionally consider the detection of stiff inclusions as a classification task and look at model performance in terms of the area under the receiver operating characteristic (AUROC) and the area under the precision-recall curve (AUPRC).

3. Results

We first optimize and evaluate our approach using our main training data, which contains homogeneous phantoms. Then, we additionally test the model generalization with heterogeneous phantoms containing stiff inclusions and report the estimation of the elastic modulus for human tissue samples.

3.1. Homogeneous phantoms

The error metrics for the test set are shown in Table 1 for all baselines and our transformer-based approach. The predictions per material are shown in Fig. 6 together with the reference measurements. Dense-M, Dense-L and VP-NET-L are omitted and only a single variant of each approach is shown to ensure good visibility. Our transformer-based approach drastically outperforms the baselines in terms of all evaluation metrics and provides a more accurate and robust elasticity reconstruction.

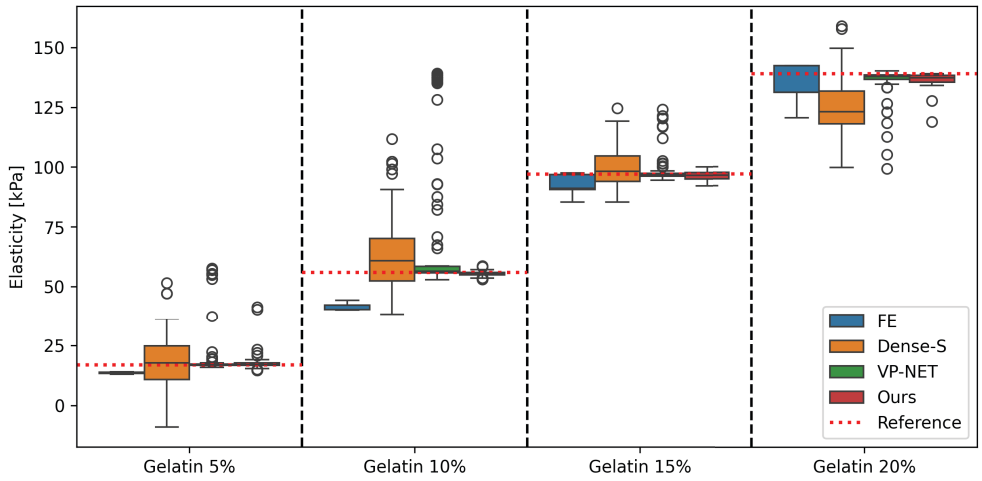

Fig. 6. Results for test set of homogeneous gelatin data for all baselines and our proposed approach. Predicted elasticity is plotted over the different phantoms with reference ground truth measurements. For clarity, only one variant of DenseNet [36] and VP-NET [38] are shown. Differences in predictions for different variants of each approach are also not statistically significant.

Our approach is optimized with respect to A-scan sequence length and PE. Performance for different temporal window sizes with increasing A-scan sequence length up to the equivalent of $t = 32$ consecutive B-scans are shown in Fig. 7. We observe performance improvements with increasing sequence length. However, the required computational load per sample also increases with increasing sequence length, even if the more efficient flash attention is used. We therefore choose a sequence length of 1880 A-scans as a reasonable compromise between model performance and required floating point operations (FLOPs) for our approach. The resulting configuration corresponds to a computational load of 162×10^9 FLOPs per sample. In

Biomedical Optics EXPRESS

Table 1. Error metrics with deviations over cross-validation folds for CNN and transformer architectures. * Conventional FE processing fails in 15.4 % of measurements resulting in unrealistically high values that are excluded here. Best results are marked in bold.

Model	RMSE [kPa]	MAE [kPa]	MAPE	R2	Weights
FE*	9.25	7.80	0.12	0.949	
Dense-S [36]	13.85(168)	10.48(126)	0.22(4)	0.906(2)	109K
Dense-M	13.30(408)	9.36(267)	0.19(4)	0.907(5)	193K
Dense-L	13.08(245)	9.43(173)	0.20(3)	0.914(3)	254K
VP-NET [38]	15.76(615)	5.55(269)	0.12(5)	0.862(8)	8.7M
VP-NET-L [38]	14.33(516)	6.03(274)	0.14(7)	0.888(6)	17.7M
Ours	**2.49(137)**	**1.64(89)**	**0.03(2)**	**0.996(1)**	**85.8M**

comparison the required computations per sample for DenseNet variants are between 32×10^9 and 47×10^9 FLOPs for Dense-S and Dense-L, respectively. VP-NET considers predictions based on a single 2D B-scan and therefore only corresponds to 55×10^6 and 153×10^6 FLOPs for VP-NET and VP-NET-L, respectively. Regarding the inference time per sample, we observe 6.71 ms to 10.61 ms, 0.71 ms to 0.75 ms and 16.5 ms for DenseNet variants, VP-NET variants and our approach, respectively.

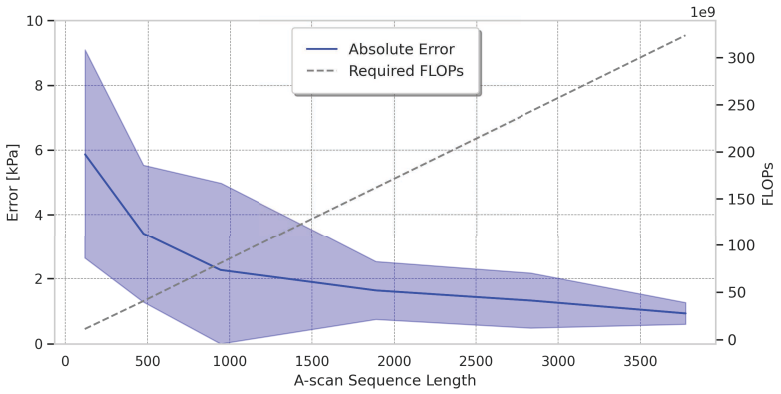

Fig. 7. RMSE and MAE plotted over A-scan sequence length where 118 A-scans are equivalent to a single B-scan. Model performance increases with sequence length but computational demand and memory requirements simultaneously increase.

Besides optimizing data processing, we also investigate our approach with different PE schemes. The resulting high errors for sinusoidal or learnable embeddings (Table 2) show that the attention-based approach is only able to effectively process the long A-scan sequences when RoPE is used. Training our approach with RoPE but without the surface data augmentation leads to an increased RMSE of 7.78(261) kPa and MAE of 2.48(130) kPa.

Finally, we also investigate patch sequencing, where 2D+t volumetric data are processed similar to the 3D DenseNets, but the patches are flattened into embeddings, as originally proposed for VIT [43]. Patch sequencing leads to errors of 3.34(20) kPa and 2.10(4) kPa for RMSE and MAE, respectively. Our approach, which directly processes A-scan sequences, achieves the overall lowest RMSE of 2.49(137) kPa and MAE of 1.64(89) kPa. The model predictions for our approach based on direct sequencing of A-scans and for patch-based sequencing are statistically different ($p<<\alpha$). The predictions between smaller and larger variants were not statistically significant for Dense-S, Dense-M and Dense-L ($p>0.1$) and also not between VP-NET and

Biomedical Optics EXPRESS

Table 2. Error metrics for alternatives we consider during optimization of transformer-based approach. We report errors for training with learnable and sinusoidal encodings instead of RoPE, with RoPE but without surface augmentation, and lastly with RoPE but for VIT-based patch sequencing instead of directly sequencing A-scans.

Parameter	RMSE [kPa]	MAE [kPa]	MAPE	R2	Params
Ours	2.49(137)	1.64(89)	0.03(2)	0.996(1)	85.8M
w/ Sinusoidal Enc.	19.74(924)	15.85(829)	0.39(16)	0.771(21)	85.8M
w/ Learnable Enc.	28.46(1292)	23.90(1191)	0.66(40)	0.528(36)	87.2M
w/o surf. augm.	7.78(261)	2.48(130)	0.03(2)	0.968(2)	85.8M
w/ Patch Sequence	3.34(20)	2.10(4)	0.04(1)	0.995(1)	86M

VP-NET-L. For the remaining analyses, we therefore only report the model performance for one variant. The differences between our approach and all baselines is statistically significant ($p<<\alpha$).

3.2. Inclusion phantoms

Next, we compare the generalization of our approach to all baselines with heterogeneous phantoms containing stiff inclusions. The predictions of the different approaches — trained on homogeneous phantom data except for FE — are shown in Fig. 8. The MAE for the simulated lesions is 13.27(2016) kPa, 24.76(1159) kPa, 28.97(2046) kPa and 7.44(1443) kPa for FE, Dense-S, VP-NET and our approach, respectively. FE leads to unrealistically high values for two measurements. The visualized predictions show that the two CNN-based baselines have difficulties to generalize to the heterogeneous samples and to highlight the simulated lesions. VP-NET leads to an overestimation of the elastic modulus near the edges around the inclusions. Overall, the CNN-based approaches lead to a poor contrast between soft surrounding and stiff inclusions. In comparison, our approach handles the heterogeneous phantom data more reliably and can effectively discriminate the simulated lesions. This becomes even clearer when we consider the AUROC and AUPRC for inclusion detection (Fig. 9). Our approach outperforms all baselines with the highest AUROC and AUPRC values of 0.997 and 0.991, respectively. While FE and Dense-S lead to similar performance, VP-NET shows the worst performance with values of 0.840 and 0.652 for AUROC and AUPRC, respectively.

3.3. Body donor tissue samples

Finally, we evaluate the performance of our approach on ex-vivo tissue from two body donors. Elasticity estimations for heart, kidney and liver tissue samples are shown in Fig. 10, top. In addition, we qualitatively compare the maximum force observed during tissue indentation over a fixed distance and the Young's modulus reconstruction of each approach. The comparison with this surrogate reference shows the highest correlation for our proposed approach (Fig. 10, bottom). Our method leads to elasticity estimates of 54.96(3645) kPa, 29.87(530) kPa and 38.67(792) kPa for heart, kidney and liver tissue, respectively. The conventional FE-based reconstruction of the elastic modulus is extremely unreliable and provides unrealistic values for 21 out of 24 measurements (87.5 %).

4. Discussion

In this work, we consider transformers for OCE in conjunction with a wave-inducing surgical tool to enable robust and efficient quantitative palpation in a minimally invasive setting. We investigate end-to-end reconstruction of Young's modulus from OCE phase data to address two challenges of conventional elasticity reconstruction. First, robust and reliable estimation of wave velocity with conventional estimators can be difficult, e.g., due to imperfect scanning, noise, or phase

Biomedical Optics EXPRESS

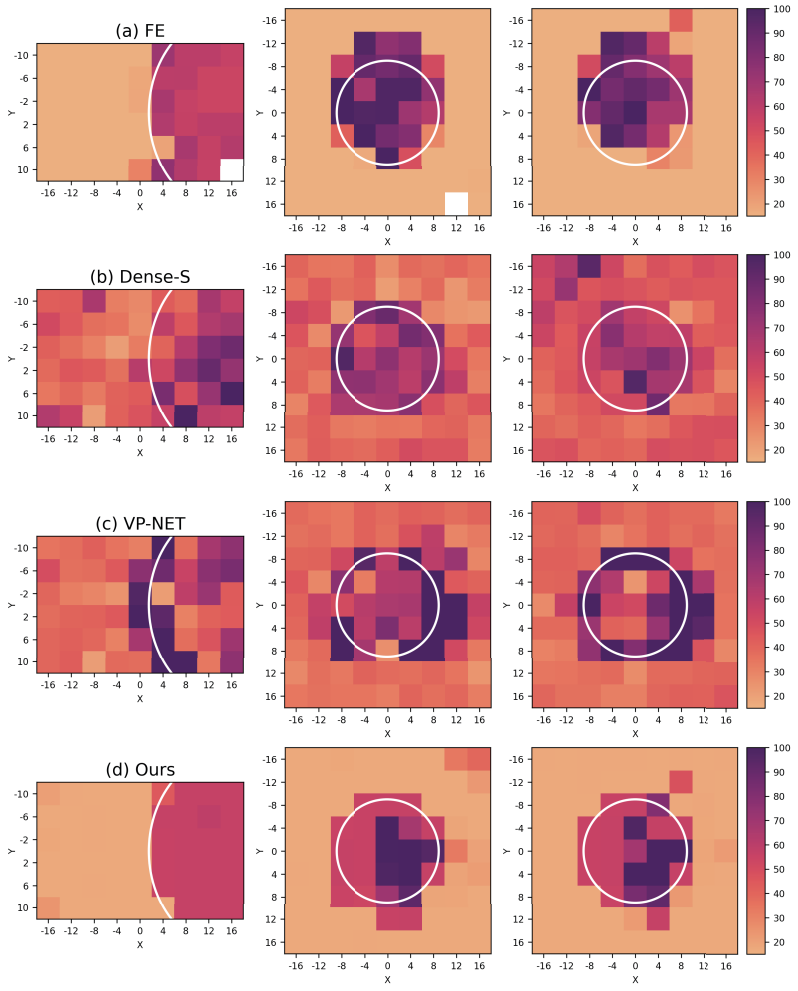

Fig. 8. Model predictions for the three heterogeneous phantoms with stiff inclusions with FE (a), Dense-S (b), VP-NET (c) and our approach (d). The columns correspond to a 56 kPa inclusion with diameter of 29 mm, and two 97 kPa inclusions with diameters of 18 mm for left, middle and right, respectively. Failed conventional FE processing depicted as white.

Biomedical Optics EXPRESS

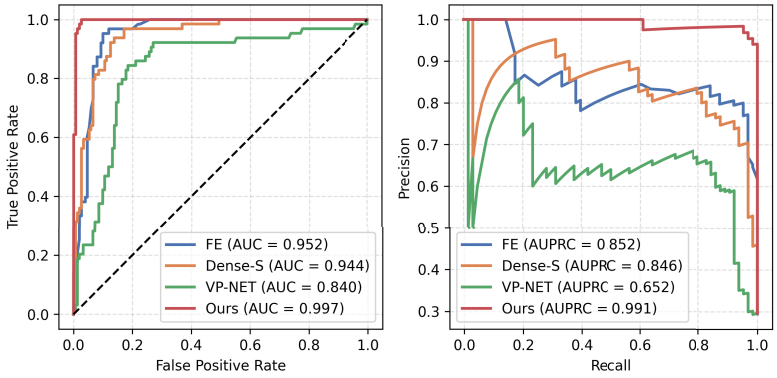

Fig. 9. AUROC and AUPRC curves when considering the different approaches for the discrimination between simulated lesions and soft surroundings for the heterogeneous phantoms.

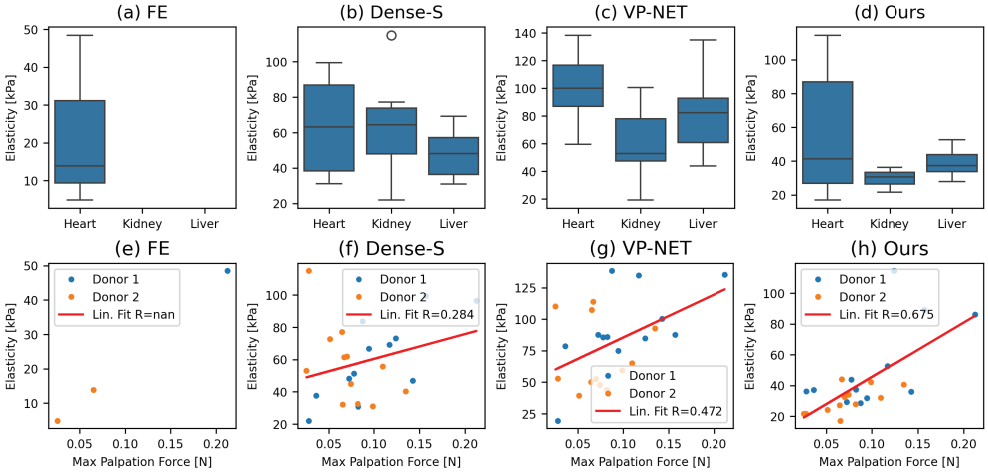

Fig. 10. Young's modulus predictions for the tissue samples for all approaches (a-d). As we do not have the reference measurements of elasticity for the organs, we palpate the tissue with the tool itself and measure the maximum contact force reached after indenting the tissue 4 mm. This method does not give us a ground truth elasticity but we investigate the correlation between predicted elasticity and indentation force (e-h).

wrapping. This is emphasized in our experiments as we observe unrealistic estimates of over 50 m s^{-1} for FE, particularly for noisy measurements of soft gelatin phantoms and tissue samples. We therefore exclude 15.4 % of the measurements for homogeneous phantoms. For our soft tissue samples only 3 out of 24 measurements result in realistic estimates. The second challenge is to correctly model the observed surface wave in order to derive accurate biomechanical properties from the estimated wave velocity. The reconstructed elasticity is highly dependent on the appropriate model selection [30] and is also influenced by the assumption of material properties that change along with elastic properties, e.g. density or Poisson's ratio (Eq. (8)). Here, we show that transformer architectures are better suited to handle the spatio-temporal A-scan sequences than previously considered learning-based approaches based on CNNs [25,36–38]. Our transformer-based approach achieves the best overall performance in our experiments.

Biomedical Optics EXPRESS

Direct processing of A-scan sequences also outperforms patch-based sequencing (Table 2). In contrast to patch inputs for static, morphological OCT imaging [43,44,46], patch sequencing in functional OCE imaging combines spatial and temporal information, resulting in less accurate elasticity reconstruction. Therefore, it seems advantageous to leverage the inherently sequential OCT data and keep the relationship between the tokens purely temporal. The spatial dependency is fully learned, which could be particularly advantageous considering the non-uniform lateral sampling caused by the sinusoidal oscillation of the resonant mirrors [56].

In optimising our approach, we find that RoPE is essential for the effective processing of long A-scan sequences. We therefore see significant performance differences in contrast to the PE comparisons performed for VIT [42]. Transformers trained with sinusoidal or learned PE lead to significantly larger errors even for homogeneous phantoms and are not able to outperform the previous CNN-based approaches. In contrast, RoPE allows us to effectively learn spatial dependencies during training. It is noteworthy that RoPE is applied in each attention layer which therefore injects positional information beyond the initial input layer and enables faster and more robust convergence [49]. In addition to PE, we also optimize our approach with respect to the length of the A-scan sequence and observe performance improvements with longer sequences and thus a longer temporal window. However, this also increase memory and computational cost and we therefore select the analysed length of 1880 A-scans as a compromise between performance and memory requirement. DenseNets contain more than an order of magnitude fewer parameters but the required computational effort and time per sample is only slightly increased for our approach, e.g. inference of 10.61 ms and 16.5 ms for Dense-L and ours, respectively. In contrast, VP-NET was specifically tailored for efficiency and only considers individual B-scans. This results in significantly lower inference times and required FLOPs. We observe better performance for VP-NET without max-pooling layers and therefore obtain larger models than in [38]. However, we find that only our attention-based approach can scale effectively in terms of computational load and model capacity. This is particularly evident as the larger variants of 3D DenseNet and 2D VP-NET do not significantly outperform their smaller counterparts. Furthermore, the performance of the model improves significantly thanks to our surface augmentation scheme, which allows the model to better learn the reconstruction of the elastic modulus regardless of the surface structure and shape.

Even though the same data augmentation is used in training VP-NETs and DenseNets, our approach shows superior performance in evaluating generalization from homogeneous to heterogeneous phantoms. Our approach shows effective discrimination of the stiff inclusions from the soft neighbourhood both qualitatively (Fig. 8) and quantitatively (Fig. 9). We also achieve better delineation of the inclusion boundaries compared to other learning-based approaches, where the B-scan may partially contain both the inclusion and the surrounding material, especially with VP-NET [38]. It is worth noting that the inclusion data is limited to 216 measurements and only 64 measurements (29.6 %) contain simulated lesions. As the inclusion data set is therefore imbalanced, the differences between the approaches are particularly notable when considering the AUPRC curve. The noisy estimates for DenseNet and VP-NET lead to high false-positive rates even at low thresholds. As expected, the conventional processing using FE generalizes relatively well to the heterogeneous environment as it does not depend on the distribution of the training data. Similar to all baselines, performance for our approach also decreases when transitioning from homogeneous to the more complex heterogeneous samples. Nevertheless, we achieve lower absolute errors and higher AUPRC and AUROC values with our proposed method.

Finally, we qualitatively evaluate the model predictions using soft tissue samples. Since we do not have gold standard reference measurements of elasticity for the organs, we palpate the tissue with the tool itself and measure the maximum contact force as a surrogate for specifying elastic properties. With this method, we do not obtain ground truth for elasticity and can only examine the correlation between predicted elasticity and indentation force. Although our approach shows

Biomedical Optics EXPRESS

a higher correlation than the baselines, this comparison is limited because the indentation force strongly depends on contact surface between tool and tissue as well as on the shape and stiffness of the tissue sample. Additionally, we note that our linear correlation analysis can only provide a rough approximation of the non-linear elasticity in tool-tissue interactions. Nevertheless, in contrast to the baselines, the elastic modulus values reconstructed using our approach are within the specified range of 8 kPa to 55 kPa [57], 25 kPa to 40 kPa [58] and 8 kPa to 48 kPa [59] for heart, kidney and liver, respectively. Future comparisons could consider alternative elastography approaches for samples with unknown elastic properties, e.g. compression-based OCE.

The conducted experiments highlight the potential of our approach. Our model accurately learns both spatial and temporal components of the wave field to estimate sample elasticity. In contrast, the FE approach shows less consistent predictions, particularly for stiffer samples (Fig. 6), suggesting spatial wave distortion effects at higher wave velocities. Modifications to the scanning setup could improve conventional processing, e.g. through rotating polygon mirrors that enable faster switching and reduce pauses between successive B-scans. However, our data-driven approach seems to inherently account for such effects present in the training data, including noisy measurements, wave distortion, and asynchronous wave excitation and scanning. However, our learning-based approach offers limited explainability in comparison to conventional methods. Physics-based models typically facilitate a more transparent analysis of potential error sources and systematic biases. Explicit models may offer insights into limitations and uncertainties related to system and scanning requirements. It will be interesting to further study improving the explainability of our approach to better address the trade-off between the improved accuracy we observed for transformers and the better interpretability of conventional methods. The phantom experiments allow a quantitative comparison in a laboratory setting, but are limited in terms of complexity of wave propagation and have limited wave distortion compared to anisotropic and heterogeneous soft tissue. The limited sample size and high standard deviation indicate that further validation using soft tissue samples will be required. For the validation of intraoperative applicability, e.g. for the assessment of tumour margins based on elasticity [60], extensive evaluation and further fine-tuning with tissue data is required. In contrast to the method proposed for VP-NET [38], where labels obtained by conventional TOF velocity estimation were used, we reconstruct the elastic modulus directly from the OCE phase data. Therefore, we train our model based on reference measurements for the elastic modulus rather than on the velocity label obtained by conventional processing. This provides the ability to accurately reconstruct elasticity independent of the limitations of the conventional Fourier or TOF estimator. However, this also limits the acquisition of training data, as the ground truth reference measurements must be performed together with the OCE. Further experiments should therefore attempt to combine the uncertain but easily obtainable conventional velocity estimation and the accurate ground truth reference measurement, e.g. via soft labels or curriculum learning. We currently also derive the Young's modulus from the OCE phase data, as this is the most commonly used elastic property for comparing tissue stiffness. However, our learning-based procedure is not limited to this linearization and further research should include the prediction of non-linear elastic properties.

5. Conclusion and outlook

To summarise, the experiments performed show how our transformer-based approach can exploit the inherently sequential nature of OCE data by directly processing A-scan sequences. The approach therefore allows us to decouple spatial and temporal information to better capture the dynamics of wave propagation. We demonstrate the potential of our approach for robust reconstruction of the elastic modulus in homogeneous and heterogeneous phantoms as well as in soft tissue samples. In combination with a miniaturized endoscopic OCT probe [6,61], our approach could be used for optical palpation in surgery or autopsy. Accurate intraoperative OCE could then give physicians back the ability to feel for changes in elastic properties during

Biomedical Optics EXPRESS

minimally invasive procedures. In addition to localizing pathological tissue, knowledge of biomechanical properties also enables better monitoring of tool-tissue interactions, e.g. in vision-based force estimation [62]. Finally, any OCT system inherently captures temporal sequences of A-scans. Further evaluation of our transformer-based approach should particularly explore tasks where conventional alternatives are limited, e.g. segmentation. Additionally, our methodology is not limited to a specific OCT system or scanning regime. However, high-speed scanning is essential for visualizing wave propagation. It will be interesting to investigate if the learning-based approach could also enable slower scanning speeds than the considered 1.5 MHz system. However, changes to any system parameters would require additional training data and fine-tuning of model weights. Our approach to directly process A-scan sequences can also be applied to any sequence length or scan protocol, e.g. M-mode and C-Mode or different scan rates.

Funding. Deutsche Forschungsgemeinschaft (Grant SCHL 1844/6-1); Technische Universität Hamburg (i^3 initiative); HORIZON EUROPE Framework Programme (grant agreement No. 101059903, EU Funds Investments 2021-2027); Technische Universität Hamburg (ICCIR); Universitätsklinikum Hamburg-Eppendorf (ICCIR); Technische Universität Hamburg (Funding Programme Open Access Publishing).

Acknowledgments. The study was conducted in accordance with the Declaration of Helsinki, and approved by the Institutional Review Board of the Hamburg Chamber of Physicians (No.: 2020-10353-BO-ff). Informed consent was obtained from all subjects involved in the study by their legal representatives and next of kin.

Disclosures. The authors declare that there are no conflicts of interest related to this article.

Data availability. Data underlying the results presented in this paper are not publicly available at this time but may be obtained from the authors upon reasonable request.

References

1. K. Hoyt, B. Castaneda, M. Zhang, *et al.*, "Tissue elasticity properties as biomarkers for prostate cancer," Cancer biomarkers **4**(4-5), 213–225 (2008).
2. T. A. Krouskop, T. M. Wheeler, F. Kallel, *et al.*, "Elastic moduli of breast and prostate tissues under compression," Ultrason. imaging **20**(4), 260–274 (1998).
3. B. F. Kennedy, K. M. Kennedy, and D. D. Sampson, "A review of optical coherence elastography: Fundamentals, techniques and prospects," IEEE J. Sel. Top. Quantum Electron. **20**(2), 272–288 (2014).
4. F. Zvietcovich and K. V. Larin, "Wave-based optical coherence elastography: The 10-year perspective," Prog. Biomed. Eng. **4**(1), 012007 (2022).
5. M. A. Kirby, I. Pelivanov, S. Song, *et al.*, "Optical coherence elastography in ophthalmology," J. Biomed. Opt. **22**(12), 1–28 (2017).
6. M. Lee, H. Bang, E. Lee, *et al.*, "Imaging peritoneal blood vessels through optical coherence tomography angiography for laparoscopic surgery," J. Biophotonics **17**(1), e202300221 (2024).
7. J. Walther, J. Golde, M. Albrecht, *et al.*, "A handheld fiber-optic probe to enable optical coherence tomography of oral soft tissue," IEEE Trans. Biomed. Eng. **69**(7), 2276–2282 (2022).
8. H. Pahlevaninezhad, M. Khorasaninejad, Y.-W. Huang, *et al.*, "Nano-optic endoscope for high-resolution optical coherence tomography in vivo," Nat. Photonics **12**(9), 540–547 (2018).
9. T. Zhang, S. Yuan, C. Xu, *et al.*, "Pneumaoct: Pneumatic optical coherence tomography endoscopy for targeted distortion-free imaging in tortuous and narrow internal lumens," Am. Assoc. for Adv. Sci. **10**(35), 1 (2024).
10. J. Li, S. Thiele, B. C. Quirk, *et al.*, "Ultrathin monolithic 3d printed optical coherence tomography endoscopy for preclinical and clinical use," Light: Sci. Appl. **9**(1), 124 (2020).
11. A. M. D. Lee, L. Cahill, K. Liu, *et al.*, "Wide-field in vivo oral oct imaging," Biomed. Opt. Express **6**(7), 2664–2674 (2015).
12. M. Ourak, J. Smits, L. Esteveny, *et al.*, "Combined oct distance and fbg force sensing cannulation needle for retinal vein cannulation: in vivo animal validation," Int. J. Comput. Assist. Radiol. Surg. **14**(2), 301–309 (2019).
13. Q. Tang, C.-P. Liang, K. Wu, *et al.*, "Real-time epidural anesthesia guidance using optical coherence tomography needle probe," Quant. Imaging Med. Surg. **5**(1), 118–124 (2015).
14. R. Mieling, S. Latus, M. Fischer, *et al.*, "Optical coherence elastography needle for biomechanical characterization of deep tissue," in *Med Image Comput Comput Assist Interv*, (Springer, 2023), pp. 607–617.
15. J. Ormachea and K. J. Parker, "Elastography imaging: the 30 year perspective," Phys. Med. Biol. **65**(24), 24TR06 (2020).
16. Q. Fang, B. Krajancich, L. Chin, *et al.*, "Handheld probe for quantitative micro-elastography," Biomed. Opt. Express **10**(8), 4034–4049 (2019).
17. X. Wang, Q. Wu, J. Chen, *et al.*, "Development of a handheld compression optical coherence elastography probe with a disposable stress sensor," Opt. Lett. **46**(15), 3669 (2021).
18. P. Gong, S. L. Chin, W. M. Allen, *et al.*, "Quantitative micro-elastography enables in vivo detection of residual cancer in the surgical cavity during breast-conserving surgery," Cancer Res. **82**(21), 4093–4104 (2022).

Biomedical Optics EXPRESS

19. L. P. Hariri, G. T. Bonnema, K. Schmidt, *et al.*, "Laparoscopic optical coherence tomography imaging of human ovarian cancer," Gynecol. Oncol. **114**(2), 188–194 (2009).
20. S. Latus, S. Grube, T. Eixmann, *et al.*, "A miniature dual-fiber probe for quantitative optical coherence elastography," IEEE Trans. Biomed. Eng. **70**(11), 3064–3072 (2023).
21. Y. Qu, T. Ma, Y. He, *et al.*, "Miniature probe for mapping mechanical properties of vascular lesions using acoustic radiation force optical coherence elastography," Sci. Rep. **7**(1), 4731 (2017).
22. A. B. Karpiouk, D. J. VanderLaan, K. V. Larin, *et al.*, "Integrated optical coherence tomography and multielement ultrasound transducer probe for shear wave elasticity imaging of moving tissues," J. Biomed. Opt. **23**(10), 1–7 (2018).
23. H. Xu, Q. Xia, C. Shu, *et al.*, "In vivo endoscopic optical coherence elastography based on a miniature probe," Biomed. Opt. Express **15**(7), 4237 (2024).
24. M. Neidhardt, S. Latus, T. Eixmann, *et al.*, "Deep learning for high speed optical coherence elastography with a fiber scanning endoscope," IEEE Trans. Med. Imaging **44**(3), 1445–1453 (2025).
25. M. Neidhardt, R. Mieling, S. Latus, *et al.*, "A modified da vinci surgical instrument for oce based elasticity estimation with deep learning,".
26. S. Wang and K. V. Larin, "Noncontact depth-resolved micro-scale optical coherence elastography of the cornea," Biomed. Opt. Express **5**(11), 3807–3821 (2014).
27. S. Song, Z. Huang, T.-M. Nguyen, *et al.*, "Shear modulus imaging by direct visualization of propagating shear waves with phase-sensitive optical coherence tomography," J. Biomed. Opt. **18**(12), 1 (2013).
28. Z. Han, M. Singh, S. R. Aglyamov, *et al.*, "Quantifying tissue viscoelasticity using optical coherence elastography and the rayleigh wave model," J. Biomed. Opt. **21**(9), 090504 (2016).
29. A. Ramier, B. Tavakol, and S.-H. Yun, "Measuring mechanical wave speed, dispersion, and viscoelastic modulus of the cornea using optical coherence elastography," Opt. Express **27**(12), 16635–16649 (2019).
30. Z. Han, J. Li, M. Singh, *et al.*, "Quantitative methods for reconstructing tissue biomechanical properties in optical coherence elastography: a comparison study," Phys. Med. Biol. **60**(9), 3531–3547 (2015).
31. X. Feng, G.-Y. Li, and S.-H. Yun, "Ultra-wideband optical coherence elastography from acoustic to ultrasonic frequencies," Nat. Commun. **14**(1), 4949 (2023).
32. G. Shi, Y. Zhang, Y. Wang, *et al.*, "Quantitative evaluation of human lens and lens capsule elasticity by optical coherence elastography based on a rayleigh wave model," J. Biophotonics **17**(12), e202400322 (2024).
33. A. Ramier, A. M. Eltony, Y. Chen, *et al.*, "In vivo measurement of shear modulus of the human cornea using optical coherence elastography," Sci. Rep. **10**(1), 17366 (2020).
34. C. S. Lee, A. J. Tyring, N. P. Deruyter, *et al.*, "Deep-learning based, automated segmentation of macular edema in optical coherence tomography," Biomed. Opt. Express **8**(7), 3440–3448 (2017).
35. A. P. Sunij, K. Saikat, S. Gayathri, *et al.*, "Octnet: A lightweight cnn for retinal disease classification from optical coherence tomography images," Comput. Methods Programs Biomed. **200**, 105877 (2021).
36. M. Neidhardt, M. Bengs, S. Latus, *et al.*, "Deep learning for high speed optical coherence elastography," in *2020 IEEE 17th International Symposium on Biomedical Imaging (ISBI)*, (IEEE, 2020), pp. 1583–1586.
37. M. Neidhardt, M. Bengs, S. Latus, *et al.*, "4d deep learning for real-time volumetric optical coherence elastography," Int. J. Comput. Assist. Radiol. Surg. **16**(1), 23–27 (2021).
38. Y. Zhang, J. Liao, Z. Feng, *et al.*, "Vp-net: an end-to-end deep learning network for elastic wave velocity prediction in human skin in vivo using optical coherence elastography," Front. Bioeng. Biotechnol. **12**, 1 (2024).
39. A. G. Howard, M. Zhu, B. Chen, *et al.*, "Mobilenets: Efficient convolutional neural networks for mobile vision applications,"
40. J. Hu, L. Shen, and G. Sun, "Squeeze-and-excitation networks," in *Proceedings of the IEEE conference on computer vision and pattern recognition*, (2018), pp. 7132–7141.
41. A. Vaswani, N. Shazeer, N. Parmar, *et al.*, "Attention is all you need," Advances in Neural Information Processing Systems **30**, (2017).
42. A. Dosovitskiy, L. Beyer, A. Kolesnikov, *et al.*, "An image is worth 16×16 words: Transformers for image recognition at scale," arXiv (2020).
43. C. Playout, R. Duval, M. C. Boucher, *et al.*, "Focused attention in transformers for interpretable classification of retinal images," Med. Image Anal. **82**, 102608 (2022).
44. Z. Tan, F. Shi, Y. Zhou, *et al.*, "A multi-scale fusion and transformer based registration guided speckle noise reduction for oct images," IEEE Trans. Med. Imaging **43**(1), 473–488 (2024).
45. B. Ait Hammou, F. Antaki, M.-C. Boucher, *et al.*, "Mbt: Model-based transformer for retinal optical coherence tomography image and video multi-classification," Int. J. Med. Informatics **178**, 105178 (2023).
46. D. Philippi, K. Rothaus, and M. Castelli, "A vision transformer architecture for the automated segmentation of retinal lesions in spectral domain optical coherence tomography images," Sci. Rep. **13**(1), 517 (2023).
47. G. Li, K. Wang, Y. Dai, *et al.*, "Physics-based optical coherence tomography angiography (octa) image correction for shadow compensation," IEEE Trans. Biomed. Eng. **72**(3), 891–898 (2025).
48. M. Raghu, T. Unterthiner, S. Kornblith, *et al.*, "Do vision transformers see like convolutional neural networks?" Advances in Neural Information Processing Systems **34**, 12116–12128 (2021).
49. J. Su, M. Ahmed, Y. Lu, *et al.*, "Roformer: Enhanced transformer with rotary position embedding," Neurocomputing **568**, 127063 (2024).

Biomedical Optics EXPRESS

50. S. Beuve, L. Kritly, S. Callé, *et al.*, "Diffuse shear wave spectroscopy for soft tissue viscoelastic characterization," Ultrasonics **110**, 106239 (2021).
51. S. Pansino and B. Taisne, "Shear wave measurements of a gelatin's young's modulus," Front. Earth Sci. **8**, 1 (2020).
52. M. Fink and M. Tanter, "Multiwave imaging and super resolution," Phys. Today **63**(2), 28–33 (2010).
53. D. P. Kingma and J. Ba, "Adam: A method for stochastic optimization," arXiv (2014).
54. T. Dao, D. Fu, S. Ermon, *et al.*, "Flashattention: Fast and memory-efficient exact attention with io-awareness," Adv. Neural Inf. Process. Syst. **35**(1189), 16344–16359 (2022).
55. S. Raschka, "Mlxtend: Providing machine learning and data science utilities and extensions to python's scientific computing stack," J. open source software **3**(24), 638 (2018).
56. B. Kowalski, V. Akondi, and A. Dubra, "Correction of non-uniform angular velocity and sub-pixel jitter in optical scanning," Opt. Express **30**(1), 112–124 (2022).
57. R. Emig, C. M. Zgierski-Johnston, V. Timmermann, *et al.*, "Passive myocardial mechanical properties: meaning, measurement, models," Biophys. Rev. **13**(5), 587–610 (2021).
58. D. Radulescu, I. Peride, L. C. Petcu, *et al.*, "Supersonic shear wave ultrasonography for assessing tissue stiffness in native kidney," Ultrasound Med. & Biol. **44**(12), 2556–2568 (2018).
59. A. Nava, E. Mazza, M. Furrer, *et al.*, "In vivo mechanical characterization of human liver," Med. Image Anal. **12**(2), 203–216 (2008).
60. D. W. Good, G. D. Stewart, S. Hammer, *et al.*, "Elasticity as a biomarker for prostate cancer: A systematic review," BJU Int. **113**(4), 523–534 (2014).
61. M. Neidhardt, S. Latus, T. Eixmann, *et al.*, "Deep learning for high speed optical coherence elastography with a fiber scanning endoscope," IEEE Transactions on Medical Imaging (2024).
62. M. Neidhardt, R. Mieling, M. Bengs, *et al.*, "Optical force estimation for interactions between tool and soft tissues," Sci. Rep. **13**(1), 506 (2023).

7.6 A Modified da Vinci Surgical Instrument for Optical Coherence Elastography with Deep Learning

Conference: 2024 10th IEEE RAS/EMBS International Conference for Biomedical Robotics and Biomechatronics (BioRob)

Year: 2024

M. Neidhardt, R. Mieling, S. Latus, M. Fischer, T. Maurer, and A. Schlaefer, "A modified da vinci surgical instrument for optical coherence elastography with deep learning," in *2024 10th IEEE RAS/EMBS International Conference for Biomedical Robotics and Biomechatronics (BioRob)*, IEEE, 2024, pp. 1196–1201

2024 10th IEEE RAS/EMBS International Conference for
Biomedical Robotics and Biomechatronics (BioRob)
1-4 September 2024. Heidelberg, Germany

A Modified da Vinci Surgical Instrument for Optical Coherence Elastography with Deep Learning

Maximilian Neidhardt[1,2]*, Robin Mieling[1]*, Sarah Latus[1], Martin Fischer[1],
Tobias Maurer[3,4], and Alexander Schlaefer[1,2]

***Abstract*— Robot-assisted surgery has advantages compared to conventional laparoscopic procedures, e.g., precise movement of the surgical instruments, improved dexterity, and high-resolution visualization of the surgical field. However, mechanical tissue properties may provide additional information, e.g., on the location of lesions or vessels. While elastographic imaging has been proposed, it is not readily available as an online modality during robot-assisted surgery. We propose modifying a da Vinci surgical instrument to realize optical coherence elastography (OCE) for quantitative elasticity estimation. The modified da Vinci instrument is equipped with piezoelectric elements for shear wave excitation and we employ fast optical coherence tomography (OCT) imaging to track propagating wave fields, which are directly related to biomechanical tissue properties. All high-voltage components are mounted at the proximal end outside the patient. We demonstrate that external excitation at the instrument shaft can effectively stimulate shear waves, even when considering damping. Comparing conventional and deep learning-based signal processing results in mean absolute errors of 19.27 kPa and 6.29 kPa for a range of 17 kPa-139 kPa, respectively. These results illustrate that precise quantitative elasticity estimates can be obtained. We also demonstrate quantitative elasticity estimation on ex-vivo tissue samples of heart, liver and stomach, and show that the measurements can be used to distinguish soft and stiff tissue types.**

I. INTRODUCTION

Robot-assisted minimally invasive surgery has advantages like improved precision, shortened recovery, and improved ergonomics for the surgeon [1]. It has been widely adopted and the da Vinci surgical system (Intuitive Surgical, Inc., USA) is the most frequently used platform for robot-assisted surgery (RAS) [2]. Typically, RAS is based on endoscopic vision, often using stereo cameras, which provide an excellent overview of the surgical field. However, the camera images only show the tissue surface and do not measure biomechanical tissue properties [3], [4], e.g., its elasticity, which may provide additional information complementary to the visual appearance. Conventionally, palpation is used to identify tissues and lesions, e.g., in open surgery, and several elastographic imaging modalities have been developed, including ultrasound elastography and magnetic resonance elastography, which allow using tissue stiffness during diagnosis. However, intra-operative real-time quantitative elastography is currently not available, particularly during minimally invasive procedures. Yet, estimating tissue elasticity is beneficial for navigation, e.g., to identify the tissue type including lesions and vessels [5], to detect the shape, e.g., of lesions, or even to generate force feedback [6]. Note, that while surgeons can train to largely compensate for the lack of haptics and force feedback, more autonomous robot assistance may still benefit from elasticity estimates, e.g., as an additional safety feature. In this context, we consider a minimally invasive RAS scenario as illustrated in Fig.1, where the instruments and the laparoscopic camera are controlled via robotic arms and quantitative elasticity values are predicted from optical measurements.

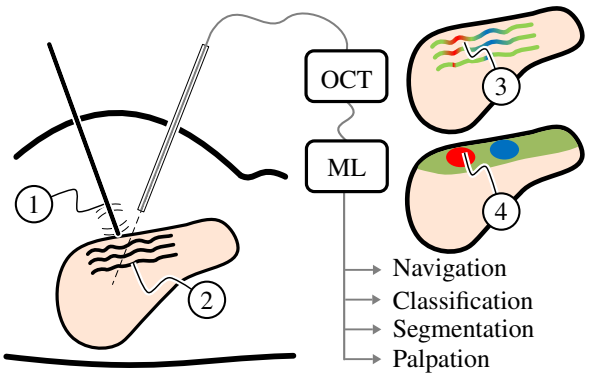

Fig. 1. **Minimal Invasive Elasticity Estimation:** A mechanical stimulation (1) excites shear waves (2) which propagates inside the tissue. Tissue displacement due to the propagating waves is imaged with OCT. Wave field characteristics are dependent on the tissue properties as indicated in color (3). A machine learning network estimates quantitative elasticity values from image data to map soft tissue properties (4). The elasticity estimates could be further used for downstream tasks.

Optical coherence elastography (OCE) is particularly interesting for imaging subsurface structures in the context of RAS due to the high spatial and temporal resolution compared to magnetic or ultrasound based imaging [7], [8]. Due to its non-invasive nature, optical elastography is safe and removes the need for direct contact between sensor and sample. In OCE, the external load is most commonly applied by excitation of shear waves on the surface of the soft tissue. By tracking the wave propagation in 2D, 3D, or

[1]Institute of Medical Technology and Intelligent Systems, Hamburg University of Technology, Hamburg, Germany maximilian.neidhardt@tuhh.de
[2]Interdisciplinary Competence Center for Interface Research at University Medical Center Hamburg-Eppendorf and Technical University of Hamburg, Germany
[3]Martini-Klinik Prostate Cancer Center Hamburg-Eppendorf, Hamburg, Germany
[4]Department of Urology, University Medical Center Hamburg-Eppendorf, Hamburg, Germany
The authors state no conflict of interest. This work was partially funded by the TUHH i^3 initiative and the Interdisciplinary Competence Center for Interface Research (ICCIR) supported by TUHH and UKE.
* Both authors contributed equally.

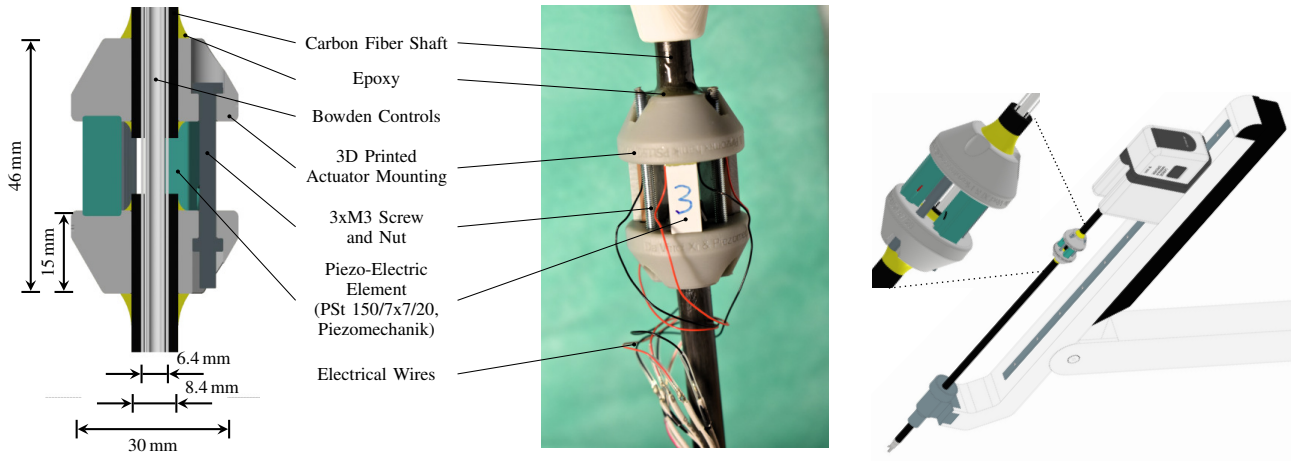

(a) CAD Design (b) da Vinci Robot

Fig. 2. **Modified da Vinci Instrument:** (a) CAD design and image of the modified da Vinci surgical instrument. The instrument is fitted with two 3D printed actuator mountings which hold three piezoelectric elements. The cables for instrument tip actuation are left unchanged and we preload the piezoelectric elements using three M3 screws. (b) The instrument can be inserted and operated with the da Vinci robot as depicted.

even 4D images a precise quantification of tissue elasticity is possible [9]. Note, that it is substantially more challenging to obtain quantitative estimates when solely tracking the robot position and the force between instrument and tip during palpation [10]. Tabletop OCE setups or OCE systems integrated into the clinical microscopes have already been demonstrated for ex-vivo or in-vivo tissue analysis, e.g. in ophthalmology [8]. But for application in RAS, both, the image acquisition and the shear wave excitation must be performed locally on the tissue surface. While optical coherence tomography (OCT) imaging through a laparoscope has been proposed [11], [12], shear wave excitation is complicated by the laparoscopic setting. In principle, shear waves can be excited using either piezoelectric elements, air-pulses, or acoustic radiation force [8]. Piezoelectric elements are most commonly used because they offer a high load force, precise frequency tuning, and a wide bandwidth of excitation frequencies. We propose placing the piezo elements outside the patient, at the base of the surgical tool. Thereby, we avoid high voltages inside the patient and modifications at the instrument tip which would hinder the operation of the tool. Hence, we investigate a novel approach using the da Vinci instrument itself for shear wave excitation.

We propose a modified da Vinci instrument with integrated piezo actuators for shear wave excitation. Although the instrument is modified, we preserve all its surgical functions, i.e., the dexterous control of the instrument tip via the robot. All additional components are located at the proximal end of the instrument, outside the patient's body. In contrast to excitation concepts where the piezoelectric elements are placed at the tissue surface, we observe a more complex transmission of vibrations to the instrument tip. Consequently, the wave fields in the acquired OCT image data may be modulated. We therefore consider deep learning to directly correlate wave field patterns to the elasticity of soft tissue. In the following, we will first present our modified da Vinci instrument for shear wave excitation. We will then validate its functionality on tissue-mimicking phantoms, ex-vivo tissue and inside a laparoscopic trainer. Finally, we demonstrate the benefits of deep learning for OCE in comparison to conventional elasticity estimation approaches.

II. MATERIAL AND METHODS

A. Surgical da Vinci Instrument

In order to realize shear wave excitation directly via the da Vinci instrument, we integrate piezoelectric actuators into the instrument shaft. Thus, we can excite the instrument itself, and thereby the tip of the instrument. The design and the individual components of the modified da Vinci instrument are depicted in Fig.2a. We integrate three piezoelectric elements (PSt 150/7x7/20, Piezomechanik GmbH, Germany) at the proximal end of the instrument. The proximal mounting ensures that all additional components are outside of the patient when operating the instrument with a robot, as depicted in Fig.2b. Each piezo has a ceramic cross-sectional area of 7 mm × 7 mm, a length of 18 mm, a maximum stroke of 28 µm and a maximum load force of 4000 N. We operate the elements with a voltage ranging from −25 V to 150 V. Our prototype is manufactured in-house by (1) removing a 10 mm section of the da Vinci tool's carbon fiber tube, (2) two mounting plates are fixed to the carbon fiber tube with epoxy adhesive, (3) the piezoelectric elements are placed between the mounting plates and tension is applied on the piezo elements with screws. During operation, the tool is mounted rigidly to the robot, the shaft is positioned inside a trocar and the grasper is in contact with the soft tissue.

B. Experimental Setup

The experimental setup is depicted in Fig.3a. We use a high-speed swept-source OCT system (SS-OCT, OMES, Optores, Germany) to acquire one-dimensional depth-resolved scans with a temporal scan rate of 1.5 MHz, a central wavelength of 1315 nm and an axial resolution of 15 µm in

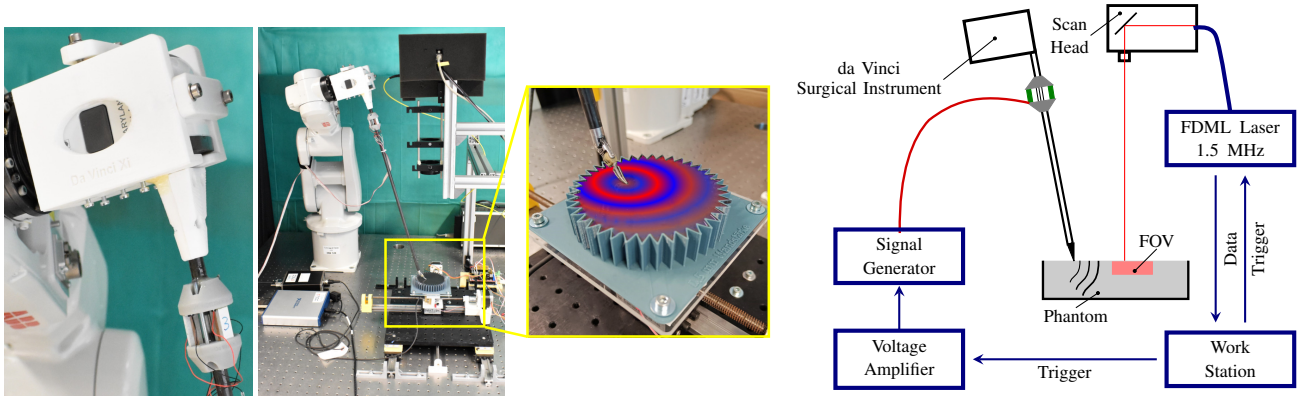

(a) (b)

Fig. 3. **Experimental Data Acquisition:** (a) Experimental setup with a robot and the custom da Vinci surgical instrument mounted to the robot's end-effector. Piezoelectric elements integrated inside the shaft of the da Vinci instrument are excited to stimulate shear waves inside the tissue, as depicted in the image on the right. We image the propagating wave-field with high-speed OCT. (b) Sketch demonstrating data acquisition. A scanner attached to the OCT system acquires cross-sectional images with a temporal scan rate of 11.4 kHz with simultaneous wave excitation.

air. We use a scan head to acquire two-dimensional images with a temporal resolution of 11.4 kHz by deflecting the light beam with resonant oscillating mirrors. We measure the field of view (FOV) with a calibration phantom (R3L3S3P, Thorlabs, Germany) and report an effective spatial size of approximately 3.5 mm × 2 mm for an image size of 118 × 400 pixels along the lateral and depth axis. We design and print an adapter to mount the da Vinci instrument to the robot's end-effector (IRB120, ABB, Switzerland) for streamlined data acquisition. The mounting includes screws that apply tension to the instrument's control gears to restrict the movement of the instrument tip during data acquisition.

C. Data Acquisition and Data Pre-Processing

We use gelatin phantoms as tissue surrogates and prepare batches of gelatin with a weight ratio of 5 %, 10 %, 15 % and 20 % gelatin to water. For each concentration, we manufacture 5 phantoms following the same recipe. During data acquisition, we place the samples on a planar motion stage as depicted in Fig.3a. The robot places the da Vinci instrument on the gelatin sample. To ensure sufficient contact between the instrument tip and soft tissue we apply a maximum contact force of approximately 100 mN which is sensed with a force sensor mounted underneath the motion stage. Next, shear waves are excited iteratively at 200 Hz, 400 Hz, 600 Hz, 800 Hz and 1000 Hz while the instrument is kept stationary. At each frequency, a dataset is acquired containing 208 cross-sectional images, creating a 3D spatio-temporal representation of propagating shear waves. In total, we acquire datasets at 25 distinct positions on each gelatin phantom which results in a total of 500 acquired datasets per excitation frequency. Each position on the phantom is separated by 5 mm to allow speckle augmentation. We perform uniform indentation tests on cylindrical gelatin samples to calculate the Young's modulus as our ground truth labels for training [13]. We obtain 17 kPa, 56 kPa, 97 kPa and 139 kPa for the four different gelatin concentrations, respectively. We pre-process each dataset by cropping 128 pixels beneath the sample surface. To reduce imaging noise, we apply a median filter with a kernel size of 3 × 3 × 3.

D. Laparoscopic Trainer and Soft Tissue

Additionally, we record data from within a laparoscopic trainer (Kroton Box, Kroton Medical Technology, Poland) to estimate the effect of damping on the instrument's shaft. We record 20 datasets with and without damping of the laparoscopic trainer (Fig.5a-5c). In addition to the gelatin phantom data, we also evaluate our methods on ex-vivo chicken heart, liver, and stomach tissue (Fig.5d-5f). In total, we record 15 datasets at various positions for each soft tissue type.

E. Spatio-Temporal Deep Learning

The acquired 3D shear wave data consists of two spatial and one temporal dimension for the processing. Spatio-temporal Convolutional Neural Networks (CNNs) [14] with 3D convolutions have shown excellent results [9], [15] by jointly learning spatial and temporal information. For efficient data processing, we resize each frame resulting in 64 × 64 pixels along the lateral and depth axis, respectively. Our model architecture (Fig.4) is based on a densely connected CNN (DenseNet) [16]. After an initial convolutional layer, we employ four DenseNet blocks and with two, four, six, and three layers per block, respectively. We use average pooling in the transition blocks and a growth factor of 6. A final fully connected layer directly outputs elasticity estimates given the 3D input sequence. We train independent networks for each excitation frequency using a mean squared error (MSE) loss. We split our data based on the different phantoms and select one independent phantom from each gelatin concentration as our test set. To make our results more robust, we conduct a nested cross-validation scheme such that every phantom is part of the test set once. For each of these five outer folds, we perform a four-fold cross-validation across the remaining

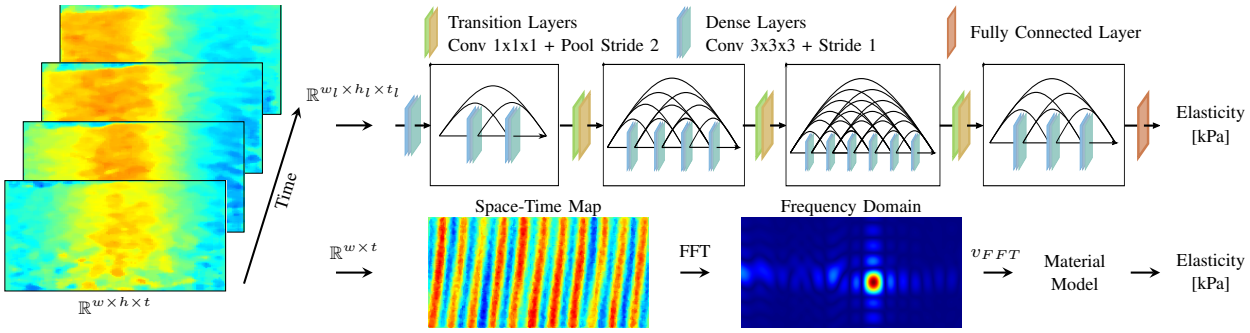

Fig. 4. **Data Processing:** The OCT phase signal is cropped below the surface and each 3D spatio-temporal shear wave dataset $\mathbb{R}^{w \times h \times t}$ is processed using conventional phase velocity estimation and our learning based approach. Using spatio-temporal deep learning (upper right), sample elasticity is directly estimated in an end-to-end fashion from a temporal window of $t_l = 16$ frames. We also downsample the spatial dimension to $w_l = h_l = 64$ to reduce computational effort. For conventional elasticity estimates (lower right), we create space-time maps for each dataset ($w = 128$, $t = 208$) and estimate shear wave velocity using Fourier domain analysis. We map wave velocity to the Young's modulus using a linear material model.

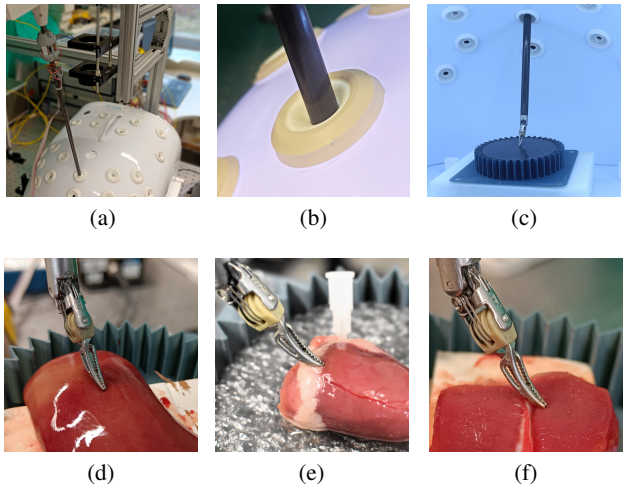

Fig. 5. **Laparoscopic Trainer and Soft Tissue Experiments:** We additionally validate wave excitation in a trainer that adds friction along the instrument shaft (a-c). Furthermore, we test our approach on ex-vivo (d) chicken liver, (e), chicken heart and (f) chicken stomach tissue.

samples. This results in a data split of 70:20:10 for training, testing, and validation respectively. Thereby, we train 20 networks for each frequency leading to 100 networks trained in total. During training, we randomly crop sequences of 16 successive frames along the temporal dimension. During testing, we apply a moving window along the temporal dimension and report the mean of all predictions from one dataset. We apply early stopping to reduce training times. While we train solely on gelatin but additionally evaluate our approach on soft tissue data.

F. Conventional Elasticity Estimation

For comparison to our deep-learning approach, we additionally consider conventional phase velocity estimation as depicted in Fig.4. We estimate the velocity of the shear waves in the frequency domain similar to Beuve et al. [17]. First, we derive Space-Time maps from a given shear wave dataset by estimating the mean along the depth axis h, resulting in an image of size of 118 × 208 pixels along the lateral w and temporal t axis. Second, we apply a 2D discrete FFT along the image axis to estimate the k-space representation. To further reduce background noise we remove pixels with $< 10\%$ of the overall maximum amplitude in the k-space. Next, we estimate the maximum amplitude in the k-space for each temporal frequency f and compute the phase velocity $v_{FFT} = f/k$ with the wavenumber k. Estimates not within $1\,\mathrm{m\,s^{-1}} < v_{FFT} > 10\,\mathrm{m\,s^{-1}}$ are considered failed estimates, which represent the typical elasticity range of soft tissue [18]. Finally, we apply a linear material model to estimate the E-Modulus from the shear wave velocity with the relation [19] $E_{ToF} = q \cdot \rho \cdot 2(1+\nu) \cdot v_{FFT}^2$ with a Possion's ratio $\nu = 0.5$ and a density $\rho = 1000\,\mathrm{kg\,m^{-3}}$. To account for constant errors between our estimates and our ground truth Young's modulus labels we estimate a linear scaling factor $q = 0.84$ by minimizing the offset.

III. RESULTS

Example data of a shear wave excited using our modified da Vinci instrument can be seen in Fig.4. Visual inspection of the acquired datasets confirmed wave propagation for all datasets and samples, with varying imaging noise dependent on material and excitation frequency. All 3D shear wave datasets for each sample were processed using the conventional approach and our spatio-temporal deep learning based elasticity estimation. The mean absolute error (MAE) and the root mean squared error (RMSE) averaged for each excitation frequency can be seen in Table I for both methods. Conventional processing displays significant variation in elasticity estimation and is outperformed by the deep learning-based approach, which enables a more accurate and more robust estimation of the elasticity independent of the excitation frequency. The elasticity estimates for each excitation frequency and sample stiffness are shown in Fig.6a for both approaches. For the conventional approach, it can be seen that the variance increases with elasticity and decreases with frequency, resulting in an MAE of 19.27 ± 23.50 kPa for the ensemble from all frequencies. In contrast, model predic-

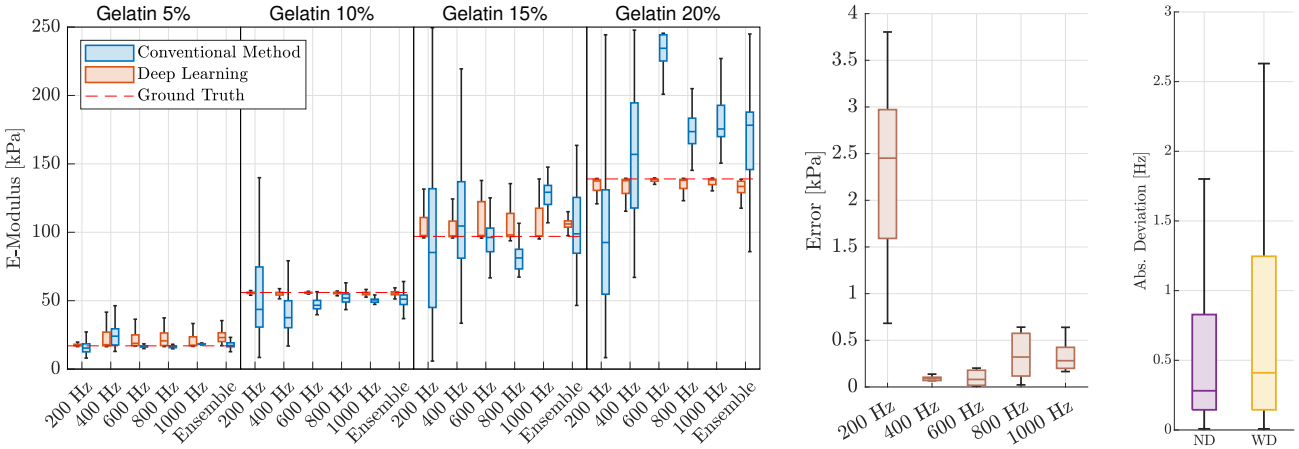

(a) Predicted Elasticity (b) Effect of Damping (c) Frequency

Fig. 6. **Experimental Results:** (a) Elasticity estimates with deep learning (red) and the conventional method (blue). The dashed red line indicated the target elasticity evaluated by uniform compression tests. (b) The error in elasticity predictions due to the damping along the instrument shaft in the laparoscopic trainer. (c) Difference between excitation frequency and measured frequency with damping (WD) and with no damping (ND).

TABLE I

MEAN ABSOLUTE ERROR OF PREDICTIONS IN KPA ON ALL GELATIN PHANTOMS WITH DIFFERENT EXCITATION FREQUENCIES.

Method	Error Metric	200 Hz	400 Hz	600 Hz	800 Hz	1000 Hz	Ensemble
Conventional	MAE	34.06±34.81	26.53±26.18	25.16±37.57	16.00±15.85	22.66±19.85	19.27±23.50
	RMSE	48.67	37.26	45.18	22.51	30.11	30.37
Deep Learning	MAE	6.42±13.45	6.73±11.97	6.25±12.61	7.58±13.63	6.66±12.63	6.29±4.99
	RMSE	14.89	13.72	14.06	15.58	14.27	8.02

tions for the learning-based approach show good agreement with the acquired ground truth independent of excitation frequency and we report a reduced MAE of 6.29 ± 4.99 kPa. We further investigate the effect of damping on the wave excitation with the instrument in the laparoscopic trainer. We report the error when damping is added (Fig.6b). We observe only marginal differences in the elasticity estimates for excitation with and without damping, with a maximum mean deviation of 2.31 kPa for the lowest excitation frequency. We further compare the excitation frequency with the measured dominant frequency component in the frequency domain (Fig.6c). The median deviation between excitation and measured shear wave frequency is 0.28 ± 1.53 Hz and 0.41 ± 1.64 Hz with and without damping, respectively. In Fig.7, the elasticity estimates of ex-vivo soft tissue samples are depicted. In average we report an elasticity of 57.73 ± 5.95 kPa, 96.39 ± 13.37 kPa and 79.27 ± 7.18 kPa for chicken liver, heart and stomach, respectively.

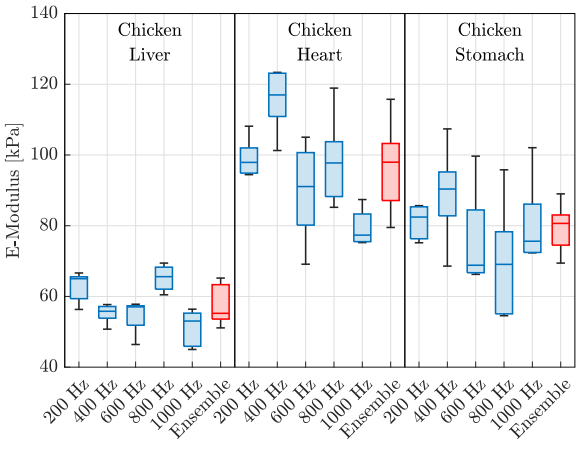

Fig. 7. **Ex-vivo Soft Tissues:** Elasticity estimates for chicken liver, stomach and heart tissue. We additionally consider the ensemble by taking the mean over the models trained for each of the five frequencies.

IV. DISCUSSION

Our experiments demonstrate the successful excitation of shear waves in phantom and ex-vivo tissue samples directly via the modified da Vinci instrument. Further, we evaluate the effect of damping on the instrument shaft, as presented in a clinical minimal invasive intervention. We observe mean deviations of less than 1 Hz between excitation frequency and measured frequency inside the tissue, both with and without additional damping in the laparoscopic trainer. Our modified instrument consequently enables a safe and reliable approach for wave excitation from outside the patient. In contrast, previously proposed probes for wave excitation involve piezoelectric elements at the tip of dedicated tools [6], [20] with high voltage cables running inside the patient. Air pulse excitation is a promising non-contact alternative and allows highly focused wave excitations [8]. However, current designs have limited bandwidth and are impractical due to their location inside the patient, close to the soft tissue.

Our experiments confirm that our approach enables the differentiation of materials based solely on the propagating shear wave field (Fig.6). The proposed spatio-temporal deep learning enables accurate elasticity estimates and outperforms conventional processing with an MAE of 6.29 ± 4.99 kPa compared to 19.27 ± 23.50 kPa, respectively. The conventional approach results in large deviations for estimates with different excitation frequencies from the same elasticity, especially for lower excitation frequencies and increased sample elasticity. In contrast, the trained models are more robust with respect to the excitation frequency and sample stiffness, especially when considering ensemble predictions. We further investigate if damping of the instrument's shaft, as given in a minimally invasive intervention, effects elasticity prediction. Considering Fig.6b, damping effects are marginal on elasticity estimates with a maximum mean estimation offset of 2.71 ± 0.80 kPa for excitation frequencies of 200 Hz. Consequently, the excitation frequency can be modulated to provide more accurate elasticity estimates.

We additionally evaluate our trained models on ex-vivo soft tissue and demonstrate that different tissue types can be differentiated based on their elasticity, with particularly good contrast between softer liver and harder heart and stomach muscle tissue. It stands out, that while training the models was solely performed on gelatin phantoms the models are able to generalize to soft tissue. The results therefore show successful shear wave excitation in soft tissue and indicate that the wave field has similar features as in gelatin phantoms. Overall, chicken heart and stomach are in the range of muscle tissue reported in the literature 98 ± 10 kPa [21]. However, a comparison to quantitative values in the literature is limited due to the not applicable ground truth elasticity of our samples as well as the varying age and the general inhomogeneity of soft-tissue samples, as well as different presumptions for elasticity estimates, e.g., the material model. In this context, our model can also be applied for respective downstream tasks, e.g., surgical navigation, tissue classification, or tactile feedback.

A refined instrument design will be required for clinical application, especially for medical autoclaving. Consequently, 3D printed parts ideal for fast prototyping would need to be replaced by metal alloys and electric wiring could be directly integrated into the existing da Vinci electrical adapter. In practice, the imaging of the tissue could be performed similarly to existing OCT handheld probes [22]. Volumetric imaging could be used to detect wave propagation along multiple spatial dimensions [9]. We note that the imaging depth of OCE is limited, but its high resolution makes it particularly useful for highly local elasticity estimation.

Currently, our study also only considers excitation with a rigid instrument tip position. Future studies will consider wave excitation with simultaneous actuation of the instrument tip, e.g., push and grabbing tasks.

In conclusion, we have demonstrated shear wave excitation directly via a modified da Vinci instrument and shown subsequent differentiation of different phantoms and soft tissue types based on their elastic properties and considering friction at the instrument shaft. The availability of quantitative elasticity estimates during minimal invasive RAS offers multiple possibilities including the assistance of the surgeon during navigation, classifying tissue types or enabling quantitative haptic feedback.

REFERENCES

[1] I. J. Y. Wee, L.-J. Kuo, and J. C.-Y. Ngu, "A systematic review of the true benefit of robotic surgery: Ergonomics," *Int J Med Robot*, vol. 16, no. 4, p. e2113, 2020.

[2] R. Farinha *et al.*, "Potential contenders for the leadership in robotic surgery," *J Endourol*, vol. 36, no. 3, pp. 317–326, 2022.

[3] N. Bandari, J. Dargahi, and M. Packirisamy, "Tactile sensors for minimally invasive surgery: A review of the state-of-the-art, applications, and perspectives," *IEEE Access*, vol. 8, pp. 7682–7708, 2020.

[4] M. Bergholz, M. Ferle, and B. M. Weber, "The benefits of haptic feedback in robot assisted surgery and their moderators: a meta-analysis," *Sci Rep*, vol. 13, no. 1, p. 19215, 2023.

[5] K. M. Kennedy *et al.*, "Diagnostic accuracy of quantitative micro-elastography for margin assessment in breast-conserving surgery," *Cancer Res*, vol. 80, no. 8, pp. 1773–1783, 2020.

[6] M. Neidhardt, R. Mieling, M. Bengs, and A. Schlaefer, "Optical force estimation for interactions between tool and soft tissues," *Sci Rep*, vol. 13, no. 1, p. 506, 2023.

[7] B. F. Kennedy, K. M. Kennedy, and D. D. Sampson, "A review of optical coherence elastography: Fundamentals, techniques and prospects," *IEEE J Sel Top Quantum Electron*, vol. 20, no. 2, 2014.

[8] F. Zvietcovich and K. V. Larin, "Wave-based optical coherence elastography: The 10-year perspective," *Prog Biomed Eng*, vol. 4, no. 1, p. 012007, 2022.

[9] M. Neidhardt, M. Bengs, S. Latus, M. Schlüter, T. Saathoff, and A. Schlaefer, "4d deep learning for real-time volumetric optical coherence elastography," *IJCARS*, vol. 16, pp. 23–27, 2021.

[10] R. Mieling, S. Latus, M. Fischer, F. Behrendt, and A. Schlaefer, "Optical coherence elastography needle for biomechanical characterization of deep tissue," in *MICCAI*. Springer, 2023, pp. 607–617.

[11] L. P. Hariri *et al.*, "Laparoscopic optical coherence tomography imaging of human ovarian cancer," *Gynecol Oncol*, vol. 114, no. 2, pp. 188–194, 2009.

[12] M. Lee *et al.*, "Imaging peritoneal blood vessels through optical coherence tomography angiography for laparoscopic surgery," *J Biophotonics*, vol. 17, no. 1, p. e202300221, 2024.

[13] M. Neidhardt *et al.*, "Ultrasound shear wave elasticity imaging with spatio-temporal deep learning," *IEEE Trans Biomed Eng*, pp. 3356–3364, 2022.

[14] D. Tran, L. Bourdev, R. Fergus, L. Torresani, and M. Paluri, "Learning spatiotemporal features with 3d convolutional networks," in *Proc IEEE Int Conf Comput Vis*, 2015, pp. 4489–4497.

[15] M. Neidhardt *et al.*, "Deep learning for high speed optical coherence elastography," in *2020 Proc (17th) IEEE Int Symp Biomed Imaging*. IEEE, 2020, pp. 1583–1586.

[16] G. Huang, Z. Liu, L. Van Der Maaten, and K. Q. Weinberger, "Densely connected convolutional networks," in *Proc IEEE Comput Soc Conf Comput Vis Pattern Recognit*, 2017, pp. 4700–4708.

[17] S. Beuve, L. Kritly, S. Callé, and J.-P. Remenieras, "Diffuse shear wave spectroscopy for soft tissue viscoelastic characterization," *Ultrasonics*, vol. 110, p. 106239, 2021.

[18] M. Fink and M. Tanter, "Multiwave imaging and super resolution," *Phys. Today*, vol. 63, no. 2, pp. 28–33, 2010.

[19] A. P. Sarvazyan, M. W. Urban, and J. F. Greenleaf, "Acoustic waves in medical imaging and diagnostics," *Ultrasound in medicine & biology*, vol. 39, no. 7, pp. 1133–1146, 2013.

[20] A. B. Karpiouk, D. J. VanderLaan, K. V. Larin, and S. Y. Emelianov, "Integrated optical coherence tomography and multielement ultrasound transducer probe for shear wave elasticity imaging of moving tissues," *J Biomed Opt*, vol. 23, no. 10, pp. 1–7, 2018.

[21] A. Roux, T.-X. Haen, I. Iordanoff, and S. Laporte, "Model of calf muscle tear during a simulated eccentric contraction, comparison between ex-vivo experiments and discrete element model," *JMBBM*, vol. 142, p. 105823, 2023.

[22] F. Benboujja, J. A. Garcia, K. Beaudette, M. Strupler, C. J. Hartnick, and C. Boudoux, "Intraoperative imaging of pediatric vocal fold lesions using optical coherence tomography," *J. Biomed. Opt.*, vol. 21, no. 1, p. 016007, 2016.

Bibliography

[1] P. R. Armijo, S. Pagkratis, E. Boilesen, T. Tanner, and D. Oleynikov, "Growth in robotic-assisted procedures is from conversion of laparoscopic procedures and not from open surgeons' conversion: A study of trends and costs," *Surgical endoscopy*, vol. 32, no. 4, pp. 2106–2113, 2018.

[2] T. Leal Ghezzi and O. Campos Corleta, "30 years of robotic surgery," *World Journal of Surgery*, vol. 40, no. 10, pp. 2550–2557, 2016.

[3] M. Diana and J. Marescaux, "Robotic surgery," *The British journal of surgery*, vol. 102, no. 2, e15–28, 2015.

[4] B. K. Varda, Y. Wang, B. I. Chung, R. S. Lee, M. P. Kurtz, C. P. Nelson, and S. L. Chang, "Has the robot caught up? national trends in utilization, perioperative outcomes, and cost for open, laparoscopic, and robotic pediatric pyeloplasty in the united states from 2003 to 2015," *Journal of Pediatric Urology*, vol. 14, no. 4, 336.e1–336.e8, 2018.

[5] I. J. Y. Wee, L.-J. Kuo, and J. C.-Y. Ngu, "A systematic review of the true benefit of robotic surgery: Ergonomics," *The International Journal of Medical Robotics and Computer Assisted Surgery*, vol. 16, no. 4, e2113, 2020.

[6] J. T. Licardo, M. Domjan, and T. Orehovački, "Intelligent robotics—a systematic review of emerging technologies and trends," *Electronics*, vol. 13, no. 3, p. 542, 2024.

[7] A. I. Aviles-Rivero, S. M. Alsaleh, J. Philbeck, S. P. Raventos, N. Younes, J. K. Hahn, and A. Casals, "Sensory substitution for force feedback recovery," *ACM Transactions on Applied Perception*, vol. 15, no. 3, pp. 1–19, 2018.

[8] M. Bergholz, M. Ferle, and B. M. Weber, "The benefits of haptic feedback in robot assisted surgery and their moderators: A meta-analysis," *Scientific Reports*, vol. 13, no. 1, p. 19 215, 2023.

[9] E. M. Overtoom, T. Horeman, F.-W. Jansen, J. Dankelman, and H. W. R. Schreuder, "Haptic feedback, force feedback, and force-sensing in simulation training for laparoscopy: A systematic overview," *Journal of Surgical Education*, vol. 76, no. 1, pp. 242–261, 2019.

[10] A. K. Golahmadi, D. Z. Khan, G. P. Mylonas, and H. J. Marcus, "Tool-tissue forces in surgery: A systematic review," *Annals of Medicine and Surgery*, vol. 65, p. 102 268, 2021.

[11] X. Huang, P. Wang, J. Chen, Y. Huang, Q. Liao, Y. Huang, Z. Liu, and D. Peng, "An intelligent grasper to provide real-time force feedback to shorten the learning curve in laparoscopic training," *BMC Medical Education*, vol. 24, no. 1, p. 161, 2024.

[12] Y. Yamasaki, M. Tokunaga, Y. Sakai, H. Kayasuga, T. Nishihara, K. Tadano, K. Kawashima, S. Haruki, and Y. Kinugasa, "Effects of a force feedback function in a surgical robot on the suturing procedure," *Surgical Endoscopy*, pp. 1–8, 2023.

[13] S.-C. Lim, H.-K. Lee, and J. Park, "Role of combined tactile and kinesthetic feedback in minimally invasive surgery," *The International Journal of Medical Robotics and Computer Assisted Surgery*, vol. 11, no. 3, pp. 360–374, 2015.

[14] K. Hoyt, B. Castaneda, M. Zhang, P. Nigwekar, P. A. Di Sant'agnese, J. V. Joseph, J. Strang, D. J. Rubens, and K. J. Parker, "Tissue elasticity properties as biomarkers for prostate cancer," *Cancer biomarkers : section A of Disease markers*, vol. 4, no. 4-5, pp. 213–225, 2008.

[15] T. A. Krouskop, T. M. Wheeler, F. Kallel, B. S. Garra, and T. Hall, "Elastic moduli of breast and prostate tissues under compression," *Ultrasonic imaging*, vol. 20, no. 4, pp. 260–274, 1998.

[16] A. Samani, J. Zubovits, and D. Plewes, "Elastic moduli of normal and pathological human breast tissues: An inversion-technique-based investigation of 169 samples," *Physics in Medicine & Biology*, vol. 52, no. 6, p. 1565, 2007.

[17] S. Kawano, M. Kojima, Y. Higuchi, M. Sugimoto, K. Ikeda, N. Sakuyama, S. Takahashi, R. Hayashi, A. Ochiai, and N. Saito, "Assessment of elasticity of colorectal cancer tissue, clinical utility, pathological and phenotypical relevance," *Cancer Science*, vol. 106, no. 9, pp. 1232–1239, 2015.

[18] D. W. Good, G. D. Stewart, S. Hammer, P. Scanlan, W. Shu, S. Phipps, R. Reuben, and A. S. McNeill, "Elasticity as a biomarker for prostate cancer: A systematic review," *BJU International*, vol. 113, no. 4, pp. 523–534, 2014.

[19] R. D. Howe, W. J. Peine, D. A. Kantarinis, and J. S. Son, "Remote palpation technology," *IEEE Engineering in Medicine and Biology Magazine*, vol. 14, no. 3, pp. 318–323, 1995.

[20] J. Troccaz, G. Dagnino, and G.-Z. Yang, "Frontiers of medical robotics: From concept to systems to clinical translation," *Annual Review of Biomedical Engineering*, vol. 21, pp. 193–218, 2019.

[21] P. Culmer, A. Alazmani, F. Mushtaq, W. Cross, and D. Jayne, "15 - haptics in surgical robots," in *Handbook of robotic and image-guided surgery*, M. H. Abedin-Nasab, Ed., Amsterdam, Netherlands: Elsevier, 2020, pp. 239–263.

[22] A. Marbán, A. Casals, J. Fernández, and J. Amat, "Haptic feedback in surgical robotics: Still a challenge," in *ROBOT2013: First Iberian Robotics Conference*, Springer, Cham, 2014, pp. 245–253.

[23] N. Simaan, R. M. Yasin, and L. Wang, "Medical technologies and challenges of robot-assisted minimally invasive intervention and diagnostics," *https://doi.org/10.1146/annurev-control-060117-104956*, vol. 1, no. 1, pp. 465–490, 2018.

[24] A. M. Okamura, L. N. Verner, C. E. Reiley, and M. Mahvash, "Haptics for robot-assisted minimally invasive surgery," in *Robotics Research*, ser. Springer Tracts in Advanced Robotics, B. Siciliano, O. Khatib, F. Groen, M. Kaneko, and Y. Nakamura, Eds., vol. 66, Berlin, Heidelberg: Springer Berlin Heidelberg, 2011, pp. 361–372.

[25] F. Amirabdollahian, S. Livatino, B. Vahedi, R. Gudipati, P. Sheen, S. Gawrie-Mohan, and N. Vasdev, "Prevalence of haptic feedback in robot-mediated surgery: A systematic review of literature," *Journal of Robotic Surgery*, vol. 12, no. 1, pp. 11–25, 2018.

[26] K. Bizheva, B. Tan, B. MacLelan, O. Kralj, M. Hajialamdari, D. Hileeto, and L. Sorbara, "Sub-micrometer axial resolution oct for in-vivo imaging of the cellular structure of healthy and keratoconic human corneas," *Biomedical Optics Express*, vol. 8, no. 2, pp. 800–812, 2017.

[27] Xin Ge, Shufen Chen, Si Chen, and Linbo Liu, "High resolution optical coherence tomography," *Journal of Lightwave Technology*, vol. 39, no. 12, pp. 3824–3835, 2021.

[28] S. L. Jacques, "Optical properties of biological tissues: A review," *Physics in Medicine and Biology*, vol. 58, no. 11, R37–61, 2013.

[29] W. Drexler and J. G. Fujimoto, *Optical coherence tomography: Technology and applications* (SpringerLink Bücher). Berlin, Heidelberg, and New York: Springer, 2008.

[30] A. M. Zysk, F. T. Nguyen, A. L. Oldenburg, D. L. Marks, and S. A. Boppart, "Optical coherence tomography: A review of clinical development from bench to bedside," *Journal of biomedical optics*, vol. 12, no. 5, p. 51 403, 2007.

[31] D. Huang, E. A. Swanson, C. P. Lin, J. S. Schuman, W. G. Stinson, W. Chang, M. R. Hee, T. Flotte, K. Gregory, C. A. Puliafito, et al., "Optical coherence tomography," *Science*, vol. 254, no. 5035, pp. 1178–1181, 1991.

[32] B. E. Bouma, J. F. de Boer, D. Huang, I. K. Jang, T. Yonetsu, C. L. Leggett, R. Leitgeb, D. D. Sampson, M. Suter, B. Vakoc, M. Villiger, and M. Wojtkowski, "Optical coherence tomography," *Nature Reviews Methods Primers*, vol. 2, no. 1, pp. 1–20, 2022.

[33] J. Fujimoto and E. Swanson, "The development, commercialization, and impact of optical coherence tomography," *Investigative Ophthalmology & Visual Science*, vol. 57, no. 9, OCT1–OCT13, 2016.

[34] I. Laíns, J. C. Wang, Y. Cui, R. Katz, F. Vingopoulos, G. Staurenghi, D. G. Vavvas, J. W. Miller, and J. B. Miller, "Retinal applications of swept source optical coherence tomography (oct) and optical coherence tomography angiography (octa)," *Progress in Retinal and Eye Research*, vol. 84, p. 100 951, 2021.

[35] N. Kobayashi, Y. Ito, M. Yamawaki, M. Araki, M. Obokata, Y. Sakamoto, S. Mori, M. Tsutsumi, Y. Honda, K. Makino, S. Shirai, M. Mizusawa, and K. Hirano, "Optical coherence tomography-guided versus intravascular ultrasound-guided rotational atherectomy in patients with calcified coronary lesions," *EuroIntervention*, vol. 16, no. 4, E313–E321, 2021.

[36] B. E. Bouma, M. Villiger, K. Otsuka, and W.-Y. Oh, "Intravascular optical coherence tomography," *Biomedical Optics Express*, vol. 8, no. 5, pp. 2660–2686, 2017.

[37] M. Araki et al., "Optical coherence tomography in coronary atherosclerosis assessment and intervention," *Nature Reviews Cardiology*, vol. 19, no. 10, pp. 684–703, 2022.

[38] J. Li, S. Thiele, B. C. Quirk, R. W. Kirk, J. W. Verjans, E. Akers, C. A. Bursill, S. J. Nicholls, A. M. Herkommer, H. Giessen, and R. A. McLaughlin, "Ultrathin monolithic 3d printed optical coherence tomography endoscopy for preclinical and clinical use," *Light: Science & Applications*, vol. 9, no. 1, p. 124, 2020.

[39] J. Olsen, J. Holmes, and G. B. Jemec, "Advances in optical coherence tomography in dermatology-a review," *Journal of Biomedical Optics*, vol. 23, no. 4, pp. 1–10, 2018.

[40] X. Liang and S. A. Boppart, "Biomechanical properties of in vivo human skin from dynamic optical coherence elastography," *IEEE transactions on bio-medical engineering*, vol. 57, no. 4, pp. 953–959, 2010.

[41] H. Liu, Di Yang, R. Jia, W. Wang, J. Shang, Q. Liu, and Y. Liang, "Dynamic optical coherence elastography for skin burn assessment: A preliminary study on mice model," *Journal of Biophotonics*, e202400028, 2024.

[42] L. Yang, Y. Chen, S. Ling, J. Wang, G. Wang, B. Zhang, H. Zhao, Q. Zhao, and J. Mao, "Research progress on the application of optical coherence tomography in the field of oncology," *Frontiers in oncology*, vol. 12, p. 953 934, 2022.

[43] L. van Manen, J. Dijkstra, C. Boccara, E. Benoit, A. L. Vahrmeijer, M. J. Gora, and J. S. D. Mieog, "The clinical usefulness of optical coherence tomography during cancer interventions," *Journal of cancer research and clinical oncology*, vol. 144, no. 10, pp. 1967–1990, 2018.

[44] Y. Duan, D. Guo, X. Zhang, L. Lan, H. Meng, Y. Wang, C. Sui, Z. Qu, G. He, C. Wang, and X. Liu, "Diagnostic accuracy of optical coherence tomography for margin assessment in breast-conserving surgery: A systematic review and meta-analysis," *Photodiagnosis and photodynamic therapy*, vol. 43, p. 103 718, 2023.

[45] M. A. Kirby, I. Pelivanov, S. Song, Ł. Ambrozinski, S. J. Yoon, L. Gao, D. Li, T. T. Shen, R. K. Wang, and M. O'Donnell, "Optical coherence elastography in ophthalmology," *Journal of Biomedical Optics*, vol. 22, no. 12, pp. 1–28, 2017.

[46] K. V. Larin and D. D. Sampson, "Optical coherence elastography - oct at work in tissue biomechanics invited," *Biomedical Optics Express*, vol. 8, no. 2, pp. 1172–1202, 2017.

[47] N. Leartprapun and S. G. Adie, "Recent advances in optical elastography and emerging opportunities in the basic sciences and translational medicine invited," *Biomedical Optics Express*, vol. 14, no. 1, pp. 208–248, 2023.

[48] M. Singh, F. Zvietcovich, and K. V. Larin, "Introduction to optical coherence elastography: Tutorial," *JOSA A*, vol. 39, no. 3, pp. 418–430, 2022.

[49] C. Wang, J. Zhu, J. Ma, X. Meng, Z. Ma, and F. Fan, "Optical coherence elastography and its applications for the biomechanical characterization of tissues," *Journal of Biophotonics*, vol. 16, no. 12, e202300292, 2023.

[50] S. Wang and K. V. Larin, "Optical coherence elastography for tissue characterization: A review," *Journal of Biophotonics*, vol. 8, no. 4, pp. 279–302, 2015.

[51] V. Y. Zaitsev, A. L. Matveyev, L. A. Matveev, A. A. Sovetsky, M. S. Hepburn, A. Mowla, and B. F. Kennedy, "Strain and elasticity imaging in compression optical coherence elastography: The two-decade perspective and recent advances," *Journal of Biophotonics*, vol. 14, no. 2, e202000257, 2021.

[52] F. Zvietcovich and K. V. Larin, "Wave-based optical coherence elastography: The 10-year perspective," *Progress in Biomedical Engineering*, vol. 4, no. 1, p. 012 007, 2022.

[53] S. Radhakrishnan, A. M. Rollins, J. E. Roth, S. Yazdanfar, V. Westphal, D. S. Bardenstein, and J. A. Izatt, "Real-time optical coherence tomography of the anterior segment at 1310 nm," *Archives of Ophthalmology*, vol. 119, no. 8, pp. 1179–1185, 2001.

[54] R. L. Shelton, W. Jung, S. I. Sayegh, D. T. McCormick, J. Kim, and S. A. Boppart, "Optical coherence tomography for advanced screening in the primary care office," *Journal of Biophotonics*, vol. 7, no. 7, pp. 525–533, 2014.

[55] F. LaRocca, D. Nankivil, T. DuBose, C. A. Toth, S. Farsiu, and J. A. Izatt, "In vivo cellular-resolution retinal imaging in infants and children using an ultracompact handheld probe," *Nature Photonics*, vol. 10, no. 9, pp. 580–584, 2016.

[56] Y.-H. Chang, C.-Y. Chen, and W.-C. Kuo, "Handheld common-path swept-source optical coherence tomography angiography," *Optics Letters*, vol. 48, no. 15, pp. 3913–3916, 2023.

[57] S. Schuh, M. Berger, S. Schiele, A. Rubeck, G. Müller, J. J. V. González, J. Holmes, and J. Welzel, "Dynamic optical coherence tomography for imaging acute wound healing," *International wound journal*, vol. 21, no. 8, e70015, 2024.

[58] A. M. Zysk, K. Chen, E. Gabrielson, L. Tafra, E. A. May Gonzalez, J. K. Canner, E. B. Schneider, A. J. Cittadine, P. Scott Carney, S. A. Boppart, K. Tsuchiya, K. Sawyer, and L. K. Jacobs, "Intraoperative assessment of final margins with a handheld optical imaging probe during breast-conserving surgery may reduce the reoperation rate: Results of a multicenter study," *Annals of Surgical Oncology*, vol. 22, no. 10, pp. 3356–3362, 2015.

[59] Y. Huang, G. J. Furtmüller, D. Tong, S. Zhu, W. P. A. Lee, G. Brandacher, and J. U. Kang, "Mems-based handheld fourier domain doppler optical coherence tomography for intraoperative microvascular anastomosis imaging," *PLOS ONE*, vol. 9, no. 12, e114215, 2014.

[60] S. J. Erickson-Bhatt, R. M. Nolan, N. D. Shemonski, S. G. Adie, J. Putney, D. Darga, D. T. McCormick, A. J. Cittadine, A. M. Zysk, M. Marjanovic, E. J. Chaney, G. L. Monroy, F. A. South, K. A. Cradock, Z. G. Liu, M. Sundaram, P. S. Ray, and S. A. Boppart, "Real-time imaging of the resection bed using a handheld probe to reduce incidence of microscopic positive margins in cancer surgery," *Cancer Research*, vol. 75, no. 18, pp. 3706–3712, 2015.

[61] Q. Fang, B. Krajancich, L. Chin, R. Zilkens, A. Curatolo, L. Frewer, J. D. Anstie, P. Wijesinghe, C. Hall, B. F. Dessauvagie, B. Latham, C. M. Saunders, and B. F. Kennedy, "Handheld probe for quantitative micro-elastography," *Biomedical Optics Express*, vol. 10, no. 8, pp. 4034–4049, 2019.

[62] Y. Shi, J. Lu, N. Le, and R. K. Wang, "Integrating a pressure sensor with an oct handheld probe to facilitate imaging of microvascular information in skin tissue beds," *Biomedical Optics Express*, vol. 13, no. 11, pp. 6153–6166, 2022.

[63] P. Gong, S. L. Chin, W. M. Allen, H. Ballal, J. D. Anstie, L. Chin, H. M. Ismail, R. Zilkens, D. D. Lakhiani, M. McCarthy, Q. Fang, D. Firth, K. Newman, C. Thomas, J. Li, R. W. Sanderson, K. Y. Foo, C. Yeomans, B. F. Dessauvagie, B. Latham, C. M. Saunders, and B. F. Kennedy, "Quantitative micro-elastography enables in vivo detection of residual cancer in the surgical cavity during breast-conserving surgery," *Cancer Research*, vol. 82, no. 21, pp. 4093–4104, 2022.

[64] P. Gong, K. Y. Foo, D. D. Lakhiani, R. Zilkens, H. M. Ismail, C. Yeomans, B. F. Dessauvagie, B. Latham, C. M. Saunders, and B. F. Kennedy, "In vivo optical coherence tomography attenuation imaging of the breast surgical cavity using a handheld probe," *Optics & Laser Technology*, vol. 166, p. 109 467, 2023.

[65] P. Gong, I. Boman, R. Zilkens, C. Yeomans, M. Hardie, A. Rijhumal, C. M. Saunders, and B. F. Kennedy, "Load-dependent optical coherence tomography attenuation imaging: How tissue mechanics can influence optical scattering," *APL Photonics*, vol. 9, no. 8, p. 086 104, 2024.

[66] X. Wang, Q. Wu, J. Chen, and J. Mo, "Development of a handheld compression optical coherence elastography probe with a disposable stress sensor," *Optics Letters*, vol. 46, no. 15, p. 3669, 2021.

[67] M. Lee, H. Bang, E. Lee, S. Park, H. Yoo, W.-Y. Oh, and S. Lee, "Imaging peritoneal blood vessels through optical coherence tomography angiography for laparoscopic surgery," *Journal of Biophotonics*, vol. 17, no. 1, e202300221, 2024.

[68] M. Aron, J. H. Kaouk, N. J. Hegarty, J. R. Colombo, G.-P. Haber, B. I. Chung, M. Zhou, and I. S. Gill, "Second prize: Preliminary experience with the niris optical coherence tomography system during laparoscopic and robotic prostatectomy," *Journal of endourology*, vol. 21, no. 8, pp. 814–818, 2007.

[69] P. P. Dangle, K. K. Shah, B. Kaffenberger, and V. R. Patel, "The use of high resolution optical coherence tomography to evaluate robotic radical prostatectomy specimens," *International braz j urol*, vol. 35, no. 3, pp. 344–353, 2009.

[70] L. P. Hariri, G. T. Bonnema, K. Schmidt, A. M. Winkler, V. Korde, K. D. Hatch, J. R. Davis, M. A. Brewer, and J. K. Barton, "Laparoscopic optical coherence tomography imaging of human ovarian cancer," *Gynecologic Oncology*, vol. 114, no. 2, pp. 188–194, 2009.

[71] J. Jing, J. Zhang, A. C. Loy, B. J. F. Wong, and Z. Chen, "High-speed upper-airway imaging using full-range optical coherence tomography," *Journal of Biomedical Optics*, vol. 17, no. 11, p. 110 507, 2012.

[72] A. M. D. Lee, L. Cahill, K. Liu, C. MacAulay, C. Poh, and P. Lane, "Wide-field in vivo oral oct imaging," *Biomedical Optics Express*, vol. 6, no. 7, pp. 2664–2674, 2015.

[73] H. Schulz-Hildebrandt, M. Pieper, C. Stehmar, M. Ahrens, C. Idel, B. Wollenberg, P. König, and G. Hüttmann, "Novel endoscope with increased depth of field for imaging human nasal tissue by microscopic optical coherence tomography," *Biomedical Optics Express*, vol. 9, no. 2, pp. 636–647, 2018.

[74] S. Latus, M. Kulas, J. Sprenger, D. Bhattacharya, P. C. Breda, L. Wittig, T. Eixmann, G. Hüttmann, L. Maack, D. Eggert, C. Betz, and A. Schlaefer, "Motion-compensated oct imaging of laryngeal tissue," in *Medical Imaging 2024: Image-Guided Procedures, Robotic Interventions, and Modeling*, vol. 12928, SPIE, 2024, pp. 37–41.

[75] G. K. Sharma, A. Chin Loy, E. Su, J. Jing, Z. Chen, B. J.-F. Wong, and S. Verma, "Quantitative evaluation of adult subglottic stenosis using intraoperative long-range optical coherence tomography," *The Annals of otology, rhinology, and laryngology*, vol. 125, no. 10, pp. 815–822, 2016.

[76] J. Walther, J. Golde, M. Albrecht, B. C. Quirk, L. Scolaro, R. W. Kirk, Y. Gruda, C. Schnabel, F. Tetschke, K. Joehrens, D. Haim, M. Buckova, J. Li, and R. A. McLaughlin, "A handheld fiber-optic probe to enable optical coherence tomography of oral soft tissue," *IEEE transactions on bio-medical engineering*, vol. 69, no. 7, pp. 2276–2282, 2022.

[77] T. Zhang, S. Yuan, C. Xu, P. Liu, H.-c. Chang, S. H. C. Ng, H. Ren, and W. Yuan, "Pneumaoct: Pneumatic optical coherence tomography endoscopy for targeted distortion-free imaging in tortuous and narrow internal lumens," *Science Advances*, vol. 10, no. 35, eadp3145, 2024.

[78] H. Pahlevaninezhad, M. Khorasaninejad, Y.-W. Huang, Z. Shi, L. P. Hariri, D. C. Adams, V. Ding, A. Zhu, C.-W. Qiu, F. Capasso, and M. J. Suter, "Nano-optic endoscope for high-resolution optical coherence tomography in vivo," *Nature Photonics*, vol. 12, no. 9, pp. 540–547, 2018.

[79] F. Benboujja, J. A. Garcia, K. Beaudette, M. Strupler, C. J. Hartnick, and C. Boudoux, "Intraoperative imaging of pediatric vocal fold lesions using optical coherence tomography," *Journal of Biomedical Optics*, vol. 21, no. 1, p. 16 007, 2016.

[80] X. Li, S. Martin, C. Pitris, R. Ghanta, D. L. Stamper, M. Harman, J. G. Fujimoto, and M. E. Brezinski, "High-resolution optical coherence tomographic imaging of osteoarthritic cartilage during open knee surgery," *Arthritis Research & Therapy*, vol. 7, no. 2, R318–23, 2005.

[81] K. Liang, O. O. Ahsen, Z. Wang, H.-C. Lee, W. Liang, B. M. Potsaid, T.-H. Tsai, M. G. Giacomelli, V. Jayaraman, H. Mashimo, X. Li, and J. G. Fujimoto, "Endoscopic forward-viewing optical coherence tomography and angiography with mhz swept source," *Optics Letters*, vol. 42, no. 16, p. 3193, 2017.

[82] A. M. Zysk, F. T. Nguyen, E. J. Chaney, J. G. Kotynek, U. J. Oliphant, F. J. Bellafiore, P. A. Johnson, K. M. Rowland, and S. A. Boppart, "Clinical feasibility of microscopically-guided breast needle biopsy using a fiber-optic probe with computer-aided detection," *Technology in cancer research & treatment*, vol. 8, no. 5, pp. 315–321, 2009.

[83] N. V. Iftimia, M. Mujat, T. Ustun, R. D. Ferguson, V. Danthu, and D. X. Hammer, "Spectral-domain low coherence interferometry/optical coherence tomography system for fine needle breast biopsy guidance," *The Review of scientific instruments*, vol. 80, no. 2, p. 024 302, 2009.

[84] R. A. McLaughlin, B. C. Quirk, A. Curatolo, R. W. Kirk, L. Scolaro, D. Lorenser, P. D. Robbins, B. A. Wood, C. M. Saunders, and D. D. Sampson, "Imaging of breast cancer with optical coherence tomography needle probes: Feasibility and initial results," *IEEE Journal on Selected Topics in Quantum Electronics*, vol. 18, no. 3, pp. 1184–1191, 2012.

[85] M. Villiger, D. Lorenser, R. A. McLaughlin, B. C. Quirk, R. W. Kirk, B. E. Bouma, and D. D. Sampson, "Deep tissue volume imaging of birefringence through fibre-optic needle probes for the delineation of breast tumour," *Scientific Reports*, vol. 6, p. 28 771, 2016.

[86] K. M. Joos and J.-H. Shen, "Miniature real-time intraoperative forward-imaging optical coherence tomography probe," *Biomedical Optics Express*, vol. 4, no. 8, pp. 1342–1350, 2013.

[87] S. Han, M. V. Sarunic, J. Wu, M. Humayun, and C. Yang, "Handheld forward-imaging needle endoscope for ophthalmic optical coherence tomography inspection," *Journal of Biomedical Optics*, vol. 13, no. 2, p. 020 505, 2008.

[88] T. Asami, H. Terasaki, Y. Ito, T. Sugita, H. Kaneko, J. Nishiyama, H. Namiki, M. Kobayashi, and N. Nishizawa, "Development of a fiber-optic optical coherence tomography probe for intraocular use," *Investigative Ophthalmology & Visual Science*, vol. 57, no. 9, OCT568–74, 2016.

[89] M. Mura, D. Iannetta, F. Nasini, F. Barca, E. Peiretti, L. Engelbrecht, M. D. de Smet, and F. Verbraak, "Use of a new intra-ocular spectral domain optical coherence tomography in vitreoretinal surgery," *Acta Ophthalmologica*, vol. 94, no. 3, pp. 246–252, 2016.

[90] M. Ourak, J. Smits, L. Esteveny, G. Borghesan, A. Gijbels, L. Schoevaerdts, Y. Douven, J. Scholtes, E. Lankenau, T. Eixmann, H. Schulz-Hildebrandt, G. Hüttmann, M. Kozlovszky, G. Kronreif, K. Willekens, P. Stalmans, K. Faridpooya, M. Cereda, A. Giani, G. Staurenghi, D. Reynaerts, and E. B. Vander Poorten, "Combined oct distance and fbg force sensing cannulation needle for retinal vein cannulation: In vivo animal validation," *International Journal of Computer Assisted Radiology and Surgery*, vol. 14, no. 2, pp. 301–309, 2019.

[91] A. Abid, R. Duval, and C. Boutopoulos, "Development and ex-vivo validation of 36g polyimide cannulas integrating a guiding miniaturized oct probe for robotic assisted subretinal injections," *Biomedical Optics Express*, vol. 13, no. 2, pp. 850–861, 2022.

[92] G. W. Cheon, Y. Huang, J. Cha, P. L. Gehlbach, and J. U. Kang, "Accurate real-time depth control for cp-ssoct distal sensor based handheld microsurgery tools," *Biomedical Optics Express*, vol. 6, no. 5, pp. 1942–1953, 2015.

[93] J. Im and C. Song, "Oblique injection depth correction by a two parallel oct sensor guided handheld smart injector," *Biomedical Optics Express*, vol. 12, no. 2, pp. 926–939, 2021.

[94] J. U. Kang and G. W. Cheon, "Demonstration of subretinal injection using common-path swept source oct guided microinjector," *Applied Sciences*, vol. 8, no. 8, p. 1287, 2018.

[95] C. Song, P. L. Gehlbach, and J. U. Kang, "Active tremor cancellation by a "smart" handheld vitreoretinal microsurgical tool using swept source optical coherence tomography," *Optics Express*, vol. 20, no. 21, pp. 23 414–23 421, 2012.

[96] Z. Yan, Y. Huang, Y. Liu, X. Li, Z. Qiao, and Q. Hao, "Fiber probe design for needle tip depth sensing in subretinal injection surgery based on sd-oct," in *AOPC 2024: Biomedical Optics*, vol. 13503, SPIE, 2024, pp. 11–20.

[97] Q. Tang, C.-P. Liang, K. Wu, A. Sandler, and Y. Chen, "Real-time epidural anesthesia guidance using optical coherence tomography needle probe," *Quantitative Imaging in Medicine and Surgery*, vol. 5, no. 1, p. 118, 2015.

[98] M.-C. Kao, Y.-T. Wu, M.-Y. Tsou, W.-C. Kuo, and C.-K. Ting, "Intelligent epidural needle placement using fiber-probe optical coherence tomography in a piglet model," *Biomedical Optics Express, Vol. 8, Issue 7, pp. 3440-3448*, vol. 9, no. 8, p. 3711, 2018.

[99] D. J. Harper, Y. Kim, A. Gómez-Ramírez, and B. J. Vakoc, "Needle guidance with doppler-tracked polarization-sensitive optical coherence tomography," *Journal of Biomedical Optics*, vol. 28, no. 10, p. 102 910, 2023.

[100] C. Wang, Y. Liu, P. Calle, X. Li, R. Liu, Q. Zhang, F. Yan, K.-m. Fung, A. K. Conner, S. Chen, C. Pan, and Q. Tang, "Enhancing epidural needle guidance using a polarization-sensitive optical coherence tomography probe with convolutional neural networks," *Journal of Biophotonics*, vol. 17, no. 2, e202300330, 2023.

[101] E. Y.-H. Huang, M.-C. Kao, C.-K. Ting, W. J. S. Huang, Y.-T. Yeh, H.-H. Ke, and W.-C. Kuo, "Needle-probe optical coherence tomography for real-time visualization of veress peritoneal needle placement in a porcine model: A new safety concept for pneumoperitoneum establishment in laparoscopic surgery," *Biomedicines*, vol. 10, no. 2, p. 485, 2022.

[102] W. A. Reed, M. F. Yan, and M. J. Schnitzer, "Gradient-index fiber-optic microprobes for minimally invasive in vivo low-coherence interferometry," *Optics Letters*, vol. 27, no. 20, pp. 1794–1796, 2002.

[103] C.-P. Liang, J. Wierwille, T. Moreira, G. Schwartzbauer, M. S. Jafri, C.-M. Tang, and Y. Chen, "A forward-imaging needle-type oct probe for image guided stereotactic procedures," *Optics Express*, vol. 19, no. 27, pp. 26 283–26 294, 2011.

[104] H. Ramakonar, B. C. Quirk, R. W. Kirk, J. Li, A. Jacques, C. R. Lind, and R. A. McLaughlin, "Intraoperative detection of blood vessels with an imaging needle during neurosurgery in humans," *Science Advances*, vol. 4, no. 12, eaav4992, 2018.

[105] C. Sun, K. K. C. Lee, B. Vuong, M. D. Cusimano, A. Brukson, A. Mauro, N. Munce, B. K. Courtney, B. A. Standish, and V. X. D. Yang, "Intraoperative handheld optical coherence tomography forward-viewing probe: Physical performance and preliminary animal imaging," *Biomedical Optics Express*, vol. 3, no. 6, pp. 1404–1412, 2012.

[106] K. M. Tan, M. Shishkov, A. Chee, M. B. Applegate, B. E. Bouma, and M. J. Suter, "Flexible transbronchial optical frequency domain imaging smart needle for biopsy guidance," *Biomedical Optics Express*, vol. 3, no. 8, p. 1947, 2012.

[107] J. Li, B. C. Quirk, P. B. Noble, R. W. Kirk, D. D. Sampson, and R. A. McLaughlin, "Flexible needle with integrated optical coherence tomography probe for imaging during transbronchial tissue aspiration," *Journal of biomedical optics*, vol. 22, no. 10, p. 106 002, 2017.

[108] L. P. Hariri, M. Mino-Kenudson, M. B. Applegate, E. J. Mark, G. J. Tearney, M. Lanuti, C. L. Channick, A. Chee, and M. J. Suter, "Toward the guidance of transbronchial biopsy: Identifying pulmonary nodules with optical coherence tomography," *Chest*, vol. 144, no. 4, p. 1261, 2013.

[109] E. Shostak, L. P. Hariri, G. Z. Cheng, D. C. Adams, and M. J. Suter, "Needle-based optical coherence tomography to guide transbronchial lymph node biopsy," *Journal of bronchology & interventional pulmonology*, vol. 25, no. 3, p. 189, 2018.

[110] G. Hohert, R. Meyers, S. Lam, A. Vertikov, A. Lee, S. Lam, and P. Lane, "Feasibility of combined optical coherence tomography and autofluorescence imaging for visualization of needle biopsy placement," *Journal of biomedical optics*, vol. 25, no. 10, p. 106 003, 2020.

[111] B. G. Muller, D. M. de Bruin, W. van den Bos, M. J. Brandt, J. F. Velu, M. T. J. Bus, D. J. Faber, D. Savci, P. J. Zondervan, T. M. de Reijke, P. L. Pes, J. de La Rosette, and T. G. van Leeuwen, "Prostate cancer diagnosis: The feasibility of needle-based optical coherence tomography," *Journal of Medical Imaging*, vol. 2, no. 3, p. 037 501, 2015.

[112] B. G. Muller, D. M. de Bruin, M. J. Brandt, W. van den Bos, S. van Huystee, D. J. Faber, D. Savci, P. J. Zondervan, T. M. de Reijke, M. P. Laguna-Pes, T. G. van Leeuwen, and J. J. M. C. H. de La Rosette, "Prostate cancer diagnosis by optical coherence tomography: First results from a needle based optical platform for tissue sampling," *Journal of Biophotonics*, vol. 9, no. 5, pp. 490–498, 2016.

[113] B. G. Muller, R. A. A. van Kollenburg, A. Swaan, E. C. H. Zwartkruis, M. J. Brandt, L. S. Wilk, M. Almasian, A. W. Schreurs, D. J. Faber, L. R. Rozendaal, A. N. Vis, J. A. Nieuwenhuijzen, J. R. J. A. van Moorselaar, J. J. M. C. H. de La Rosette, D. M. de Bruin, and T. G. van Leeuwen, "Needle-based optical coherence tomography for the detection of prostate cancer: A visual and quantitative analysis in 20 patients," *Journal of Biomedical Optics*, vol. 23, no. 8, pp. 1–11, 2018.

[114] A. Swaan, C. K. Mannaerts, B. G. Muller, R. A. van Kollenburg, M. Lucas, C. D. Savci-Heijink, T. G. van Leeuwen, T. M. de Reijke, and D. M. de Bruin, "The first in vivo needle-based optical coherence tomography in human prostate: A safety and feasibility study," *Lasers in Surgery and Medicine*, vol. 51, no. 5, pp. 390–398, 2019.

[115] X. Li, C. Chudoba, T. Ko, C. Pitris, and J. G. Fujimoto, "Imaging needle for optical coherence tomography," *Optics Letters*, vol. 25, no. 20, pp. 1520–1522, 2000.

[116] T. Han, S. Qian, J. Meng, L. Zhou, G. Xi, L. Yang, L. Chen, L. Zhang, R. Jiang, C. Wang, B. Niu, S. Satapathi, J. Zhang, C. He, K. Sun, S. Zhuo, Z. Ding, and Z. Liu, "Detection of human cervical cancer by probe–based quantitative optical coherence tomography," *Laser & Photonics Reviews*, vol. 19, no. 9, 2025.

[117] K. M. Kennedy, B. F. Kennedy, R. A. McLaughlin, and D. D. Sampson, "Needle optical coherence elastography for tissue boundary detection," *Optics Letters*, vol. 37, no. 12, pp. 2310–2312, 2012.

[118] K. M. Kennedy, R. A. McLaughlin, B. F. Kennedy, A. Tien, B. Latham, C. M. Saunders, and D. D. Sampson, "Needle optical coherence elastography for the measurement of microscale mechanical contrast deep within human breast tissues," *Journal of Biomedical Optics*, vol. 18, no. 12, p. 121 510, 2013.

[119] X. Liu, F. R. Zaki, H. Wu, C. Wang, and Y. Wang, "Temporally and spatially adaptive doppler analysis for robust handheld optical coherence elastography," *Biomedical Optics Express*, vol. 9, no. 7, pp. 3335–3353, 2018.

[120] Q. Fang, A. Curatolo, P. Wijesinghe, Y. L. Yeow, J. Hamzah, P. B. Noble, K. Karnowski, D. D. Sampson, R. Ganss, J. K. Kim, W. M. Lee, and B. F. Kennedy, "Ultrahigh-resolution optical coherence elastography through a micro-endoscope: Towards in vivo imaging of cellular-scale mechanics," *Biomedical Optics Express*, vol. 8, no. 11, pp. 5127–5138, 2017.

[121] Y. Qiu, F. R. Zaki, N. Chandra, S. A. Chester, and X. Liu, "Nonlinear characterization of elasticity using quantitative optical coherence elastography," *Biomedical Optics Express*, vol. 7, no. 11, pp. 4702–4710, 2016.

[122] Y. Qiu, Y. Wang, Y. Xu, N. Chandra, J. Haorah, B. Hubbi, B. J. Pfister, and X. Liu, "Quantitative optical coherence elastography based on fiber-optic probe for in situ measurement of tissue mechanical properties," *Biomedical Optics Express*, vol. 7, no. 2, pp. 688–700, 2016.

[123] X. Liu, F. Zaki, and Y. Wang, "Quantitative optical coherence elastography for robust stiffness assessment," *Applied Sciences*, vol. 8, no. 8, p. 1255, 2018.

[124] Y. Qu, T. Ma, Y. He, M. Yu, J. Zhu, Y. Miao, C. Dai, P. Patel, K. K. Shung, Q. Zhou, and Z. Chen, "Miniature probe for mapping mechanical properties of vascular lesions using acoustic radiation force optical coherence elastography," *Scientific Reports*, vol. 7, no. 1, p. 4731, 2017.

[125] A. B. Karpiouk, D. J. VanderLaan, K. V. Larin, and S. Y. Emelianov, "Integrated optical coherence tomography and multielement ultrasound transducer probe for shear wave elasticity imaging of moving tissues," *Journal of Biomedical Optics*, vol. 23, no. 10, pp. 1–7, 2018.

[126] S. Latus, C. Otte, M. Schlüter, J. Rehra, K. Bizon, H. Schulz-Hildebrandt, T. Saathoff, G. Hüttmann, and A. Schlaefer, "An approach for needle based optical coherence elastography measurements," in *International Conference on Medical Image Computing and Computer-Assisted Intervention*, 2017, pp. 655–663.

[127] S. Latus, S. Grube, T. Eixmann, M. Neidhardt, S. Gerlach, R. Mieling, G. Huttmann, M. Lutz, and A. Schlaefer, "A miniature dual-fiber probe for quantitative optical coherence elastography," *IEEE transactions on bio-medical engineering*, vol. 70, no. 11, pp. 3064–3072, 2023.

[128] T. Wang, T. Pfeiffer, A. Akyildiz, H. M. M. van Beusekom, R. Huber, A. F. W. van der Steen, and G. van Soest, "Intravascular optical coherence elastography," *Biomedical Optics Express*, vol. 13, no. 10, pp. 5418–5433, 2022.

[129] R. Bu, S. Balakrishnan, N. Iftimia, H. Price, C. Zdanski, and A. L. Oldenburg, "Airway compliance measured by anatomic optical coherence tomography," *Biomedical Optics Express*, vol. 8, no. 4, pp. 2195–2209, 2017.

[130] R. Bu, S. Balakrishnan, H. Price, C. Zdanski, S. Mitran, and A. L. Oldenburg, "Localized compliance measurement of the airway wall using anatomic optical coherence elastography," *Optics Express*, vol. 27, no. 12, pp. 16 751–16 766, 2019.

[131] R. Bu, S. Balakrishnan, N. Iftimia, H. Price, C. Zdanski, S. Mitran, and A. L. Oldenburg, "Sensing inhalation injury-associated changes in airway wall compliance by anatomic optical coherence elastography," *IEEE transactions on bio-medical engineering*, vol. 68, no. 8, pp. 2360–2367, 2021.

[132] H. Xu, Q. Xia, C. Shu, J. Lan, X. Wang, W. Gao, S. Lv, R. Lin, Z. Xie, X. Xiong, F. Li, J. Zhang, and X. Gong, "In vivo endoscopic optical coherence elastography based on a miniature probe," *Biomedical Optics Express*, vol. 15, no. 7, p. 4237, 2024.

[133] N. Gessert, T. Priegnitz, T. Saathoff, S.-T. Antoni, D. Meyer, M. F. Hamann, K.-P. Jünemann, C. Otte, and A. Schlaefer, "Needle tip force estimation using an oct fiber and a fused convgru-cnn architecture," in *Medical Image Computing and Computer Assisted Intervention – MICCAI 2018*, Cham: Springer, 2018, pp. 222–229.

[134] N. Gessert, T. Priegnitz, T. Saathoff, S. T. Antoni, D. Meyer, M. F. Hamann, K. P. Jünemann, C. Otte, and A. Schlaefer, "Spatio-temporal deep learning models for tip force estimation during needle insertion," *International Journal of Computer Assisted Radiology and Surgery*, vol. 14, no. 9, pp. 1485–1493, 2019.

[135] M. Gromniak, N. Gessert, T. Saathoff, and A. Schlaefer, "Needle tip force estimation by deep learning from raw spectral oct data," *International Journal of Computer Assisted Radiology and Surgery*, vol. 15, no. 10, pp. 1699–1702, 2020.

[136] S. Latus, J. Sprenger, M. Neidhardt, J. Schädler, A. Ron, A. Fitzek, M. Schlüter, P. Breitfeld, A. Heinemann, K. Püschel, and A. Schlaefer, "Rupture detection during needle insertion using complex oct data and cnns," *IEEE Transactions on Biomedical Engineering*, vol. 68, no. 10, pp. 3059–3067, 2021.

[137] C. Otte, G. Hüttmann, and A. Schlaefer, "Feasibiliy of optical detection of soft tissue deformation during needle insertion," *Medical Imaging 2012: Image-Guided Procedures, Robotic Interventions, and Modeling*, vol. 8316, pp. 282–292, 2012.

[138] C. Wang, P. Calle, N. B. Tran Ton, Z. Zhang, F. Yan, A. M. Donaldson, N. A. Bradley, Z. Yu, K.-m. Fung, C. Pan, and Q. Tang, "Deep-learning-aided forward optical coherence tomography endoscope for percutaneous nephrostomy guidance," *Biomedical Optics Express*, vol. 12, no. 4, pp. 2404–2418, 2021.

[139] G. Maguluri, J. Grimble, A. Caron, G. Zhu, S. Krishnamurthy, A. McWatters, G. Beamer, S.-Y. Lee, and N. Iftimia, "Core needle biopsy guidance based on tissue morphology assessment with ai-oct imaging," *Diagnostics*, vol. 13, no. 13, p. 2276, 2023.

[140] D. Bhattacharya, S. Latus, F. Behrendt, F. Thimm, D. Eggert, C. Betz, and A. Schlaefer, "Tissue classification during needle insertion using self-supervised contrastive learning and optical coherence tomography," in *2023 45th Annual International Conference of the IEEE Engineering in Medicine & Biology Society (EMBC)*, IEEE, 2023, pp. 1–4.

[141] S. Lee and J. Kang, "Cnn-based cp-oct sensor integrated with a subretinal injector for retinal boundary tracking and injection guidance," *Journal of Biomedical Optics*, vol. 26, no. 6, p. 068 001, 2021.

[142] R. Mieling, C. Stapper, S. Gerlach, M. Neidhardt, S. Latus, M. Gromniak, P. Breitfeld, and A. Schlaefer, "Proximity-based haptic feedback for collaborative robotic needle insertion," in *International Conference on Human Haptic Sensing and Touch Enabled Computer Applications EuroHaptics 2022*, ser. Lecture Notes in Computer Science, Springer, 2022, pp. 301–309.

[143] R. Mieling, M. Neidhardt, S. Latus, C. Stapper, S. Gerlach, I. Kniep, A. Heinemann, B. Ondruschka, and A. Schlaefer, "Collaborative robotic biopsy with trajectory guidance and needle tip force feedback," in *2023 IEEE International Conference on Robotics and Automation (ICRA)*, IEEE, 2023, pp. 6893–6900.

[144] R. Mieling, S. Latus, M. Fischer, F. Behrendt, and A. Schlaefer, "Optical coherence elastography needle for biomechanical characterization of deep tissue," in *Medical Image Computing and Computer Assisted Intervention – MICCAI 2023*, ser. Lecture Notes in Computer Science, Cham: Springer, 2023, pp. 607–617.

[145] M. Neidhardt, R. Mieling, M. Bengs, and A. Schlaefer, "Optical force estimation for interactions between tool and soft tissues," *Scientific Reports*, vol. 13, no. 1, p. 506, 2023.

[146] M. Neidhardt, R. Mieling, S. Latus, M. Fischer, T. Maurer, and A. Schlaefer, "A modified da vinci surgical instrument for optical coherence elastography with deep learning," in *2024 10th IEEE RAS/EMBS International Conference for Biomedical Robotics and Biomechatronics (BioRob)*, IEEE, 2024, pp. 1196–1201.

[147] Robin Mieling, Maximilian Neidhardt, Finn Behrendt, Sarah Latus, Axel Heinemann, Benjamin Ondruschka, and Alexander Schlaefer, "A-scan sequence transformers for palpation with optical coherence elastography," *Biomedical Optics Express*, vol. 16, no. 5, pp. 1925–1943, 2025.

[148] M. Neidhardt, S. Gerlach, R. Mieling, M.-H. Laves, T. Weib, M. Gromniak, A. Fitzek, D. Mobius, I. Kniep, A. Ron, J. Schadler, A. Heinemann, K. Puschel, B. Ondruschka, and A. Schlaefer, "Robotic tissue sampling for safe post-mortem biopsy in infectious corpses," *IEEE Transactions on Medical Robotics and Bionics*, vol. 4, no. 1, pp. 94–105, 2022.

[149] N. Gessert, M. Schlüter, and A. Schlaefer, "A deep learning approach for pose estimation from volumetric oct data," *Medical image analysis*, vol. 46, pp. 162–179, 2018.

[150] J. Sprenger, M. Neidhardt, M. Schlüter, S. Latus, T. Gosau, J. Kemmling, S. Feldhaus, U. Schumacher, and A. Schlaefer, "In-vivo markerless motion detection from volumetric optical coherence tomography data using cnns," in *Medical Imaging 2021: Image-Guided Procedures, Robotic Interventions, and Modeling*, vol. 11598, 2021, pp. 400–405.

[151] M. Neidhardt, M. Bengs, S. Latus, M. Schluter, T. Saathoff, and A. Schlaefer, "Deep learning for high speed optical coherence elastography," in *2020 IEEE 17th International Symposium on Biomedical Imaging (ISBI)*, IEEE, 2020, pp. 1583–1586.

[152] M. Neidhardt, M. Bengs, S. Latus, M. Schlüter, T. Saathoff, and A. Schlaefer, "4d deep learning for real-time volumetric optical coherence elastography," *International Journal of Computer Assisted Radiology and Surgery*, vol. 16, no. 1, pp. 23–27, 2021.

[153] Y. Zhang, J. Liao, Z. Feng, W. Yang, A. Perelli, Z. Wang, C. Li, and Z. Huang, "Vp-net: An end-to-end deep learning network for elastic wave velocity prediction in human skin in vivo using optical coherence elastography," *Frontiers in Bioengineering and Biotechnology*, vol. 12, p. 1 465 823, 2024.

[154] M. Neidhardt, S. Latus, T. Eixmann, G. Hüttmann, and A. Schlaefer, "Deep learning for high speed optical coherence elastography with a fiber scanning endoscope," *IEEE Transactions on Medical Imaging*, p. 1, 2024.

[155] N. Gessert, J. Beringhoff, C. Otte, and A. Schlaefer, "Force estimation from oct volumes using 3d cnns," *International Journal of Computer Assisted Radiology and Surgery*, vol. 13, no. 7, pp. 1073–1082, 2018.

[156] N. Gessert, M. Bengs, M. Schlüter, and A. Schlaefer, "Deep learning with 4d spatio-temporal data representations for oct-based force estimation," *Medical image analysis*, vol. 64, p. 101 730, 2020.

[157] M. Neidhardt, N. Gessert, T. Gosau, J. Kemmling, S. Feldhaus, U. Schumacher, and A. Schlaefer, "Force estimation from 4d oct data in a human tumor xenograft mouse model," *Current Directions in Biomedical Engineering*, vol. 6, no. 1, 2020.

[158] C. Wu, Z. Qiao, N. Zhang, X. Li, J. Fan, H. Song, D. Ai, J. Yang, and Y. Huang, "Phase unwrapping based on a residual en-decoder network for phase images in fourier domain doppler optical coherence tomography," *Biomedical Optics Express*, vol. 11, no. 4, pp. 1760–1771, 2020.

[159] B. Dong, N. Huang, Y. Bai, and S. Xie, "Deep-learning-based approach for strain estimation in phase-sensitive optical coherence elastography," *Optics Letters*, vol. 46, no. 23, pp. 5914–5917, 2021.

[160] X. Feng, G.-Y. Li, and S.-H. Yun, "Ultra-wideband optical coherence elastography from acoustic to ultrasonic frequencies," *Nature Communications*, vol. 14, no. 1, p. 4949, 2023.

[161] G. Shi, Y. Zhang, Y. Wang, S. Ai, C. Zhang, X. He, and X. Zheng, "Quantitative evaluation of human lens and lens capsule elasticity by optical coherence elastography based on a rayleigh wave model," *Journal of Biophotonics*, vol. 17, no. 12, e202400322, 2024.

[162] A. Ramier, A. M. Eltony, Y. Chen, F. Clouser, J. S. Birkenfeld, A. Watts, and S.-H. Yun, "In vivo measurement of shear modulus of the human cornea using optical coherence elastography," *Scientific Reports*, vol. 10, no. 1, p. 17 366, 2020.

[163] A. Adnan and R. A. Sheth, "Image-guided percutaneous biopsy of the liver," *Techniques in Vascular and Interventional Radiology*, vol. 24, no. 4, p. 100 773, 2021.

[164] G. A. McLeod, "Novel approaches to needle tracking and visualisation," *Anaesthesia*, vol. 76, pp. 160–170, 2021.

[165] J. I. Son, S. Y. Rhee, J.-T. Woo, W. S. Park, J. K. Byun, Y.-J. Kim, J. M. Byun, S. O. Chin, S. Chon, S. Oh, S. W. Kim, and Y. S. Kim, "Insufficient experience in thyroid fine-needle aspiration leads to misdiagnosis of thyroid cancer," *Endocrinology and metabolism*, vol. 29, no. 3, pp. 293–299, 2014.

[166] U. Fehrenbach, R. Thiel, P.-D. Bady, T. A. Auer, A. Kahl, D. Geisel, E. Lopez Hänninen, R. Öllinger, J. Pratschke, B. Gebauer, and T. Denecke, "Ct fluoroscopy-guided pancreas transplant biopsies: A retrospective evaluation of predictors of complications and success rates," *Transplant international : official journal of the European Society for Organ Transplantation*, vol. 34, no. 5, pp. 855–864, 2021.

[167] P. Kulkarni, S. Sikander, P. Biswas, S. Frawley, and S.-E. Song, "Review of robotic needle guide systems for percutaneous intervention," *Annals of Biomedical Engineering*, vol. 47, no. 12, pp. 2489–2513, 2019.

[168] L. R. Philipp, C. M. Matias, S. Thalheimer, S. H. Mehta, A. Sharan, and C. Wu, "Robot-assisted stereotaxy reduces target error: A meta-analysis and meta-regression of 6056 trajectories," *Neurosurgery*, vol. 88, no. 2, pp. 222–233, 2021.

[169] F. J. Siepel, B. Maris, M. K. Welleweerd, V. Groenhuis, P. Fiorini, and S. Stramigioli, "Needle and biopsy robots: A review," *Current Robotics Reports*, vol. 2, no. 1, pp. 73–84, 2021.

[170] D. Glauser, H. Fankhauser, M. Epitaux, J.-L. Hefti, and A. Jaccottet, "Neurosurgical robot minerva: First results and current developments," *Computer Aided Surgery*, vol. 1, no. 5, pp. 266–272, 1995.

[171] S. Lim, C. Jun, D. Chang, D. Petrisor, M. Han, and D. Stoianovici, "Robotic transrectal ultrasound guided prostate biopsy," *IEEE transactions on bio-medical engineering*, vol. 66, no. 9, pp. 2527–2537, 2019.

[172] M. Z. Mahmoud, M. Aslam, M. Alsaadi, M. A. Fagiri, and B. Alonazi, "Evolution of robot-assisted ultrasound-guided breast biopsy systems," *Journal of Radiation Research and Applied Sciences*, vol. 11, no. 1, pp. 89–97, 2018.

[173] M. Pavone, B. Seeliger, E. Teodorico, M. Goglia, C. Taliento, N. Bizzarri, L. Lecointre, C. Akladios, A. Forgione, G. Scambia, J. Marescaux, A. C. Testa, and D. Querleu, "Ultrasound-guided robotic surgical procedures: A systematic review," *Surgical Endoscopy*, vol. 38, no. 5, pp. 2359–2370, 2024.

[174] W. Wang, B. Pan, J. Yan, Y. Fu, and Y. Liu, "Magnetic resonance imaging and transrectal ultrasound prostate image segmentation based on improved level set for robotic prostate biopsy navigation," *The International Journal of Medical Robotics and Computer Assisted Surgery*, vol. 17, no. 1, pp. 1–14, 2021.

[175] M. K. Welleweerd, F. J. Siepel, V. Groenhuis, J. Veltman, and S. Stramigioli, "Design of an end-effector for robot-assisted ultrasound-guided breast biopsies," *International Journal of Computer Assisted Radiology and Surgery*, vol. 15, no. 4, pp. 681–690, 2020.

[176] M. K. Welleweerd, D. Pantelis, A. G. de Groot, F. J. Siepel, and S. Stramigioli, "Robot-assisted ultrasound-guided biopsy on mr-detected breast lesions," in *2020 IEEE/RSJ International Conference on Intelligent Robots and Systems (IROS)*, IEEE, 2020, pp. 2965–2971.

[177] E. Ben-David, M. Shochat, I. Roth, I. Nissenbaum, J. Sosna, and S. N. Goldberg, "Evaluation of a ct-guided robotic system for precise percutaneous needle insertion," *Journal of vascular and interventional radiology : JVIR*, vol. 29, no. 10, pp. 1440–1446, 2018.

[178] L. C. Ebert, W. Ptacek, S. Naether, M. Fürst, S. Ross, U. Buck, S. Weber, and M. Thali, "Virtobot - a multi-functional robotic system for 3d surface scanning and automatic post mortem biopsy," *International Journal of Medical Robotics and Computer Assisted Surgery*, vol. 6, no. 1, pp. 18–27, 2010.

[179] T. Hiraki, T. Kamegawa, T. Matsuno, J. Sakurai, Y. Kirita, R. Matsuura, T. Yamaguchi, T. Sasaki, T. Mitsuhashi, T. Komaki, Y. Masaoka, Y. Matsui, H. Fujiwara, T. Iguchi, H. Gobara, and S. Kanazawa, "Robotically driven ct-guided needle insertion: Preliminary results in phantom and animal experiments," *Radiology*, vol. 285, no. 2, pp. 454–461, 2017.

[180] W. J. Heerink, S. J. S. Ruiter, J. P. Pennings, B. Lansdorp, R. Vliegenthart, M. Oudkerk, and K. P. de Jong, "Robotic versus freehand needle positioning in ct-guided ablation of liver tumors: A randomized controlled trial," *Radiology*, vol. 290, no. 3, pp. 826–832, 2019.

[181] T. Hiraki, T. Kamegawa, T. Matsuno, J. Sakurai, T. Komaki, T. Yamaguchi, K. Tomita, M. Uka, Y. Matsui, T. Iguchi, H. Gobara, and S. Kanazawa, "Robotic needle insertion during computed tomography fluoroscopy–guided biopsy: Prospective first-in-human feasibility trial," *European radiology*, vol. 30, no. 2, pp. 927–933, 2019.

[182] S. Levy, S. N. Goldberg, I. Roth, M. Shochat, J. Sosna, I. Leichter, and S. Flacke, "Clinical evaluation of a robotic system for precise ct-guided percutaneous procedures," *Abdominal radiology*, vol. 46, no. 10, pp. 5007–5016, 2021.

[183] M. C. Bernardes, P. Moreira, D. Lezcano, L. Foley, K. Tuncali, C. Tempany, J. S. Kim, N. Hata, I. Iordachita, and J. Tokuda, "In vivo feasibility study: Evaluating autonomous data-driven robotic needle trajectory correction in mri-guided transperineal procedures," *IEEE Robotics and Automation Letters*, vol. 9, no. 10, pp. 8975–8982, 2024.

[184] M. C. Hoang, V. H. Le, K. T. Nguyen, van Nguyen, J. Kim, E. Choi, S. Bang, B. Kang, J.-O. Park, and C.-S. Kim, "A robotic biopsy endoscope with magnetic 5-dof locomotion and a retractable biopsy punch," *Micromachines*, vol. 11, no. 1, 2020.

[185] Z. Liang, L. Lindenroth, R. Hashem, S. Bandula, D. Stoyanov, and A. Stilli, "Magnetic resonance imaging-guided needle insertion robots: A review of systems for liver and kidney interventions," *IEEE Robotics & Automation Magazine*, pp. 2–25, 2024.

[186] M. G. Schouten, J. G. R. Bomers, D. Yakar, H. Huisman, E. Rothgang, D. Bosboom, T. W. J. Scheenen, S. Misra, and J. J. Fütterer, "Evaluation of a robotic technique for transrectal mri-guided prostate biopsies," *European radiology*, vol. 22, pp. 476–483, 2012.

[187] H. Xu, A. Lasso, S. Vikal, P. Guion, A. Krieger, A. Kaushal, L. L. Whitcomb, and G. Fichtinger, "Mri-guided robotic prostate biopsy: A clinical accuracy validation," in *Medical Image Computing and Computer-Assisted Intervention–MICCAI 2010: 13th International Conference, Beijing, China, September 20-24, 2010, Proceedings, Part III 13*, vol. 13, Springer, 2010, pp. 383–391.

[188] A. M. Okamura, C. Simone, and M. D. O'Leary, "Force modeling for needle insertion into soft tissue," *IEEE Transactions on Biomedical Engineering*, vol. 51, no. 10, pp. 1707–1716, 2004.

[189] D. J. van Gerwen, J. Dankelman, and J. J. van den Dobbelsteen, "Needle-tissue interaction forces - a survey of experimental data," *Medical Engineering and Physics*, vol. 34, no. 6, pp. 665–680, 2012.

[190] M. Aggravi, D. A. L. Estima, A. Krupa, S. Misra, and C. Pacchierotti, "Haptic teleoperation of flexible needles combining 3d ultrasound guidance and needle tip force feedback," *IEEE Robotics and Automation Letters*, vol. 6, no. 3, pp. 4859–4866, 2021.

[191] S. Elayaperumal, J. H. Bae, D. Christensen, M. R. Cutkosky, B. L. Daniel, J. M. Costa, R. J. Black, F. Faridian, and B. Moslehi, "Mr-compatible biopsy needle with enhanced tip force sensing," *World Haptics Conference. World Haptics Conference*, vol. 2013, pp. 109–114, 2013.

[192] A. K. Han, J. H. Bae, K. C. Gregoriou, C. J. Ploch, R. E. Goldman, G. H. Glover, B. L. Daniel, and M. R. Cutkosky, "Mr-compatible haptic display of membrane puncture in robot-assisted needle procedures," *IEEE Transactions on Haptics*, vol. 11, no. 3, pp. 443–454, 2018.

[193] D. de Lorenzo, Y. Koseki, E. de Momi, K. Chinzei, and A. M. Okamura, "Coaxial needle insertion assistant with enhanced force feedback," *IEEE Transactions on Biomedical Engineering*, vol. 60, no. 2, pp. 379–389, 2013.

[194] Y. Wang and H. Li, "Penetration detection with intention recognition for cooperatively controlled robotic needle insertion," *Transactions of the Institute of Measurement and Control*, vol. 44, no. 10, pp. 1979–1992, 2022.

[195] A. Asadian, M. R. Kermani, and R. V. Patel, "A novel force modeling scheme for needle insertion using multiple kalman filters," *IEEE Transactions on Instrumentation and Measurement*, vol. 61, no. 2, pp. 429–438, 2012.

[196] Z. Cheng, M. Koskinopoulou, S. Bano, D. Stoyanov, T. Rajeeth Savarimuthu, and L. S. Mattos, "Sensing technologies for guidance during needle-based interventions," *IEEE Transactions on Instrumentation and Measurement*, vol. 73, pp. 1–15, 2024.

[197] S. P. DiMaio and S. E. Salcudean, "Needle insertion modelling for the interactive simulation of percutaneous procedures," in *International Conference on Medical Image Computing and Computer-Assisted Intervention*, 2002, pp. 253–260.

[198] S. Jiang, P. Li, Y. Yu, J. Liu, and Z. Yang, "Experimental study of needle-tissue interaction forces: Effect of needle geometries, insertion methods and tissue characteristics," *Journal of Biomechanics*, vol. 47, no. 13, pp. 3344–3353, 2014.

[199] M. Khadem, C. Rossa, R. S. Sloboda, N. Usmani, and M. Tavakoli, "Mechanics of tissue cutting during needle insertion in biological tissue," *IEEE Robotics and Automation Letters*, vol. 1, no. 2, pp. 800–807, 2016.

[200] M. Mahvash and P. E. Dupont, "Mechanics of dynamic needle insertion into a biological material," *IEEE Transactions on Biomedical Engineering*, vol. 57, no. 4, pp. 934–943, 2010.

[201] C. Yang, Y. Xie, S. Liu, and D. Sun, "Force modeling, identification, and feedback control of robot-assisted needle insertion: A survey of the literature," *Sensors*, vol. 18, no. 2, p. 561, 2018.

[202] R. Chadda, S. Wismath, M. Hessinger, N. Schafer, A. Schlaefer, and M. Kupnik, "Needle tip force sensor for medical applications," in *2019 IEEE SENSORS*, 2019, pp. 1–4.

[203] D. Uzun, O. Ulgen, and O. Kocaturk, "Optical force sensor with enhanced resolution for mri guided biopsy," *IEEE Sensors Journal*, vol. 20, no. 16, pp. 9202–9208, 2020.

[204] S. Beekmans, T. Lembrechts, J. van den Dobbelsteen, and D. van Gerwen, "Fiber-optic fabry-pérot interferometers for axial force sensing on the tip of a needle," *Sensors*, vol. 17, no. 1, p. 38, 2017.

[205] H. Su, M. Zervas, G. A. Cole, C. Furlong, and G. S. Fischer, "Real-time mri-guided needle placement robot with integrated fiber optic force sensing," in *2011 IEEE International Conference on Robotics and Automation*, IEEE, 2011, pp. 1583–1588.

[206] Z. Mo, X. Mao, K. O. Hicks, and W. Xu, "In-vivo tissue identification on mice using a fiber optical tip force sensing needle," *IEEE Sensors Journal*, vol. 18, no. 15, pp. 6352–6359, 2018.

[207] N. O. Ulgen, D. Uzun, and O. Kocaturk, "Phantom study of a fiber optic force sensor design for biopsy needles under mri," *Biomedical Optics Express*, vol. 10, no. 1, pp. 242–251, 2019.

[208] L. Schoevaerdts, G. Borghesan, M. Ourak, D. Reynaerts, and E. V. Poorten, "Electrical bio-impedance proximity sensing for vitreo-retinal micro-surgery," *IEEE Robotics and Automation Letters*, vol. 4, no. 4, pp. 4086–4093, 2019.

[209] A. Iele, A. Ricciardi, C. Pecorella, A. Cirillo, F. Ficuciello, B. Siciliano, R. La Rocca, V. Mirone, M. Consales, and A. Cusano, "Miniaturized optical fiber probe for prostate cancer screening," *Biomedical Optics Express*, vol. 12, no. 9, pp. 5691–5703, 2021.

[210] S. V. Beekmans and D. Iannuzzi, "Characterizing tissue stiffness at the tip of a rigid needle using an opto-mechanical force sensor," *Biomedical Microdevices*, vol. 18, no. 1, p. 15, 2016.

[211] H. Coussons, J. Feldstein, and S. McCarus, "Senhance surgical system in benign hysterectomy: A real-world comparative assessment of case times and instrument costs versus da vinci robotics and laparoscopic-assisted vaginal hysterectomy procedures," *The International Journal of Medical Robotics and Computer Assisted Surgery*, vol. 17, no. 4, e2261, 2021.

[212] P. Biswas, S. Sikander, and P. Kulkarni, "Recent advances in robot-assisted surgical systems," *Biomedical Engineering Advances*, vol. 6, p. 100 109, 2023.

[213] H. Sang, J. Yun, R. Monfaredi, E. Wilson, H. Fooladi, and K. Cleary, "External force estimation and implementation in robotically assisted minimally invasive surgery," *The International Journal of Medical Robotics and Computer Assisted Surgery*, vol. 13, no. 2, e1824, 2017.

[214] Z. Li, X. Li, J. Lin, Y. Pang, D. Yang, L. Zhong, and J. Guo, "Design and application of multidimensional force/torque sensors in surgical robots: A review," *IEEE Sensors Journal*, vol. 23, no. 12, pp. 12 441–12 454, 2023.

[215] G. G. Muscolo and P. Fiorini, "Force–torque sensors for minimally invasive surgery robotic tools: An overview," *IEEE Transactions on Medical Robotics and Bionics*, vol. 5, no. 3, pp. 458–471, 2023.

[216] W. Wang, J. Wang, Y. Luo, X. Wang, and H. Song, "A survey on force sensing techniques in robot-assisted minimally invasive surgery," *IEEE Transactions on Haptics*, vol. 16, no. 4, pp. 702–718, 2023.

[217] Y. Hao, H. Zhang, Z. Zhang, C. Hu, and C. Shi, "Development of force sensing techniques for robot-assisted laparoscopic surgery: A review," *IEEE Transactions on Medical Robotics and Bionics*, vol. 6, no. 3, pp. 868–887, 2024.

[218] A. A. Nazari, F. Janabi-Sharifi, and K. Zareinia, "Image-based force estimation in medical applications: A review," *IEEE Sensors Journal*, vol. 21, no. 7, pp. 8805–8830, 2021.

[219] K. Miller, K. Chinzei, G. Orssengo, and P. Bednarz, "Mechanical properties of brain tissue in-vivo: Experiment and computer simulation," *Journal of Biomechanics*, vol. 33, no. 11, pp. 1369–1376, 2000.

[220] X. Wang, G. K. Ananthasuresh, and J. P. Ostrowski, "Vision-based sensing of forces in elastic objects," *Sensors and Actuators A: Physical*, vol. 94, no. 3, pp. 142–156, 2001.

[221] W. Kim, S. Seung, H. Choi, S. Park, S. Y. Ko, and J.-O. Park, "Image-based force estimation of deformable tissue using depth map for single-port surgical robot," in *2012 12th International Conference on Control, Automation and Systems*, 2012, pp. 1716–1719.

[222] S. Giannarou, M. Ye, G. Gras, K. Leibrandt, H. J. Marcus, and G.-Z. Yang, "Vision-based deformation recovery for intraoperative force estimation of tool-tissue interaction for neurosurgery," *International Journal of Computer Assisted Radiology and Surgery*, vol. 11, no. 6, pp. 929–936, 2016.

[223] N. Haouchine, W. Kuang, S. Cotin, and M. Yip, "Vision-based force feedback estimation for robot-assisted surgery using instrument-constrained biomechanical three-dimensional maps," *IEEE Robotics and Automation Letters*, vol. 3, no. 3, pp. 2160–2165, 2018.

[224] C. W. Kennedy and J. P. Desai, "A vision-based approach for estimating contact forces: Applications to robot-assisted surgery," *Applied Bionics and Biomechanics*, vol. 2, no. 1, pp. 53–60, 2005.

[225] C. Otte, J. Beringhoff, S. Latus, S. T. Antoni, O. Rajput, and A. Schlaefer, "Towards force sensing based on instrument-tissue interaction," in *IEEE International Conference on Multisensor Fusion and Integration for Intelligent Systems*, vol. 0, Institute of Electrical and Electronics Engineers Inc, 2016, pp. 180–185.

[226] A. I. Aviles, A. Marban, P. Sobrevilla, J. Fernandez, and A. Casals, "A recurrent neural network approach for 3d vision-based force estimation," in *2014 4th International Conference on Image Processing Theory, Tools and Applications (IPTA)*, IEEE, 2014, pp. 1–6.

[227] A. I. Aviles, S. Alsaleh, P. Sobrevilla, and A. Casals, "Sensorless force estimation using a neuro-vision-based approach for robotic-assisted surgery," in *2015 7th International IEEE/EMBS Conference on Neural Engineering (NER)*, 2015, pp. 86–89.

[228] A. I. Aviles, S. M. Alsaleh, J. K. Hahn, and A. Casals, "Towards retrieving force feedback in robotic-assisted surgery: A supervised neuro-recurrent-vision approach," *IEEE Transactions on Haptics*, vol. 10, no. 3, pp. 431–443, 2017.

[229] P. V. Sabique, P. Ganesh, and R. Sivaramakrishnan, "Stereovision based force estimation with stiffness mapping in surgical tool insertion using recurrent neural network," *The Journal of Supercomputing*, vol. 78, no. 12, pp. 14 648–14 679, 2022.

[230] P. Fekri, H. Khodashenas, K. Lachapelle, R. Cecere, M. Zadeh, and J. Dargahi, "Y-net: A deep convolutional architecture for 3d estimation of contact forces in intracardiac catheters," *IEEE Robotics and Automation Letters*, vol. 7, no. 2, pp. 3592–3599, 2022.

[231] M. D. I. Reyzabal, M. Chen, W. Huang, S. Ourselin, and H. Liu, "Dafoes: Mixing da tasets towards the generalization of vision-state deep-learning fo rce es timation in minimally invasive robotic surgery," *IEEE Robotics and Automation Letters*, pp. 1–8, 2024.

[232] Y. Wang, Z. Ye, M. Wen, H. Liang, and X. Zhang, "Transvfs: A spatio-temporal local-global transformer for vision-based force sensing during ultrasound-guided prostate biopsy," *Medical image analysis*, vol. 94, p. 103 130, 2024.

[233] S. Yang, M. H. Le, K. R. Golobish, J. C. Beaver, and Z. Chua, "Vision-based force estimation for minimally invasive telesurgery through contact detection and local stiffness models," *Journal of Medical Robotics Research*, vol. 09, no. 03n04, 2024.

[234] W.-J. Jung, K.-S. Kwak, and S.-C. Lim, "Vision-based suture tensile force estimation in robotic surgery," *Sensors*, vol. 21, no. 1, p. 110, 2020.

[235] D.-H. Lee, W. Hwang, and S.-C. Lim, "Interaction force estimation using camera and electrical current without force/torque sensor," *IEEE Sensors Journal*, vol. 18, no. 21, pp. 8863–8872, 2018.

[236] A. Marban, V. Srinivasan, W. Samek, J. Fernández, and A. Casals, "A recurrent convolutional neural network approach for sensorless force estimation in robotic surgery," *Biomedical Signal Processing and Control*, vol. 50, pp. 134–150, 2019.

[237] Z. Chua, A. M. Jarc, and A. M. Okamura, "Toward force estimation in robot-assisted surgery using deep learning with vision and robot state," in *2021 IEEE International Conference on Robotics and Automation (ICRA)*, IEEE, 2021, pp. 12 335–12 341.

[238] P. V. Sabique, G. Pasupathy, S. Ramachandran, and G. Shanmugasundar, "Investigating the influence of dimensionality reduction on force estimation in robotic-assisted surgery using recurrent and convolutional networks," *Engineering Applications of Artificial Intelligence*, vol. 126, p. 107 045, 2023.

[239] N. Herzig, P. Maiolino, F. Iida, and T. Nanayakkara, "A variable stiffness robotic probe for soft tissue palpation," *IEEE Robotics and Automation Letters*, vol. 3, no. 2, pp. 1168–1175, 2018.

[240] Z. Zhou, B. Huang, R. Zhang, M. Yin, C. Liu, Y. Liu, Z. Yi, and X. Wu, "Methods to recognize depth of hard inclusions in soft tissue using ordinal classification for robotic palpation," *IEEE Transactions on Instrumentation and Measurement*, vol. 71, pp. 1–12, 2022.

[241] S. Konishi, Y. Kakehi, and Y. Hori, "Directional touch sensing for stiffness singularity search in an object using microfinger with tactile sensor," *Scientific Reports*, vol. 12, no. 1, p. 21 374, 2022.

[242] S. Davaria, F. Najafi, M. J. Mahjoob, and S. M. Motahari-Bidgoli, "Design and fabrication of a robotic tactile device for abdominal palpation," in *2014 Second RSI/ISM International Conference on Robotics and Mechatronics (ICRoM)*, IEEE, 2014, pp. 339–344.

[243] T. Batty, A. Ehrampoosh, B. Shirinzadeh, Y. Zhong, and J. Smith, "A transparent teleoperated robotic surgical system with predictive haptic feedback and force modelling," *Sensors*, vol. 22, no. 24, p. 9770, 2022.

[244] S. Zhao, C. C. Nguyen, T. T. Hoang, T. N. Do, and H.-P. Phan, "Transparent pneumatic tactile sensors for soft biomedical robotics," *Sensors*, vol. 23, no. 12, p. 5671, 2023.

[245] D. G. Raitt, M. Huseynov, S. Homer-Vanniasinkam, H. A. Wurdemann, and S.-A. Abad, "Soft-tipped sensor with compliance control for elasticity sensing and palpation," *IEEE Transactions on Robotics*, vol. 40, pp. 2430–2441, 2024.

[246] S.-H. Cho, S.-M. Lee, N.-Y. Lee, B. C. Ko, H. Kim, D.-J. Jang, and J.-H. Lee, "High-resolution tactile-sensation diagnostic imaging system for thyroid cancer," *Sensors*, vol. 23, no. 7, p. 3451, 2023.

[247] C.-H. Won, J.-H. Lee, and F. Saleheen, "Tactile sensing systems for tumor characterization: A review," *IEEE Sensors Journal*, vol. 21, no. 11, pp. 12 578–12 588, 2021.

[248] R. Hampson, G. West, and G. Dobie, "Tactile, orientation, and optical sensor fusion for tactile breast image mosaicking," *IEEE Sensors Journal*, vol. 23, no. 5, pp. 5315–5324, 2023.

[249] N. Gonzalo, G. J. Tearney, P. W. Serruys, G. van Soest, T. Okamura, Garcéctor M, R. J. van Geuns, M. van der Ent, J. Ligthart, B. E. Boum, et al., "Second-generation optical coherence tomography in clinical practice. high-speed data acquisition is highly reproducible in patients undergoing percutaneous coronary intervention," *Revista Española de Cardiología (English Edition)*, vol. 63, no. 8, pp. 893–903, 2010.

[250] S. H. Yun, G. J. Tearney, J. F. de Boer, and B. E. Bouma, "Motion artifacts in optical coherence tomography with frequency-domain ranging," *Optics Express*, vol. 12, no. 13, pp. 2977–2998, 2004.

[251] C. Gorecki and S. Bargiel, "Mems scanning mirrors for optical coherence tomography," *Photonics*, vol. 8, no. 1, p. 6, 2021.

[252] O. M. Carrasco-Zevallos, C. Viehland, B. Keller, M. Draelos, A. N. Kuo, C. A. Toth, and J. A. Izatt, "Review of intraoperative optical coherence tomography: Technology and applications," *Biomedical Optics Express*, vol. 8, no. 3, pp. 1607–1637, 2017.

[253] S. Aumann, S. Donner, J. Fischer, and F. Müller, "Optical coherence tomography (oct): Principle and technical realization," in *High Resolution Imaging in Microscopy and Ophthalmology*, Springer, 2019, pp. 59–85.

[254] R. Mieling, "Deep learning for quantitative measurements with novel optical coherence elastography needle probes," Master's Thesis, Technical University of Hamburg, Hamburg, Germany, 2021.

[255] A. Gunalan and L. S. Mattos, "Towards oct-guided endoscopic laser surgery-a review," *Diagnostics*, vol. 13, no. 4, p. 677, 2023.

[256] M. B. Muijzer, P. A. W. J. Schellekens, H. J. M. Beckers, J. H. de Boer, S. M. Imhof, and R. P. L. Wisse, "Clinical applications for intraoperative optical coherence tomography: A systematic review," *Eye*, vol. 36, no. 2, pp. 379–391, 2022.

[257] J. Li, E. Pijewska, Q. Fang, M. Szkulmowski, and B. F. Kennedy, "Analysis of strain estimation methods in phase-sensitive compression optical coherence elastography," *Biomedical Optics Express*, vol. 13, no. 4, pp. 2224–2246, 2022.

[258] Y. Li, S. Moon, J. J. Chen, Z. Zhu, and Z. Chen, "Ultrahigh-sensitive optical coherence elastography," *Light: Science & Applications*, vol. 9, no. 1, p. 58, 2020.

[259] Y. Wang, D. Huang, Y. Su, and X. S. Yao, "Two-dimensional phase unwrapping in doppler fourier domain optical coherence tomography," *Optics Express*, vol. 24, no. 23, pp. 26 129–26 145, 2016.

[260] S. Burhan, N. Detrez, K. Rewerts, P. Strenge, S. Buschschlüter, J. Kren, C. Hagel, M. M. Bonsanto, R. Brinkmann, and R. Huber, "Phase unwrapping for mhz optical coherence elastography and application to brain tumor tissue," *Biomedical Optics Express*, vol. 15, no. 2, pp. 1038–1058, 2024.

[261] J. Schmitt, "Oct elastography: Imaging microscopic deformation and strain of tissue," *Optics Express*, vol. 3, no. 6, pp. 199–211, 1998.

[262] W. M. Allen, L. Chin, P. Wijesinghe, R. W. Kirk, B. Latham, D. D. Sampson, C. M. Saunders, and B. F. Kennedy, "Wide-field optical coherence micro-elastography for intraoperative assessment of human breast cancer margins," *Biomedical Optics Express*, vol. 7, no. 10, pp. 4139–4153, 2016.

[263] B. F. Kennedy, T. R. Hillman, R. A. McLaughlin, B. C. Quirk, and D. D. Sampson, "In vivo dynamic optical coherence elastography using a ring actuator," *Optics Express*, vol. 17, no. 24, pp. 21 762–21 772, 2009.

[264] B. F. Kennedy, X. Liang, S. G. Adie, D. K. Gerstmann, B. C. Quirk, S. A. Boppart, and D. D. Sampson, "In vivo three-dimensional optical coherence elastography," *Optics Express*, vol. 19, no. 7, p. 6623, 2011.

[265] B. F. Kennedy, S. H. Koh, R. A. McLaughlin, K. M. Kennedy, P. R. T. Munro, and D. D. Sampson, "Strain estimation in phase-sensitive optical coherence elastography," *Biomedical Optics Express*, vol. 3, no. 8, pp. 1865–1879, 2012.

[266] K. M. Kennedy, S. Es'haghian, L. Chin, R. A. McLaughlin, D. D. Sampson, and B. F. Kennedy, "Optical palpation: Optical coherence tomography-based tactile imaging using a compliant sensor," *Optics Letters*, vol. 39, no. 10, p. 3014, 2014.

[267] B. F. Kennedy, R. A. McLaughlin, K. M. Kennedy, L. Chin, A. Curatolo, A. Tien, B. Latham, C. M. Saunders, and D. D. Sampson, "Optical coherence micro-elastography: Mechanical-contrast imaging of tissue microstructure," *Biomedical Optics Express*, vol. 5, no. 7, pp. 2113–2124, 2014.

[268] K. M. Kennedy, L. Chin, R. A. McLaughlin, B. Latham, C. M. Saunders, D. D. Sampson, and B. F. Kennedy, "Quantitative micro-elastography: Imaging of tissue elasticity using compression optical coherence elastography," *Scientific Reports*, vol. 5, no. 1, p. 15 538, 2015.

[269] K. L. Metzner, Q. Fang, R. W. Sanderson, A. Mowla, and B. F. Kennedy, "Analysis of friction in quantitative micro-elastography," *Biomedical Optics Express*, vol. 14, no. 10, pp. 5127–5147, 2023.

[270] K. L. Metzner, Q. Fang, R. W. Sanderson, Y. L. Yeow, C. Green, F. Abdul-Aziz, J. Hamzah, A. Mowla, and B. F. Kennedy, "A novel stress sensor enables accurate estimation of micro-scale tissue mechanics in quantitative micro-elastography," *APL Bioengineering*, vol. 8, no. 3, p. 036 115, 2024.

[271] F. Navaeipour, M. S. Hepburn, J. Li, K. L. Metzner, S. E. Amos, D. Vahala, S. Maher, Y. S. Choi, and B. F. Kennedy, "In situ stress estimation in quantitative micro-elastography," *Biomedical Optics Express*, vol. 15, no. 6, pp. 3609–3626, 2024.

[272] E. V. Gubarkova, A. A. Sovetsky, L. A. Matveev, A. L. Matveyev, D. A. Vorontsov, A. A. Plekhanov, S. S. Kuznetsov, S. V. Gamayunov, A. Y. Vorontsov, M. A. Sirotkina, N. D. Gladkova, and V. Y. Zaitsev, "Nonlinear elasticity assessment with optical coherence elastography for high-selectivity differentiation of breast cancer tissues," *Materials*, vol. 15, no. 9, p. 3308, 2022.

[273] E. V. Gubarkova, D. A. Vorontsov, A. A. Sovetsky, E. L. Bederina, M. A. Sirotkina, A. Yu Bogomolova, S. V. Gamayunov, A. Yu Vorontsov, P. V. Krivorotko, V. Y. Zaitsev, and N. D. Gladkova, "Quantification of linear and nonlinear elasticity by compression optical coherence elastography for determining lymph node status in breast cancer," *Laser Physics Letters*, vol. 20, no. 6, p. 065 601, 2023.

[274] M. R. Ford, W. J. Dupps, A. M. Rollins, R. A. Sinha, and Z. Hu, "Method for optical coherence elastography of the cornea," *Journal of Biomedical Optics*, vol. 16, no. 1, p. 016 005, 2011.

[275] V. S. de Stefano, M. R. Ford, I. Seven, and W. J. Dupps, "Live human assessment of depth-dependent corneal displacements with swept-source optical coherence elastography," *PLOS ONE*, vol. 13, no. 12, e0209480, 2018.

[276] M. Singh, A. Nair, S. R. Aglyamov, and K. V. Larin, "Compressional optical coherence elastography of the cornea," *Photonics*, vol. 8, no. 4, p. 111, 2021.

[277] W. M. Allen, K. M. Kennedy, Q. Fang, L. Chin, A. Curatolo, L. Watts, R. Zilkens, S. L. Chin, B. F. Dessauvagie, B. Latham, C. M. Saunders, and B. F. Kennedy, "Wide-field quantitative micro-elastography of human breast tissue," *Biomedical Optics Express*, vol. 9, no. 3, pp. 1082–1096, 2018.

[278] E. V. Gubarkova, A. A. Sovetsky, V. Y. Zaitsev, A. L. Matveyev, D. A. Vorontsov, M. A. Sirotkina, L. A. Matveev, A. A. Plekhanov, N. P. Pavlova, S. S. Kuznetsov, A. Y. Vorontsov, E. V. Zagaynova, and N. D. Gladkova, "Oct-elastography-based optical biopsy for breast cancer delineation and express assessment of morphological/molecular subtypes," *Biomedical Optics Express*, vol. 10, no. 5, pp. 2244–2263, 2019.

[279] E. V. Gubarkova, E. B. Kiseleva, M. A. Sirotkina, D. A. Vorontsov, K. A. Achkasova, S. S. Kuznetsov, K. S. Yashin, A. L. Matveyev, A. A. Sovetsky, L. A. Matveev, A. A. Plekhanov, A. Y. Vorontsov, V. Y. Zaitsev, and N. D. Gladkova, "Diagnostic accuracy of cross-polarization oct and oct-elastography for differentiation of breast cancer subtypes: Comparative study," *Diagnostics*, vol. 10, no. 12, p. 994, 2020.

[280] E. V. Gubarkova, A. A. Sovetsky, D. A. Vorontsov, P. A. Buday, M. A. Sirotkina, A. A. Plekhanov, S. S. Kuznetsov, A. L. Matveyev, L. A. Matveev, S. V. Gamayunov, A. Y. Vorontsov, V. Y. Zaitsev, and N. D. Gladkova, "Compression optical coherence elastography versus strain ultrasound elastography for breast cancer detection and differentiation: Pilot study," *Biomedical Optics Express*, vol. 13, no. 5, pp. 2859–2881, 2022.

[281] A. A. Plekhanov, M. A. Sirotkina, A. A. Sovetsky, E. V. Gubarkova, S. S. Kuznetsov, A. L. Matveyev, L. A. Matveev, E. V. Zagaynova, N. D. Gladkova, and V. Y. Zaitsev, "Histological validation of in vivo assessment of cancer tissue inhomogeneity and automated morphological segmentation enabled by optical coherence elastography," *Scientific Reports*, vol. 10, no. 1, p. 11 781, 2020.

[282] A. A. Plekhanov, E. V. Gubarkova, M. A. Sirotkina, A. A. Sovetsky, D. A. Vorontsov, L. A. Matveev, S. S. Kuznetsov, A. Y. Bogomolova, A. Y. Vorontsov, A. L. Matveyev, S. V. Gamayunov, E. V. Zagaynova, V. Y. Zaitsev, and N. D. Gladkova, "Compression oct-elastography combined with speckle-contrast analysis as an approach to the morphological assessment of breast cancer tissue," *Biomedical Optics Express*, vol. 14, no. 6, pp. 3037–3056, 2023.

[283] A. A. Plekhanov, D. S. Kozlov, A. A. Shepeleva, E. B. Kiseleva, L. E. Shimolina, I. N. Druzhkova, M. A. Plekhanova, M. M. Karabut, E. V. Gubarkova, A. I. Gavrina, D. P. Krylov, A. A. Sovetsky, S. V. Gamayunov, D. S. Kuznetsova, V. Y. Zaitsev, M. A. Sirotkina, and N. D. Gladkova, "Tissue elasticity as a diagnostic marker of molecular mutations in morphologically heterogeneous colorectal cancer," *International Journal of Molecular Sciences*, vol. 25, no. 10, p. 5337, 2024.

[284] S. Wang and K. V. Larin, "Noncontact depth-resolved micro-scale optical coherence elastography of the cornea," *Biomedical Optics Express*, vol. 5, no. 11, pp. 3807–3821, 2014.

[285] M. Singh, J. Li, S. Vantipalli, S. Wang, Z. Han, A. Nair, S. R. Aglyamov, M. D. Twa, and K. V. Larin, "Noncontact elastic wave imaging optical coherence elastography for evaluating changes in corneal elasticity due to crosslinking," *IEEE Journal of Selected Topics in Quantum Electronics*, vol. 22, no. 3, pp. 266–276, 2016.

[286] G. Lan, B. Gu, K. V. Larin, and M. D. Twa, "Clinical corneal optical coherence elastography measurement precision: Effect of heartbeat and respiration," *Translational Vision Science & Technology*, vol. 9, no. 5, p. 3, 2020.

[287] G. Lan, S. R. Aglyamov, K. V. Larin, and M. D. Twa, "In vivo human corneal shear-wave optical coherence elastography," *Optometry and Vision Science*, vol. 98, no. 1, pp. 58–63, 2021.

[288] Z. Han, M. Singh, S. R. Aglyamov, C.-h. Liu, A. Nair, R. Raghunathan, C. Wu, J. Li, and K. V. Larin, "Quantifying tissue viscoelasticity using optical coherence elastography and the rayleigh wave model," *Journal of Biomedical Optics*, vol. 21, no. 9, p. 90 504, 2016.

[289] Z. Jin, Y. Zhou, M. Shen, Y. Wang, F. Lu, and D. Zhu, "Assessment of corneal viscoelasticity using elastic wave optical coherence elastography," *Journal of Biophotonics*, vol. 13, no. 1, e201960074, 2020.

[290] G. Shi, Y. Zhang, S. Ai, Y. Wang, Y. Li, X. He, and X. Zheng, "In vivo imaging and evaluation of corneal biomechanics after corneal transplantation by optical coherence elastography," *Journal of Biophotonics*, vol. 17, no. 12, e202400207, 2024.

[291] X. Liang, A. L. Oldenburg, V. Crecea, E. J. Chaney, and S. A. Boppart, "Optical micro-scale mapping of dynamic biomechanical tissue properties," *Optics Express*, vol. 16, no. 15, pp. 11 052–11 065, 2008.

[292] J. R. Wilkins, C. A. Puliafito, M. R. Hee, J. S. Duker, E. Reichel, J. G. Coker, J. S. Schuman, E. A. Swanson, and J. G. Fujimoto, "Characterization of epiretinal membranes using optical coherence tomography," *Ophthalmology*, vol. 103, no. 12, pp. 2142–2151, 1996.

[293] M. E. Brezinski, G. J. Tearney, S. A. Boppart, E. A. Swanson, J. F. Southern, and J. G. Fujimoto, "Optical biopsy with optical coherence tomography: Feasibility for surgical diagnostics," *Journal of Surgical Research*, vol. 71, no. 1, pp. 32–40, 1997.

[294] J. P. Ehlers, "Intraoperative optical coherence tomography: Past, present, and future," *Eye*, vol. 30, no. 2, pp. 193–201, 2016.

[295] B. C. H. Ang, S. Y. Lim, and S. Dorairaj, "Intra-operative optical coherence tomography in glaucoma surgery-a systematic review," *Eye*, vol. 34, no. 1, pp. 168–177, 2020.

[296] M. T. El-Haddad and Y. K. Tao, "Advances in intraoperative optical coherence tomography for surgical guidance," *Current Opinion in Biomedical Engineering*, vol. 3, pp. 37–48, 2017.

[297] F. W. Price, "Intraoperative optical coherence tomography: Game-changing technology," *Cornea*, vol. 40, no. 6, pp. 675–678, 2021.

[298] A. Pujari, D. Agarwal, R. Chawla, A. Kumar, and N. Sharma, "Intraoperative optical coherence tomography guided ocular surgeries: Critical analysis of clinical role and future perspectives," *Clinical Ophthalmology*, pp. 2427–2440, 2020.

[299] J. S. Titiyal, M. Kaur, S. Nair, and N. Sharma, "Intraoperative optical coherence tomography in anterior segment surgery," *Survey of Ophthalmology*, vol. 66, no. 2, pp. 308–326, 2021.

[300] B. H. Lee, E. J. Min, and Y. H. Kim, "Fiber-based optical coherence tomography for biomedical imaging, sensing, and precision measurements," *Optical Fiber Technology*, vol. 19, no. 6, pp. 729–740, 2013.

[301] D. Lorenser, R. A. McLaughlin, and D. D. Sampson, "Optical coherence tomography in a needle format," in *Optical Coherence Tomography*, Springer, Cham, 2015, pp. 2413–2472.

[302] Y. LeCun, Y. Bengio, and G. Hinton, "Deep learning," *Nature*, vol. 521, no. 7553, p. 436, 2015.

[303] I. Goodfellow, Y. Bengio, and A. Courville, *Deep learning* (Adaptive computation and machine learning). MIT Press, 2016.

[304] X. Chen, X. Wang, K. Zhang, K.-m. Fung, T. C. Thai, K. Moore, R. S. Mannel, H. Liu, B. Zheng, and Y. Qiu, "Recent advances and clinical applications of deep learning in medical image analysis," *Medical image analysis*, vol. 79, p. 102 444, 2022.

[305] V. Nair and G. E. Hinton, "Rectified linear units improve restricted boltzmann machines," in *Proceedings of the 27th international conference on machine learning (ICML-10)*, 2010, pp. 807–814.

[306] D. P. Kingma and J. Ba, "Adam: A method for stochastic optimization," *arXiv preprint arXiv:1412.6980*, 2014.

[307] Ashish Vaswani, Noam Shazeer, Niki Parmar, Jakob Uszkoreit, Llion Jones, Aidan N. Gomez, Łukasz Kaiser, and Illia Polosukhin, "Attention is all you need," *Advances in Neural Information Processing Systems*, vol. 30, 2017.

[308] S. Ioffe and C. Szegedy, "Batch normalization: Accelerating deep network training by reducing internal covariate shift," in *International conference on machine learning*, 2015, pp. 448–456.

[309] K. He, X. Zhang, S. Ren, and J. Sun, "Deep residual learning for image recognition," in *Proceedings of the IEEE conference on computer vision and pattern recognition*, 2016, pp. 770–778.

[310] G. Huang, Z. Liu, L. van der Maaten, and K. Q. Weinberger, "Densely connected convolutional networks," in *Proceedings of the IEEE conference on computer vision and pattern recognition*, 2017, pp. 4700–4708.

[311] J. Hu, L. Shen, and G. Sun, "Squeeze-and-excitation networks," in *Proceedings of the IEEE conference on computer vision and pattern recognition*, 2018, pp. 7132–7141.

[312] A. G. Howard, M. Zhu, B. Chen, D. Kalenichenko, W. Wang, T. Weyand, M. Andreetto, and H. Adam, "Mobilenets: Efficient convolutional neural networks for mobile vision applications," *arXiv preprint arXiv:1704.04861*, 2017.

[313] O. Ronneberger, P. Fischer, and T. Brox, "U-net: Convolutional networks for biomedical image segmentation," in *Medical image computing and computer-assisted intervention–MICCAI 2015: 18th international conference, Munich, Germany, October 5-9, 2015, proceedings, part III 18*, Springer, 2015, pp. 234–241.

[314] R. T. Yanagihara, C. S. Lee, D. S. W. Ting, and A. Y. Lee, "Methodological challenges of deep learning in optical coherence tomography for retinal diseases: A review," *Translational Vision Science & Technology*, vol. 9, no. 2, p. 11, 2020.

[315] A. R. Ran, C. C. Tham, P. P. Chan, C.-Y. Cheng, Y.-C. Tham, T. H. Rim, and C. Y. Cheung, "Deep learning in glaucoma with optical coherence tomography: A review," *Eye*, vol. 35, no. 1, pp. 188–201, 2021.

[316] I. A. Viedma, D. Alonso-Caneiro, S. A. Read, and M. J. Collins, "Deep learning in retinal optical coherence tomography (oct): A comprehensive survey," *Neurocomputing*, vol. 507, pp. 247–264, 2022.

[317] N. D. Koseoglu, A. Grzybowski, and T. Y. A. Liu, "Deep learning applications to classification and detection of age-related macular degeneration on optical coherence tomography imaging: A review," *Ophthalmology and Therapy*, vol. 12, no. 5, pp. 2347–2359, 2023.

[318] D. Yang, A. R. Ran, T. X. Nguyen, T. P. H. Lin, H. Chen, T. Y. Y. Lai, C. C. Tham, and C. Y. Cheung, "Deep learning in optical coherence tomography angiography: Current progress, challenges, and future directions," *Diagnostics*, vol. 13, no. 2, p. 326, 2023.

[319] N. Gessert, M. Lutz, M. Heyder, S. Latus, D. M. Leistner, Y. S. Abdelwahed, and A. Schlaefer, "Automatic plaque detection in ivoct pullbacks using convolutional neural networks," *IEEE transactions on medical imaging*, vol. 38, no. 2, pp. 426–434, 2018.

[320] C. Kolluru, D. Prabhu, Y. Gharaibeh, H. Bezerra, G. Guagliumi, and D. Wilson, "Deep neural networks for a-line-based plaque classification in coronary intravascular optical coherence tomography images," *Journal of Medical Imaging*, vol. 5, no. 4, p. 044 504, 2018.

[321] J. Lee, J. N. Kim, L. A. P. Dallan, V. N. Zimin, A. Hoori, N. S. Hassani, M. H. E. Makhlouf, G. Guagliumi, H. G. Bezerra, and D. L. Wilson, "Deep learning segmentation of fibrous cap in intravascular optical coherence tomography images," *Scientific Reports*, vol. 14, no. 1, p. 4393, 2024.

[322] H. Li, M. Bhatt, Z. Qu, S. Zhang, M. C. Hartel, A. Khademhosseini, and G. Cloutier, "Deep learning in ultrasound elastography imaging: A review," *Medical physics*, vol. 49, no. 9, pp. 5993–6018, 2022.

[323] J. M. Scott, A. Arani, A. Manduca, K. P. McGee, J. D. Trzasko, J. Huston, R. L. Ehman, and M. C. Murphy, "Artificial neural networks for magnetic resonance elastography stiffness estimation in inhomogeneous materials," *Medical image analysis*, vol. 63, p. 101 710, 2020.

[324] Y. Yu, X. Si, C. Hu, and J. Zhang, "A review of recurrent neural networks: Lstm cells and network architectures," *Neural computation*, vol. 31, no. 7, pp. 1235–1270, 2019.

[325] S. Hochreiter, "Long short-term memory," *Neural computation*, vol. 9, no. 8, pp. 1735–1780, 1997.

[326] K. Cho, B. van Merriënboer, C. Gulcehre, D. Bahdanau, F. Bougares, H. Schwenk, and Y. Bengio, "Learning phrase representations using rnn encoder-decoder for statistical machine translation," *arXiv preprint arXiv:1406.1078*, 2014.

[327] N. Ballas, L. Yao, C. Pal, and A. Courville, "Delving deeper into convolutional networks for learning video representations," *arXiv preprint arXiv:1511.06432*, 2015.

[328] M. Siam, S. Valipour, M. Jagersand, and N. Ray, "Convolutional gated recurrent networks for video segmentation," in *2017 IEEE International Conference on Image Processing (ICIP)*, 2017, pp. 3090–3094.

[329] C. Wang, Y. Jin, X. Chen, and Z. Liu, "Automatic classification of volumetric optical coherence tomography images via recurrent neural network," *Sensing and Imaging*, vol. 21, no. 1, 2020.

[330] D. Schwartz, T. W. Sawyer, N. Thurston, J. Barton, and G. Ditzler, "Ovarian cancer detection using optical coherence tomography and convolutional neural networks," *Neural computing & applications*, vol. 34, no. 11, pp. 8977–8987, 2022.

[331] D. Romo-Bucheli, U. S. Erfurth, and H. Bogunovic, "End-to-end deep learning model for predicting treatment requirements in neovascular amd from longitudinal retinal oct imaging," *IEEE journal of biomedical and health informatics*, vol. 24, no. 12, pp. 3456–3465, 2020.

[332] D. M. Rajani, F. Seghizzi, Y.-L. Lai, K. G. Buchta, and M. Draelos, "Dynamics-aware deep predictive adaptive scanning optical coherence tomography," *Biomedical Optics Express*, vol. 16, no. 1, p. 186, 2025.

[333] S. Pannek, S. Dehghani, M. Sommersperger, P. Zhang, P. Gehlbach, M. A. Nasseri, I. Iordachita, and N. Navab, "Exploring the needle tip interaction force with retinal tissue deformation in vitreoretinal surgery," in *2024 IEEE International Conference on Robotics and Automation (ICRA)*, 2024, pp. 16 999–17 005.

[334] A. Dosovitskiy, L. Beyer, A. Kolesnikov, D. Weissenborn, X. Zhai, T. Unterthiner, M. Dehghani, M. Minderer, G. Heigold, S. Gelly, J. Uszkoreit, and N. Houlsby, "An image is worth 16x16 words: Transformers for image recognition at scale," *arXiv preprint arXiv:2010.11929*, 2020.

[335] D. Song, B. Fu, F. Li, J. Xiong, J. He, X. Zhang, and Y. Qiao, "Deep relation transformer for diagnosing glaucoma with optical coherence tomography and visual field function," *IEEE transactions on medical imaging*, vol. 40, no. 9, pp. 2392–2402, 2021.

[336] C. Playout, R. Duval, M. C. Boucher, and F. Cheriet, "Focused attention in transformers for interpretable classification of retinal images," *Medical image analysis*, vol. 82, p. 102 608, 2022.

[337] J. Shen, Y. Hu, X. Zhang, Y. Gong, R. Kawasaki, and J. Liu, "Structure-oriented transformer for retinal diseases grading from oct images," *Computers in Biology and Medicine*, vol. 152, p. 106 445, 2023.

[338] Y. Zhou, M. A. Chia, S. K. Wagner, M. S. Ayhan, D. J. Williamson, R. R. Struyven, T. Liu, M. Xu, M. G. Lozano, P. Woodward-Court, Y. Kihara, A. Altmann, A. Y. Lee, E. J. Topol, A. K. Denniston, D. C. Alexander, and P. A. Keane, "A foundation model for generalizable disease detection from retinal images," *Nature*, vol. 622, no. 7981, pp. 156–163, 2023.

[339] Y. Peng, A. Lin, M. Wang, T. Lin, L. Liu, J. Wu, K. Zou, T. Shi, L. Feng, Z. Liang, T. Li, D. Liang, S. Yu, D. Sun, J. Luo, L. Gao, X. Chen, C.-Y. Cheng, H. Fu, and H. Chen, "Enhancing ai reliability: A foundation model with uncertainty estimation for optical coherence tomography-based retinal disease diagnosis," *Cell Reports Medicine*, vol. 6, no. 1, p. 101 876, 2024.

[340] G. Li, K. Wang, Y. Dai, D. Zheng, K. Wang, L. Zhang, and T. Kamiya, "Physics-based optical coherence tomography angiography (octa) image correction for shadow compensation," *IEEE Transactions on Biomedical Engineering*, pp. 1–8, 2024.

[341] J. Liao, S. Yang, T. Zhang, C. Li, and Z. Huang, "A hand-held optical coherence tomography angiography scanner based on angiography reconstruction transformer networks," *Journal of Biophotonics*, vol. 16, no. 9, e202300100, 2023.

[342] Z. Tan, F. Shi, Y. Zhou, J. Wang, M. Wang, Y. Peng, K. Xu, M. Liu, and X. Chen, "A multi-scale fusion and transformer based registration guided speckle noise reduction for oct images," *IEEE transactions on medical imaging*, vol. 43, no. 1, pp. 473–488, 2024.

[343] D. Philippi, K. Rothaus, and M. Castelli, "A vision transformer architecture for the automated segmentation of retinal lesions in spectral domain optical coherence tomography images," *Scientific Reports*, vol. 13, no. 1, p. 517, 2023.

[344] X. Tan, X. Chen, Q. Meng, F. Shi, D. Xiang, Z. Chen, L. Pan, and W. Zhu, "Oct2former: A retinal oct-angiography vessel segmentation transformer," *Computer Methods and Programs in Biomedicine*, vol. 233, p. 107 454, 2023.

[345] G. Cao, S. Zhang, H. Mao, Y. Wu, D. Wang, and C. Dai, "A single-step regression method based on transformer for retinal layer segmentation," *Physics in Medicine and Biology*, vol. 67, no. 14, p. 145 008, 2022.

[346] G. Schreiber, A. Stemmer, and R. Bischoff, "The fast research interface for the kuka lightweight robot," in *IEEE workshop on innovative robot control architectures for demanding (Research) applications how to modify and enhance commercial controllers (ICRA 2010)*, 2010, pp. 15–21.

[347] J. Roy and L. L. Whitcomb, "Adaptive force control of position/velocity controlled robots: Theory and experiment," *IEEE Transactions on Robotics and Automation*, vol. 18, no. 2, pp. 121–137, 2002.

[348] J. Su, M. Ahmed, Y. Lu, S. Pan, W. Bo, and Y. Liu, "Roformer: Enhanced transformer with rotary position embedding," *Neurocomputing*, vol. 568, p. 127 063, 2024.

[349] T. Dao, D. Fu, S. Ermon, A. Rudra, and C. Ré, "Flashattention: Fast and memory-efficient exact attention with io-awareness," *Advances in Neural Information Processing Systems*, vol. 35, pp. 16 344–16 359, 2022.

[350] B. Guiu, T. de Baère, G. Noel, and M. Ronot, "Feasibility, safety and accuracy of a ct-guided robotic assistance for percutaneous needle placement in a swine liver model," *Scientific Reports*, vol. 11, no. 1, p. 5218, 2021.

[351] M. Ferro, C. Gaz, M. Anzidei, and M. Vendittelli, "Online needle-tissue interaction model identification for force feedback enhancement in robot-assisted interventional procedures," *IEEE Transactions on Medical Robotics and Bionics*, vol. 3, no. 4, pp. 936–947, 2021.

[352] Y. Fukushima, K. Saito, and K. Naemura, "Estimation of the cutting force using the dynamic friction coefficient obtained by reaction force during the needle insertion," *Procedia CIRP*, vol. 5, pp. 265–269, 2013.

[353] W. Liu, Z. Yang, P. Li, J. Zhang, and S. Jiang, "Mechanics of tissue rupture during needle insertion in transverse isotropic soft tissue," *Medical and Biological Engineering and Computing*, vol. 57, no. 6, pp. 1353–1366, 2019.

[354] M. Terzano, D. Dini, F. Rodriguez y Baena, A. Spagnoli, and M. Oldfield, "An adaptive finite element model for steerable needles," *Biomechanics and Modeling in Mechanobiology 2020 19:5*, vol. 19, no. 5, pp. 1809–1825, 2020.

[355] X. Xuan, Y. Yang, Z. Wang, S. Deng, and X. Liu, "Force modeling for needle insertion into corneal tissue," *Gaojishu Tongxin/Chinese High Technology Letters*, vol. 19, no. 9, pp. 951–956, 2009.

[356] B. J. Briscoe, K. S. Sebastian, and M. J. Adams, "The effect of indenter geometry on the elastic response to indentation," *Journal of Physics D: Applied Physics*, vol. 27, no. 6, pp. 1156–1162, 1994.

[357] C. T. McKee, J. A. Last, P. Russell, and C. J. Murphy, "Indentation versus tensile measurements of young's modulus for soft biological tissues," *Tissue engineering. Part B, Reviews*, vol. 17, no. 3, pp. 155–164, 2011.

[358] Z. Han, J. Li, M. Singh, C. Wu, C.-h. Liu, S. Wang, R. Idugboe, R. Raghunathan, N. Sudheendran, S. R. Aglyamov, M. D. Twa, and K. V. Larin, "Quantitative methods for reconstructing tissue biomechanical properties in optical coherence elastography: A comparison study," *Physics in Medicine and Biology*, vol. 60, no. 9, pp. 3531–3547, 2015.

[359] J. J. Pitre, M. A. Kirby, D. S. Li, T. T. Shen, R. K. Wang, M. O'Donnell, and I. Pelivanov, "Nearly-incompressible transverse isotropy (niti) of cornea elasticity: Model and experiments with acoustic micro-tapping oce," *Scientific Reports*, vol. 10, no. 1, p. 12 983, 2020.

[360] H. C. Liu, M. Abbasi, Y. H. Ding, T. Roy, M. Capriotti, Y. Liu, S. Fitzgerald, K. M. Doyle, M. Guddati, M. W. Urban, and W. Brinjikji, "Characterizing blood clots using acoustic radiation force optical coherence elastography and ultrasound shear wave elastography," *Physics in Medicine and Biology*, vol. 66, no. 3, p. 35 013, 2021.

[361] J. R. Rippy, M. Singh, S. R. Aglyamov, and K. V. Larin, "Ultrasound shear wave elastography and transient optical coherence elastography: Side-by-side comparison of repeatability and accuracy," *IEEE Open Journal of Engineering in Medicine and Biology*, vol. 2, pp. 179–186, 2021.

[362] A. B. Rosenkrantz, S. Verma, P. Choyke, S. C. Eberhardt, S. E. Eggener, K. Gaitonde, M. A. Haider, D. J. Margolis, L. S. Marks, P. Pinto, G. A. Sonn, and S. S. Taneja, "Prostate magnetic resonance imaging and magnetic resonance imaging targeted biopsy in patients with a prior negative biopsy: A consensus statement by aua and sar," *The Journal of Urology*, vol. 196, no. 6, pp. 1613–1618, 2016.

[363] M. Oderda, G. Marra, S. Albisinni, E. Altobelli, E. Baco, V. Beatrici, A. Cantiani, A. Carbone, M. Ciccariello, J.-L. Descotes, M. Dubreuil-Chambardel, D. Eldred-Evans, G. Fasolis, M. Ferriero, G. Fiard, V. Forte, A. Giacobbe, P. Kumar, V. Lacetera, P. Mozer, G. Muto, R. Papalia, A. Pastore, A. Peltier, T. Piechaud, G. Simone, J.-B. Roche, M. Roupret, O. Rouviere, R. van Velthoven, and P. Gontero, "Accuracy of elastic fusion biopsy in daily practice: Results of a multicenter study of 2115 patients," *International Journal of Urology*, vol. 25, no. 12, pp. 990–997, 2018.

[364] Q. Fang, S. Choi, A. Taba, D. D. Lakhiani, K. Newman, R. Zilkens, R. W. Sanderson, B. F. Dessauvagie, C. M. Saunders, and B. F. Kennedy, "Stereoscopic optical palpation for tumour margin assessment in breast-conserving surgery," *Optics and Lasers in Engineering*, vol. 166, p. 107 582, 2023.

[365] J. Jordan, N. Jaitner, T. Meyer, L. Bramè, M. Ghrayeb, J. Köppke, O. Böhm, S. K. Chandia, V. Zaburdaev, L. Chai, H. Tzschätzsch, J. Mura, J. Braun, A. I. H. Hagemann, and I. Sack, "Rapid stiffness mapping in soft biologic tissues with micrometer resolution using optical multifrequency time-harmonic elastography," *Advanced science*, vol. 12, no. 8, e2410473, 2025.

[366] L. P. Carvalho, A. Agarwal, F. T. Kashiwagi, I. Corrêa, J. E. G. Pereira, and R. El Dib, "Commonly-used versus less commonly-used methods in the loss of resistance technique for identification of the epidural space: A systematic review and meta-analysis of randomized controlled trials," *Journal of Clinical Anesthesia*, vol. 38, pp. 41–51, 2017.

[367] R. R. Postema, D. Cefai, B. van Straten, R. Miedema, L. L. Hardjo, J. Dankelman, F. Nickel, and T. Horeman-Franse, "A novel veress needle mechanism that reduces overshooting after puncturing the abdominal wall," *Surgical endoscopy*, vol. 35, no. 10, pp. 5857–5866, 2021.